

**Development of Near Infrared Emitting Cationic Ag₂S
Quantum Dots as Drug-Gene Delivery and Optical Imaging
Agents**

by

Fatma Demir Duman

**A Thesis Submitted to the
Graduate School of Sciences and Engineering
in Partial Fulfillment of the Requirements for
the Degree of**

Doctor of Philosophy

in

Material Science and Engineering

Koc University

January 2017

Koc University
Graduate School of Sciences and Engineering

This is to certify that I have examined this copy of a Ph.D. thesis by

Fatma Demir Duman

and have found that it is complete and satisfactory in all respects,
and that any and all revisions required by the final
examining committee have been made.

Committee Members:

Havva F. Yağcı Acar, Ph. D. (Advisor)

Halil Kavaklı, Ph. D.

Uğur Ünal, Ph. D.

Duygu Avcı Semiz, Ph. D.

Engin Ulukaya, Ph. D.

Date:

ABSTRACT

Luminescent quantum dots (QDs) are widely studied in optical imaging, luminescent labelling, drug/gene delivery and for the combination of these. QDs are remarkable optical probes since they offer size tunable strong luminescence along with large absorption coefficients across a wide spectral range, long luminescence lifetime and superior stability against photo bleaching, allowing simultaneous detection and long working times. However, despite of such great promise, there is no clinical use of QDs, mostly due to the toxicity of the commercially available and most frequently used QDs and their emission in the visible range (400-700 nm). Visible light has low photon penetration depth, absorbed and scattered by some biological constituents. Besides, auto-fluorescence of collagen in the living tissue, decreases the contrast. On the other hand, emission in the near infrared I (NIR-I) (700-900 nm) offers high-resolution, high sensitivity, deeper penetration of light providing lower signal loss and thus greater signal/background ratio. Therefore, NIR emitting QDs have emerged as a new class of fluorescent probes for biological/medical use in the recent years. Ag₂S QDs are the most promising NIR-emitting QDs with high cytocompatibility compared to heavy metal containing, more traditional QDs such as PbS, PbSe, CdHgTe.

In this thesis work, we aimed to develop cytocompatible, cationic Ag₂S NIRQDs with strong emission in the NIR I as theranostic nanoparticles to deliver genes or drugs to target cells and provide strong optical signal in the cells to detect the location of the delivery vehicle. Another objective of this work is to produce such QDs in a simple, green and economically viable way.

Briefly, cationic Ag₂S NIRQDs have been synthesized in a very simple one step aqueous synthetic route with a mixed coating of branched polyethyleneimine (PEI) and small capping agents at low temperatures. Molecular weight of the PEI (25kDa to 1.8 kDa), type of small molecule and PEI/small molecule ratio as well as the Ag/S, Ag/coating ratio, reaction duration, temperature and pH were all studied to tune emission wavelength and to maximize the colloidal stability, luminescence quantum yield while keeping the size small and transfection efficiency high. 2-mercaptopropionic acid (2MPA), l-cysteine (Cys), l-arginine,

l-histidine and l-glutamic acid were tested as the small molecule component of the coating. These small molecules were chosen based on their functionalities, in case of the amino acids based on the side chain functionality. Low molecular weight PEI and small molecules without the thiol functionality have failed to produce colloiddally stable and luminescent Ag₂S. PEI coated Ag₂S does not luminesce, but the ones with the mixed coating are strongly luminescent in the NIR I region. Best composition was determined as PEI/2MPA (80/20 mol/mol %) and PEI/Cys (60/40 mol/mol %) coatings, Ag/S ratio of 4 and coating/Ag of 5. Incorporation of 2MPA and Cys as a co-stabilizer reduced the surface defects on the crystal surface formed due to the inability of polymeric coating in providing a dense surface adsorption. This provided non-radiative events and hence provided strong luminescence. The most important results needed to be emphasized that the resulting quantum dots (1) have the highest quantum yield reported for Ag₂S QDs until now (150 % - 157 % at pH 7.4 with respect to LDS 798 NIR dye), (2) are the first cationic ones of this class, (3) are smaller than 100 nm which is suitable for targeting and *in vivo* applications.

The *in vitro* and *in vivo* optical imaging studies performed in cellular level, in worms and mice showed that Ag₂S NIRQDs are very promising optical agents with efficient cell internalization and strong luminescence. Cationic nature of the particles was exploited for gene delivery using a standard gene, green fluorescent protein (GFP) and higher transfection efficiency was recorded especially with PEI(25kDa)/2MPA coated Ag₂S QDs compared to commercial transfection reagents.

The nanoparticles were also PEGylated to increase their biocompatibility further, and used for delivery of an anticancer drug, Doxorubicin, to cancer cells, *in vitro*. Selective delivery of nanoparticles via receptor-mediated endocytosis was also demonstrated via folic acid conjugation, which preferentially delivered DOX loaded Ag₂S QDs to FR positive cell lines, inducing a strong apoptotic mechanism. In another study, the PEGylated nanoparticles were loaded with p53-GFP gene, a tumor suppressor gene, and used in the p53 -/- cancer cell lines. However, the transfection ability of the QDs dropped dramatically after PEGylation.

Overall, within the scope of this thesis work, the very first and currently only cationic Ag₂S NIRQDs was produced in an industrially feasible one step green synthesis, with the

highest quantum yield ever reported for any Ag_2S NIRQDs with excellent stability over 4 years now and in small sizes, allowing drug and gene delivery, molecular targeting and optical imaging. This work provides a practical QD composition which has high potential for clinical use.



ÖZET

Lüminesan kuantum noktacıklar (KNlar), optik görüntüleme, lüminesan etiketleme ve ilaç/gen salımında ve bunların kombine tedavilerinde sıklıkla çalışılmaktadır. Geniş spektral bölgede büyük absorpsiyon faktörü ile boyut ayarlanabilir güçlü lüminesan, uzun lüminesan ömrü ve eş zamanlı tespit ve uzun çalışma süresine izin veren, foto sönmelenmeye karşı üstün kararlılıkları ile KNlar dikkat çekici optik problemlerdir. Fakat, bu kadar muazzam umut veren özelliklerine rağmen KNlar, ticari olarak kullanılanları ve sıklıkla kullanılanlarının yüksek toksisiteye sahip olması ve görünür bölgede (400-700 nm) ışığa vermeleri nedeniyle klinik olarak kullanıma sahip değildirler. Görünür ışık, düşük foton penetrasyon derinliği, bazı biyolojik yapıların absorpsiyonu veya ışık saçılımına sahiptir. Ayrıca, canlı hücrelerdeki kolajenin otofloresansı da kontrastın azalmasına neden olur. Diğer taraftan, yakın kızılötesi bölge-I (700-900 nm) deki emisyon daha düşük sinyal kaybı ve böylece daha büyük sinyal/arka plan oranı sağlayarak yüksek çözünürlük, yüksek hassasiyet ve daha derin ışık penetrasyonu sunar. Bu yüzden, son yıllarda biyolojik/medikal kullanım için floresan problemlerin yeni bir sınıfı olarak yakın kızılötesi ışık veren kuantum noktacıklar ortaya çıkmıştır. Ag_2S KNlar, PbS , $PbSe$, $CdHgTe$ gibi ağır metal içeren, daha geleneksel KNlara göre yüksek sitokompatibiliteleri ile en umut verici yakın kızılötesi KNlardır.

Bu tez çalışmasında, gen ve ilaçları hedef hücrelere göndermek için ve salım ajanının hücrede lokasyonunu ve tespitini sağlayacak, güçlü optik sinyale sahip teranöстик nanoparçacıklar olarak, yakın kızılötesi-I de güçlü emisyonları ile biyoyumlu, katyonik Ag_2S yakın kızılötesi kuantum noktacıkları geliştirmeyi amaçlıyoruz. Bu tez çalışmasının diğer bir amacı ise, bu özellikteki KNları basit, güvenli ve ekonomik olarak uygulanabilir yol ile üretmektir.

Kısaca, katyonik Ag_2S yakın kızılötesi KNlar basit, tek basamaklı, suda sentez yöntemi ile dallı polietileniminleri (PEI) ve küçük kaplama ajanlarını düşük sıcaklıkta karıştırarak üretilmişlerdir. Boyutunu küçük ve transfeksiyon verimini yüksek tutarak emisyon dalgaboyunu ayarlamak ve kolloidal kararlılığı ve lüminesan kuantum verimini maksimize etmek için Ag/S , Ag /kaplama oranı, reaksiyon zamanı, sıcaklık ve pH ile birlikte PEI nin

(25kDa'dan 1.8 kDa'a) moleküler ağırlığının, küçük molekül çeşidinin, PEI/küçük molekül oranının etkisi çalışılmıştır. 2-merkaptopropionik asit (2MPA), l-sistein (Cys), l-arjinin, l-histidin ve l-glutamik asit, kaplamanın küçük molekül bileşenleri olarak çalışılmıştır. Bu küçük moleküller, fonksiyonelliklerine göre, amino asit olduklarında ise yan gruplarına göre seçilmişlerdir. Düşük moleküler ağırlıktaki PEI ve tiyol fonksiyonsuz küçük moleküller, kolloidal olarak kararlı ve lüminesan Ag₂S üretmede başarısız olmuşlardır. Sadece PEI kaplı Ag₂S lüminesan vermezken, küçük moleküllerle olan karışık kompozisyonları yakın kızılötesi-I bölgesinde güçlü lüminesan vermişlerdir. En iyi kompozisyonlar, PEI/2MPA (80/20 mol/mol %) ve PEI/Cys (60/40 mol/mol %) kaplamalı, Ag/S'ün 4 ve kaplama/Ag'ün 5 olduğu oranlar olarak karar verilmiştir. 2MPA'in ve Cys'in kostabilizör olarak kullanılması yoğun yüzey adsorpsiyonu sağlayarak polimerik kaplamanın yeteneksizliğinden dolayı kristal yüzeyinde oluşan yüzey hatalarını azaltır. Bu, ışınımsal olmayan olayları azaltır ve böylece güçlü lüminesan sağlar. Elde edilen KNların vurgulanması gereken en önemli sonuçları (1) KNların, şu ana kadar rapor edilen Ag₂S KNlar içinde en yüksek kuantum verimine sahip olanlar olmaları (LDS 798 yakın kızılötesi boyaya göre pH 7.4'te % 150- % 157 kuantum verimi), (2) bu sınıfın ilk katyonik olanları olması, (3) 100 nm'den küçük olmaları sayesinde *in vivo* ve hedefleme çalışmaları için uygun olmalarıdır. Hücresel seviyede, kurtçuklarda ve farelerde yapılan *in vitro* ve *in vivo* optik görüntüleme çalışmaları Ag₂S yakın kızılötesi kuantum noktalarının etkili hücre internalizasyonu ve güçlü lüminesanı ile oldukça umut vadeden optik ajanlar olduğunu göstermiştir. Parçacıkların katyonik doğası, standart bir gen olan yeşil floresan proteini (YFP) ile gösterilmiş ve özellikle PEI(25 kDa)/2MPA kaplı Ag₂S KNlar ile ticari transfeksiyon ajanlara göre daha yüksek transfeksiyon verimi elde edilmiştir. Nanoparçacıklar, biyouyumluluklarını daha da arttırmak için ayrıca PEGlenmişleridir ve antikanser bir ilaç olan doksorubisinin kanser hücrelerine *in vitro* olarak salımı için kullanılmışlardır. Folik asit konjugasyonu ile tercihen DOX yüklü Ag₂S leri folik asit reseptörü pozitif hücre hatlarına göndererek, güçlü apoptoz mekanizması indüklenmiş ve reseptör aracılı endositoz ile nanoparçacıkların seçici olarak salımı gösterilmiştir. Başka bir çalışmada, PEGlenmiş nanoparçacıklar, bir tümör baskılayıcı gen olan p53-GFP geni ile

yüklenmiş ve p53 -/- kanser hücre hatlarında kullanılmışlardır. Fakat, PEGilasyondan sonra KNların transfeksiyon yeteneği dramatik bir şekilde düşmüştür.

Sonuç olarak, bu tez çalışmasının amacı dahilinde, endüstriyel olarak uygulanabilir tek basamaklı güvenilir sentez ile şimdiye kadarki Ag₂S KNlar içinde rapor edilmiş en yüksek kuantum verimli, şimdiden 4 seneyi aşkın süredir mükemmel kararlılığa sahip ve ilaç ve gen salımı, moleküler hedefleme ve optik görüntülemeye izin veren küçük boyutlu Ag₂S KNlar üretilmiştir. Bu çalışma, klinik uygulamalar için yüksek potansiyele sahip, pratik bir KN kompozisyonunu sağlamaktadır.



*Dedicated to my lovely husband,
Ali Duman.*

ACKNOWLEDGEMENTS

First of all, I would like to thank to my supervisor, Assoc. Prof. Havva Funda Yağcı Acar for her guidance, great support, trust, patience and encouragement throughout my PhD research studies and also in my life. Her positive perspective and confidence in me, made me more productive. When I fell into despair, she was my Savior. I feel infinite compassion, sincerity, sympathy and endless energy when I look into her eyes. I am deeply indebted to her.

I am deeply grateful to my old and dear friend Caner Nazlı for introducing me to Funda Hoca and his support during my PhD.

I would like to thank Assoc. Prof. Uğur Ünal for his support, understanding, sincerity, friendly attitude, empathy and help in every issue that I needed his contribution or guidance during my PhD.

I would like to express my gratitude to my thesis committee members Prof. Halil Kavaklı, Prof. Duygu Avcı Semiz, Prof. Engin Ulukaya and Assoc. Prof. Uğur Ünal for their attention, suggestions and time that they have devoted for the evaluation of my thesis. I am also grateful to them for their guidance and assistance that they have provided during my studies.

I would like to thank to many valuable and respectable collaborators, as well. I am very grateful to Assoc. Prof. Özgür Birer and Assoc. Prof. Uğur Ünal for establishing a home-made photoluminescence measurement set up to be able to record the near IR emission intensities of our quantum dots. I would like to thank Assoc. Prof. Devrim Gözüaçık and his humble PhD students, Deniz Gülfem Öztürk and Yunus Akkoç for their invaluable contributions to in vitro evaluation of the particles. I am deeply grateful to Prof. Engin Ulukaya, Assoc. Prof. Ferda Arı and their hardworking student Merve Erkisa for their tremendous support and valuable contributions to the detailed cytotoxicity studies of the

particles developed in this thesis. I would like to express my appreciation to Prof. Alper Kiraz for his support on the NIR confocal laser scanning microscope imaging which was essential to prove the imaging modality of the particles. I would like to thank Assist. Prof. Halil Bayraktar, Assist Prof. Nathan Lack and Selçuk Çakmak who provided help with the Live Cell Imaging Microscope System. I would like to thank Dr. Rouhullah Khodadust for in vivo imaging studies. I am very grateful to Assist Prof. Funda Şar and her dear students Fatma Sevde Coşkun and Hale Şiir Hasdemir for their work on the C.Elegans.

I deeply appreciate the assistance, patience and friendship of Koç University Surface Technology Research Center (KUYTAM) team, Dr. Barış Yağcı, Cansu Yıldırım, Dr. Natali Çizmeciyan Sözüdoğru and Dr. Gülsu Şimsek.

I would like to thank to Koç University, Graduate School of Sciences and Engineering and The Scientific and Technological Research Council of Turkey for the funding.

I am deeply grateful to Dr. İbrahim Hocaoğlu for his friendship, trust, guidance, contributions to my studies and his never ending positive attitude. I would like to thank Didar Aşık for her endless energy, friendship and help on in vitro studies.

I would like to express my sincere thanks to Dr. Umut Aydemir and Dr. Ahmet Tuna Bölükbaşı for their friendship, motivation, support, guidance and encouragement. They are my heroes.

I would like to thank my former and present office-mates Dr. Ali Bateni, Müjde Yahyaoğlu, Kübra Bilici, Zeynep Gizem Narin and Meltem İpekçi for their friendship and support during my PhD.

I would like to express my sincere thanks to members of “Polymers and Nanomaterials Research Group”: my dear friends Özlem Ünal, Özge Çavuşlar, Enes Buz, Gökay Avcı,

Pelin Turhan, İrem Ülkü, Gözde Demirci, Kübra Bilici, Mona Nejatpour, Emek Durmuşođlu and Yasemin Yar for their friendship, support, help on almost everything and for making me feel better. I am deeply indebted to them.

I would like to express my sincere thanks to my family. I am very grateful to my mother Nihal Demir, my father Mehmet Demir, my sister Gülşah Demir and my brother Kadir Demir for their endless, unconditional support, trust, encouragement, guidance and love throughout my whole life. I would like to also thank my second family, my mother Suna Duman, my father İsmail Duman and my sister Özgür Sezgi Duman for their support, motivation, trust, understanding and the love.

Finally, many thanks to sun of my life, my beloved husband Ali Duman for his continuous and unfailing love, unconditional support, understanding, guidance, motivation, trust and encouragement during my PhD and in my life. He is who I have dedicated this thesis and my life.

TABLE OF CONTENTS

TABLE OF CONTENTS	xiii
LIST OF TABLES	xix
LIST OF FIGURES	xxi
LIST OF SCHEME	xxxiii
NOMENCLATURE	xxxiv
1. INTRODUCTION	1
1.1 Quantum Dots.....	1
1.2 Size Dependent Energy Band Gap and Quantum Confinement.....	2
1.3 Mechanism of Fluorescence.....	6
1.4 Synthesis of QDs	8
1.5 Biomedical Applications of QDs	11
1.6 Near Infra-Red Emitting Quantum Dots (NIRQDs) as Optical Bioimaging Agents	14
1.6.1 Ag ₂ S NIRQDs	17
1.6.2 Ag ₂ S QDs developed in our group	23
1.7 Gene and Drug Delivery.....	26
1.7.1 Gene Delivery.....	26
1.7.2 Drug Delivery.....	30
1.8 Proposal and Aim of This Thesis Work	32
2. SYNTHESIS AND CHARACTERIZATION OF PEI/2MPA COATED CATIONIC Ag₂S NIR-EMITTING QUANTUM DOTS AND GENE TRANSFECTION	37
2.1 Introduction	37
2.2 Materials and Methods	40
2.2.1 Materials.....	40
2.2.2 Preparation of PEI and 2MPA coated Ag ₂ S QDs.....	41
2.2.3 Characterization Methods.....	42
2.2.4 Cell lines, cell culture.....	43

2.2.5 Gene Delivery.....	43
2.2.6 Cytotoxicity assay	44
2.2.7 In vitro cell imaging	45
2.2.8 In vivo imaging studies	45
2.3 Results and Discussions	46
2.3.1 PEI coated NIR-emitting Ag ₂ S quantum dots.....	46
2.3.1.1 Influence of Ag/S mole ratio on particle properties.....	46
2.3.1.2 Influence of Ag/PEI ratio on particle properties	47
2.3.2 PEI/2MPA coated NIR-emitting Ag ₂ S quantum dots.....	47
2.3.2.1 Influence of reaction time on particle properties.....	47
2.3.2.2 Influence of PEI/2MPA ratio on particle properties	48
2.3.2.3 Influence of the pH on particle properties.....	51
2.3.2.4 Influence of the reaction temperature.....	55
2.3.2.5 Long term stability of Ag ₂ S-PEI/2MPA QDs.....	56
2.3.3 Particle characterization	57
2.3.4 Cytocompatibility of quantum dots.....	59
2.3.5 In vitro cell internalization and optical imaging	61
2.3.6 In vivo imaging	62
2.3.7 Use of Ag ₂ S-PEI/2MPA NIRQDs as in vitro transfection agents.....	64
2.4 Conclusions	67
3. PEGYLATION OF CATIONIC Ag₂S NIRQDs FOR DRUG AND GENE DELIVERY IN CANCER TREATMENT	69
3.1 Introduction	69
3.2 Materials and Methods	71
3.2.1 Materials.....	71
3.2.2 Preparation of PEI/2MPA coated Ag ₂ S (Ag ₂ S) NIRQDs	72
3.2.3 Preparation of CDI-activated methoxy-PEG (mPEG-CDI)	72
3.2.4 PEGylation of Ag ₂ S NIRQDs	73
3.2.5 DOX loading on PEGylated Ag ₂ S QDs	73

3.2.6 Characterization methods	74
3.2.7 Cell culture	75
3.2.8 In vitro cytotoxicity studies	75
3.2.9 In vitro cell imaging	76
3.2.10 PI cell cycle analysis	76
3.2.11 Immunoblotting	76
3.2.12 In vitro transfection studies	77
3.2.13 Statistical analysis	78
3.3 Results and Discussion	79
3.3.1 Characterization of mPEG-Ag ₂ S QDs	79
3.3.2 Assessment of in vitro cytotoxicity	80
3.3.3 Microscopy Studies	82
3.3.4 Evaluation of Cell Cycle Analysis	83
3.3.5 Evaluation of immunoblotting	85
3.3.6 Transfection Studies	86
3.4 Conclusion	88
4. EVALUATION OF PEI/AMINO ACID COMBINATIONS AS A COATING AND DEVELOPMENT OF PEI/L-CYSTEINE COATED CATIONIC Ag₂S QUANTUM DOTS AS THERANOSTIC NANOPARTICLES	90
4.1 Introduction	90
4.2 Materials and methods	92
4.2.1 Materials	92
4.2.2 Preparation of PEI and amino acid coated Ag ₂ S QDs	92
4.2.3 Preparation of PEI and Cys coated Ag ₂ S QDs	93
4.2.4 Characterization methods	94
4.2.5 Cell culture	96
4.2.6 Cytotoxicity assay	96
4.2.7 In vitro cell imaging	96
4.2.8 In vivo imaging	97

4.2.9 In vitro transfection studies	97
4.2.10 Statistical analysis	98
4.3 Results and Discussion	98
4.3.1 Influence of PEI molecular weight and amino acids on Ag ₂ S QDs.....	98
4.3.1.1 PEI-25 kDa Ag ₂ S QDs	99
4.3.1.1.a L-arginine and l-arginine/PEI (branched, 25 kDa) Ag ₂ S QDs	99
4.3.1.1.b L-Glutamic acid and l-glutamic acid /PEI (branched, 25 kDa) Ag ₂ S QDs	99
4.3.1.1.c L-histidine and l-histidine/PEI (branched, 25 kDa) Ag ₂ S QDs...	100
4.3.1.1.d L-cysteine and l-cysteine/PEI (branched, 25 kDa) Ag ₂ S QDs....	101
4.3.1.2 PEI-10 kDa Ag ₂ S QDs	101
4.3.1.2.a PEI (branched, 10 kDa) coated Ag ₂ S	101
4.3.1.2.b PEI (branched, 10 kDa)/l-cysteine Ag ₂ S QDs.....	102
4.3.1.2.c PEI (branched, 10 kDa)/2MPA Ag ₂ S QDs.....	103
4.3.1.3 PEI-1.8 kDa Ag ₂ S QDs	103
4.3.1.3.a PEI (branched, 1.8 kDa)/cysteine Ag ₂ S QDs	103
4.3.1.3.b PEI (branched, 1.8 kDa)/2MPA Ag ₂ S QDs	104
4.3.2 Synthesis and optical characterization of PEI/Cys Ag ₂ S QDs	104
4.3.3 Characterization of PEI/Cys coated Ag ₂ S QDs.....	113
4.3.4 Evaluation of in vitro cytotoxicity of Ag ₂ S QDs	117
4.3.5 In vitro and in vivo optical imaging	119
4.3.6 In vitro transfection studies	121
4.3.6.1 GFP/PEI/Cys Ag ₂ S QDs	121
4.3.6.2 p53-GFP / PEI/cys Ag ₂ S QDs	122
4.4 Conclusions	125
5. TUMOR-TARGETED THERAPY OF FOLIC ACID CONJUGATED DOX LOADED Ag₂S NIRQDS	128

5.1 Introduction	128
5.2 Materials and Methods	130
5.2.1 Materials	130
5.2.2 Synthesis of Ag ₂ S NIRQDs.....	131
5.2.3 Preparation of FA–PEG-COOH conjugate	131
5.2.4 Preparation of FA–PEG-Ag ₂ S NIRQDs.....	131
5.2.5 DOX loading on FA-PEG-Ag ₂ S NIRQDs	133
5.2.6 Characterization Methods.....	133
5.2.7 Cell culture	134
5.2.8 In vitro cytotoxicity studies	134
5.2.8.1 MTT assay	134
5.2.8.2 ATP assay.....	135
5.2.9 Intracellular uptake of QDs	135
5.2.10 Apoptosis and Necrosis	136
5.2.10.1 Annexin V-FITC/PI apoptosis assay	136
5.2.10.2 M30 Assay.....	136
5.2.10.3 Mitochondrial membrane potential ($\Delta\psi_m$) analysis.....	136
5.2.11 Statistical Analysis	137
5.3 Results and Discussion.....	137
5.3.1 Preparation and characterization of Ag ₂ S, FA-PEG-Ag ₂ S and DOX loaded FA-PEG-Ag ₂ S NIRQDs.....	137
5.3.2 In vitro cytotoxicity studies.....	140
5.3.3 Cellular Uptake.....	142
5.3.4 Determination of Apoptosis and Necrosis.....	144
5.4 Conclusion.....	147
6. CONCLUSIONS AND FUTURE DIRECTION	149
6.1 Publications, Conferences & Patents.....	151
A Appendix A	155

A. CALCULATION OF PARTICLE SIZE FOR Ag₂S QDs BY BRUS EQUATION.....155
 A.1 Band gap determination from absorption spectra..... 155
B. Appendix B 162
B.GENE DELIVERY APPLICATIONS OF FA-PEG-PEI/Cys Ag₂S QDs..... 162
 B.1 poly(I:C) transfection using DOX loaded FA-PEG-Ag₂S QDs 162
 B.2 GFP and p53-GFP transfection using FA-PEG-Ag₂S QDs..... 166
BIBLIOGRAPHY 169
VITA.....184

LIST OF TABLES

Table 1. 1 Bandgap energies of some common semiconductors [25].	5
Table 1. 2 Comparison of Ag ₂ S QDs synthesized in the literature and their bioapplications.	21
Table 2. 1 Effect of the reaction time on the properties of Ag ₂ S NIRQDs.....	48
Table 2. 2 Effect of PEI/2MPA ratios on the properties of Ag ₂ S NIRQDs.....	51
Table 2. 3 Influence of pH on the properties of Ag ₂ S-PEI/2MPA QDs.....	54
Table 2. 4 Time dependent changes in particle properties.*	57
Table 3. 1 Number-average size distribution and zeta potential of NIRQDs.....	80
Table 4. 1 Structures and pKa values of amino acids used as coating in the study [210]....	91
Table 4. 2 QD and plasmid DNA concentrations used in the transfection studies.....	98
Table 4. 3 Synthesis conditions of l-arginine and l-arginine/branched PEI-25 kDa coated Ag ₂ S QDs.....	99
Table 4. 4 Synthesis conditions of glutamic acid and glutamic acid/branched PEI-25 kDa coated Ag ₂ S QDs.	100
Table 4. 5 Synthesis conditions of l-histidine and l-histidine/branched PEI-25 kDa coated Ag ₂ S QDs.....	101
Table 4. 6 Synthesis conditions of branched PEI-10 kDa coated Ag ₂ S QDs.	102
Table 4. 7 Synthesis conditions of branched PEI-10 kDa/l-cysteine Ag ₂ S QDs.	102
Table 4. 8 Synthesis conditions of branched PEI-10 kDa/2MPA Ag ₂ S QDs.....	103
Table 4. 9 Synthesis conditions of branched PEI-1.8 kDa/l-cysteine Ag ₂ S QDs.....	104
Table 4. 10 Effect of the PEI/Cys ratio on the properties of Ag ₂ S QDs.	108
Table 4. 11 Effect of coating/Ag ratio on the properties of Ag ₂ S QD (QD60).*	109
Table 4. 12 Effect of the Ag/S on the properties of Ag ₂ S QDs (QD60)*	109
Table 4. 13 Effect of reaction temperature on the properties of PEI/Cys - Ag ₂ S QDs.....	110
Table 4. 14 Properties of QD50-RT Ag ₂ S QDs. *	111
Table 4. 15 Fluorescence lifetime analysis of QD60-RT*	114
Table 4. 16 Composition analysis of Ag ₂ S QDs.....	119

Table 5. 1 Hydrodynamic size and surface charge of Ag ₂ S QD compositions.....	139
Table 5. 2 Ag and DOX content in the nanoparticles	139
Table A. 1 Particle size of Ag ₂ S NIRQDs with respect to absorbance edges calculated from Brus equation.....	156
Table B. 1 Number-based size distribution and zeta potential values of QDs.....	163
Table B. 2 QD and plasmid DNA concentrations used in the transfection studies.....	167



LIST OF FIGURES

Figure 1. 1 Electromagnetic spectrum (left) and size dependent luminescence color of CdSe QDs under excitation of a near-ultraviolet lamp (top); and photoluminescence spectra of some of these CdSe QDs [4].	1
Figure 1. 2 Band gap difference in a metal, a semiconductor and an insulator [17].	2
Figure 1. 3 Exciton formation [19].	3
Figure 1. 4 Schematic representation of the density of states (DOS) in bulk semiconductor (3D), quantum well (2D), quantum wire (1D) and quantum dot (0D) [22].	4
Figure 1. 5 Relative energy levels in a (a) single atom, (b) two atoms, (c) five atoms and (d) a solid with billions of atoms [23].	4
Figure 1. 6 (a) CdSe/ZnS core/shell QDs with CdSe core diameters range from 6.9 nm to 1.8 nm in diameter; (b) quantum confinement on splitting of energy levels in QDs. Decrease in size of the structures due to increase of semiconductor band gap; (c) absorption (top) and emission (bottom) spectra of CdSe quantum dots [27].	6
Figure 1. 7 Jablonski diagram for absorption, fluorescence and phosphorescence [29].	7
Figure 1. 8 Spectrum of absorption and emission cross-sections of the 1500-nm PbS QDs developed by Evident Technologies [30].	7
Figure 1. 9 Schematic representation of (a) the nucleation and growth process of QDs based on La Mer model: Precursors form monomers at the first step, then nuclei form and the nanocrystals aggregate to form larger particles, (b) apparatus used in the synthesis of QDs [35].	9
Figure 1. 10 Silanization of TOPO-capped CdSe/ZnS QDs [46].	10
Figure 1. 11 MSA-capped CdTe/CdS QDs at different time points of synthesis. Photo image of QDs under excitation of 365 nm UV lamp (top) and their UV-Vis absorption (A) and photoluminescence (B) spectra [54].	11

Figure 1. 12 Applications of quantum dots as multimodal contrast agents in bioimaging [56].	12
Figure 1. 13 Photostability of QDs versus conventional organic fluorescence dyes. a) Top row: Simultaneous labeling of 3T3 cells with QD 630-streptavidin (red) for nucleus and Alexa Fluor 488 (green) for microtubules. Bottom row: Labeling of nucleus with Alexa Fluor 488 (green) and microtubules with QD 630-streptavidin (red). b) Time dependent fluorescence intensity of QDs covered with silane shell versus Rhodamine 6G [57]......	13
Figure 1. 14 Fluorescence microscope images of QDs introduced into cells and tissues. (a) Actin staining on fixed 3T3 fibroblast cells (green color). (b) Live MDA-MB-231 breast tumor cells labeled with urokinase plasminogen receptor targeting red QD-antibody. (c) Labeling of live mammalian cells with QD-Tat peptide conjugates [58]. (d) Frozen tissue specimens labeled by red QDs targeting the CXCR4 receptor and a nuclear dye in green color. (e) Ex vivo cancer tissue examination using QDs in a mouse lung [63]. (f) NIR fluorescence image of water-soluble type II QDs in sentinel lymph nodes of a mouse [64] (g) Simultaneous in vivo imaging of multicolor QD-encoded microbeads [58]. (h) In vivo imaging and targeting of a prostate tumor by using a QD-antibody conjugate emitting in red color [58]......	14
Figure 1. 15 Extinction coefficient value of oxy- and deoxy-hemoglobin and water from visible to NIR window [68].	15
Figure 1. 16 Wavelength-dependent autofluorescence of tissues. (a) White light color image of a mouse. Glad bladder (GB), small intestine (SI), and bladder (Bl) were illustrated. Tissue auto-fluorescence under three excitation/emission filter sets: (b) Blue/green (460–500 nm/505–560 nm), (c) green/red (525–555 nm/590–650 nm) and NIR (725–775 nm/790–830 nm) filter sets [69]......	15
Figure 1. 17 Composition, emission range and size of some NIR-emitting QDs synthesized through solution-based methods [31]......	17
Figure 1. 18 Synthetic approaches and applications of silver chalcogenides [89].	18
Figure 1. 19 Some aqueous synthesis methods for Ag ₂ S QDs. A) Synthesis from single precursor [95]. B) Synthesis in organic coating [103]......	19

Figure 1. 20 PEGylated Ag₂S QDs. A) Photoluminescence spectrum upon excitation at 658 nm. Inset shows an NIR-II PL image of the PEGylated-Ag₂S QD suspension under an 808 nm excitation. B) A NIR-II PL image recorded between 1100-1700 nm regions of a tumor-bearing Balb/c mouse subjected to 15 mg/kg dose of PEGylated-Ag₂S QDs at 24 h. C) The blood circulation curve and D) Long-term biodistribution of QDs at this concentration. E) Concentrations of QDs in urine and feces over two months after treatment [99]. 20

Figure 1. 21 Synthetic strategy of Ag₂S QDs in cultured HepG2 cancer cells [103]. 20

Figure 1. 22 Ag₂S QDs prepared in different sizes. A) Photoluminescence spectra under an excitation of 785 nm. B) Absorption spectra of QDs. C) Daylight and D) NIR-II fluorescence images. E) Photoluminescence excitation spectra (a) and time-resolved photoluminescence spectra of Ag₂S QDs in different sizes [110]. 22

Figure 1. 23 A) Schematic representation of synthesis of Ag₂S, Ag₂S-DOX and Ag₂S-DOX-cRGD. B) Fluorescence spectra of nanoparticles. C) In vivo fluorescence imaging in MDA-MB-231 tumor-bearing mice, injected with Ag₂S-DOX-cRGD. D) Peripheral and central slices of the tumor under LSCM. E) Fluorescence intensities of tumor and major organs (heart, liver, bladder and intestine) at 10 min, 3 h and 8 h post-injection of QDs [112]. 23

Figure 1. 24 2MPA coated Ag₂S QDs developed by Acar and coworkers [105]. (a) Schematic representation of aqueous synthesis of 2MPA-Ag₂S NIRQDs. (b) Absorbance and photoluminescence spectra of Ag₂S QDs. (c) Cellular uptake of QDs by NIH/3T3 cells A: Fluorescence, B: transmission and C: merged images taken by confocal microscope. The scale bar = 20 μm. 24

Figure 1. 25 Intracellular uptake of Ag₂S–DMSA NIRQDs at a concentration of 150 μg/mL by HeLa cells after 6 h incubation. (A) Fluorescence, (B) transmission and (C) merged channels of the confocal micrographs. Scale bar = 5 μm. 24

Figure 1. 26 Schematic illustration of aqueous synthesis of Ag₂S–PEG QDs, folic acid conjugation, DOX loading and intracellular uptake of such nanoparticles [118]. 25

Figure 1. 27 Hybrid nanoparticles. (A) Preparation using ligand exchange technique. (B) Cell viability (%) measured by MTT assay on HeLa and NIH/3T3 cells exposed to nanoparticles in the absence and presence of magnetic field [119]. 26

Figure 1. 28 Gene and drug delivery application platform [124].	27
Figure 1. 29 The most frequently used synthetic and biological polymers with the chemical structures in gene delivery applications [120].	28
Figure 1. 30 Schematic representation of the proton sponge effect of PEI [133].	29
Figure 1. 31 Schematic illustration of passive and active targeting on tumor cells [136].	30
Figure 2. 1 Synthesis of PEI and 2MPA coated Ag ₂ S NIRQDs.	41
Figure 2. 2 Photoluminescence (a) and absorbance (b) spectra of PEI coated Ag ₂ S QDs prepared at different Ag/S mole ratios.	46
Figure 2. 3 Photoluminescence (a) and absorbance (b) spectra of PEI coated Ag ₂ S NIRQDs prepared at different Ag/PEI mole ratios.	47
Figure 2. 4 (a) Absorbance calibrated photoluminescence and (b) Normalized absorbance graphs of the Ag ₂ S NIRQDs prepared with PEI/2MPA 60/40 mixed coating at different time points during the reaction.	48
Figure 2. 5 Photoluminescence spectra of Ag ₂ S NIRQDs prepared with different PEI/ 2MPA ratios (Ag: S = 4, room temperature, reaction pH: 10, 5 min reaction).	50
Figure 2. 6 Absorbance spectra of Ag ₂ S NIRQDs prepared with different PEI/ 2MPA ratios (Ag: S = 4, RT, reaction pH: 10, 5 min reaction).	50
Figure 2. 7 Photoluminescence spectra of Ag ₂ S NIRQDs prepared with (a) 60/40 PEI/2MPA (Rxn 4) and (b) 80/20 PEI/2MPA (Rxn 3) coating formulation. Spectra were taken particles are washed and solution pH was adjusted to 7.4 to prevent difference in intensity based on pH.	52
Figure 2. 8 Normalized absorbance graphs of the PEI/2MPA coated Ag ₂ S NIRQDs synthesized in different pHs during reaction: (a) 60 % PEI / 40 % 2MPA ; (b) 80 % PEI / 20 % 2MPA.	52
Figure 2. 9 Photoluminescence spectra of aqueous Ag ₂ S NIRQDs at different pH values. NIRQDs were prepared with 80/20 PEI/2MPA coating formulation, washed and pH was adjusted (Ag: S = 4, Ag: PEI = 1: 4, Ag: 2MPA = 1: 1, T = RT, reaction pH = 9, reaction time = 5 min).	53

Figure 2. 10 Normalized absorbance graphs of Ag ₂ S NIRQDs (80/20 PEI/2MPA) at different pH values.....	53
Figure 2. 11 Photoluminescence spectra of aqueous Ag ₂ S NIRQDs (80/20 PEI/2MPA at pH7.4) in water (left) and LDS 798 NIR dye in MeOH (right) at different concentrations.	55
Figure 2. 12 Plot of the the integrated luminescence intensities of the dye and QD samples against the absorbance. Inset shows the slope of each line corresponding to QD and dye samples.....	55
Figure 2. 13 Normalized absorbance spectra of Ag ₂ S NIRQDs with 80/20 PEI/2MPA at different time points following its synthesis.....	56
Figure 2. 14 TEM images of Ag ₂ S NIRQDs (80/20 PEI/2MPA; synthesized at pH 9.0) at different magnifications (a and b); Diffraction of Ag ₂ S crystal lattice (c); d-spacing determined by a focused image (d).....	57
Figure 2. 15 TG/DTA graph of the PEI/2MPA coated Ag ₂ S QDs.....	58
Figure 2. 16 XRD pattern of the Ag ₂ S NIRQD (80/20 PEI/2MPA; synthesized at pH 9.0).	58
Figure 2. 17 (a) Ag 3d, (b) S 2p and (c) N 1s XPS spectra of Ag ₂ S-PEI/2MPA (80/20) QDs.....	59
Figure 2. 18 Percent viability of HeLa cells exposed to Ag ₂ S NIRQD with PEI, 2MPA and 80/20 PEI/2MPA mixed coatings determined by MTT assay. Concentrations are based on Ag ⁺ ion concentration in QD solutions as determined by ICP-OES. This concentration range corresponds to 4.6-115 µg QD/mL.....	60
Figure 2. 19 Percent viability of HeLa cells exposed to PEI as determined by MTT assay. These five PEI concentrations correspond to maximum possible amount in Ag ₂ S NIRQDs synthesized with 80/20 PEI/2MPA coating and tested (Figure 2. 18). As an example, in 1.6 mg nanoparticle/mL there is 1 µg/mL Ag ⁺ and 2.8 µg/mL PEI.....	61
Figure 2. 20 Cellular uptake and localization of PEI/2MPA coated Ag ₂ S NIRQDs by HeLa cells. Near IR (a), transmission (b) merged image (c) of an individual cell. Red color shows the quantum dots. Arrows show some of the QDs in the cell.....	62
Figure 2. 21 Confocal images of HeLa cells. Cells untreated with QDs (a), cells with QDs (b). Red color shows the quantum dots. The scale means the intensity of QD emission. ..	62

Figure 2. 22 Simplified body plan of a *C. elegans* adult hermaphrodite. 63

Figure 2. 23 Inverted fluorescence microscopy images of *C. elegans* incubated with 200 $\mu\text{g}/\text{mL}$ of PEI/2MPA Ag_2S QDs (80/20 PEI-25kDa/2MPA). Top line shows control group without QDs and bottom line shows DIC, NIR and merged images of Ag_2S QDs introduced worms. Images were taken with a 10x objective. Excitation at 550 nm and NIR filter was used in the emission. 63

Figure 2. 24 Microscope images of *C. elegans* incubated with PEI/2MPA Ag_2S QDs (80/20 PEI/2MPA) at a concentration of 200 $\mu\text{g}/\text{mL}$. The images were taken using 20x and 40x objectives. 64

Figure 2. 25 Transfection of MCF-7 cells: (Top) Cells were transfected with pMax-GFP plasmid using Ag_2S -PEI/2MPA NIRQD or control PEI (1 $\mu\text{g}/\text{ml}$). Transfection efficiency was assessed under a fluorescent microscope. Hoechst staining was used to show the nuclei of all cells in the field. (Bottom) Quantitative analysis of GFP positive cells in (Top) (mean \pm SD of independent experiments, n = 3). 65

Figure 2. 26 Transfection of HeLa cells. (Top) Cells were transfected with pMax-GFP plasmid using Ag_2S -PEI/2MPA NIRQDs or control PEI (1 $\mu\text{g}/\text{ml}$). Transfection efficiency was assessed under a fluorescent microscope. Hoechst staining was used to show the nuclei of all cells in the field. (Bottom) Quantitative analysis of GFP positive cells in (Top) (mean \pm SD of independent experiments, n = 3). 66

Figure 2. 27 Cellular uptake and localization of GFP loaded PEI/2MPA coated Ag_2S NIRQDs in MCF-7 cells. Near IR (a), transmission (b) and merged images (c) of an individual cell. Arrows show QDs in the cell. 67

Figure 3. 1 Cellular response to stress signals by p53 activation [200].....71

Figure 3. 2 Concentration dependent absorbance calibration curve for free DOX plotted with absorbance intensity of known concentrations of DOX at 485 nm. 74

Figure 3. 3 The structure of p53/GFP plasmid used in the study, which was inserted in DH5-alpha *E. coli*. 77

Figure 3. 4 Simple illustration of cultivation steps of *E. coli* and plasmid DNA purification. 78

Figure 3. 5 Photoluminescence and corresponding absorbance spectra of PEI/2MPA coated Ag₂S QDs (Ag₂S QDs) and the PEGylated formulations..... 80

Figure 3. 6 Cell viability of HeLa cells treated with Ag₂S, mPEG-Ag₂S and DOX loaded PEG-Ag₂S for 48 hours, performed by MTT assay. Untreated cells were accepted as positive control. The data were expressed as mean ± S.D. (n=3), (p < 0.05(*), p < 0.01 (**), p < 0.001 (***) and p < 0.0001 (****))..... 81

Figure 3. 7 Cell viability of MCF-7 cells treated with Ag₂S, mPEG-Ag₂S and DOX loaded PEG-Ag₂S for 48 hours, performed by MTT assay. Untreated cells were accepted as positive control. The data were expressed as mean ± S.D. (n=3), (p < 0.05(*), p < 0.01 (**), p < 0.001 (***) and p < 0.0001 (****))..... 81

Figure 3. 8 Cell viability of HCT 116 cells treated with free DOX and DOX loaded PEG-Ag₂S for 48 hours, performed by MTT assay. Untreated cells were accepted as positive control. The data were expressed as mean ± S.D. (n=3), (p < 0.05(*), p < 0.01 (**), p < 0.001 (***) and p < 0.0001 (****))..... 82

Figure 3. 9 Fluorescence microscopy images of HeLa cells treated with mPEG-Ag₂S and DOX loaded mPEG-Ag₂S QDs at 2.5 µg/mL Ag concentration. Untreated cells were used as controls. (a, d) Control cells. (b,e) mPEG -Ag₂S. (c,f) DOX loaded mPEG-Ag₂S. (a) is merged image from the bright field, DAPI, CY3 and NIR filters. (b) is merged image from the bright field, DAPI and NIR filters. (c) is merged image from the bright field, DAPI and CY3 filters. (d, e and f) is the corresponding fluorescence images without bright field. Blue signal shows DAPI staining for cell nuclei. Red signals in (b and e) indicate QD emission; in (c and f) DOX emission..... 83

Figure 3. 10 Topoisomerase function during DNA replication [206]. 84

Figure 3. 11 Flow cytometric analysis of cell cycle with propidium iodide fluorescent staining. Free DOX and DOX loaded mPEG-Ag₂S QDs were used in 10 µM DOX concentration..... 84

Figure 3. 12 Apoptosis pathway by caspase activity and PARP cleavage [207]..... 85

Figure 3. 13 Western blot analysis of protein extracts of HCT 116 cells treated with free DOX and DOX-mPEG-Ag₂S QDs. The samples were used in equivalent DOX

concentrations. The bands of c-C3 (cleaved caspase-3) and c-PARP (cleaved PARP) are clearly seen at 10 μ M DOX and 10 μ M DOX including mPEG-Ag ₂ S QD concentrations.	86
Figure 3. 14 Flow cytometry evaluations of transfection efficiencies of HCT 116 wt and HCT 116 p53 -/- cells treated with p53-GFP/mPEG-Ag ₂ S or p53-GFP /DOX-mPEG-Ag ₂ S QDs in N/P ratio of 40/1. Values are means mean \pm S.D. (n=3), (p < 0.05(*), p < 0.01 (**)).	87
Figure 3. 15 Flow cytometry evaluations of transfection efficiencies of HCT 116 wt and HCT 116 p53 -/- cells treated with p53-GFP /mPEG-Ag ₂ S QDs in different N/P ratios. Values are means mean \pm S.D. (n=3), (p < 0.05(*), p < 0.01 (**)).	88
Figure 4. 1 Photoluminescence spectra of PEI/Cys coated Ag ₂ S QDs synthesized at (a) different PEI/Cys ratios, (b) Ag/coating (PEI + Cys), (c) Ag/S mole ratios and (d) at different temperatures.	105
Figure 4. 2 Absorbance spectra of PEI/Cys coated Ag ₂ S QDs synthesized at different PEI/Cys (a), Ag/coating (PEI and Cys) (b) Ag/S mole ratios (c), temperature (d) and photoluminescence spectra of QD100 and QD0 (e).	107
Figure 4. 3 Photoluminescence spectra of the best luminescing PEI/Cys coated Ag ₂ S QDs.	111
Figure 4. 4 Plot of the the integrated luminescence intensities of the reference dye and Ag ₂ S QDs against the absorbance. Inset shows the slope of each line corresponding to Ag ₂ S and dye samples.	112
Figure 4. 5 Time resolved photoluminescence decay curve of QD60-RT. Black dots are scattered and red line is fitted data.	114
Figure 4. 6 XPS spectra of Ag ₂ S (QD60-RT) QDs. (a) Ag 3d, (b) S 2p and (c) N 1s.	115
Figure 4. 7 TEM analyses of PEI/Cys coated Ag ₂ S QDs (QD60-RT). (a) and (b) TEM images of nanoparticles at different magnifications, (c) interplanar spacing and corresponding plane and (d) size distribution of nanoparticles.	115
Figure 4. 8 IR spectrum of PEI/l-cysteine coated Ag ₂ S QDs (QD60-RT).	116
Figure 4. 9 Thermogravimetric analysis of PEI/Cys coated Ag ₂ S (QD60-RT).	116

Figure 4. 10 Viability of HeLa cells treated with PEI/Cys coated Ag₂S QDs after 24 hours incubation measured by MTT assay compared to untreated HeLa cells. The data are expressed as mean \pm S.D. (n = 8)..... 118

Figure 4. 11 Viability of HeLa cells treated with QD100-70 (QD100) (a), QD80-70 (b), QD60-RT (c) and QD50-RT (d) after 24 hours incubation measured by MTT assay compared to untreated HeLa cells. The data are expressed as mean \pm S.D. (n = 8). (p<0.05)..... 118

Figure 4. 12 Cellular localization of PEI/Cys coated Ag₂S NIRQDs (QD60-RT) by HeLa cells. DIC (a), DAPI and NIR (b), and merged (c) images of control cells and DIC (d), DAPI and NIR (e), and merged (f) images of QD treated cells. The scale bar shows 100 μ m. .. 120

Figure 4. 13 In vivo fluorescence image of a BALB/c mice (left image) 1 h after intraperitoneal injection of the QD60-RT and (right image) the control mice with no QD injection (Excitation at 740 nm. Emission filter: 840 nm long-pass). 120

Figure 4. 14 Transfection of HeLa cells with GFP plasmid using PEI/Cys Ag₂S NIRQDs. QD/pDNA complexes prepared at 15/1 N/P ratio were introduced into the cells in different concentrations. Cells without any treatments were used as control. Images were taken with an inverted fluorescence microscope. DAPI staining was used to show nuclei of all cells in the field (blue color). Red signals indicate QD internalization into the cells. Green signals show GFP transfection. 121

Figure 4. 15 Transfection of HeLa cells with p53-GFP plasmid using PEI/Cys Ag₂S QDs. QD/pDNA complexes prepared at 15/1 N/P ratio (Table 4. 2) were introduced into the cells in different concentrations. Cells without any treatments were used as control. Images were taken with an inverted fluorescence microscope. DAPI staining was used to show nuclei of all cells in the field (blue color). Red signals indicate QD internalization into the cells. Green signals show GFP transfection. 123

Figure 4. 16 Transfection of (A) MEF p53 ^{-/-} and (B) MEF wt cells with p53-GFP plasmid using PEI/Cys Ag₂S NIRQDs. QD/pDNA complexes prepared at 15/1 N/P ratio were used in different concentrations. Cells without any treatments were employed as control. Images were taken with an inverted fluorescence microscope. DAPI staining was used to show nuclei

of all cells in the field (blue color). Red signals indicate QD internalization into the cells. Green signals show GFP transfection.	124
Figure 4. 17 Transfection of MEF p53 ^{-/-} cells with p53-GFP plasmid using PEI/Cys Ag ₂ S QDs. Different N/P ratios were employed at a concentration of 2.36 μg/mL. Cells without any treatments were used as control. Images were taken with an inverted fluorescence microscope. DAPI staining was used to show nuclei of all cells in the field (blue color). Red signals indicate QD internalization into the cells. Green signals show GFP transfection.	125
Figure 5. 1 Concentration dependent absorbance (at 320 nm) calibration curve for free folic acid.	132
Figure 5. 2 Concentration dependent absorbance (at 485 nm) calibration curve for free DOX.	133
Figure 5. 3 Normalized photoluminescence (excitation at 360 nm) (a) and normalized absorbance spectra (b) of Ag ₂ S, FA-PEG-Ag ₂ S, DOX loaded FA-PEG-Ag ₂ S NIRQDs and free folic acid and DOX as references.	138
Figure 5. 4 TEM image of FA-PEG-Ag ₂ S.	139
Figure 5. 5 Viability of HeLa and A549 cells treated with Ag ₂ S, FA-PEG-Ag ₂ S, FA-PEG-Ag ₂ S-DOX and free DOX after 48 hours incubation assessed by MTT and ATP assays. Viability of HeLa (a) and A549 (b) cells determined by MTT assay; viability of HeLa (c) and A549 (d) cells determined by ATP assay; viability of cells treated with free DOX based on MTT (e) and ATP (f) assays. Data are expressed as mean ± S.D. (n = 3), (p < 0.05(*), p < 0.01 (**)).	141
Figure 5. 6 Intracellular quantification of QDs in HeLa and A549 cells. Samples at 2 μg/mL Ag concentration were incubated with cells for 1 h. Measurements were done by ICP-MS instrument. The data are expressed as mean ± S.D. (n = 3), (p < 0.05(*)).	143
Figure 5. 7 Fluorescence microscopy images of control HeLa cells (a, b) and control A549 cells (g, h); HeLa cells after 1 h of incubation with FA-PEG-Ag ₂ S (c, d) and FA-PEG-Ag ₂ S-DOX QDs (e, f) at 2 μg/mL Ag concentration; A549 cells after 1 h of incubation with FA-PEG-Ag ₂ S (i, j) DOX FA-PEG-Ag ₂ S-DOX QDs (k, l) in 2 μg/mL Ag concentration. Images a and g are merged images from the bright field, DAPI, CY3 and NIR filters; b and h are	

merged images from DAPI, CY3 and NIR filters; images c and i are merged images from the bright field, DAPI and NIR filters; d and j are merged images from DAPI and NIR filters; e and k are merged images from the bright field, DAPI and CY3 filters; f and k are merged images from DAPI and CY3 filters. Blue emission indicates DAPI staining for cell nuclei. Red emission originates from QDs in images c, d, I and j; and from DOX in images e, f, k and l..... 144

Figure 5. 8 (A) Fluorescence staining of HeLa and (B) A549 cells with Hoechst 33342 (blue), Annexin V-FITC (green) and Propidium Iodide (red) after being treated with Ag₂S, FA-PEG-Ag₂S, and FA-PEG-Ag₂S-DOX QDs at 1.5 µg/ml Ag concentration and free DOX at 0.27 µg/mL for 24 h (n = 3). Untreated cells were used as control. (C) M30 antigen level of HeLa and A549 cells incubated with nanoparticles at 1.5 µg/ml Ag concentration for 48 h. The data are expressed as mean ± S.D. (n = 2), (p < 0.05(*), p < 0.01 (**)). 146

Figure 5. 9 Mitochondrial membrane potential assay in HeLa and A549 cells visualized by fluorescence microscopy. The cells were exposed to Ag₂S, FA-PEG-Ag₂S, FA-PEG-Ag₂S-DOX QDs at 1.5 µg/mL Ag concentration and free DOX at equivalent concentrations of DOX-PEG-FA-Ag₂S QDs for 24 h. Untreated cells were used as control. Red fluorescence indicates high membrane potential and green fluorescence indicates loss of mitochondrial membrane potential..... 147

Figure A. 1 Absorbance spectrum of Ag₂S NIRQDs for determination of crystal band gap.....155

Figure B. 1 ATP cell viability assay on HeLa and A549 cells treated with Ag₂S, FA-PEG-Ag₂S, DOX+FA-PEG-Ag₂S and poly(I:C) loaded DOX+FA-PEG-Ag₂S NIRQDs for 48 hours. The data are expressed as mean ± S.D. (n = 3).....164

Figure B. 2 Indication of apoptosis and necrosis of HeLa cells induced by DOX+FA-PEG-Ag₂S or poly(I:C)-DOX+FA-PEG-Ag₂S NIRQDs. Fluorescence staining of HeLa cells with Hoechst 33342 (blue), Annexin V-FITC (green) and Propidium Iodide (red) after being treated with QDs at 1.5 µg/ml Ag concentration for 24 hours. 164

Figure B. 3 Indication of apoptosis and necrosis of A549 cells induced by DOX+FA-PEG-Ag₂S or poly(I:C)-DOX+FA-PEG-Ag₂S NIRQDs. Fluorescence staining of A549 cells with

Hoechst 33342 (blue), Annexin V-FITC (green) and Propidium Iodide (red) after being treated with QDs at 1.5 $\mu\text{g}/\text{ml}$ Ag concentration for 24 hours.	165
Figure B. 4 Mitochondrial membrane potential assay in HeLa and A549 cells visualized by fluorescence microscopy. The cells were exposed to DOX+FA-PEG-Ag ₂ S and poly(I:C)-DOX+FA-PEG-Ag ₂ S NIRQDs at 1.5 $\mu\text{g}/\text{mL}$ Ag for 24 hours. Red fluorescence indicates high membrane potential and green fluorescence indicates loss of mitochondrial membrane potential depending on apoptotic event in the cells.	165
Figure B. 5 M30 antigen assay on HeLa and A549 cells incubated with nanoparticles at 1.5 $\mu\text{g}/\text{ml}$ Ag concentration for 48 hours (n = 2).....	166
Figure B. 6 Transfection of HeLa cells with GFP (A) and p53-GFP (B) plasmids using FA-PEG-Ag ₂ S NIRQDs. QD/pDNA conjugates prepared at 15/1 N/P ratio were introduced into the cells in different concentrations. Images were taken with an inverted fluorescence microscope. DAPI staining was used to show nuclei of all cells in the field (blue color). Red signals indicate QD internalization into the cells. Green signals show GFP transfection.	167
Figure B. 7 Transfection of MEF p53 ^{-/-} and MEF wt cells with p53-GFP plasmid using FA-PEG-Ag ₂ S NIRQDs. QD/pDNA conjugates prepared at 15/1 N/P ratio were used in different concentrations. Images were taken with an inverted fluorescence microscope. DAPI staining was used to show nuclei of all cells in the field (blue color). Red signals indicate QD internalization into the cells. Green signals show GFP transfection.	168

LIST OF SCHEME

Scheme 2. 1 Schematic representation of aqueous synthesis of PEI and 2MPA coated Ag ₂ S NIRQDs.	41
Scheme 3. 1 Synthesis of PEGylated-Ag ₂ S NIRQDs and DOX loading via non-covalent complexation.....	73
Scheme 4. 1 Aqueous synthesis of PEI/Cys Ag ₂ S NIRQDs.....	93
Scheme 5. 1 Schematic representation of aqueous synthesis of FA-PEG-conjugated Ag ₂ S NIRQDs and DOX loading via non-covalent complexation.....	132
Scheme B. 1 Schematic representation of electrostatic interaction between poly(I:C) and DOX loaded FA-PEG-(PEI/Cys)-Ag ₂ S NIRQDs.....	163
Scheme B. 2 Schematic representation of electrostatic interaction between GFP or p53-GFP and DOX loaded FA-PEG-(PEI/Cys)-Ag ₂ S NIRQDs.	166

NOMENCLATURE

2MPA	2-Mercaptopropionic Acid
AA	Amino acid
AgNO ₃	Silver(I)nitrate
Ag ₂ S	Silver(I)sulfide
Bp	Base pair
bPEI	Branched Polyethyleneimine
CB	Conduction Band
Cys	Cysteine
Da	Dalton
DAPI	4',6-diamidino-2-phenylindole
DIC	Differential interference contrast
Dh	Average hydrodynamic size
DLS	Dynamic Light Scattering
DNA	Deoxyribonucleic acid
DMEM	Dulbecco's Modified Eagle Medium
DMSO	Dimethyl Sulfoxide
DOS	Density of States
DOX	Doxorubicin
EBR	Electron Bohr Radius
E _g	Band gap energy
EDX	Electron Dispersive X-ray
Eqn	Equation
EtOH	Ethanol
FA	Folic Acid
FBS	Fetal Bovine Serum
FTIR	Fourier Transform Infrared Spectra
FWHM	Full Width at Half Maximum

GFP	Green Fluorescent Protein
h	Planck's constant
HCT116	Human Colon Carcinoma
HeLa	Human Cervical Carcinoma
ICP-MS	Inductively Coupled Plasma – Mass Spectrometer
ICP-OES	Inductively Coupled Plasma Optical Emission Spectrometer
IR	InfraRed
InGaAs	Indium Gallium Arsenide
kDa	Kilo Dalton
LDS 798	4-[4-[4-(dimethylamino)phenyl]-1,3-butadienyl]-1-ethyl quinolinium perchlorate
IPEI	Linear polyethyleneimine
m_e	Effective mass of electron
m_h	Effective mass of hole
MRI	Magnetic Resonance Imaging
MTT	Thiazolyl blue tetrazolium bromide
MW	Molecular Weight
NaOH	Sodium Hydroxide
Na ₂ S	Sodium Sulfide
NC	Nano-Crystal
NIH3T3	Mouse embryo fibroblast cell line
NIR	Near InfraRed
NIRQDs	Near Infrared Emitting Quantum Dots
PBS	Phosphated Buffer Saline
PEG	Polyethylene glycol
PEI	Polyethyleneimine
PL	PhotoLuminescence
PLQY	PhotoLuminescence Quantum Yield
PMT	PhotoMultiplier Tube

QD	Quantum Dot
QY	Quantum Yield
-SH	Thiol
TAA	Thioacetamide
TEM	Transmission Electron Microscopy
UV	Ultra Violet
VB	Valence Band
Vis	Visible
WT	Wild Type
XPS	X-Ray Photoelectron Spectroscopy
XRD	X-Ray Diffraction

Chapter 1

1. INTRODUCTION

1.1 Quantum Dots

Semiconductor quantum dots (QDs) are crystalline semiconductor nanostructures with diameters usually in the range of 2-10 nanometers (10-50 atoms) [1]. They were discovered initially in 1980s by Alexei Ekimov in a glass matrix [2] and by Brus in colloidal solutions [3]. These structures are intermediate between the bulk and molecular forms. The most important result of this is the size dependent fluorescence.

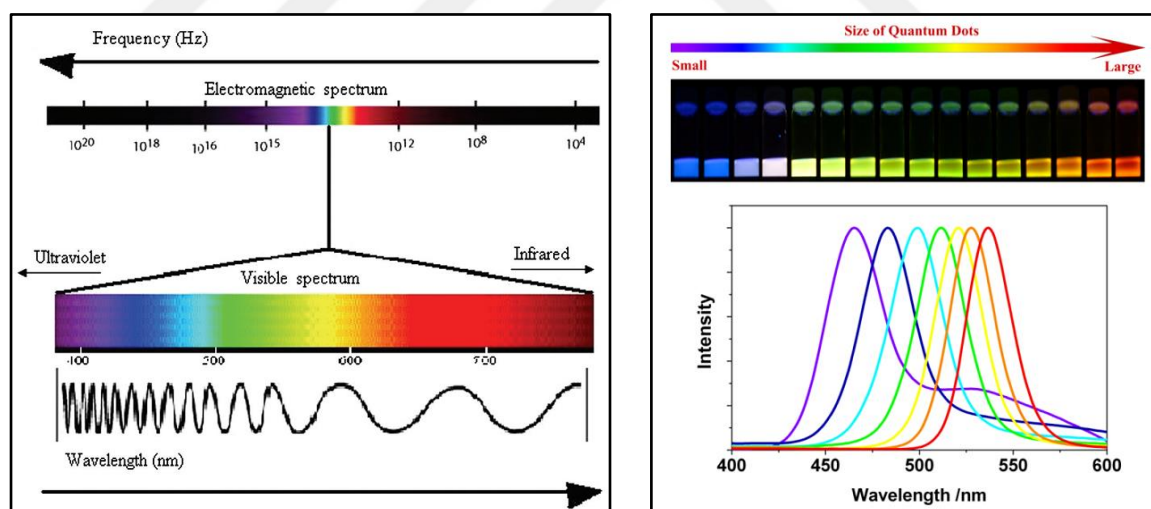


Figure 1. 1 Electromagnetic spectrum (left) and size dependent luminescence color of CdSe QDs under excitation of a near-ultraviolet lamp (top); and photoluminescence spectra of some of these CdSe QDs [4].

QDs have interesting photophysical properties that include size-tunable luminescence, narrow photoluminescence (PL) bands, broad and continuous excitation spectra, high fluorescence quantum yield (QY), long luminescence lifetime and superior

stability against photobleaching [5]. These remarkable properties make QDs unique in a variety of application areas. Most studied QDs are the composed of group II-VI (CdTe, CdS, CdSe, ZnS) [6-9], III-V (InAs, InP) [10, 11] and IV-VI (SnSe, PbS, PbTe) atoms [12-15]. Size tunable emission of CdSe QDs are shown as an example in Figure 1. 1.

1.2 Size Dependent Energy Band Gap and Quantum Confinement

Each atom has bounded electrons in discrete energy levels. When a large number of atoms come together, the discrete energy levels of each atom create a continuous energy band. The highest range of electron energies which is completely filled with electrons is called as valance band. Above the valance band, there is a conduction band which is the lowest range of vacant electronic states. The separation of the two is the band gap. When an external stimulus like voltage, heat or photon flux is applied, electrons of the valance band jump to the conduction band. This band gap has an important role on determination of the type of the materials as a conductor, semiconductor or an insulator. If there is no gap between the conduction and the valance band, the two overlap, and the material is considered as a metal. If the band gap is relatively small, excited electrons can reach to the conduction band leaving a positive hole behind, and the material is considered as a semiconductor. If the band gap is relatively large, it is an insulator [16] (Figure 1. 2). In general, materials with a band gap energy higher than 3 eV are classified as insulators.

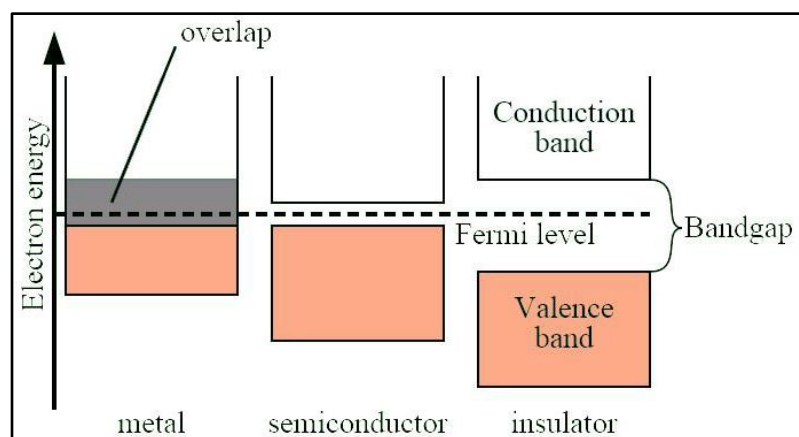


Figure 1. 2 Band gap difference in a metal, a semiconductor and an insulator [17].

In addition, the highest energy level that an electron may occupy at absolute zero temperature is called Fermi level and it is located right in the middle of the band gap [18].

Electrons in the valance band of the semiconductors can be excited to the conduction band with an external energy, equal or greater than the band gap energy of the material. This mechanism creates a positively charged hole and a negatively charged electron pair which is called as an exciton (Eqn 1.1, Figure 1. 3).

$$h\nu \leftrightarrow e^{-}(CB) + h^{+}(VB) \quad (\text{Eqn 1.1})$$

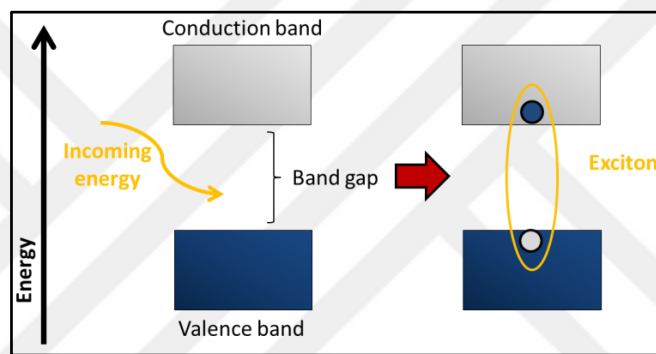


Figure 1. 3 Exciton formation [19].

The distance between the electron and hole pair of the exciton is named as Exciton Bohr Radius (EBR) and it is a characteristic property for each material. EBR is critical for confinement in semiconductors. If the EBR is equal or larger than the diameter of the QD, a strong confinement is obtained. However, if the EBR is smaller than the size of the particle, a weak confinement occurs in the material. In addition, there is no confinement in a bulk semiconductor and electrons move freely in all directions, but in quantum wells and quantum wires, there is confinement in one and two dimensions, respectively [20]. However, spherical QDs have discrete, quantized energy levels that confine the motion of conduction band electrons, valence band holes, or excitons in all three spatial directions [21] (Figure 1. 4).

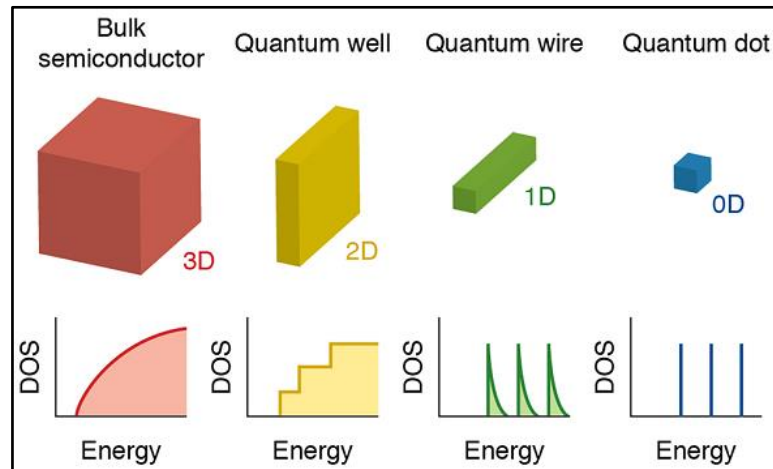


Figure 1. 4 Schematic representation of the density of states (DOS) in bulk semiconductor (3D), quantum well (2D), quantum wire (1D) and quantum dot (0D) [22].

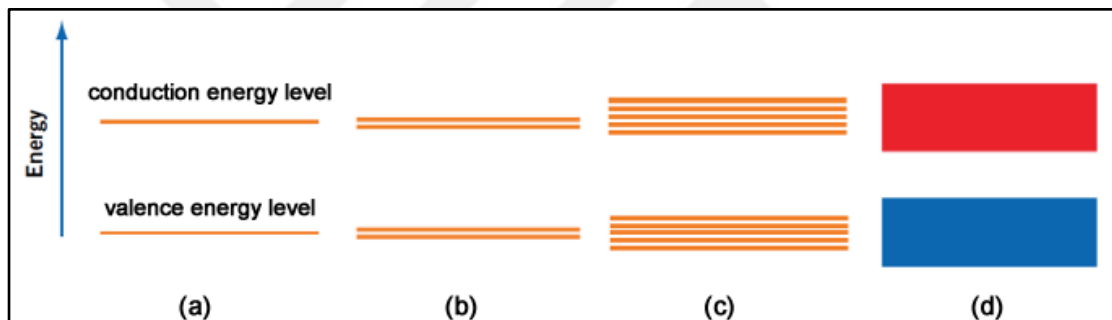


Figure 1. 5 Relative energy levels in a (a) single atom, (b) two atoms, (c) five atoms and (d) a solid with billions of atoms [23].

Confinement to atomic levels makes the density of states discrete while it is continuous and like a band in bulk semiconductors that have billions of atoms overlap (Figure 1. 5). This phenomenon indicates increasing band gap and confinement with the decreasing size of the QD (less number of atoms). This relation between the bandgap energy ($E_g(QD)$) and the radius of the quantum dot (R) was stated by Louis Brus in the Eqn 1.2 which is known as the “ Brus equation”:

$$E_g(QD) = E_g(Bulk) + \frac{\hbar^2}{8R^2} \left[\frac{1}{m_e} + \frac{1}{m_h} \right] - 1.8 \frac{e^2}{4\pi\epsilon\epsilon_0 R} \quad (\text{Eqn 1.2})$$

where $E_g(Bulk)$ is the band gap energy of the semiconductor, h is the Planck's constant, m_e is the mass of the excited electron, m_h is the mass of the electron hole, e is the charge of an electron, ϵ is the dielectric constant of the material (Eqn 1.2) [24]. The particle size calculated here is a theoretical calculation instead of particle size measured by TEM, SEM, XRD or other characterization tools. The equation clearly shows that the bandgap energy of the particles increases, as the size of the particles decreases. Bandgap energies of some common semiconductors are listed in Table 1. 1.

Table 1. 1 Bandgap energies of some common semiconductors [25].

Semiconductor Structure	Bandgap Energy (eV)
ZnSe	2.58
CdS	2.53
CdSe	1.74
CdTe	1.50
InP	1.35
Ag ₂ S	0.9
Ag ₂ Te	0.65
GaAs	1.43
PbS	0.41

Size dependent band gap of semiconductor QDs, create size dependent or size tunable optical properties which enable their application in various areas, but also necessitate size controlled synthesis of QDs. The QD composition, reagents used and synthesis conditions can be modified for size tuning of QDs and hence emission over a broad frequency range covering visible to IR [26] (Figure 1. 6). Bandgap energy increases with the decreasing crystal size.

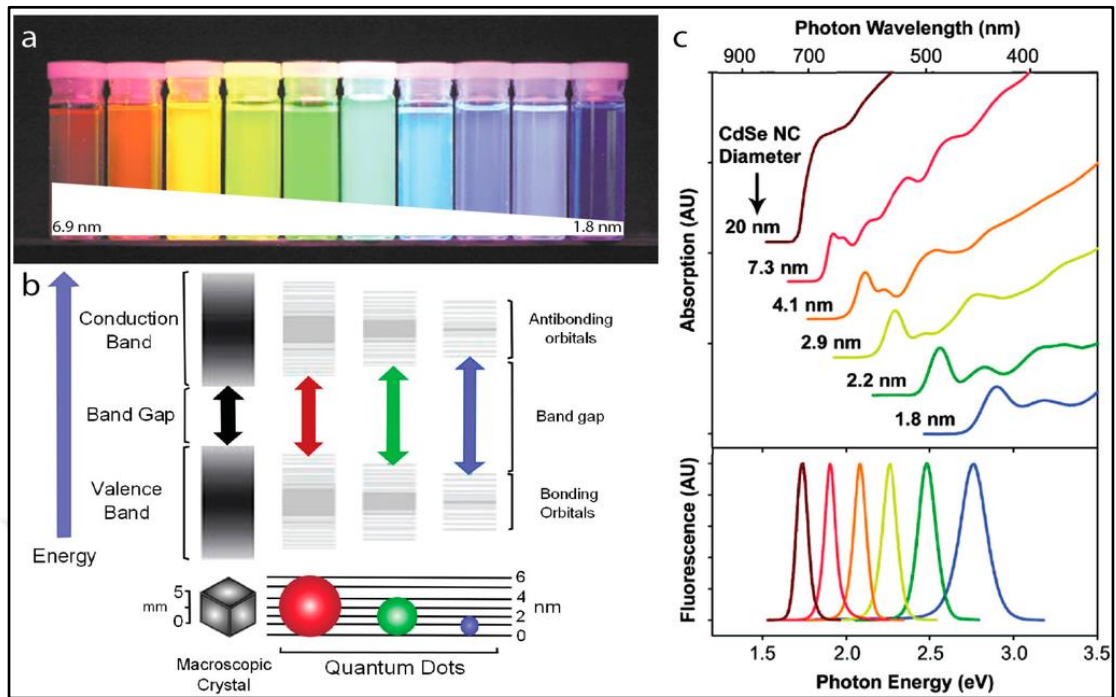


Figure 1. 6 (a) CdSe/ZnS core/shell QDs with CdSe core diameters range from 6.9 nm to 1.8 nm in diameter; (b) quantum confinement on splitting of energy levels in QDs. Decrease in size of the structures due to increase of semiconductor band gap; (c) absorption (top) and emission (bottom) spectra of CdSe quantum dots [27].

1.3 Mechanism of Fluorescence

When a quantum dot absorbs a photon with enough energy equal or bigger than its band gap energy, an electron is promoted from valance band to conduction band, leaving a hole in the valence band (exciton generation). This phenomenon is known as absorption of light or excitation of the electron in the lower energy level. These excited electrons are not stable and drop back to valance band with radiative and non-radiative decay paths (Figure 1. 7). These may be called as relaxation, as well. These pathways are summarized as follows:

1. A photon is emitted; this process is named as fluorescence or radiative decay.
2. The absorbed energy is emitted thermally by a series of vibrational transitions; this is known as nonradiative decay or vibrational relaxation.
3. Some photochemical reactions can occur.

4. The energy can be converted to a lower energy state like triplet state and then, released either via a radiative (phosphorescence) or nonradiative (vibration) decay, or it can undergo a photochemical reaction [28].

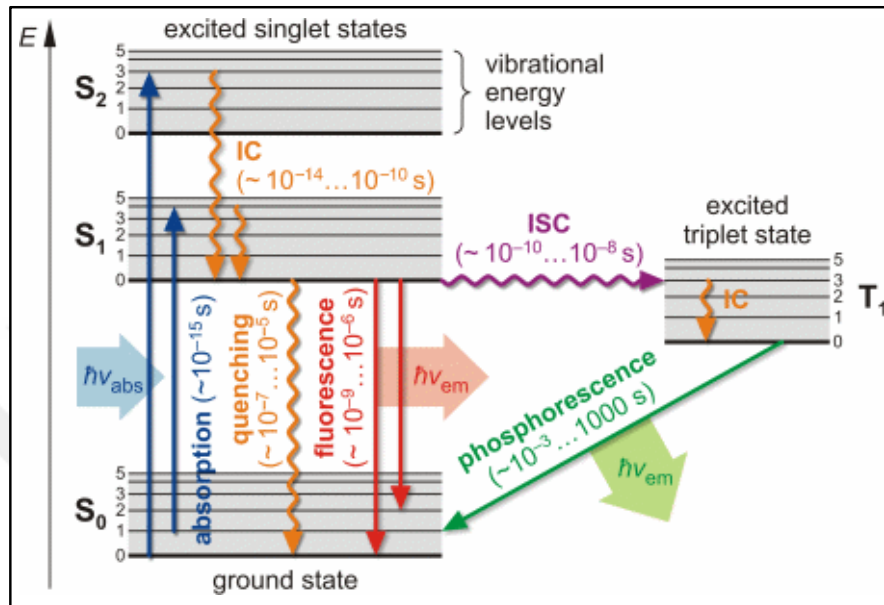


Figure 1. 7 Jablonski diagram for absorption, fluorescence and phosphorescence [29].

The wavelength of the emitted photon is longer than the wavelength of absorbed light (Figure 1. 8). This phenomenon is known as “Stokes shift”. The lost energy is due to vibrational relaxations and solvent interaction.

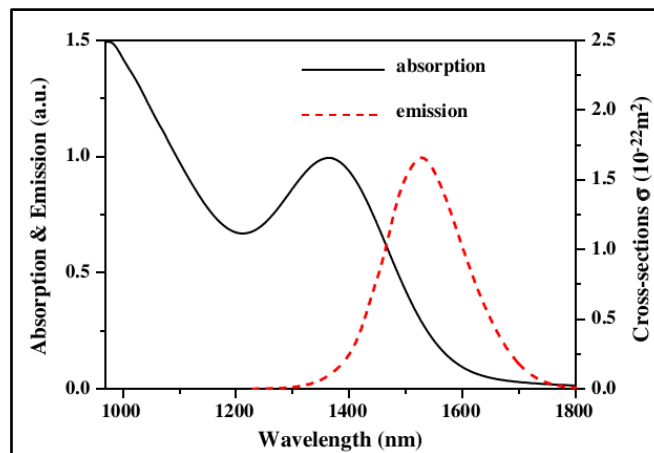


Figure 1. 8 Spectrum of absorption and emission cross-sections of the 1500-nm PbS QDs developed by Evident Technologies [30].

In addition to changes in size and composition of QDs, doping the semiconductor host QDs with a small amount of impurities can alter the bandgap, as well [20, 31].

1.4 Synthesis of QDs

QDs are composed of an inorganic semiconductor core responsible for size-tuned emission and an organic coating bound on the surface of the core. The organic coating, which may be called as the ligand as well, controls the crystal growth during the synthesis by passivating the growing crystal surface, protects the core from the surrounding medium and reduces its reactivity, preventing oxidation provides solvent interaction and hence colloidal stability, prevents agglomeration, and, functionalizes the surface. The coating material is selected according to desired applications of QDs [32]. There are a variety of techniques to synthesize QDs with different compositions and properties. The most frequently used approaches are high-temperature synthesis in organic solvents and aqueous synthesis of QDs.

Organic solvent synthesis: Synthesis of QDs in organic solvents via organometallic precursors consists of three main components; precursors, organic surfactant and solvents. Surfactants can serve also as solvents in some cases. In this method, two common events occur: (1) nucleation: precursors undergo pyrolysis and decompose or react to generate a supersaturation of monomers and nucleation [33] (2) nuclei formation continues from molecular precursors via Oswald ripening (Figure 1. 9) [34, 35]. Organic solvents, such as TOPO (trioctylphosphine oxide) [36], HAD (hexadecylamine) [37], octadecene (ODE) [38] are frequently employed solvents in this procedure. The common properties of the solvents are their high boiling point allowing high reaction temperatures (200-400 °C). They can control the speed of the reaction, coordinate with unsaturated metal atoms on the surface of QDs and prevent formation of a bulk material.

Organometallic synthesis route is an efficient technique to produce high-quality semiconductor nanocrystals. However, some reactants employed during synthesis are extremely toxic, explosive and pyrophoric. QD synthesis from non-organometallic precursors is a safer approach used in alternative methods. For example, Qu et al. showed the synthesis of CdS, CdSe and CdTe QDs from CdO [39, 40].

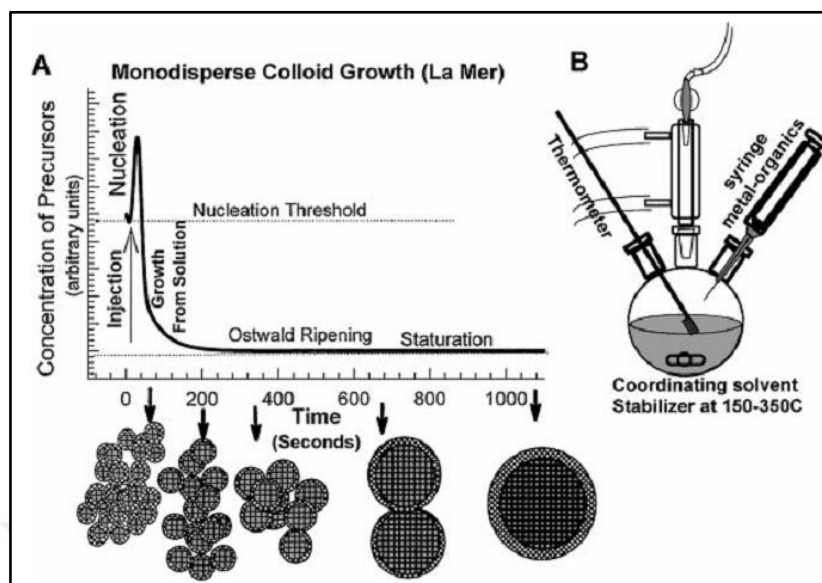


Figure 1. 9 Schematic representation of (a) the nucleation and growth process of QDs based on La Mer model: Precursors form monomers at the first step, then nuclei form and the nanocrystals aggregate to form larger particles, (b) apparatus used in the synthesis of QDs [35].

Microwave synthesis is also one of the successful synthesis techniques to obtain high quality QDs under microwave instead of thermal heating. Most of the chalcogenides can absorb the microwave energy selectively. Nucleation and growth of the QDs take place upon microwave irradiation in non-microwave absorbing alkane solvents.

These techniques generally produce nanocrystals in narrow size distributions with high fluorescence intensity and stability. Yet, these procedures produce hydrophobic particles and post-synthetic procedures have to be employed in order to obtain an aqueous colloidal solution of these QDs. Biomedical applications require aqueous QDs [41]. Hydrophobic QDs produced in organic solvents are unsuitable for direct use in *in vitro* and *in vivo* studies [42]. For the biological applications, the QDs must be transferred to aqueous medium and then conjugated with required biomolecules [43]. Transfer of QDs from organic to aqueous phase is obstructed due to their poor solubility in aqueous medium. Therefore, several strategies have been applied to solubilize QDs synthesized in organic solvents to aqueous ones. Ligand exchange is mostly used technique for this purpose. One of the initial studies in this area was achieved by Quantum Dot Corporation (found within Invitrogen) by the production of silica encapsulated CdSe QDs and their

conjugation with various biomolecules [44]. The silanization technique was reported first from Bruchez et al. In this approach, a silica shell was grown around TOPO-capped CdSe/ZnS QDs through replacement of TOPO molecules from the surface of QD by mercaptopropyltris(methoxy) silane. Here, methoxysilane groups are hydrolyzed into silanol groups and fresh silane precursors with functional groups soluble in water are reacted with these particles (Figure 1. 10) [45].

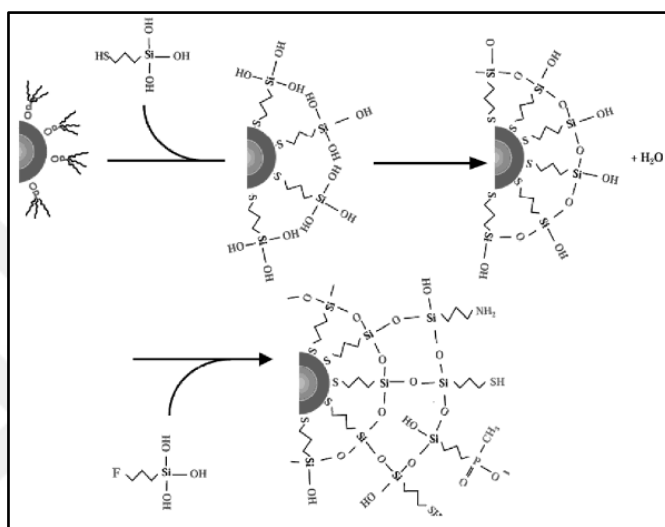


Figure 1. 10 Silanization of TOPO-capped CdSe/ZnS QDs [46].

Another technique is encapsulation of QDs by a shell to make them water-soluble. Phospholipids, amphiphilic polymers (poly(acrylic acid), polyethylene glycol (PEG)) or silica can be employed to encapsulate the QDs instead of ligand exchange and to obtain biocompatible and water-soluble QDs [18].

Aqueous synthesis: QDs can be also directly synthesized in water using appropriate reagents and capping agents. Thiolated molecules such as thioglycolic acid (TGA), 3-mercaptopropionic acid (3MPA), 2-mercaptopropionic acid, 1-cysteine, glutathione, meso-2,3-dimercaptosuccinic acid (DMSA), 1-thioglycerol (1-TGL) [47-49]), peptides, water-soluble polymers (PEG, polyethyleneimine (PEI), poly(acrylic acid), etc. [50]) are some of the capping agents used to passivate the crystal surface and provide colloidal solutions in water. This is more practical than rendering hydrophobic QDs hydrophilic via methods described above. Based there is no loss of luminescence, aggregation and an increase in size distribution like in other water-solubilization cases [51].

Another parameter for QD synthesis is determination of chalcogen sources. NaHX (X: Se, Te), Na₂X (X:S, Se,Te), thiourea and thioacetamide are the mostly used sources for aqueous synthesis of QDs. NaHX and Na₂X are air sensitive.

Reaction conditions also take effective role on synthesis of QDs. Reaction temperature, pH and duration are effective parameters on the nucleation, size, stability, emission range and intensity of semiconductor nanocrystals. Reaction temperature can be adjusted from ambient to 100°C (reflux). As the reaction temperature increases, nanoparticles produced are larger. The QDs are in broader size distribution and lower crystallinity compared to hydrophobic QDs synthesized by organic route due to limitation of maximum temperature of aqueous synthesis. Reaction pH is also a significant factor on crystal growth and quality because different complexes may be formed by the capping agents and the cation (Ag⁺, Cd₂⁺, etc.) [52, 53]. Reaction duration is another parameter for nucleation and maturation of QDs. Generally, crystal size increases over time. In Figure 1. 11, the effect of the reaction time is illustrated.

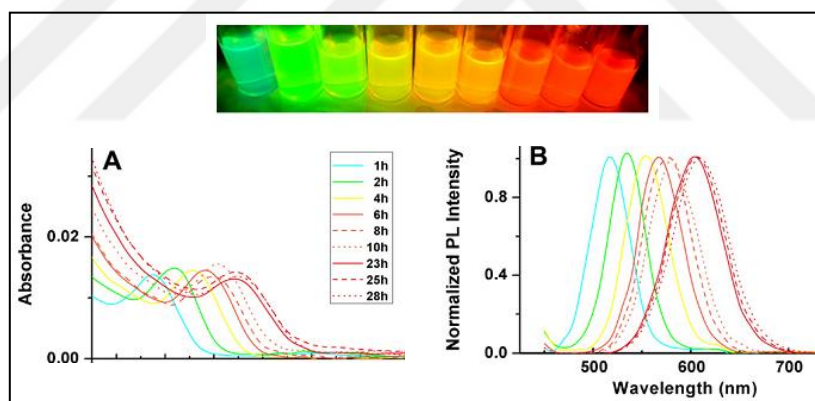


Figure 1. 11 MSA-capped CdTe/CdS QDs at different time points of synthesis. Photo image of QDs under excitation of 365 nm UV lamp (top) and their UV-Vis absorption (A) and photoluminescence (B) spectra [54].

1.5 Biomedical Applications of QDs

The excellent properties of QDs make them powerful agents for various applications such as for photovoltaic devices (solar cells), biomedicine, light emitting diodes, quantum computation, flat-panel displays, memory elements, photodetectors and lasers. Especially the application of QDs in biomedicine such as labeling of cells and tissues, *in vivo*

targeting, diagnosis, bioanalytical assays, biosensors, drug-gene delivery, disease treatment, tracking cell migration have an important place in recent years (Figure 1. 12) [55, 56].

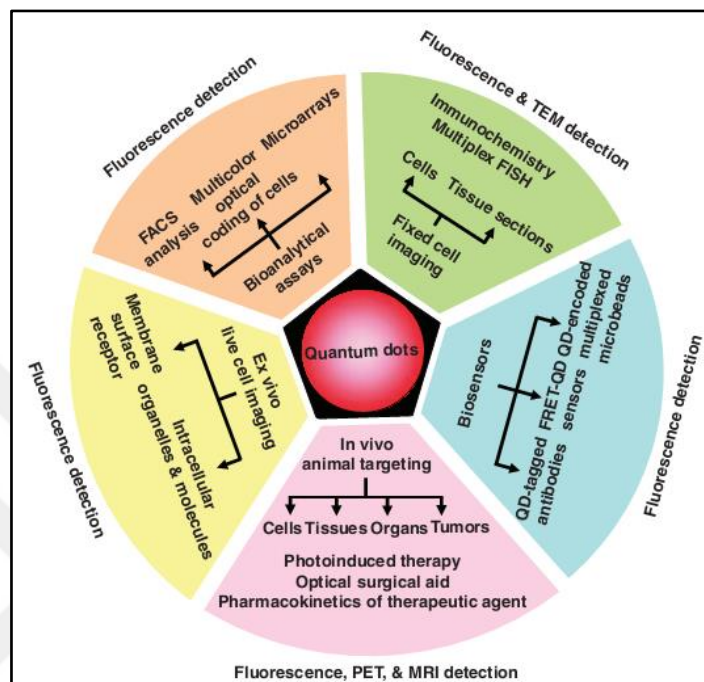


Figure 1. 12 Applications of quantum dots as multimodal contrast agents in bioimaging [56].

Size-tunable light emission, effective signal brightness, large absorption coefficients across a wide spectral range, photo stability and resistance to photo bleaching show superiority against conventional organic fluorescence dyes used in biomedical applications. Organic fluorophores bleach after few minutes (or seconds) of exposure to the external irradiation. However, QDs keep their emission capabilities for several hours. Figure 1. 13 depicts photo stability of a streptavidin modified red QD (QD 630-streptavidin) and an organic fluorophore (Alexa Fluor 488) in 3T3 cells depending on imaging time length. It is clearly seen that Alexa 488 photo bleaches within 60 s while QDs retain intense emission [57].

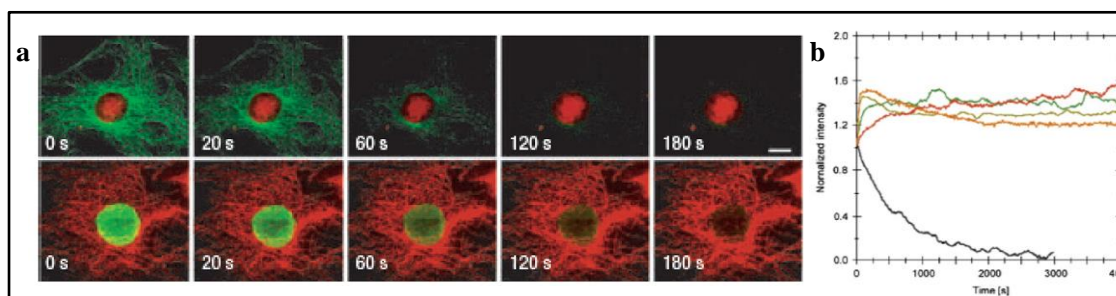


Figure 1. 13 Photostability of QDs versus conventional organic fluorescence dyes. a) Top row: Simultaneous labeling of 3T3 cells with QD 630-streptavidin (red) for nucleus and Alexa Fluor 488 (green) for microtubules. Bottom row: Labeling of nucleus with Alexa Fluor 488 (green) and microtubules with QD 630-streptavidin (red). b) Time dependent fluorescence intensity of QDs covered with silane shell versus Rhodamine 6G [57].

Semiconductor QDs can be utilized for fluorescent labeling of cells, specific organelles, or cellular molecules. Hence, can provide ability to optically track particles inside the cell and/or body to determine the biodistribution, or detect any abnormality in a diagnostic manner. Additionally, QDs can be targeted to specific cells with relevant ligands for the cell surface receptors overexpressed particularly in target cells/tissue/diseased site. Great surface to volume ratio enables conjugation of multiple therapeutic agents and targeting ligands to surface. In Figure 1. 14, some examples for fluorescence micrographs of labeled cells with QDs are represented. Actin compartment of 3T3 cells can be efficiently stained with QDs (Figure 1. 14a). Targeting of urokinase plasminogen receptor on MDA-MB-231 breast tumor cell line is achieved via QD-antibody conjugate (Figure 1. 14b). Mammalian cells are labelled using QD-Tat peptide structures (Figure 1. 14c) [58]. (Figure 1. 14d) CXCR4 receptors on cells are targeted by red emitting QDs [59]. The brightness of QDs is retained after *ex vivo* and *in vivo* treatment of the particles in mice (Figure 1. 14e-h) [58]. The images imply excellent applicability and great potential in optical bioimaging and diagnosis.

In another study performed by Ballou et al., powerful brightness of QDs in lymph nodes of mice was indicated for four months [60].

Particles also allow real-time tracking of molecules and cells. Dahan, Jovin and their coworkers reported real-time visualization of single-molecule movement in single living

cells [61, 62]. These studies have been a guide to understand receptor diffusion dynamics, biomolecular transport, ligand–receptor interactions, molecular motors and enzyme activity.

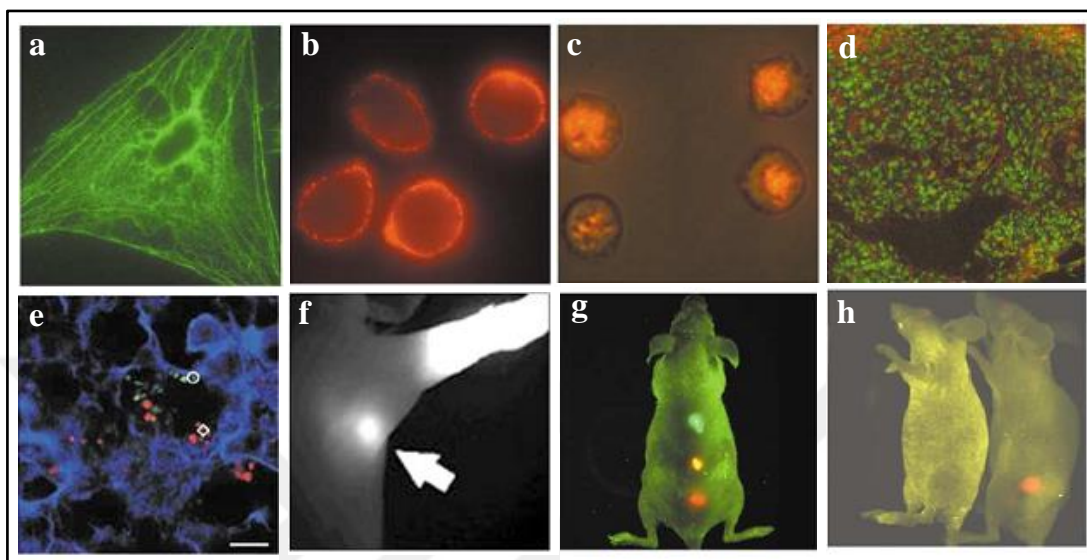


Figure 1. 14 Fluorescence microscope images of QDs introduced into cells and tissues. (a) Actin staining on fixed 3T3 fibroblast cells (green color). (b) Live MDA-MB-231 breast tumor cells labeled with urokinase plasminogen receptor targeting red QD-antibody. (c) Labeling of live mammalian cells with QD-Tat peptide conjugates [58]. (d) Frozen tissue specimens labeled by red QDs targeting the CXCR4 receptor and a nuclear dye in green color. (e) *Ex vivo* cancer tissue examination using QDs in a mouse lung [63]. (f) NIR fluorescence image of water-soluble type II QDs in sentinel lymph nodes of a mouse [64] (g) Simultaneous *in vivo* imaging of multicolor QD-encoded microbeads [58]. (h) *In vivo* imaging and targeting of a prostate tumor by using a QD-antibody conjugate emitting in red color [58].

1.6 Near Infra-Red Emitting Quantum Dots (NIRQDs) as Optical Bioimaging Agents

Although, well separated emission from blue to red with well-prepared QDs is even commercially available, they use in optical imaging of the biological species are limited. Low photon penetration depth of visible light [65, 66], absorption and scattering of light by hemoglobin and deoxyhemoglobin, and significant auto-fluorescence of collagen in the living tissue, makes visible window impractical for optical contrast generation [67].

Overlap of the tissue auto-fluorescence with the emission spectra of QDs, resolution of signal becomes difficult and a strong contrast cannot be achieved [68] [67]. Hence, QD emission above 700 nm would be more preferable but considering that water absorption becomes dominant after 900 nm, most suitable imaging window is determined as 700-900 nm (Figure 1. 15).

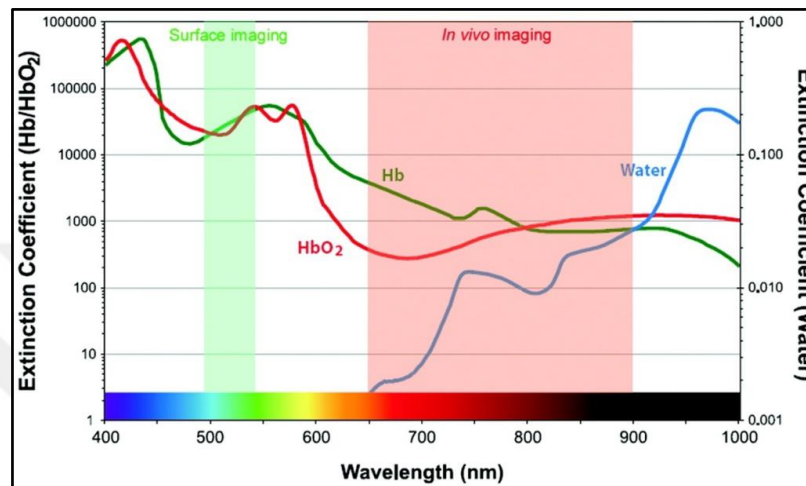


Figure 1. 15 Extinction coefficient value of oxy- and deoxy-hemoglobin and water from visible to NIR window [68].

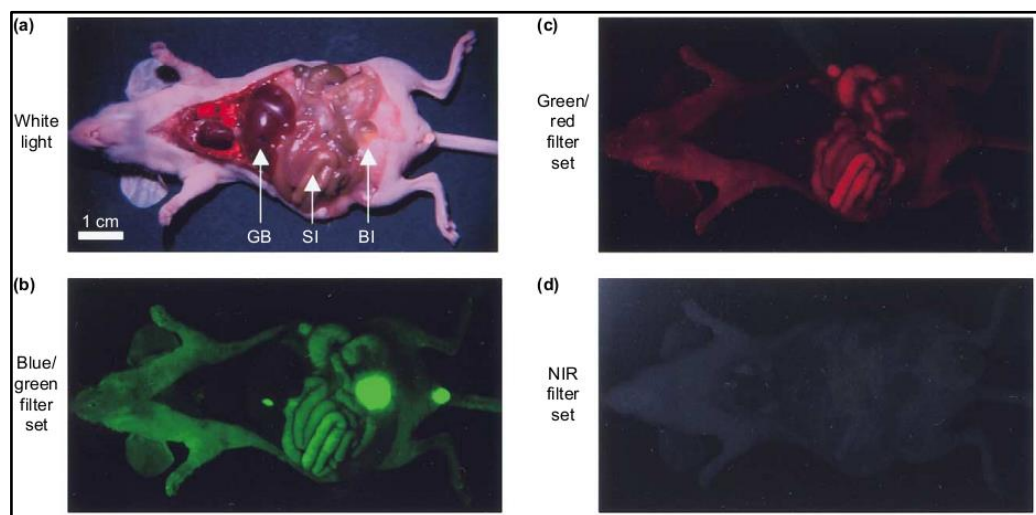


Figure 1. 16 Wavelength-dependent autofluorescence of tissues. (a) White light color image of a mouse. Glad bladder (GB), small intestine (SI), and bladder (BI) were illustrated. Tissue auto-fluorescence under three excitation/emission filter sets: (b) Blue/green (460–500 nm/505–560 nm), (c) green/red (525–555 nm/590–650 nm) and NIR (725–775 nm/790–830 nm) filter sets [69].

Imaging in the NIR-I region (700-900 nm) enhances the sensitivity and resolution by eliminating the scattering and absorption effects as well as the autofluorescence and hence, increase the signal/noise ratio (Figure 1. 16). In addition, light penetrates deeper into the tissue at such longer wavelengths, allowing deeper tissue imaging. For this reasons, the NIR region between 700-900 nm is known as therapeutic window or optical window for biomedical applications [70].

These superiorities have promoted the development of NIR emitting quantum dots. *In vitro* and *in vivo* optical imaging, for labeling or diagnostic purposes, and photodynamic therapy are some of the application areas of NIRQDs [71-73]. Various Cd and Pb-containing NIR emitting quantum dots have been synthesized, such as CdTe (II-VI) [74], PbS (IV-VI) [75], type-II hetero structured quantum dots (CdTe/CdSe, CdSe/CdTe and CdSe/ZnTe) [76, 77] and used for optical imaging (Figure 1. 17). For example, Kim et al. used CdTe/CdSe QDs for imaging of sentinel lymph nodes in mice [64]. Prasad et al. demonstrated imaging of a PANC-1 tumor [78]. Morgan et al. used CdMnTe/Hg QDs as angiographic contrast agents [79].

However, these structures contain heavy metals and have intrinsic toxicity to living organisms and this situation limits their further bio-applications. Several studies have shown the release of heavy metals such as Cd from the core of QDs into living tissues [42, 80]. Wang et al. have reported that even in nanomolar concentrations, QDs can cause toxic effect by DNA damage and protein degradation in microorganisms [81]. Therefore, development of nontoxic QDs for clinical applications is an urgent demand.

III-V quantum dots (InAs, InP) are cadmium and lead free NIR fluorescent materials developed in the past decades. However, their synthesis require expensive and hazardous $(\text{TMS})_3\text{P}$ and $(\text{TMS})_3\text{As}$ as precursors [10, 82].

Ternary I-III-VI quantum dots (CuInS_2 , Cu-In-Se, AgInS_2) are another class of heavy metal free quantum dots [83, 84]. The problem of these quantum dot compositions is the difficulty in controlling the composition due to the different activities of the cation precursors.

Moreover, many of these developed quantum dots were synthesized in organic phase and could not be directly used in biological systems without post-synthetic modification. The bioapplication of QDs requires additional water dispersion process such as transfer

into water or modification with water soluble biocompatible molecules [85, 86]. However, these steps usually cause a significant decrease in the luminescence of the nanoparticles.

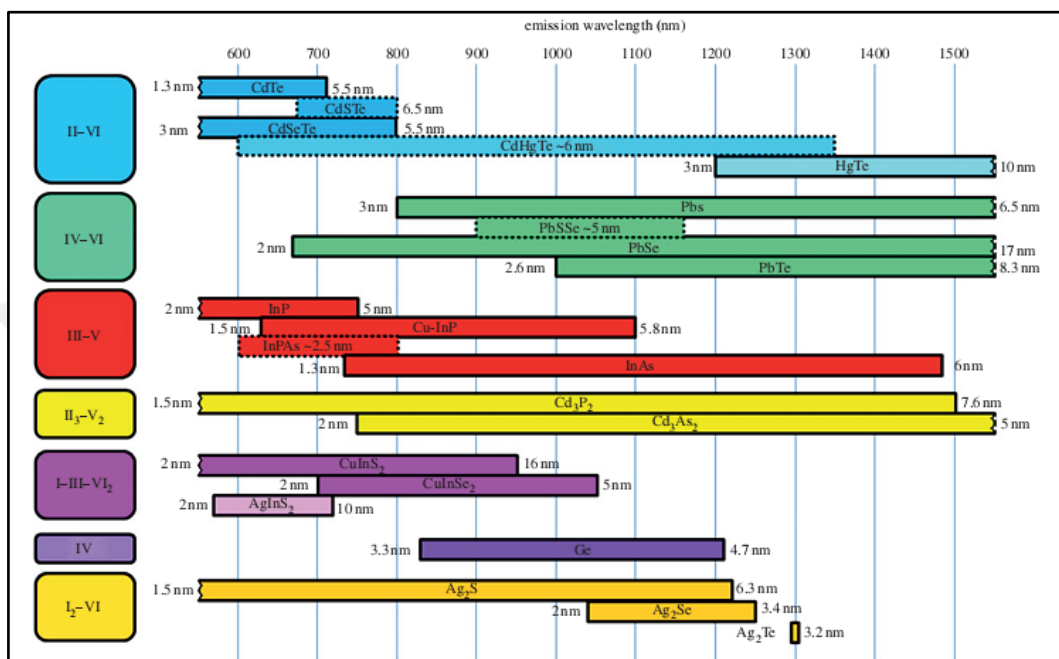


Figure 1.17 Composition, emission range and size of some NIR-emitting QDs synthesized through solution-based methods [31].

1.6.1 Ag₂S NIRQDs

Silver chalcogenide quantum dots with a band gap of 0.9 (Ag₂S), 0.15 (Ag₂Se) and 0.67 (Ag₂Te) eV and emission range between 650-1200 nm are of great interest in recent years as a new class of NIR emitting QDs due to their highly biocompatible nature (Figure 1.18) [87, 88]. Their ultralow solubility product constants (*e.g.*, $K_{sp}(\text{Ag}_2\text{S}) = 6.3 \times 10^{-50}$; $K_{sp}(\text{Ag}_2\text{Se}) = 2.0 \times 10^{-64}$; correspondingly $K_{sp}(\text{CdS}) = 8.0 \times 10^{-27}$; $K_{sp}(\text{CdSe}) = 6.31 \times 10^{-36}$) prevent release of Ag ions into biological systems and make them excellent probes for optical bioimaging.

Ag₂S QDs are very popular in silver chalcogenides due to emission in the medical window and excellent biocompatibility. Besides, emission in the NIR-I can be relatively easily detected with the existing detection equipments mostly containing Si or PMT detectors.

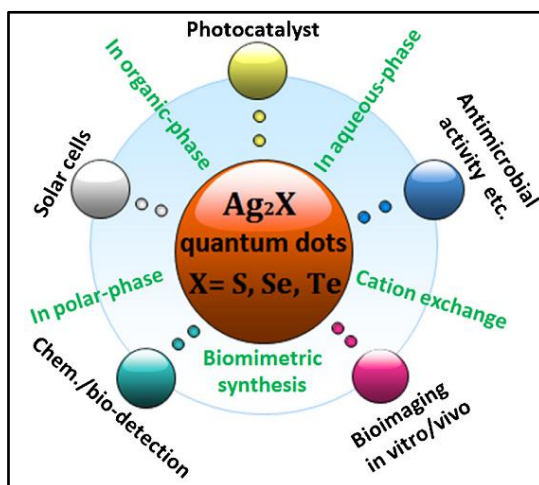


Figure 1. 18 Synthetic approaches and applications of silver chalcogenides [89].

Ag_2S QDs are in α -phase with a monoclinic crystal structure [90]. First Ag_2S semiconductor colloidal nanoparticles were reported by Brelle et al. They were capped by cysteine and glutathione (GSH) and had an average diameter of 9 nm. No information on the optical properties of these particles were reported [91]. In 2003, controllable assemblies of ordered semiconductor Ag_2S nanostructures were demonstrated by Zhao et al [92]. In 2004, metal-thiolate and thioacetamide were reacted in a pure dodecanethiol solvent and monodisperse Ag_2S nanoclusters were obtained [93]. Ag_2S QDs synthesized in water-in- CO_2 microemulsions were reported by Liu et al. [94]. Finally in 2010, the first photoluminescent Ag_2S QDs were reported by Wang et al. using single source precursors as shown in Figure 1. 19A [95] and afterwards, more reports on the synthesis and use of Ag_2S QDs came out. Actually, Wang et al. produced hydrophobic Ag_2S NIRQDs emitting at 1058 nm from $(\text{C}_2\text{H}_5)_2\text{NCS}_2\text{Ag}$ [95] and then PEGylated ones via ligand exchange with DHLA and conjugation with PEG. This Ag_2S NIRQDs emitting at 1200 nm showed enhanced spatial resolution in the *in vivo* imaging of angiogenesis [96] and allowed tracking of mesenchymal stem cells *in vivo* [97]. They have also studied long-term *in vivo* effect and biodistribution of PEGylated- Ag_2S QDs as well its NIR-II imaging potential *in vivo*. These QDs mainly accumulated in the reticuloendothelial system (RES), especially in the liver and spleen and cleared from the body by fecal excretion [98][98]. They showed no appreciable cytotoxicity at the tested doses (15 and 30 mg/kg) over a period of 2 months indicating a highly biocompatible nature *in vivo*, as well (Figure 1. 21) [99]. In the last four years there has been a tremendous amount of effort in aqueous

synthesis of Ag_2S NIRQDs. Tian et al. synthesized water-soluble Ag_2S quantum dots coated with 3-mercaptopropionic acid and demonstrated its use as an optical probe in the *in vivo* studies using mice [100]. Cui and Su et al. synthesized Ag_2S NIRQDs using RNase A as template in aqueous medium via biomimetic route [101]. Pang et al. prepared emission-tunable Ag_2S quantum dots in a two-step procedure [88]. Yan et al. reported bovine serum albumin (BSA)-stabilized NIR emitting Ag_2S NIRQDs and its conjugation with endothelial growth factor (VEGF) antibody for targeted cancer imaging (Figure 1. 19B) [102].

Most of the Ag_2S QDs synthesized by aqueous methods were done using a water soluble organic coating as illustrated in Figure 1. 19B. In addition, Ag_2S QDs were synthesized in cultured cancer cells using same approach by delivering quantum dot precursors into cultured hepatoma carcinoma cells. Here, endogenous glutathione in the cell was used as the coating of the crystal (Figure 1. 21).

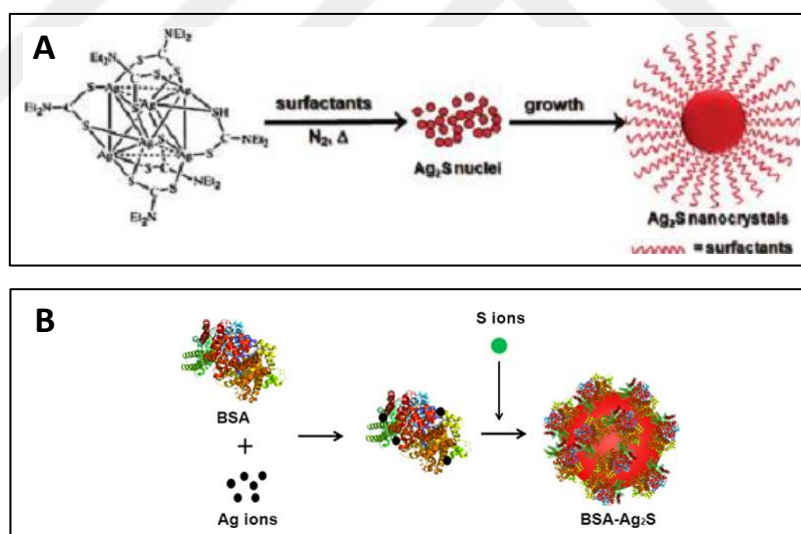


Figure 1. 19 Some aqueous synthesis methods for Ag_2S QDs. A) Synthesis from single precursor [95]. B) Synthesis in organic coating [103].

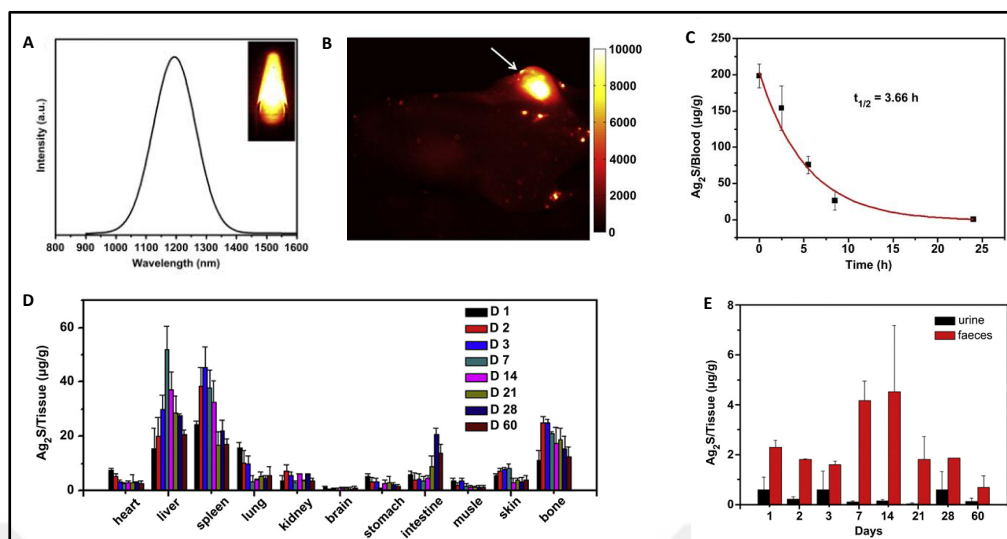


Figure 1. 20 PEGylated Ag_2S QDs. A) Photoluminescence spectrum upon excitation at 658 nm. Inset shows an NIR-II PL image of the PEGylated- Ag_2S QD suspension under an 808 nm excitation. B) A NIR-II PL image recorded between 1100–1700 nm regions of a tumor-bearing Balb/c mouse subjected to 15 mg/kg dose of PEGylated- Ag_2S QDs at 24 h. C) The blood circulation curve and D) Long-term biodistribution of QDs at this concentration. E) Concentrations of QDs in urine and feces over two months after treatment [99].

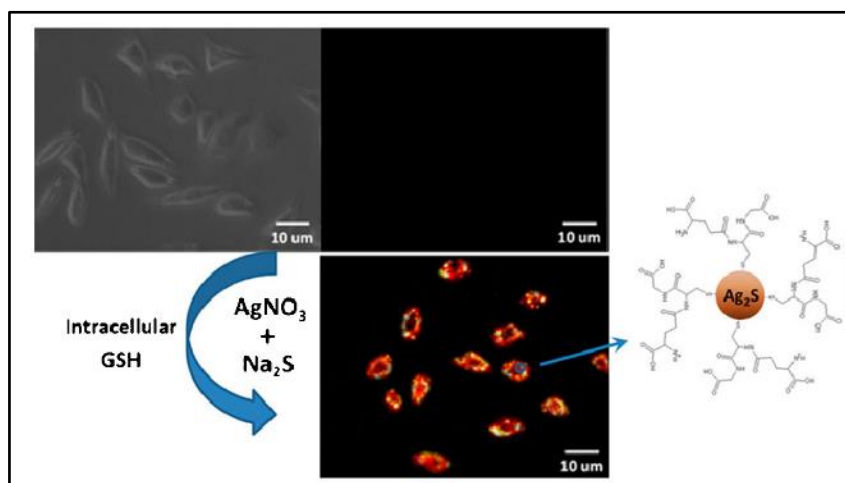


Figure 1. 21 Synthetic strategy of Ag_2S QDs in cultured HepG2 cancer cells [103].

Table 1. 2 presents the details of most of the Ag_2S QDs developed in the literature, so far.

Table 1. 2 Comparison of Ag₂S QDs synthesized in the literature and their bioapplications.

Core	Coating	Synthesis approach	λ_{em} max (nm)	Size (nm)	QY (%)	Area of application	Ref
Ag ₂ S	Ribonuclease-A	In aqueous phase via biomimetic route	980	5.6	NR	<i>In vitro</i> cytotoxicity in HEK 293T	[104]
Ag ₂ S	2MPA	Aqueous-phase synthesis	780 - 950	2.3 - 3.1	7 - 39	<i>In vitro</i> cytotoxicity in NIH/3T3 and imaging	[105]
Ag ₂ S	Glutathione	Phase transfer-based synthesis and ligand exchange	1045	3.7	2.5	<i>In vitro</i> cytotoxicity in L929 cells	[106]
Ag ₂ S	DHLA (dihydrolipoic acid), PEG	Organic synthesis route, ligand exchange	1200	5.6	~16	<i>In vivo</i> visualization of the circulatory system, including lymphatic drainage, vascular networks and angiogenesis	[107]
Ag ₂ S	DHLA, PEG	Organic synthesis route, ligand exchange	1200	No report	NR	Long-term <i>in vivo</i> biodistribution, imaging, toxicity	[99]
Ag ₂ S	DHLA, PEG	Organic synthesis route, ligand exchange	1200	26.8 (hydrodynamic size)	15.5	<i>In vivo</i> tumor imaging, biodistribution	[108]
Ag ₂ S	Bovine serum albumin	Aqueous-phase synthesis	1050 - 1294	1.6 - 6.8	1.8	<i>In vitro</i> cytotoxicity in HIEC cells and hemolysis test	[103]
Ag ₂ S	Glutathione	Aqueous-phase synthesis	624 - 724	1.7 - 3.7	0.5 - 0.1	<i>In vitro</i> cytotoxicity and imaging in MC3T3-EI cells	[109]
Ag ₂ S	Oleic acid, octadecylamine, 1-octadecane	Single-source precursor method (Pyrolysis of Ag(DDTC))	1058	10.2 ± 0.4	NR	No report	[95]
Ag ₂ S	1-Dodecanethiol (DT)	Aqueous-phase synthesis	975 - 1175	2.4 - 7.0	NR	No report	[110]
Ag ₂ S	A designed aptamer (Apt43)	Aqueous-phase synthesis	978 - 1179	2.5 - 4.4	1 - 1.3	<i>In vitro</i> imaging and <i>in vivo</i> photothermal therapy	[111]
Ag ₂ S	1-octylamine and myristic acid	Organic synthesis route	690 - 1227	1.5 - 4.6	0.18	No report	[88]
Ag ₂ S	meso-2,3-dimercaptosuccinic acid	Aqueous-phase synthesis	730 - 900	2.20 - 2.89	6.5	<i>In vitro</i> cytotoxicity and imaging in HeLa and NIH/3T3 cells and Hemocompatibility	[49]
Ag ₂ S	3-mercaptopropionic acid and cRGD for cancer targeting	Aqueous-phase synthesis	800	No report	37.9	Tumor-targeting, cancer imaging and therapy <i>in vivo</i>	[112]
Ag ₂ S	Bovine serum albumin and antiVEGF for cancer targeting	Aqueous-phase synthesis	660 - 840	2.1 ± 0.3	0.75 - 1.8	Targeted cancer imaging <i>in vivo</i>	[113]
Ag ₂ S	Glutathione	In cultured cancer cells	945	1.56±0.21	5.45	<i>In vitro</i> and <i>in vivo</i> imaging	[114]
Ag ₂ S	PEG	Organic synthesis route	~ 1100	13.4 (hydrodynamic size)	17	Real-time <i>in vivo</i> visualization of tumor therapy	[115]
Ag ₂ S	3-mercaptopropionic acid, silica	Viscosity modulated approach	500 - 1200	1.5 - 9	4.4 - 22.7	<i>In vivo</i> integrin-targeted cancer imaging	[116]
Ag ₂ S	DL, DHLA, PEG	Organic synthesis route, ligand exchange	1150 - 1200	5.4 - 10	5.8	<i>In vitro</i> targeting and imaging of MDA-MB-468 and U87MG	[117]

ND: Not reported

Wang et al. demonstrated the size range necessary for quantum confinement of Ag₂S QDs as 2.4 to 4.4 nm. No size-dependent optical property was demonstrated from particles bigger than 4 nm. In addition, the luminescence decay time increases from 57 to 181 ns as QDs growing from 2.4 to 7 nm (Figure 1. 22) [110].

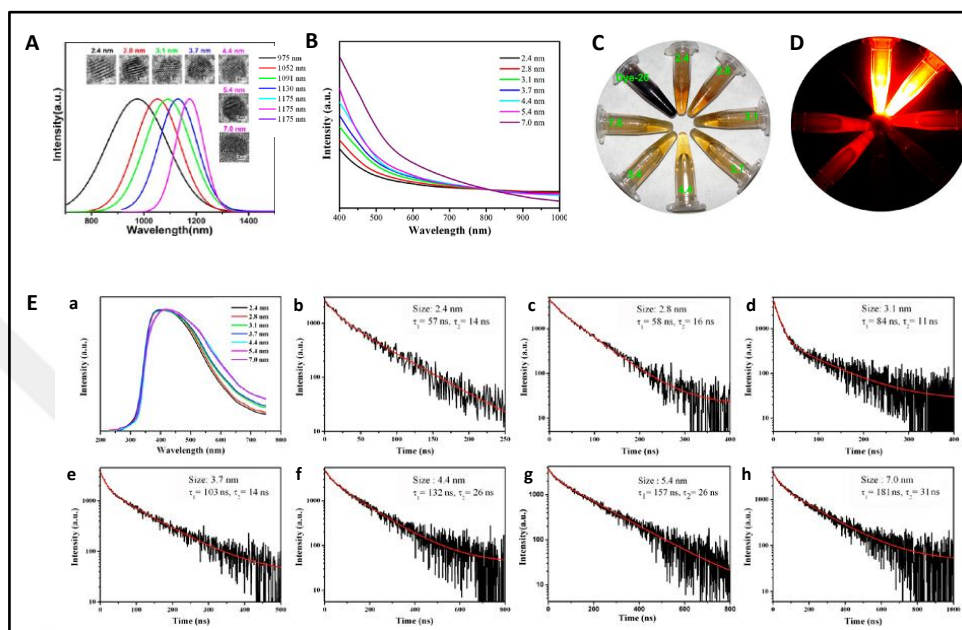


Figure 1. 22 Ag₂S QDs prepared in different sizes. A) Photoluminescence spectra under an excitation of 785 nm. B) Absorption spectra of QDs. C) Daylight and D) NIR-II fluorescence images. E) Photoluminescence excitation spectra (a) and time-resolved photoluminescence spectra of Ag₂S QDs in different sizes [110].

Ag₂S QDs are also efficiently employed as therapeutic agents besides their diagnostic/imaging properties. Chen et al. demonstrated targeted therapy of cancer by cyclic RGD peptide (cRGD), a tumor targeting tripeptide, tagged Ag₂S QDs loaded with doxorubicin, a widely used chemotherapeutic drug. Selective imaging and tumor inhibition of QDs at both cellular level and animal studies proved the excellent multifunctional features of Ag₂S QDs (Figure 1. 23) [112].

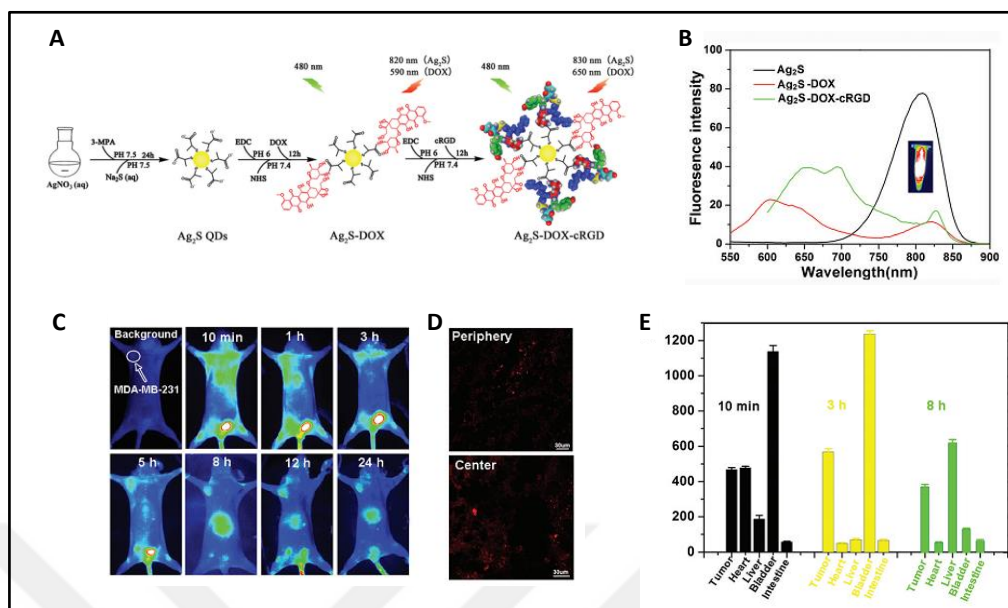


Figure 1. 23 A) Schematic representation of synthesis of Ag_2S , $\text{Ag}_2\text{S-DOX}$ and $\text{Ag}_2\text{S-DOX-cRGD}$. B) Fluorescence spectra of nanoparticles. C) *In vivo* fluorescence imaging in MDA-MB-231 tumor-bearing mice, injected with $\text{Ag}_2\text{S-DOX-cRGD}$. D) Peripheral and central slices of the tumor under LSCM. E) Fluorescence intensities of tumor and major organs (heart, liver, bladder and intestine) at 10 min, 3 h and 8 h post-injection of QDs [112].

1.6.2 Ag_2S QDs developed in our group

Acar et al. have shown aqueous synthesis of 2-mercaptoacetic acid (2MPA) coated Ag_2S QDs with high luminescence and biocompatibility. The emission from QDs could be easily tuned from 780 nm to 950 nm by change the reaction conditions such as temperature and Ag/S ratio. The resulting nanocrystals demonstrated photoluminescence quantum yields around 7-39 % which was the highest reported value at that time. In addition, even at high QD concentrations, cytotoxicity of particles was very low (Figure 1. 24) [105].

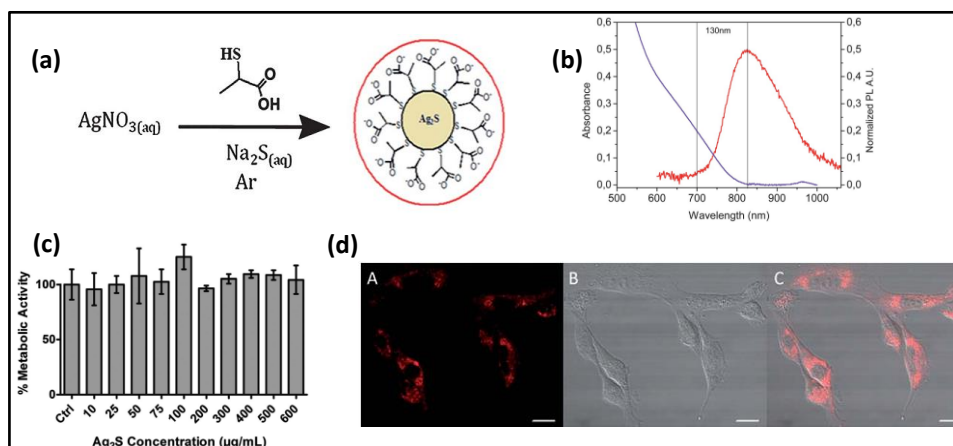


Figure 1. 24 2MPA coated Ag_2S QDs developed by Acar and coworkers [105]. (a) Schematic representation of aqueous synthesis of 2MPA- Ag_2S NIRQDs. (b) Absorbance and photoluminescence spectra of Ag_2S QDs. (c) Cellular uptake of QDs by NIH/3T3 cells A: Fluorescence, B: transmission and C: merged images taken by confocal microscope. The scale bar = 20 μm .

In another study, *meso*-2,3-dimercaptosuccinic acid (DMSA) which is an FDA approved drug used in heavy metal poisoning, was effectively used as a coating agent and sulfide source for Ag_2S synthesis. The resulting particles show emission maximum between 730–860 nm with a quantum yield around 6.5 %. They are highly cyto- and hemo-compatible and present strong photoluminescence emission in the cells [49] (Figure 1. 25).

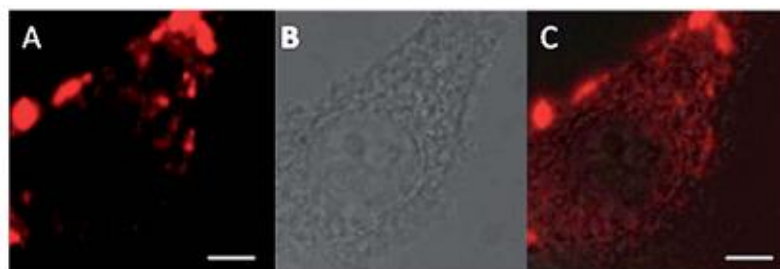


Figure 1. 25 Intracellular uptake of Ag_2S -DMSA NIRQDs at a concentration of 150 $\mu\text{g}/\text{mL}$ by HeLa cells after 6 h incubation. (A) Fluorescence, (B) transmission and (C) merged channels of the confocal micrographs. Scale bar = 5 μm .

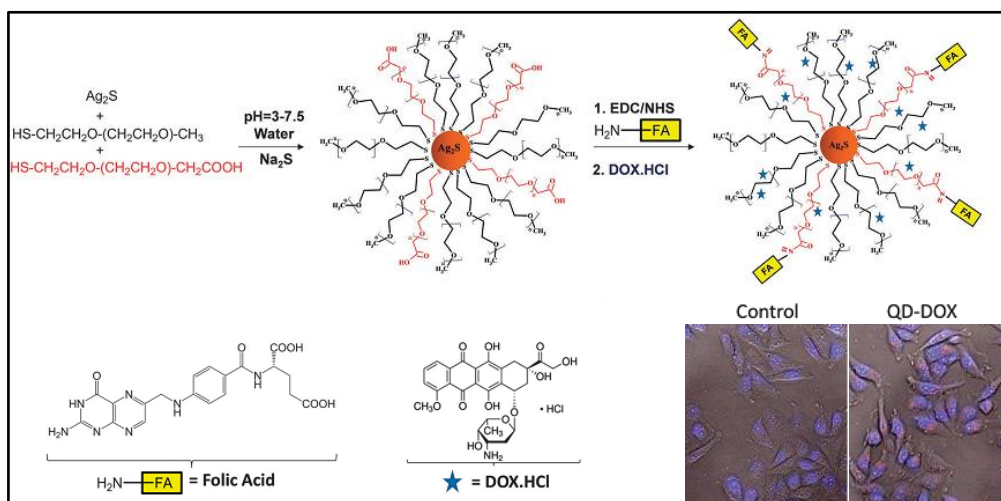


Figure 1. 26 Schematic illustration of aqueous synthesis of Ag₂S–PEG QDs, folic acid conjugation, DOX loading and intracellular uptake of such nanoparticles [118].

PEGylation of nanoparticles decreases the cytotoxicity and non-specific uptake while increasing blood half-life and water-solubility. From this perspective, Acar and coworkers synthesized Ag₂S QDs directly in aqueous solution of HS-PEG and conjugated the nanoparticles by folic acid and loaded with doxorubicin (DOX) to use them for cancer targeted drug therapy and optical imaging. Changing the reaction variables such as PEG molecular weight, precursor ratios and pH, a quantum yield between 2 and 65 % was obtained. After folic acid attachment and DOX loading, the uptake of QDs significantly enhanced in folate receptor positive HeLa cells and 50 % cell death was achieved with the particles containing as low as 15 nM DOX. They also demonstrated strong NIR signal in the *in vitro* imaging studies (Figure 1. 26) [118].

After the development of Ag₂S QDs with excellent features, they were combined with superparamagnetic iron oxide nanoparticles (SPION), producing unique multifunctional nanocomposites. Simple extraction method utilizing ligand exchange mechanism was employed for the preparation of such structures in small size regime (less than 100 nm). Resulting hybrid nanoparticles showed both luminescence in the NIR region and strong magnetic response under magnetic field. They had also good cyto/hemocompatibility and intracellular uptake confirmed with confocal microscopy analysis. Magnetic component of the hybrid particles were exploited for magnetic

targeting successfully in the *in vitro* 2D cell studies. These results imply that the hybrid nanoparticles can be employed as effective dual imaging agents (optical imaging and MRI) and can be magnetically dragged to the site of interest (Figure 1. 27) [119].

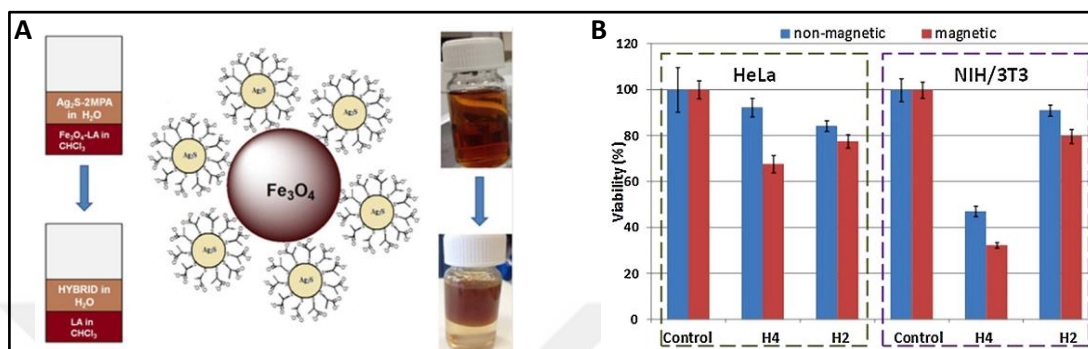


Figure 1. 27 Hybrid nanoparticles. (A) Preparation using ligand exchange technique. (B) Cell viability (%) measured by MTT assay on HeLa and NIH/3T3 cells exposed to nanoparticles in the absence and presence of magnetic field [119].

1.7 Gene and Drug Delivery

1.7.1 Gene Delivery

Gene therapy is a technique based on delivery of genetic material into patient's cells, which provides a therapeutic effect through the following paths: repairing genetic defects, suppressing the expression of genes, overexpressing therapeutic proteins. Introduction of functional genes into patient's cells presents a powerful treatment way for many diseases such as autoimmune disorders, monogenic and cardiovascular diseases, neurodegenerative diseases, tissue engineering, regenerative medicine and cancers (Figure 1. 28) [120].

Cancer gene therapy promises lots of reformist treatments against cancer related mortality, generally using genes to stimulate an antitumor immune response which fails in cancer tissues. Mutations of most of the genes cause carcinogenesis. Mutations of *p53* gene is one of the most frequently occurring abnormality during the formation of cancer [121]. *P53* is a tumor suppressor gene and accepted as "the guardian of the genome" because it plays a central role in the prevention of tumor development. In a case of a DNA mutation, the gene stops cellular activities such as division and starts the repair mechanism of cell, or if the mutation is very critical, the cell undergoes to apoptosis and

removed from the body [122]. However, the abnormalities on *p53* gene shut down these regulations and cancerous tissues continue to grow. Clinical gene therapy studies performed by delivery of healthy *p53* gene into cancer cells significantly minimized tumor size. China takes the lead in the clinical trial of *p53* gene therapy. Chinese State Food and Drug Administration was approved the therapy for treatment of head and neck cancer in 2003 with *p53*. Its approval by FDA is expected shortly [123].

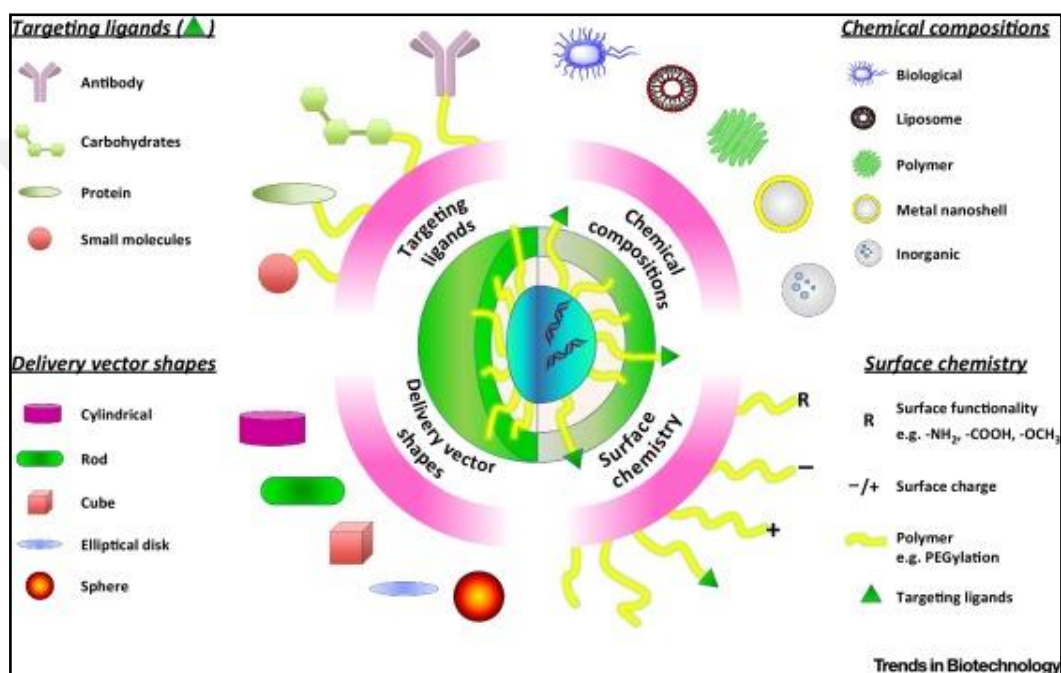


Figure 1.28 Gene and drug delivery application platform [124].

The efficient delivery of nucleic acid into the tissues is central aspect of gene therapy. Naked oligonucleotides are rapidly broken down in the circulation of body by nucleases and accumulate in reticuloendothelial system such as in kidney and liver, hence removed from the body [120]. Therefore, delivery of nucleic acids by carriers has a significant importance in successful gene therapy. Potential gene vectors should condense and protect nucleic acids effectively [125]. So far, two major approaches utilized in nucleic acid delivery are the use of viral and non-viral delivery vectors. Safety hazards of viral vectors remain as a big handicap despite of their high transfection efficiency. Non-viral vectors are usually liposomes, dendrimers, polymers, solid lipid nanoparticles, nanosuspensions or nanoparticles [126-129]. Non-viral vectors offer multiple advantages

such as easy modification, high nucleic acid binding capacity, safe and targeted delivery of genes into desired tissues [130].

Nucleic acids can be conjugated with nanocarriers in several ways: encapsulation within the nanoparticle such as in liposomes, covalent conjugation or electrostatic interaction. For electrostatic interaction, positively charged nanoparticles are needed to complex the negatively charged nucleic acids. Therefore, nanoparticles are generally coated with cationic polymers. Commonly used cationic polymers are shown in Figure 1. 29. As seen in the figure, synthetic polymers such as polyethylenimine (PEI), poly(L-lysine) (PLL), poly(lactic-co-glycolic acid) (PLGA), poly(amidoamine) (PAMAM), polypropyleneimine (PPI) and biological polymers such as chitosan and alginate are frequently used polymers in gene delivery applications [120].

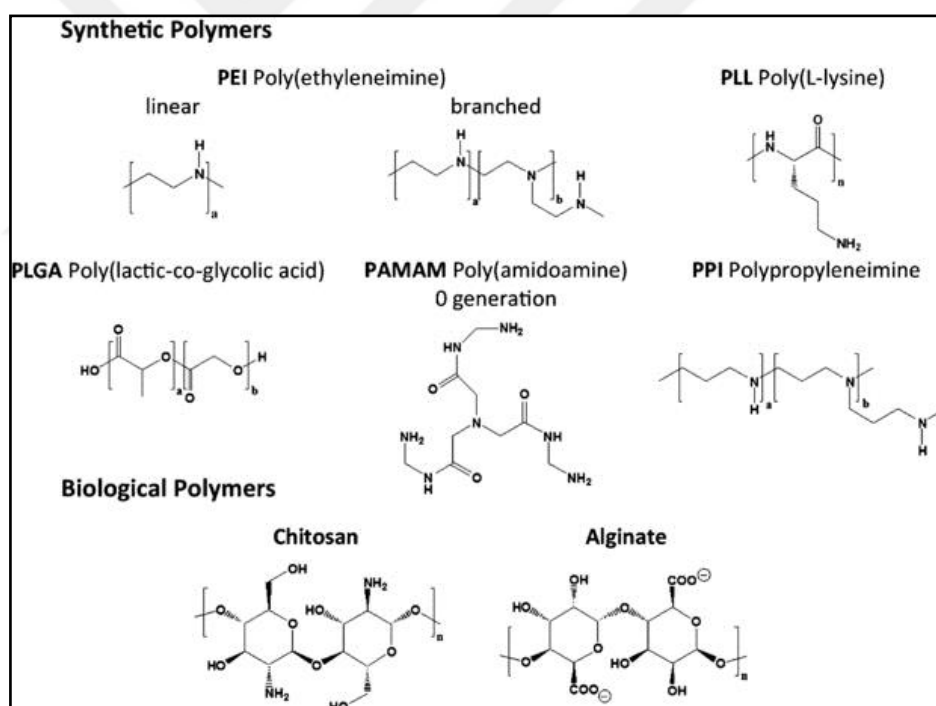


Figure 1. 29 The most frequently used synthetic and biological polymers with the chemical structures in gene delivery applications [120].

Branched polyethylenimine with 25 kDa molecular weight (MW) has highest transfection efficiency in these polymers and hence, accepted as the golden standard in gene delivery applications. The high transfection efficiency of the polymer originates from its “proton sponge” effect which is a well-known hypothesis. PEI has buffering

capacity to endosomal environment. The polymer enters into the cell via endocytosis and retained in the endosome. In acidic conditions of the endosome, the polymer is protonated by the help of the membrane bound ATPase proton pumps and resists the decrease of endosomal pH. Therefore, more protons are pumped into the endosome in order to achieve lower pH. However, chloride ions enter to endosome to maintain electrical neutrality. This process results in rise of ionic concentration and water influx due to osmotic pressure and as a result, endosome swells and ruptures before lysosomal degradation. Hence, the polymer releases the oligonucleotide which is delivered to nucleus successfully [131, 132] (Figure 1. 30).

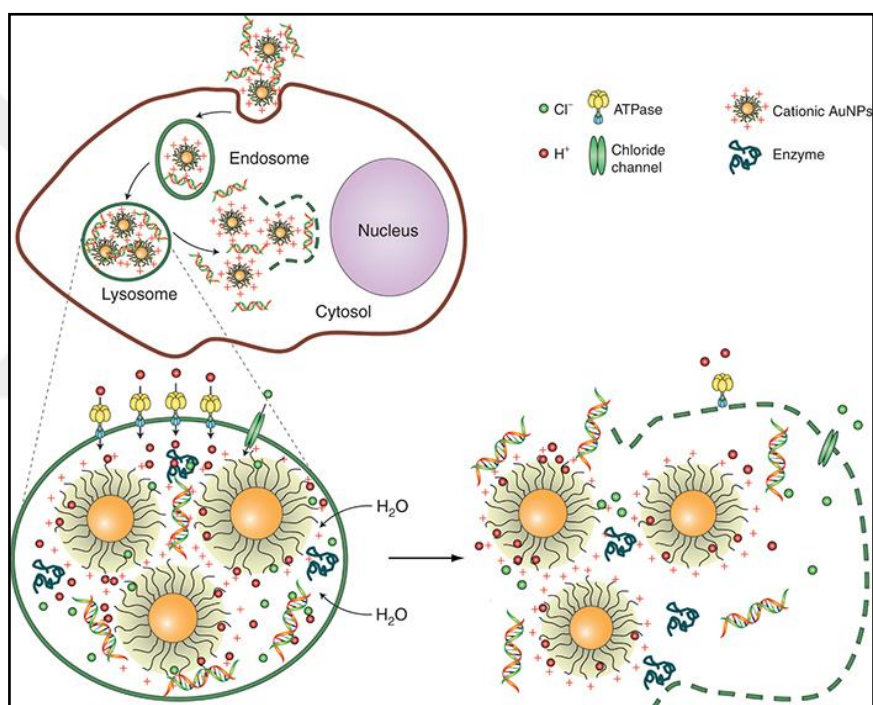


Figure 1. 30 Schematic representation of the proton sponge effect of PEI [133].

Inorganic nanoparticles coated with cationic polymers are exploited as gene transfection vectors and in deed are more advantages to polymeric, dendrimeric or liposomal structures which lacks imaging/tracking modality. Quantum dots in this platform offer many advantages: optical tracking of the delivery vehicle, stable fluorescence which can be adjusted within the medical imaging window , high surface to volume ratio which enables loading of multiple therapeutic agents such as gene and drug as well as and tumor or disease targeting molecules. So, QDs can be employed as

multifunctional vehicles combining diagnostic and therapeutic applications in a single entity [120].

1.7.2 Drug Delivery

Over the past few decades, there has been a considerable interest in developing drug delivery systems for various diseases. Engineered nanoparticles such as polymeric nanoparticles, quantum dots or liposomes are powerful vehicles to carry drugs like in gene delivery. These delivery vehicles are usually designed to improve the therapeutic effect of various water soluble or insoluble clinical drugs by increasing their solubility, retention time or bioavailability in blood. Drugs can be protected from enzymatic degradation and their intracellular penetration increases with a delivery vehicle [134]. Drug can be encapsulated by nanocarriers, covalently attached or electrostatically bound to the nanoparticles [135].

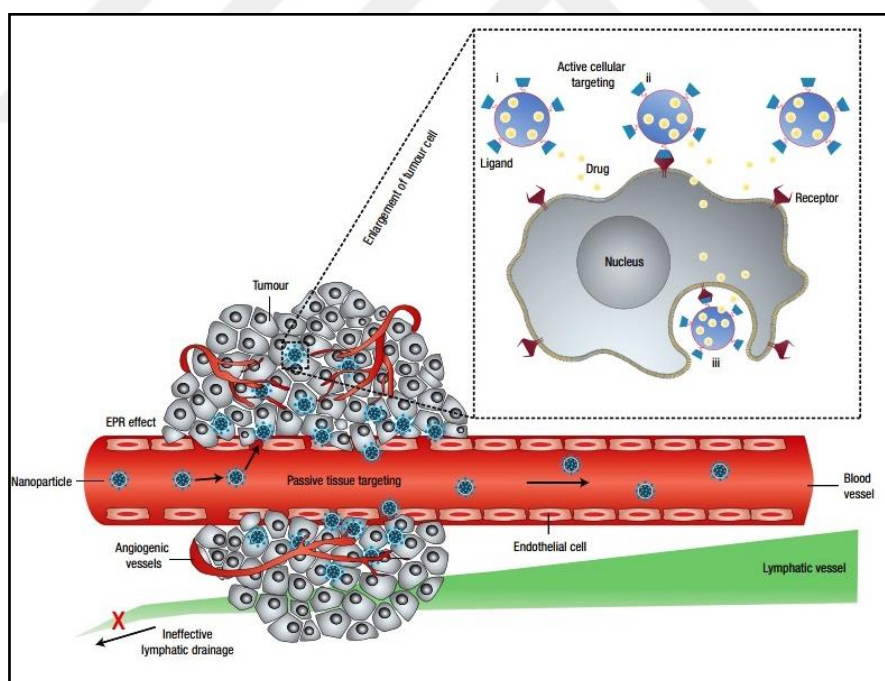


Figure 1. 31 Schematic illustration of passive and active targeting on tumor cells [136].

There are two main ways for delivery of the drug/nanoparticle complexes in the body: passive and active delivery/targeting (Figure 1. 31). Passive delivery is the addition of the complexes into blood circulation and accumulation of the drug in desired tissues

by some physical properties of the target tissues such as low pH, high temperature or leaky vascularization of tumor region. Typically, tumor vessels have a large number of pores and enlarged gap junctions between endothelial cells and lymphatic drainage which refers to enhanced permeability and retention (EPR) effect. This structure allows migration of nanoparticles/macromolecules up to 400 nm in diameter into the tumor tissues. On the other hand, nanoparticles should be smaller than 100 nm to avoid the capture by the liver and larger than 10 nm to avoid the filtration by the kidneys [137]. Very high accumulation of drug-loaded nanoparticles can be obtained at the tumor region by passive targeting/delivery by means of EPR effect. However, passive delivery has some limitations. The delivery mechanism depends on physiological structure of the target tissue. In some cases, this structure is not enough to accumulate the drug in the desired region in sufficient concentrations, hence specific targeting of the tissue is a better approach to increase the drug efficiency. Attachment of targeting ligands to the surface of nanoparticles which binds to relevant receptors expressed at the target site but not by the normal cells, can selectively deliver the drug at high concentration to the site of interest. This not only increases the drug efficacy but also reduces the side effects. This delivery or targeting mechanism is known as active delivery/targeting. After molecular recognition of the diseased cells and binding to the receptor, drug loaded nanoparticles internalized by the cells via receptor-mediated endocytosis. In this technique, drugs can be more specifically accumulated in the desired tissues compared to passive delivery. For this purpose, a great number of ligands have been used. These ligands can be monoclonal antibodies, peptides, aptamers or small molecules with a specific target receptor [136]. The most frequently applied ligands for cancer targeting can be summarized as follows:

Antibody fragments can be utilized to target specific tissues. For example, Fab part of antibody fragments is used to target NCA-90 (granulocyte), HER2 (in breast, ovarian, stomach cancer), CEA (carcino-embryonic antigen, apical surface of gastrointestinal epithelium, lung tissues, breast, and colorectal cancer), VEGF (breast, colon, lung, gastric, renal, and oropharyngeal cancers), whereas scFv part of antibody fragment is used to target CEA and HER2.

Monoclonal antibodies such as trastuzumab targets HER2, alemtuzumab targets CD52 (lymphocytes, monocytes, macrophages, monocyte-derived dendritic cells),

rituximab targets CD20 (pre-B and B-cell), bevacizumab targets VEGF, cetuximab targets EGF receptor (colorectal cancer), gefinitib targets EGFR (advanced non-small cell lung cancer), gemtuzumab targets CD33 (acute myelogenous leukemia), ibritumomab tiuxetan targets CD20 (non-hodgkins lymphoma), ipilimumab targets CTLA-4 (advanced melanoma), ofatumumab targets CD20 (chronic lymphocytic leukemia), tosiptomab targets CD20 (lymphoma) and panitumumab targets EGFR (breast, head, neck, gastric, colorectal, prostate, bladder, pancreatic, ovarian, renal cancers).

Cell-penetrating peptides and proteins such as RGD (Arg–Gly–Asp) is used to target integrins $\alpha_v\beta_5$ which is overexpressed on tumor endothelium, DARPins to target CD4 (T helper cells, monocytes, macrophages, and dendritic cells), HER2, HIV-TAT protein, VP22 from Herpes simplex virus type I.

DNA or RNA oligonucleotides such as aptamers are applied to target proteins and surface receptors.

And **other targeting molecules** can be used to target receptors overexpressed on cancer cells. Examples are folic acid (folate) to target folate receptors (in ovarian, brain, head and neck, renal, and breast cancers), lectins to target DC-SIGN (dendritic cells), CLR (C-type lectin receptor) and transferrin to target CD71 [138-140].

1.8 Proposal and Aim of This Thesis Work

Developments in the field of nanotechnology led into innovative techniques for the early detection, treatment, and prevention of numerous diseases, especially cancer. Cancer is one of the first three reasons of death globally and nationally. Early detection of cancer is one of the most important steps in the fight against the disease. The most important requirements for early diagnosis is sensitive detection modality/tool coupled with non-toxic contrast agents with high sensitivity, creating a strong contrast. Amongst different modalities of diagnostic imaging, optical imaging gained significant importance within the last decade due to the advancements in the optics and quantum dots technology. One important aspect in diagnostics is the combination of modalities such as MRI, which provides pre-operational localization, and optical imaging, which highlights the resection border in-operation.

In the therapy of cancer, chemotherapeutic small molecules or antibodies and radiotherapy are the two major approaches. Both has advantages and disadvantages and many times used in combination. Gene therapy is considered as an important alternative and/or complementary therapy. Yet, genes need a delivery vehicle of optimum size, charge, stability to allow protection in the blood stream and efficient release within the tumor. One of the most desired advancement in the therapy in deed is the selectivity, specific delivery of the agent to the tumor to enhance its efficacy at lower doses and reduce its side effects to other organs.

All can be achieved by using nanoparticles. If contrast generating nanoparticles are used, it would be possible to tract the biodistribution of the therapeutic agents and possibly the progress of treatment as well.

In the past few years, quantum dots have emerged as popular nanoparticles with favorable luminescence properties coupled with therapeutic potential via drug and gene delivery. The emission wavelength of quantum dots can be easily tuned from visible to NIR range by changing particle size and composition.

NIR fluorescence is most favorable for biological applications since it provides a higher penetration depth into the tissues than visible light, lower background fluorescence, lower signal loss, thus a greater signal to background ratio [141, 142]. The absorption by biological constituents is minimal between 700-1300 nm and QDs emitting in this region are by far more advantageous for biological applications, especially for *in vivo* imaging [143-146]. Such potential accelerated the development of NIR-emitting quantum dots such as PbSe [147], PbS [13], CdHgTe [148]. However, the intrinsic toxicity of Pb, Cd, or Hg is a significant limitation [149].

Ag₂S QDs are a new class of NIR emitting QDs. They are quite biocompatible and highly luminescent and have colloidal and long term stability. By these excellent properties, these structures have gained a remarkable popularity both for *in vitro* and *in vivo* biomedical applications in recent years.

In bioapplication, stable aqueous suspensions of nanoparticles are needed. However, most of the NIRQDs are synthesized in organic solvents and later transferred into water. This not only cause deterioration of properties but also adds to the cost of nanoparticle production and move away from practicality. Hence, development of high quality Ag₂S

NIRQDs from safe precursors and directly in water is an urge demand in realization of practical NIRQDs.

Based on such developments in the quantum dot technologies and the needs of the cancer diagnosis and therapy, the subject of this thesis work is the development of cationic, small, Ag₂S NIRQDs in a simple and economically viable way with strong emission in the medical window and acceptable level of cytocompatibility as a new theranostic nanoparticle. A detailed physical, chemical and *in vitro* cytotoxicity study of these particles were planned to identify some compositions as promising candidates for combination of optical diagnosis/imaging combined with targeted gene and drug delivery to cancer cells/tissue.

The first immediate goal of the thesis work is the emission tunable synthesis of small, stable, cationic Ag₂S QDs with strong emission in the medical window (700-900 nm). To achieve this, one step aqueous synthesis of cationic Ag₂S from safe and cheap AgNO₃ and TAA or Na₂S in the presence of a mixed coating comprised of the cationic branched PEI and a small molecule was suggested. In such a synthetic method, several variable were studied to achieve the desired properties with small hydrodynamic size and colloidal stability. These include Ag/S, Ag/coating ratio, synthesis temperature, synthesis duration, synthesis pH and pH after synthesis as the basic synthetic parameters. Also, PEI/small molecule ratio and molecular weight of PEI were studied.

In the coating approach, a synergy is targeted: PEI, golden standard for non-viral gene transfection, would provide the cationic nature and colloidal stability. Yet, polymer coatings usually leave defects on the crystal surface which hampers the luminescence properties. This may be overcome by using a small molecule that can bind to surface of Ag₂S densely. Hence, a mixture of branched PEI with various small molecules are suggested to obtain size tunability, stability and strong emission (high quantum yield). 2-Mercaptopropionic acid (2MPA), l-cysteine (Cys), l-arginine, l-histidine and l-glutamic acid were suggested as small molecules.

2MPA was previously proven as a superior coating compared to traditional 3-mercaptopropionic or thioglycolic acid by our group.[50]. It provided long-term stability and high quantum yield with enhanced cytocompatibility [50] [105]. 2MPA coated Ag₂S NIRQDs with the highest QY by that time with no significant cytotoxicity even at high

concentrations and strong endosomal optical signal, eliminating tissue autofluorescence [105]. Cys, an amino acid, is also a frequently used coating material in quantum dot applications due to thiol group which strongly binds to crystal surface and co-existence of amine and carboxylic acid groups allowing surface functionalization. Cys was applied to aqueous CdS [150], CdSe [151], CdSe/CdS [152, 153] and CdTe [154] QDs. In this thesis work other amino acids such as L-arginine, L-histidine and L-glutamic acid which have no thiol groups were also employed during QD synthesis and their potential as a coating material alone or in combination with PEI was evaluated.

The second goal of this thesis work is to evaluate Ag₂S QDs as optical probes for biological applications. Because of that *in vitro* cytotoxicity evaluation, *in vitro* and *in vivo* optical imaging studies of Ag₂S QDs were performed. For *in vitro* imaging studies, a variety of cancerous and healthy cell lines were used. For *in vivo* imaging, cationic Ag₂S NIRQDs were incubated with *C. elegans* and BALB/c mice.

The third goal of this thesis work is to use Ag₂S NIRQDs as transfection agents. PEI 25kDa is the best polymeric gene delivery vehicle, so far [155]. However, at such relatively high molecular weight, it has dose limiting toxicity. Its toxicity decreases with molecular weight but also the transfection efficiency declines. To overcome this problem, use of lower molecular weight PEI (specifically 10 and 1.8 kDa) as well as 25 kDa was suggested in the development of cationic Ag₂S QDs as well. The resulting particles were characterized in detailed in terms of the optical properties, colloidal stability, size and surface charge, cytotoxicity and transfection efficiency. For the evaluation of transfection ability and efficiency, green fluorescent protein (GFP) gene, which is a typical standard proof-of-concept material, *p53-GFP*, which is an apoptotic gene used in cancer gene therapy, and polyinosinic:polycytidylic acid (poly (I:C)) as a synthetic oligonucleotide which induces apoptosis were employed.

The fourth goal of the study is to use Ag₂S QDs as a drug delivery agent. In this thesis work, doxorubicin was chosen as an anticancer drug to be loaded to Ag₂S NIRQDs. In this step, two different approaches were suggested: passive drug delivery/targeting and active drug delivery/targeting. In the passive approach, the nanoparticles are injected into blood circulation and the nanoparticle/drug complex is accumulated in tumorous tissues by enhanced permeability and retention (EPR) effect. In active targeting, a receptor

overexpressed on cancer cells is targeted with a ligand bound to the nanoparticle which can selectively bind to the receptor. Folate receptor (FR) targeting is one of the frequently used targeting strategies. In this thesis work, both folic acid tagged Ag₂S QDs and untagged ones were studied, evaluating both approaches. For efficient drug loading and improved biocompatibility, PEGylation of cationic Ag₂S QDs was performed. PEG increases loading of drugs like doxorubicin into nanoparticles via hydrophobic interactions.



Chapter 2

2. SYNTHESIS AND CHARACTERIZATION OF PEI/2MPA COATED CATIONIC Ag₂S NIR-EMITTING QUANTUM DOTS AND GENE TRANSFECTION

2.1 Introduction

Gene therapy has emerged as a very promising method in the fight against genetic disorders. The major issue in gene therapy is the safe delivery of the gene to target. Potential gene vectors should condense and protect nucleic acids effectively [125]. Non-viral cationic vectors such as liposomes, dendrimers or polymers are preferred materials due to safety and potential for functionalization to tune stability and toxicity, for ability to capture also drugs or conjugation with targeting molecules [126-129]. One of the best performing synthetic materials is known as polyethyleneimine (PEI). PEI can easily penetrate into cells and disrupt endosomal organelles due to the “proton sponge effect” and release its cargo [156-158]. Transfection efficiency of PEI is molecular weight dependent and increases with increasing molecular weight yet, high molecular weight PEI has significant toxicity as well. So, dosing requires a critical balance of these two factors [159].

Semiconductor quantum dots (QD) are the new class of fluorescent probes for cellular, molecular and *in-vivo* imaging applications, due to their stable and size-tunable fluorescence. Narrow emission, broad absorption window, large molar extinction coefficient, and high chemical stability are also major advantages of QDs over organic fluorophores which make them promising optical imaging agents [160-162]. Majority of the examples in the literature involve QDs with luminescence in the visible region.

However, in the visible window photons are scattered and absorbed by biological constituents such as hemoglobin. Near-infrared (NIR) fluorescence is most favorable for biological applications since it provides a higher penetration depth into the tissues than visible light, lower background fluorescence, lower signal loss, thus a greater signal to background ratio [141, 142]. The absorption by biological constituents is minimal between 700-1300 nm and QDs emitting in this region are by far more advantageous for biological applications, especially for *in vivo* imaging [143-146]. Such potential accelerated the development of NIR-emitting quantum dots such as PbSe [147], PbS [13], CdHgTe [148]. However, the intrinsic toxicity of Pb, Cd, or Hg is a significant limitation [149].

Quantum dots (QD) with size tunable emission, long luminescence lifetime and large surface/volume ratio are attractive inorganic nanoparticles for optical imaging *in vitro* and *in vivo*. QD surface can be rendered cationic by appropriate selection of a coating molecule suitable for gene delivery. This approach combines the therapy with imaging, which is a valuable means to track the biodistribution of the oligonucleotide, and even to monitor the treatment success. Organic corona may effectively bind chemotherapy drugs for combination therapy and QDs may be further conjugated with targeting ligands for selective delivery of the nanoparticles to target tissues. QDs with strong emission in the near-infrared (NIR) region are preferred materials due to relatively deeper penetration depth into the tissue than visible light, lower background fluorescence, lower signal loss, thus a greater signal to background ratio [141, 142] [143-146]. Considering the exceptional biocompatibility of heavy-metal free Ag₂S with strong emission in the medical imaging window, development of cationic Ag₂S is a critical step in development of QD-based gene transfection agents with dual action: therapy and imaging [88, 98, 100-102, 117, 163, 164]. Best examples to aqueous Ag₂S NIRQDs for bio-applications are the those formed by Wang et al. in multistep: synthesis of hydrophobic Ag₂S NIRQDs emitting at 1058 nm from (C₂H₅)₂NCS₂Ag [95], ligand exchange with DHLA and finally conjugation with PEG. This Ag₂S NIRQDs emitting at 1200 nm showed enhanced spatial resolution in the *in vivo* imaging of angiogenesis [96] and allowed tracking of mesenchymal stem cells *in vivo* [97]. Others are 3-mercaptopropionic acid coated Ag₂S which was successfully used as an optical probe in the *in vivo* studies using mice [100], Ag₂S NIRQDs synthesized from RNase A via biomimetic route [101], bovine serum

albumin (BSA)-stabilized Ag₂S NIRQDs which was also conjugated with endothelial growth factor (VEGF) antibody for targeted cancer imaging [102].

Hocaoglu and Acar reported one of the first examples of simple aqueous synthesis of highly luminescent and cytocompatible Ag₂S quantum dots which were stabilized with 2-mercaptopropionic acid [165]. These Ag₂S NIRQDs have the highest QY reported in the literature so far with 39 %, upon aging. The effective imaging properties of Ag₂S NIRQDs were demonstrated in mammalian cells for the first time in the literature and enhanced cytocompatibility was shown even at extremely high doses (up to 200 µg/mL). In addition, the synthesis protocol is very simple, highly reproducible and safe. Acar et al. demonstrated that 2MPA produces strongly luminescent QDs due to the interaction of carboxylate groups with crystal surface in addition to strong thiol binding which was shown by ab initio calculations and supported by luminescence life time measurements [166]. Previously, Acar et al. has also shown that when a mixture of a polymeric material and a small thiolated ligand were used as a coating for CdS, both the ability to tune crystal size and the quantum yield of CdS QDs has improved dramatically [167].

One of the most important factors in getting good quality QDs is the surface passivation. Packing density of the coating material on crystal surface and the binding strength are also important. Uncoordinated sides on the crystal surface may act as defects and cause non-radiative coupling events, causing relatively low luminescence intensity. As optical probes, QDs with strong luminescence are highly desirable as they would provide a better signal to noise ratio and may allow usage of lower doses.

Therefore, in an effort of developing theranostic nanoparticles which can be detected optically in the medical window and deliver genes to target sites, Ag₂S NIRQDs with a mixed coating of bPEI (25 kDa) and 2MPA was suggested.

We have designed these cationic NIRQDs based on our experience and the literature with a cytocompatible NIR emitting QD core which is Ag₂S, kept the crystal size small to obtain emission in the NIR-I window to allow fluorescence imaging using a confocal microscope, used the golden standard of synthetic transfection agents which is the 25 kDa branched PEI, but mixed it with a stable and effective 2MPA to enhance luminescence efficiency and balance the toxicity coming from the cationic coating without PEGylation. Also, this strategy allowed us to synthesize these particles directly in aqueous solution which eliminated ligand exchange steps which usually hurts the optical properties of the

particles. The influence of reaction variables such as coating type, PEI/2MPA ratio, pH and reaction time on the optical properties of the QDs was studied systematically. Aq. Ag₂S with the highest reported quantum yield was obtained under optimized conditions of synthesis. These are also the first cationic Ag₂S NIRQDs in the literature. Cytocompatibility of the developed cationic Ag₂S QDs were evaluated using HeLa cell lines. Suitability of particles for imaging was demonstrated in the HeLa and MCF-7 cell lines using confocal laser microscopy and in *C. elegans* as *in vivo* imaging. Potential of these particles as gene vectors were tested in *in vitro* transfection experiments. Transfection efficiency of PEI-2MPA coated Ag₂S NIRQDs was determined in HeLa and MCF-7 cells using green fluorescence protein plasmid (pGFP) and results were compared with a standard transfection agent (25 kDa PEI) in its standard procedure in a standard protocol. This is the first example to gene transfection and optical imaging performed with Ag₂S NIRQD, *in vitro*.

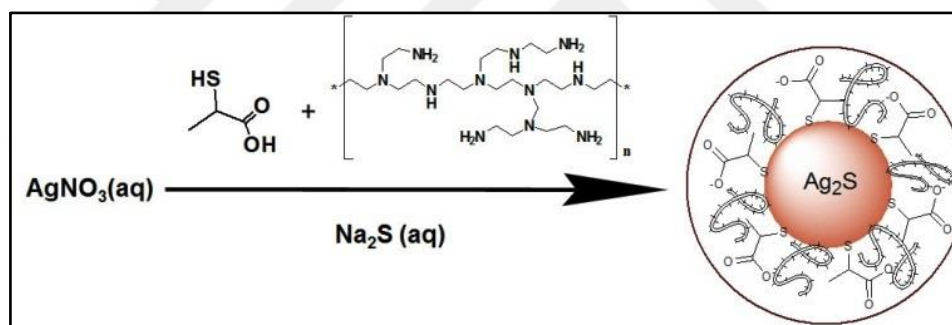
2.2 Materials and Methods

2.2.1 Materials

All reagents were analytical grade or the highest purity. Silver nitrate (AgNO₃) was purchased from Sigma-Aldrich. Sodium sulfide (Na₂S) was purchased from Alfa-Aesar. Branched polyethyleneimine (PEI) (Mw 25 kDa) was purchased from Aldrich (Germany). Linear PEI (25 kDa) was purchased from PolySciences, Inc (USA). Sodium hydroxide (NaOH), 2-mercaptopropionic acid (2MPA), ethanol and acetic acid (CH₃COOH) were purchased from Merck (USA). LDS 798 Near-IR laser dye was purchased from Exciton, Inc (USA). Only Milli-Q water (18.2 M Ohm) was used when necessary. DMEM (Dulbecco's Modified Eagle Medium with 4500 mg/L glucose, 4.0 mM L-glutamine, and 110 mg/L sodium pyruvate), trypsin-EDTA, penicillin-streptomycin and fetal bovine serum (FBS) were purchased from HyClone, USA. Thiazolyl blue tetrazolium bromide (MTT) *Biochemica* was purchased from AppliChem, Germany. Paraformaldehyde solution 4 % in PBS and UltraCruz™ 96 well plates were purchased from Santa Cruz Biotechnology, Inc., USA. Glass bottom dishes were purchased from MadTek, USA. Dimethyl sulfoxide Hybri-Max™ and phosphate buffered saline (pH 7.4) were purchased from Sigma, USA.

2.2.2 Preparation of PEI and 2MPA coated Ag₂S QDs

All reactions were performed under an inert atmosphere. Typically, 42.5 mg of AgNO₃ (0.25 mmol) and 4.9 mg Na₂S (0.0625 mmol) were dissolved in 75 ml and 25 mL of deoxygenated water respectively in separate round bottom flasks. PEI and 2MPA in desired ratios, as listed in Table 2. 2, were added to the AgNO₃ solution, respectively. Total coating/Ag mole ratio kept constant at 5. For 2MPA, moles of thiol groups and for PEI moles of amine groups were considered. As an example, a mixed coating containing 20 % 2MPA, had 1 equivalent of thiol (0.25mmol) and 4 equivalents of amine (1 mmol) with respect to Ag. The pH of the final solution was adjusted using NaOH and CH₃COOH solutions (2.5 M). Na₂S solution was added to this reaction mixture under vigorous mechanical stirring at 5000 rpm and at room temperature (25 °C). During the reaction, samples were taken at different time points to follow the particle growth. Prepared quantum dot solutions were washed with deionized water using Amicon-Ultra centrifugal filters (30000 Da cut off) and stored in the dark at 4 °C (Scheme 2. 1, Figure 2. 1).



Scheme 2. 1 Schematic representation of aqueous synthesis of PEI and 2MPA coated Ag₂S NIRQDs.



Figure 2. 1 Synthesis of PEI and 2MPA coated Ag₂S NIRQDs.

2.2.3 Characterization Methods

Absorbance spectra of the prepared Ag₂S quantum dots were recorded by a Shimadzu 3101 PC UV-Vis-NIR spectrometer in the 300-1100 nm range. Crystal sizes of Ag₂S nanoparticles were calculated from absorption spectra of the particles using absorption edge in the Brus equation (Equation 1):

$$\Delta E = \frac{\hbar^2 \pi^2}{8R^2} \left[\frac{1}{m_e} + \frac{1}{m_h} \right] - 1.8 \frac{e^2}{\epsilon_{\text{Ag}_2\text{S}} 4\pi \epsilon_0 R} \quad (1)$$

Where R is the radius of the nanocrystal, m_e (0.286 m_0) and m_h (1.096) are the respective effective electron and hole masses for inorganic core, and $\epsilon_{\text{Ag}_2\text{S}}$ (5.95) is the dielectric constant and ΔE is the band gap energy difference between the bulk semiconductor and the nanocrystal.

A homemade set up was used in the photoluminescence measurements. Ag₂S NIRQDs were excited with a frequency doubled output of a DPSS laser (532 nm). After the luminescence was filtered by 590 nm long pass filter, it was collected with a 1/8 Newport Cornerstone 130 monochromator having 6001/mm grating and operating in 400-1000 nm range. The wavelength selected signals were detected by a femtowatt sensitive Si detector (Thorlabs PDF10A, 1.4×10^{-15} W/Hz^{1/2}).

For Quantum Yield (QY) calculations, QD samples in water and a NIR dye in methanol were prepared at five different concentrations having absorbance values at the excitation wavelength at and below 0.15. These five concentrations were adjusted in such a way that absorbance values of the dye samples and QD samples are close to each other. LDS 798 NIR dye (quantum yield reported as 14 % in MeOH by the producer) was used as the reference. Photoluminescence of these solutions were recorded at excitation wavelength of 532 nm, and the integrated areas under the curves were plotted against the absorbance (Fig. S1 and S2). QY was calculated from the ratio of the slope of these plots, using the refractive index of the water and MeOH based on equation 2, as reported in the literature [167-169].

$$\Phi_{\text{QD}} = \left(\frac{\text{Grad}_{\text{QD}}}{\text{Grad}_{\text{REF}}} \right) \left(\frac{\eta_{\text{water}}^2}{\eta_{\text{MeOH}}^2} \right) \times 100 \quad (2)$$

The XRD pattern of the quantum dots was recorded between 2θ angles of 10° and 90° using a Bruker D2 Phaser Benchtop XRD system with Cu K- α radiation ($\lambda=1.5406 \text{ \AA}$). About one gram of dried sample was placed in between gelatine film. Air bubbles were removed and the sample was placed on a sample holder. TEM analysis of nanoparticles was performed using a JEOL JEM-ARM200CFEG UHR-Transmission Electron Microscope (JEOL, Japan). The hydrodynamic size and zeta potential of the aqueous nanoparticles were measured with a Malvern Zetasizer Nano-ZS. A Thermo Scientific K-Alpha XPS with Al K-alpha monochromatic radiation (1486.3 eV) was used for XPS analysis of QDs. Dried samples were placed on adhesive aluminum tape. A $400 \mu\text{m}$ x-ray spot size and 50.0 eV pass energy corresponding to a resolution of roughly 0.5 eV were used. The base pressure and experimental pressure were below 3×10^{-9} mbar and about 1×10^{-7} mbar. C1s peak at 285.0 eV was assigned as the reference signal for evaluations.

Ag⁺ concentration of QD solutions was determined by Spectro Genesis FEE Inductively Coupled Plasma Optical Emission Spectrometer (ICP OES). QDs were exposed to acids (suprapur nitric acid 65 % and suprapur sulphuric acid 96 %) for digestion and diluted to certain volumes. Ag⁺ ion concentrations in solutions were calculated using a standard curve of known Ag⁺ ion concentrations.

Amount of the organic content of QDs was determined on a TG/DTA (SII EXSTAR 6300) under argon gas flow from room temperature to 600°C with a heating rate of $10^\circ\text{C}/\text{min}$.

2.2.4 Cell lines, cell culture

MCF-7 human breast carcinoma and HeLa cervical cancer cell lines were cultured in DMEM (Sigma, 05671) supplemented with 10 % (v/v) fetal bovine serum (FBS; Biochrom KG, S0115) and 1 % antibiotics (Penicillin/Streptomycin; Biological Industries, 03-031-1B) in a 5 % CO₂-humidified incubator at 37°C .

2.2.5 Gene Delivery

Ag₂S-PEI-2MPA mediated transfections were conducted by mixing various concentrations of QDs (according to measured concentrations of Ag⁺ ions by ICP OES) (1 $\mu\text{g}/\text{ml}$, 1.5 $\mu\text{g}/\text{ml}$, 2 $\mu\text{g}/\text{ml}$ and 2.5 $\mu\text{g}/\text{ml}$) with 4 μg pMax-GFP vector DNA (Lonza)

in 50 μ l serum-free DMEM. Mixtures were allowed to incubate for 10 min and were added to cells seeded in 12-well plates (MCF-7: 100.000 cells/well, HeLa: 75.000 cells/well). After six hours post-transfection, cells were washed with PBS and fresh medium was added. Control transfections were conducted similarly, using the linear 25 kDa polyethyleneimine (PEI) (1 μ g/ml) as one of the standard transfection agents.

Transfection efficiency was checked 48 h post-transfection. Prior to analysis, cell nuclei were stained with the Hoechst dye (Invitrogen, 33342) to better assess the ratio of GFP positive cells to the total cell population. Hoechst dye was added to the cells at a final concentration of 1 μ g/ml. After 20 minutes incubation, cells were washed with PBS to remove excess amount of dye. Cells were fixed in 3.7 % paraformaldehyde for 20 min, washed with PBS, mounted in 50 % glycerol in PBS and inspected under 20x or 40x magnification using an BX60 fluorescence microscope (Olympus). At least 150 cells per condition were analyzed and results were expressed as a percentage of GFP positive cells versus total number of cells (Hoechst dye positive nuclei). All measurements were repeated in at least 3 independent experiments.

2.2.6 Cytotoxicity assay

To study the cytotoxicity of the prepared QDs on the HeLa cells lines, thiazolyl blue tetrazolium bromide (3-(4,5-dimethyl-thiazol-2-yl)-2,5-diphenyltetrazolium bromide, MTT) was utilized. Cells were cultured in the 96-well plates with complete medium at 37 °C and 5 % CO₂ for 24 h. On the second day, the medium was renewed and QDs were added to the culture medium at different concentrations and incubated for another 24 h. On the third day, cells were washed with PBS. MTT solution was added on the cells and incubated for 4 h. Purple formazan was dissolved with DMSO : Ethanol (1:1) by gentle shaking for 15 min. Absorbance of formazan was measured by reading absorbance at a wavelength of 600 nm with a reference at 630 nm on a microplate reader (BioTek ELx800 Absorbance Microplate Reader). QD absorbance in a complete medium was measured as well and subtracted from the MTT solution to correct the result. Experiments were repeated four times. Statistical analysis was performed with GraphPad Prism Software (Graphpad Software, Inc., USA). Columns were compared as pairs by Tukey's multiple comparison test of one way ANOVA test with Tukey's multiple comparison test or by

using a two tailed student's t-test. All data were represented as mean \pm SD (standard deviation). The confidence level was accepted as 95 % (significant at $p < 0.05$).

2.2.7 *In vitro* cell imaging

Imaging of HeLa and MCF-7 cells was performed using two different confocal laser scanning microscopes in order to visualize NIR emission of QDs and GFP signal. For QD localization analysis, 50,000 HeLa cells were cultured in glass bottom dishes and incubated for 18 h. Following incubation, the culture medium was replenished and cells were incubated with QD solution which has 2.5 $\mu\text{g}/\text{mL}$ of Ag⁺ ion for 6 h. Cells were washed with PBS (pH 7.2) and fixed with 4 % paraformaldehyde for 15 min. Finally, the washing step was repeated and cells were kept in PBS to protect the cells from drying. To detect intracellular uptake and localization of Ag₂S NIRQD, a home-made sample scanning confocal microscope system equipped with Si avalanche photodetector and a 60X (NA : 1.49) oil immersion objective was used. Excitation laser beam at 532 nm was transmitted through neutral density filters and reflected by a broadband dichroic mirror (Chroma 10/90 beamsplitter). A long pass glass filter RG665 was placed before the detectors to collect the QD emission.

Confocal laser microscopy studies performed to visualize the green fluorescence in transfected cells by GFP/Ag₂S NIRQDs. Initially, 150,000 MCF-7 or HeLa cells were cultured in 12-well plates with cover slides. After overnight incubation, transfection with a QD solution (at concentration of 2.5 $\mu\text{g}/\text{mL}$ of Ag⁺) conjugated to pMax-GFP plasmid was performed. Cells were washed with PBS after 6 hours of incubation. At 48 hours after transfection, cells were fixed in 3.7 % paraformaldehyde for 20 min, washed with PBS and mounted in 50 % glycerol in PBS. Cells were imaged using a Nikon Eclipse Te2000-U confocal microscope to detect the GFP signal after transfection.

2.2.8 *In vivo* imaging studies

In vivo imaging studies were performed on *Caenorhabditis elegans* (*C. elegans*) which is a model organism. For microscopy imaging, worms were incubated in PEI/2MPA Ag₂S QD solutions at a concentration of 200 $\mu\text{g}/\text{mL}$ for 2 hours and the nanoparticles were allowed to eat by worms. The images were recorded by an inverted fluorescence microscope using NIR filters.

2.3 Results and Discussions

2.3.1 PEI coated NIR-emitting Ag₂S quantum dots

Direct aqueous synthesis was utilized in the synthesis of cationic NIR-emitting Ag₂S NIRQDs as a greener and a facile synthesis method. Cationic Ag₂S NIRQDs were synthesized directly in water from AgNO₃ and Na₂S under inert atmosphere at room temperature with branched PEI (25 kDa), as a coating. Factors that usually affect the particle size and the quality such as reaction duration, Ag/S and PEI/Ag ratio were studied to investigate the ability to tune size and therefore, the emission wavelength of QDs, and to find out the conditions which would produce the best luminescing particles within the 700-900 nm range. The pH of the reaction solution was around 9-10 due to the presence of PEI. Results indicated that PEI can stabilize QDs in the aq. medium; however, these variables did not allow efficient size tuning and the luminescence of the particles were poor (Figure 2. 1 and Figure 2. 2). In polymer coated particles, due to the lack of dense packing on the particle surface, a significant amount of defects may exist resulting in non-radiative coupling events and hence, low luminescence.

2.3.1.1 Influence of Ag/S mole ratio on particle properties

In the synthesis of PEI coated Ag₂S NIRQDs, Ag/S mole ratio of 2.5 and 4 were studied under identical conditions: coating/Ag ratio of 5, pH 10. Photoluminescence and absorbance graphs of these two particles prepared at room temperature and quenched in 75 min were shown in Figure 2. 2.

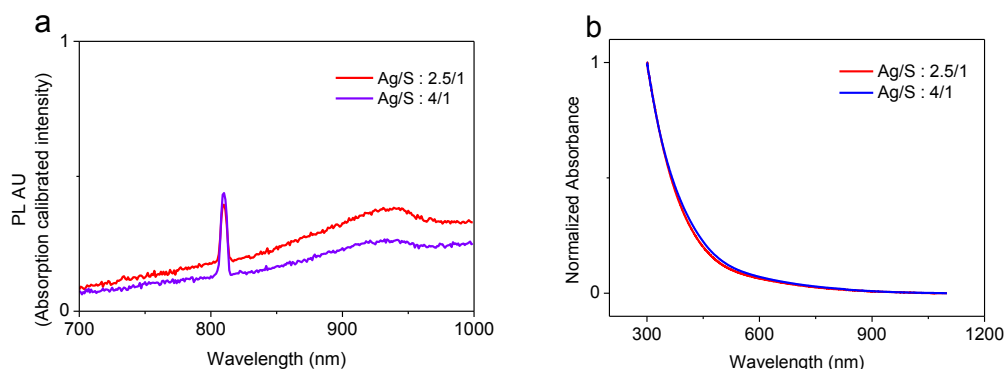


Figure 2. 2 Photoluminescence (a) and absorbance (b) spectra of PEI coated Ag₂S QDs prepared at different Ag/S mole ratios.

2.3.1.2 Influence of Ag/PEI ratio on particle properties

In order to determine the best Ag/PEI ratio which would provide effective surface passivation and strong luminescence as well as to influence the crystal size, different Ag/PEI ratios were studied under identical reaction conditions: Ag/S=4, room temperature, pH 10. Photoluminescence and absorbance graphs of PEI coated Ag₂S NIRQDs synthesized with Ag/PEI ratio of 1/5 and 1/15 are shown in Figure 2. 3. As seen in the figure, there is no significant difference between the ratios in terms of luminescence intensity.

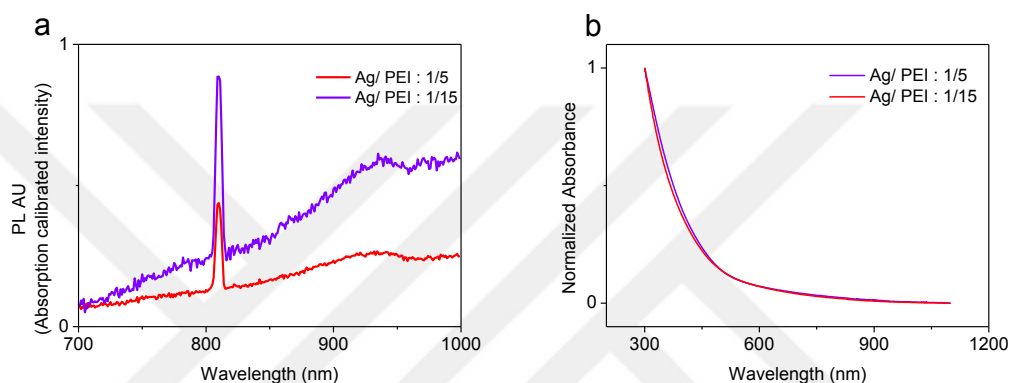


Figure 2. 3 Photoluminescence (a) and absorbance (b) spectra of PEI coated Ag₂S NIRQDs prepared at different Ag/PEI mole ratios.

2.3.2 PEI/2MPA coated NIR-emitting Ag₂S quantum dots

2.3.2.1 Influence of reaction time on particle properties

Usually, reaction time allowed for the crystal growth may act as a factor in tuning particle size. However, initial experiments done with 100 % PEI and 60/40 PEI/2MPA have shown that particle size or luminescence peak maximum of resulting QDs does not change after 5 min (Figure 2. 4) following the addition of Na₂S. Therefore, all comparative reactions were quenched in liq. nitrogen at 5 min after sulfide addition.

Aliquots from reaction mixture were taken out with a syringe at different time points and particle growth and luminescence peak were monitored by UV-absorbance and photoluminescence spectra. Figure 2. 4 and Table 2. 1 summarizes the effects of reaction time on the particle properties for Ag₂S NIRQDs synthesized with 60/40 PEI/2MPA at pH 10 with Ag/S ratio of 4 and coating/Ag ratio of 5 at room temperature.

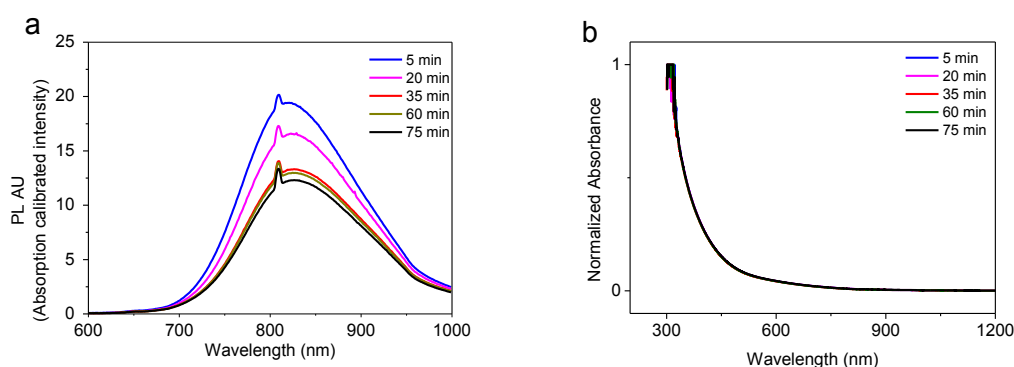


Figure 2. 4 (a) Absorbance calibrated photoluminescence and (b) Normalized absorbance graphs of the Ag₂S NIRQDs prepared with PEI/2MPA 60/40 mixed coating at different time points during the reaction.

Table 2. 1 Effect of the reaction time on the properties of Ag₂S NIRQDs

Reaction time (min)	$\lambda_{\text{abs(cutoff)}}^{\text{a)}$ (nm)	Size ^{b)} (nm)	Band gap (eV)	$\lambda_{\text{em (max)}}$ (nm)	FWHM (nm)
5	777	2.52	1.60	820	147
20	777	2.52	1.60	825	148
35	777	2.52	1.60	828	152
60	777	2.52	1.60	828	150
75	777	2.52	1.60	828	148

^{a)} Absorbance onset; ^{b)} Diameter of Ag₂S crystal calculated by Brus equation. Reaction formulation and conditions: Ag/S = 4, Ag/ PEI = 1: 3, Ag/ 2MPA = 1: 2, reaction pH: 10, R T.

2.3.2.2 Influence of PEI/2MPA ratio on particle properties

In order to improve the luminescence quality of Ag₂S NIRQDs and achieve size tunability, mixed coating formulations composed of PEI and 2MPA were used. Ag₂S NIRQDs with only 2MPA coating was also prepared for comparison of the properties. All particles were synthesized under identical conditions (Table 2. 2).

In the QD synthesis, pH of the reaction mixture was adjusted to 10 before the addition of Na₂S, except in the case of 100 mol % 2MPA which was performed at pH 7.5, since Ag-2MPA complex precipitates at higher pH values. The pH of the PEI solution is usually around 10, but after the addition of 2MPA to the reaction mixture, a significant drop in pH was observed. As an example, pH drops to 7.5 - 7.8 with 20 mol % 2MPA,

and to 3.0-3.5 in the case of 40 mol % 2MPA. pK_a of PEI is in the range of 8.2 to 9.5 [170-172]. Protonation of the amines is problematic since they will be responsible from the binding of PEI to the QD surface. Thus, pH was readjusted to 10 before the addition of the sulfur source to the reaction mixture.

In comparable reactions in which Ag/S ratio and coating/Ag ratio were set at 4 and 5, respectively, only the PEI/2MPA ratio was changed to study the influence of coating composition on particle properties. All reactions with up to 40 mol % 2MPA formed stable colloidal suspension of QDs with a dramatically improved luminescence intensity over the ones with 100 mol % PEI coating (Figure 2. 5). Besides, these QDs also outperformed the luminescence intensity of 100 mol % 2MPA coated Ag₂S NIRQDs which were the best luminescing Ag₂S NIRQDs reported in the literature until now [165]. Amongst the PEI/2MPA coated Ag₂S NIRQDs, the best luminescence intensity was obtained with 20 and 40 mol % 2MPA in the coating mixture (Figure 2. 5). Non-luminescent bulk material was obtained when 60 mol % 2MPA was used. Therefore, higher 2MPA content in the mixture was not attempted. Addition of 2MPA as co-stabilizer also reduced the particle (inorganic crystal) size (Figure 2. 6 and Table 2. 2). Actually, all QDs prepared with the mixed coating formulations are also smaller than 100 mol % 2MPA coated QDs with better luminescence indicating a synergy. This is in agreement with the results obtained from poly(acrylic acid)/mercaptoacetic acid coated CdS QDs [167, 173]. In case of polymeric coatings, the lack of dense surface passivation causes poor control in crystal growth and poor surface quality resulting in large crystals with surface defects possibly responsible from nonradiative couplings reducing the quantum yield and the luminescence intensity. Addition of a small thiolated ligand which binds strongly and densely to the surface left uncapped by the polymeric coating both limits crystal growth more effectively and reduce surface defects. As a result, mixed coatings produce smaller particles with better luminescence intensity. Increasing 2MPA amount decreased the crystal size slightly, causing a slight blue shift in the emission peak (Figure 2. 5, Figure 2. 6 and Table 2. 2). Overall, all Ag₂S NIRQDs with mixed coating emit between 817-838 nm, which is within the so called diagnostic window, with a full-width-at half maximum (FWHM) around 170 nm and better luminescence than 2MPA or PEI coated particles.

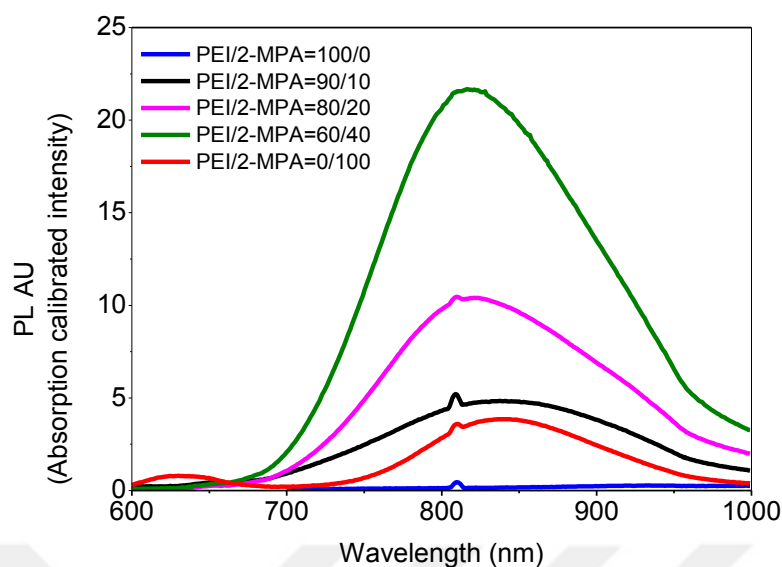


Figure 2. 5 Photoluminescence spectra of Ag₂S NIRQDs prepared with different PEI/ 2MPA ratios (Ag: S = 4, room temperature, reaction pH: 10, 5 min reaction).

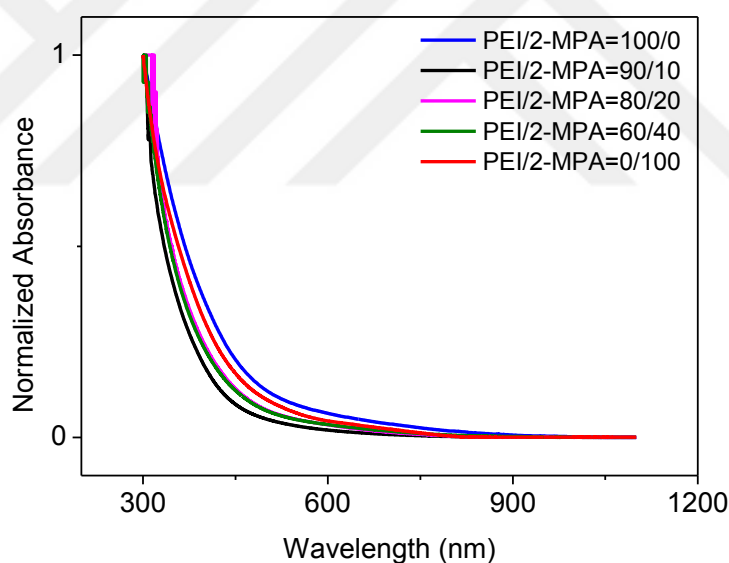


Figure 2. 6 Absorbance spectra of Ag₂S NIRQDs prepared with different PEI/ 2MPA ratios (Ag: S = 4, RT, reaction pH: 10, 5 min reaction).

Figure 2. 6 is the normalized absorbance spectra of the quantum dots prepared with mixed PEI/2MPA coating under identical conditions.

Table 2. 2 Effect of PEI/2MPA ratios on the properties of Ag₂S NIRQDs.

Rxn Code	PEI (%) ^{a)}	2MPA (%) ^{a)}	Rxn pH	λ_{abs} ^{b)} (nm)	Size ^{c)} (nm)	Band gap (eV)	$\lambda_{\text{em (max)}}$ (nm)	FWHM (nm)	Dh ^{d)} (nm)	Zeta pot. (mV)
1	100	0	10	906	2.94	1.37	-	-	4.0	51
2	90	10	10	674	2.23	1.48	838	175	2.9	34
3	80	20	10	761	2.48	1.63	819	173	3.5	28
4	60	40	10	777	2.52	1.60	817	168	3.8	36
5	0	100	7.5	806	2.61	1.54	837	128	7.10	-62

^{a)}Mol %; ^{b)} Absorbance onset measured from absorbance spectrum (Figure 2. 6); ^{c)}Diameter of Ag₂S crystal calculated by Brus equation; ^{d)} Hydrodynamic diameter measured by DLS at pH 7.4 and reported as the number average. All reactions were quenched in 5 min.

Ag₂S-PEI/2MPA QDs were designed as potential theranostic nanoparticles with cationic surfaces. Zeta potential of the Ag₂S-PEI is 51 mV and it drops down to - 62 mV in case of Ag₂S-2MPA (Table 2. 2). Although 2MPA decreases the cationic coating content, QDs with mixed coatings are still cationic enough (ca 30 mV) for possible use as oligonucleotide condensing vectors.

2.3.2.3 Influence of the pH on particle properties

Protonation of PEI with the addition of 2MPA is an important issue. AgNO₃ and coating mixture formulated at PEI/2MPA ratios of 60/40 and 80/20 were prepared at different pH values between 5.5-11. Figure 2. 7 shows the photoluminescence spectra of Ag₂S NIRQDs prepared with (a) 60/40 PEI/2MPA (Rxn 4) and (b) 80/20 PEI/2MPA (Rxn 3) coating formulation and Figure 2. 8 shows the normalized absorbance of these synthesized Ag₂S NIRQDs. Between the pH values of 5.5 and 11 (before the addition of sulfur source) no significant change in the particle size or the position of emission maximum was observed for Ag₂S-PEI/2MPA NIRQDs with 20 and 40 mol % 2MPA in the coating composition (Figure 2. 7 and Figure 2. 8).

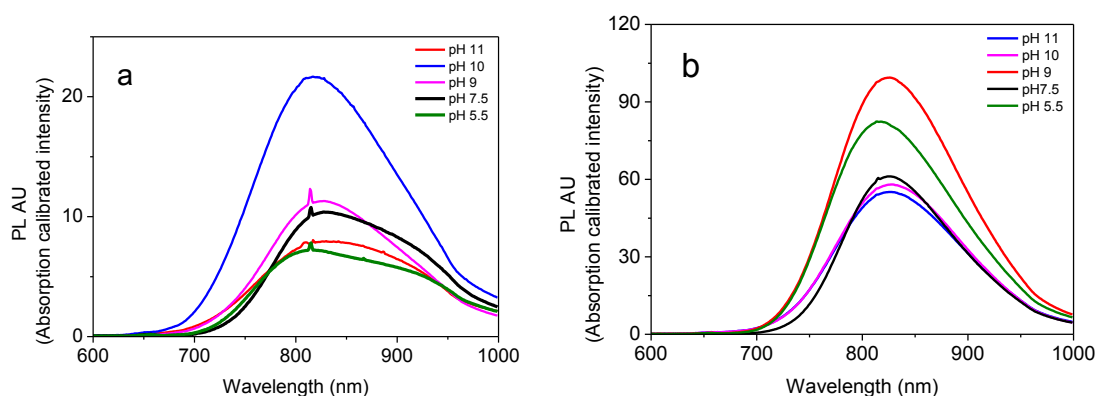


Figure 2. 7 Photoluminescence spectra of Ag₂S NIRQDs prepared with (a) 60/40 PEI/2MPA (Rxn 4) and (b) 80/20 PEI/2MPA (Rxn 3) coating formulation. Spectra were taken particles are washed and solution pH was adjusted to 7.4 to prevent difference in intensity based on pH.

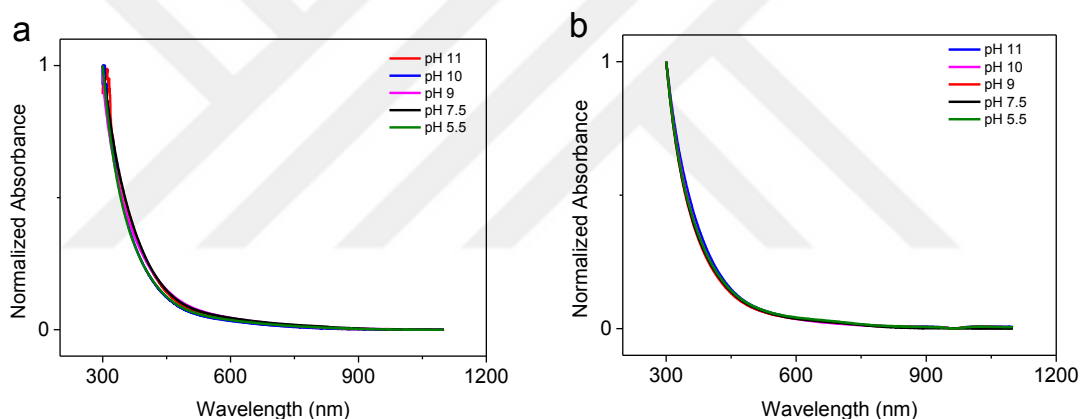


Figure 2. 8 Normalized absorbance graphs of the PEI/2MPA coated Ag₂S NIRQDs synthesized in different pHs during reaction: (a) 60 % PEI / 40 % 2MPA ; (b) 80 % PEI / 20 % 2MPA.

After all, pH had a strong influence on the luminescence intensity. The best luminescence was obtained at pH 10 with 60/40 PEI/2MPA composition and pH 9 for 80/20 PEI/2MPA. In addition, emission peaks with 60/40 PEI/2MPA of Ag₂S NIRQDs has two emission maximum and have poor colloidal stability at pH values below 9. However, Ag₂S NIRQDs with 80/20 PEI/2MPA are stable and have strong emission at all pH values. With a motivation to understand the behavior of these QDs in different pH media such as physiologic media like blood (~pH 7.4) or in endosome (~pH 5.5), luminescence of Ag₂S NIRQDs with 80/20 PEI/2MPA was evaluated at pH 5.5, 7.4 and

9, after being synthesized at pH 9 and washed. As seen in Figure 2. 9, Figure 2. 10 and Table 2. 3, luminescence peak position or absorption onset did not change much with the changes in pH within this range, which indicates that the PEI/2MPA coating provided a strong protection to the Ag₂S core.

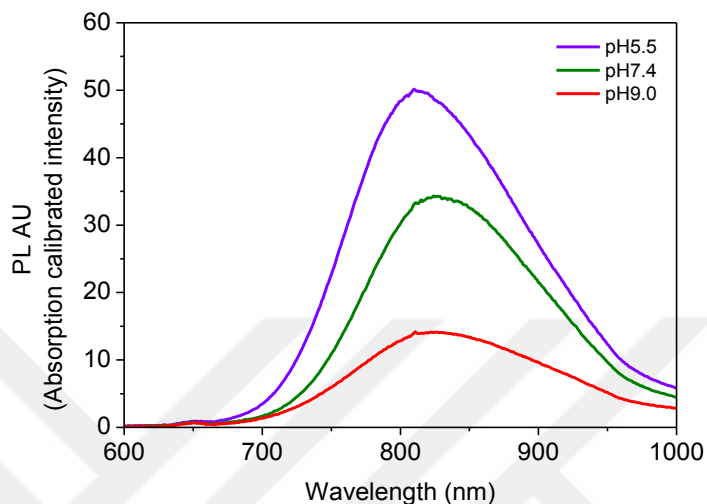


Figure 2. 9 Photoluminescence spectra of aqueous Ag₂S NIRQDs at different pH values. NIRQDs were prepared with 80/20 PEI/2MPA coating formulation, washed and pH was adjusted (Ag: S = 4, Ag: PEI = 1: 4, Ag: 2MPA = 1: 1, T = RT, reaction pH = 9, reaction time = 5 min).

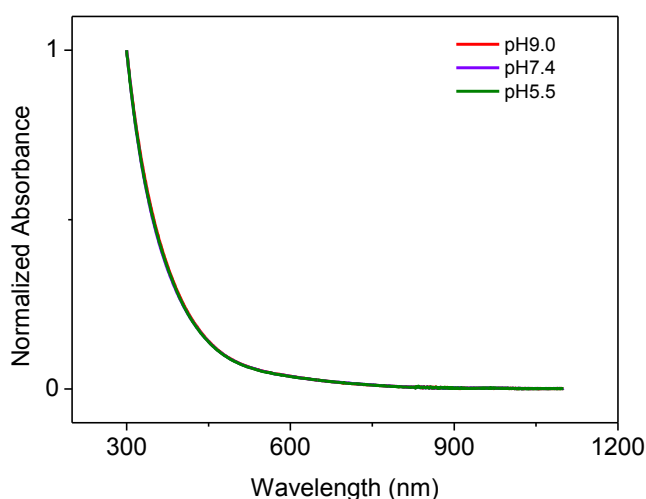


Figure 2. 10 Normalized absorbance graphs of Ag₂S NIRQDs (80/20 PEI/2MPA) at different pH values.

Table 2. 3 Influence of pH on the properties of Ag₂S-PEI/2MPA QDs.

pH	$\lambda_{\text{abs(cutoff)}}^{\text{a)}$ (nm)	Size ^{b)} (nm)	Band gap (eV)	$\lambda_{\text{em (max)}}$ (nm)	FWHM (nm)	Dh ^{c)} (nm)	Zeta pot. (mV)	QY (%)
5.5	783	2.54	1.59	812	151	9.4	63	166
7.4	783	2.54	1.59	828	150	8.9	60	150
9.0	783	2.54	1.59	825	170	8.0	32	77

^{a)}Absorbance onset; ^{b)}Crystal diameter calculated by Brus equation; ^{c)}Hydrodynamic diameter measured by DLS and reported as the number average; ^{d)}Quantum yield calculated with respect to LDS 798 near-IR dye (Ag: S = 4, Ag: PEI = 1: 4, Ag: 2MPA = 1: 1, Temp = RT, reaction pH = 9, reaction time = 5 min).

As expected, zeta potential increased substantially with decreasing pH upon protonation of the PEI. This caused a dramatic increase in the quantum yield. There may be two factors responsible such behavior: 1) a possible disaggregation of particles upon charge repulsion; 2) elimination of free electrons which may act as a hole trap. A major jump in the QY and zeta potential was observed when pH was dropped from 9 to 7.4 where secondary amines were protonated, as well. QY was doubled reaching to a value of 150 % with respect to LDS 798 near-IR dye (quantum yield reported as 14 % by the producer). Further acidification to pH 5.5 caused an additional 10 % increase in the QY (166 %). These QYs are the highest among Ag₂S NIRQDs reported in the literature to the best of our knowledge.

Quantum yield calculation: For Quantum Yield (QY) calculations, QD samples in water and a NIR dye in methanol were prepared at five different concentrations having absorbance values at the excitation wavelength at and below 0.15. These five concentrations were adjusted in such a way that absorbance values of the dye samples and QD samples are close to each other. LDS 798 NIR dye (quantum yield reported as 14 % in MeOH by the producer) was used as the reference. Photoluminescence of these solutions were recorded at excitation wavelength of 532 nm, and the integrated areas under the curves were plotted against the absorbance (Figure 2. 11 and Figure 2. 12). QY was calculated from the ratio of the slope of these plots, using the refractive index of the water and MeOH based on equation 2, as reported in the literature [167-169].

$$\Phi_{\text{QD}} = \left(\frac{\text{Grad}_{\text{QD}}}{\text{Grad}_{\text{REF}}} \right) \left(\frac{\eta_{\text{water}}^2}{\eta_{\text{MeOH}}^2} \right) \times 100 \quad (2)$$

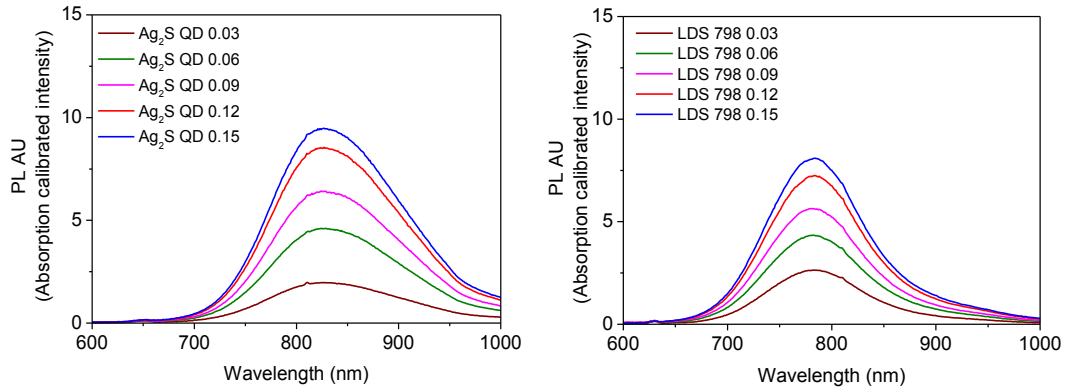


Figure 2. 11 Photoluminescence spectra of aqueous Ag₂S NIRQDs (80/20 PEI/2MPA at pH7.4) in water (left) and LDS 798 NIR dye in MeOH (right) at different concentrations.

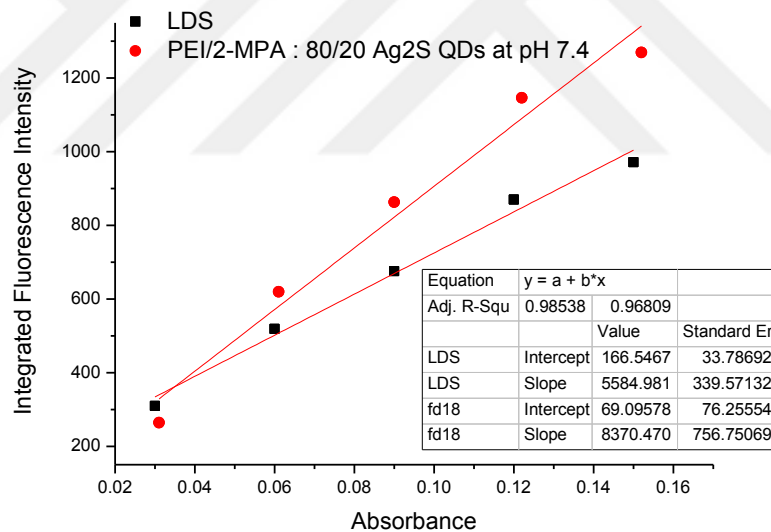


Figure 2. 12 Plot of the the integrated luminescence intensities of the dye and QD samples against the absorbance. Inset shows the slope of each line corresponding to QD and dye samples.

2.3.2.4 Influence of the reaction temperature

One of the most important parameters affecting crystal growth is temperature. To observe the temperature effect, the reaction was performed at 50 °C using the 60/40

PEI/2MPA coating formulation (pH=10). However, temperature is further accelerated the 5-min reaction non-luminescent bulk material was obtained.

2.3.2.5 Long term stability of Ag₂S-PEI/2MPA QDs

Long term colloidal and luminescence stability of QDs are crucial for practical applications. To observe the effect of aging on particle properties, Ag₂S NIRQDs synthesized with 80/20 PEI/2MPA coating formulation at pH 9.0 was used. Sample pH was adjusted to 7.4 before measurements. Even after 1 year, particles showed colloidal stability was noticed and they were analyzed at extended time periods to detect any change in the stability and QY (Table 2. 4). During these time periods, while the inorganic core size of Ag₂S NIRQDs which was measured with the Brus equation stays the same, the QY decreased to 38 % in 1-year (Figure 2. 13). However, this value is still as high as the highest recorded QY reported so far for Ag₂S NIRQD [165]. All particles are stable and had no precipitation even after 1 year.

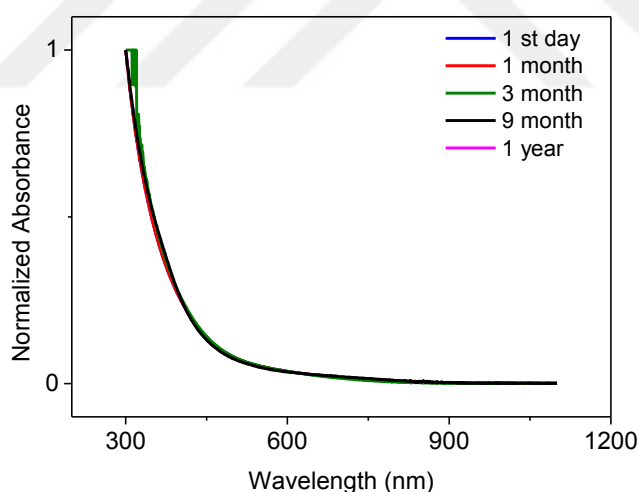


Figure 2. 13 Normalized absorbance spectra of Ag₂S NIRQDs with 80/20 PEI/2MPA at different time points following its synthesis.

Table 2. 4 Time dependent changes in particle properties.*

Time	$\lambda_{\text{abs(cutoff)}}^{\text{a)}$ (nm)	Size ^{b)} (nm)	$\lambda_{\text{em(max)}}^{\text{c)}$ (nm)	FWHM (nm)	QY (%) ^{c)}
1 st day	783	2.54	828	150	150
1 st month	783	2.54	828	150	111
3 rd month	783	2.54	828	150	93
9 th month	783	2.54	828	150	42
1 year	783	2.54	828	150	38

*Ag₂S NIRQDs synthesized with 80/20 PEI/2MPA coating formulation at pH 9.0 was used. Sample pH was adjusted to 7.4 before measurements. ^{a)} Absorbance onset; ^{b)} Crystal diameter calculated by Brus equation; ^{c)} Quantum yield calculated with respect to LDS 798 near-IR dye.

2.3.3 Particle characterization

PEI/2MPA coated Ag₂S NIRQDs are crystalline materials having the size distribution between 2-4 nm depicted from the TEM images (Figure 2. 14a and Figure 2. 14b). Broad size distribution is also possibly responsible from broad FWHM of the emission peaks. Crystal structures of the nanoparticles were observed well in the focused images (Figure 2. 14c and Figure 2. 14d). The interplanar distance measured from the focused images is 0.221 nm and it fits well to the reported values for the 031 plane of monoclinic Ag₂S [174, 175].

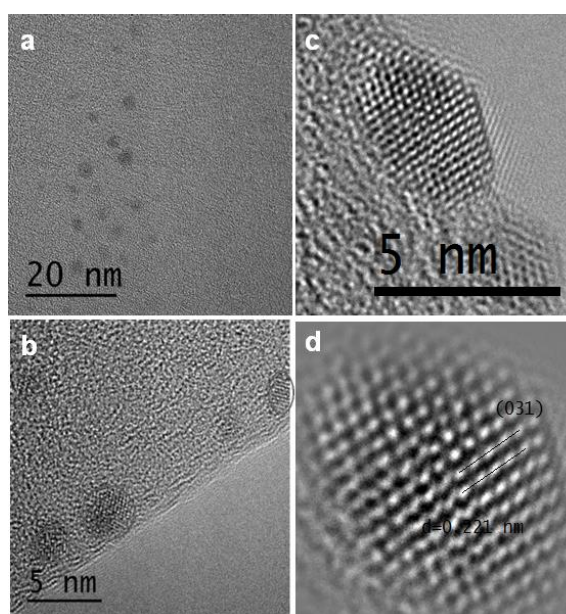


Figure 2. 14 TEM images of Ag₂S NIRQDs (80/20 PEI/2MPA; synthesized at pH 9.0) at different magnifications (a and b); Diffraction of Ag₂S crystal lattice (c); d-spacing determined by a focused image (d).

Organic content amount of the best emitting 80 % PEI / 20 % 2MPA Ag₂S QDs (Ag/S/coating ratio is 4/1/20, synt. at RT and pH 9.0) was determined by TG/DTA studies. According to the results, 49.3 % organic content was measured in the sample. This is the total amount of bPEI -25 kDa and 2MPA (Figure 2. 15).

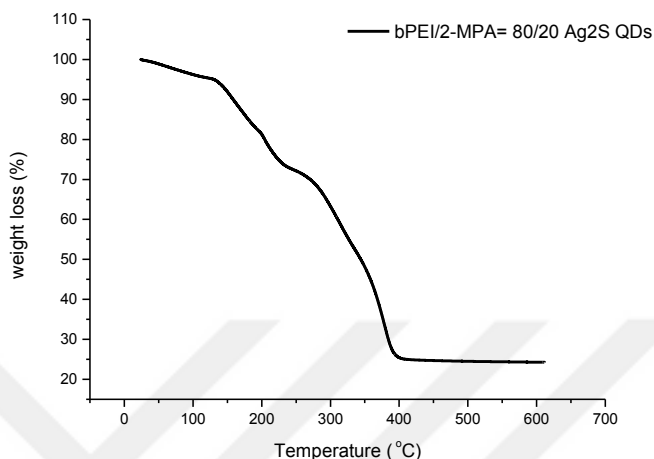


Figure 2. 15 TG/DTA graph of the PEI/2MPA coated Ag₂S QDs.

XRD analysis did not provide well resolved peaks due to the presence of polymer (Figure 2. 16). However, XPS analysis indicates formation of Ag₂S (Figure 2. 17). Ag 3d core level peaks at the binding energies (BE) of 367.41 (3d_{5/2}) and 373.45 (3d_{3/2}) eV fits well to the Ag⁺ of Ag₂S. There are two different S based on the doublets fitted to S 2p signal: S 2p_{3/2} at BE of 160.82 eV and 162.05 eV fits to the S-Ag and S of 2MPA, respectively [165] N 1s region can be fitted to three peaks at 398.25, 398.75 and 400.56 eV corresponding to tertiary, secondary and primary N of PEI. Based on the literature values reported for primary amine of free PEI (399.84 eV), this shift to higher BE indicates surface binding of primary N and electron donation to QD [176].

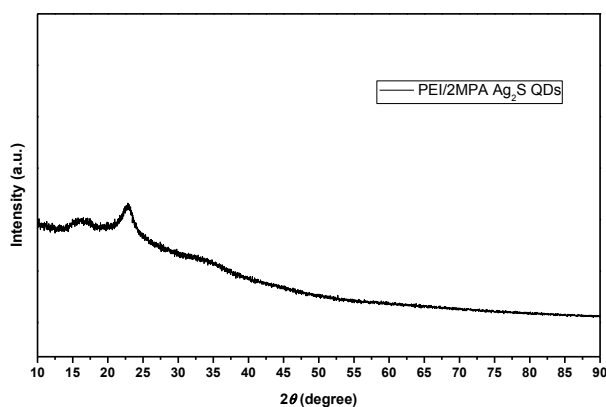


Figure 2. 16 XRD pattern of the Ag₂S NIRQD (80/20 PEI/2MPA; synthesized at pH 9.0).

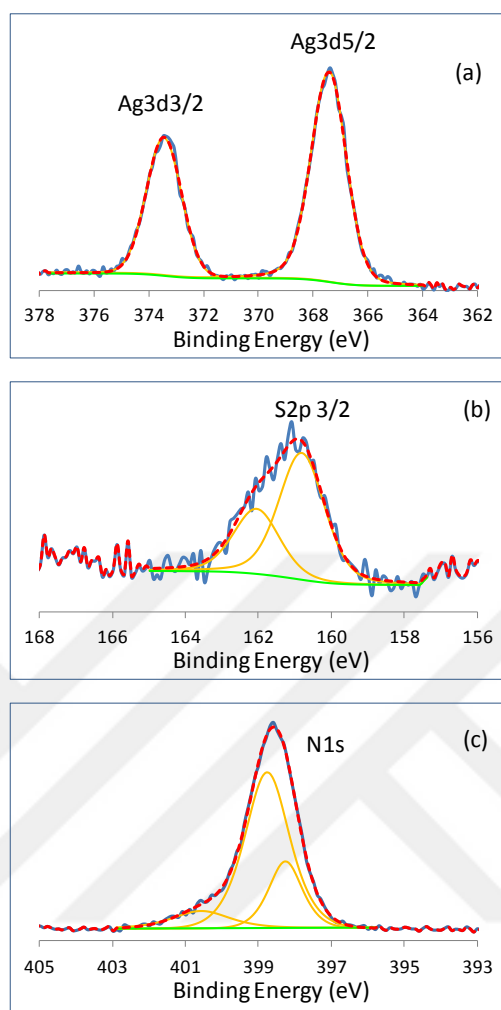


Figure 2. 17 (a) Ag 3d, (b) S 2p and (c) N 1s XPS spectra of Ag₂S-PEI/2MPA (80/20) QDs.

2.3.4 Cytocompatibility of quantum dots

The most stable and most strongly luminescing Ag₂S NIRQD (80/20 PEI/2MPA) was subjected to *in vitro* cytotoxicity studies. For comparison, Ag₂S-PEI and Ag₂S-2MPA NIRQDs were also subjected to same tests. Viability of HeLa cells after 24 h incubation with QDs at 1-25 $\mu\text{g Ag}^+/\text{mL}$ concentrations, which correspond to 4.6-115 $\mu\text{g QD}/\text{mL}$, were determined with widely used MTT assay (Figure 2. 18). As seen in Figure 2. 18, 100 % 2MPA coated Ag₂S NIRQDs are not toxic within this dose range as expected based on previously published data [165] On the other hand, PEI (branched, 25 kDa) is known to be toxic.

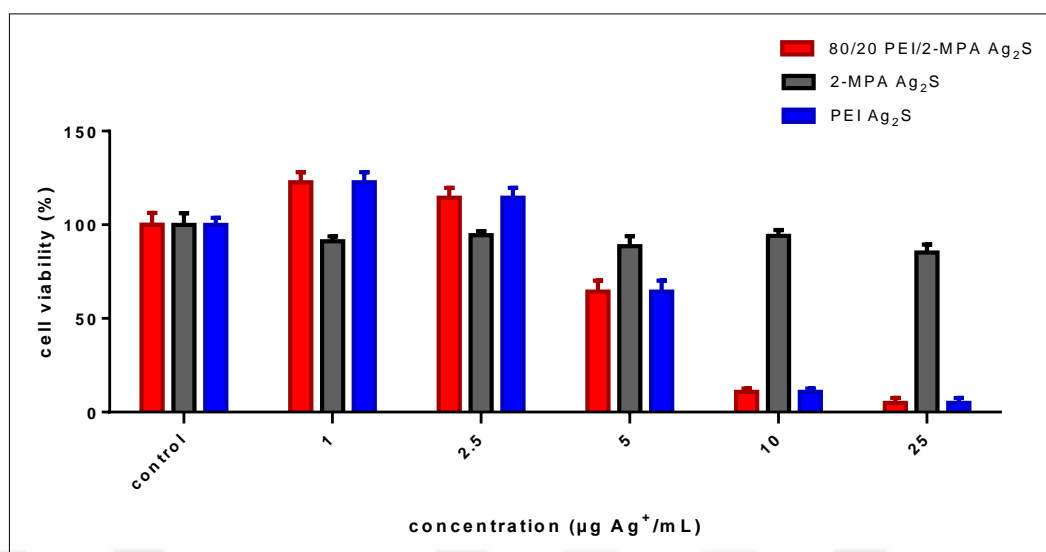


Figure 2. 18 Percent viability of HeLa cells exposed to Ag₂S NIRQD with PEI, 2MPA and 80/20 PEI/2MPA mixed coatings determined by MTT assay. Concentrations are based on Ag⁺ ion concentration in QD solutions as determined by ICP-OES. This concentration range corresponds to 4.6-115 µg QD/mL.

To understand its possible contribution to NIRQD toxicity, amount of PEI coming from the formulation, was applied to the HeLa cells as well. As an example, in 4.6 µg nanoparticle/mL, there is 1 µg/mL Ag⁺ (measured by ICP-OES) and 2.8 µg/mL PEI. So, for 4.6-115 µg QD/mL dose range, 2.8-70 µg/mL PEI dose range was tested (Figure 2. 19). Drop in the cell viability at all doses with respect to control is statistically significant ($p < 0.05$), but the differences between each concentration of PEI are insignificant. Overall, PEI was highly toxic even at the lowest dose of 2.8 µg/mL (less than 50 % viability). However, binding PEI to Ag₂S surface improved cytocompatibility dramatically with respect to free PEI. Ag₂S NIRQDs with 100 mol % PEI or 80/20 PEI/2MPA coating showed no statistically significant drop in the cell viability up to 2.5 µg Ag⁺/mL, but at 5 µg Ag⁺/mL viability dropped to 64 ± 12 %. Using mixed coating at given Ag⁺ concentration meant a lower amount of PEI for the given dose, but the improvement over the pure PEI is much more dramatic than what this 20 % less PEI may cause. One possible reason may be the occupation of some amine groups with crystal surface binding. Considering the high cytocompatibility of 2MPA coated Ag₂S, it is safe to say that toxicity originates from the PEI component. Looking at the similarities of PEI

and PEI/2MPA coated particles in cell viability (Figure 2. 18), it may be reasonable to say that 2MPA did not impact viability much. 2MPA is the smaller size component of the coating mixture with a tight binding to crystal surface which is embedded in the relatively thicker PEI coating. Therefore, 2MPA did not interact with the cell, but PEI did. Therefore, at all doses, pure PEI or PEI/2MPA mixed coating resulted in similar viability levels.

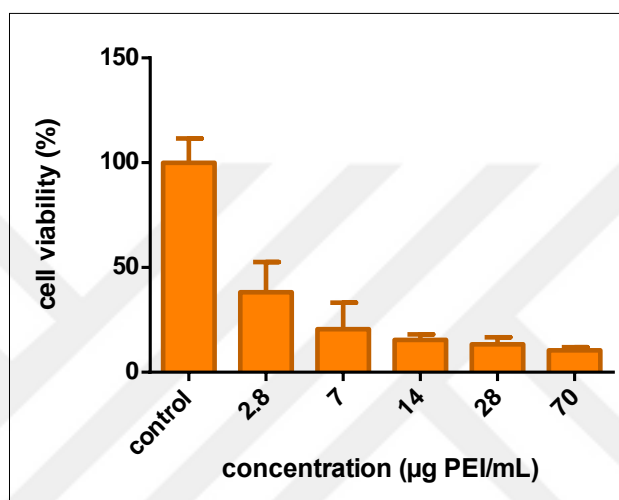


Figure 2. 19 Percent viability of HeLa cells exposed to PEI as determined by MTT assay. These five PEI concentrations correspond to maximum possible amount in Ag₂S NIRQDs synthesized with 80/20 PEI/2MPA coating and tested (Figure 2. 18). As an example, in 1.6 mg nanoparticle/mL there is 1 µg/mL Ag⁺ and 2.8 µg/mL PEI.

2.3.5 *In vitro* cell internalization and optical imaging

Strong emission in the NIR, cytocompatibility at low doses and effective gene delivery would make these particles excellent theranostic tools. For diagnostic purposes, strong intracellular signals originating from QDs is very important. Confocal images of the HeLa and MCF-7 cells incubated with Ag₂S NIRQDs with 80/20 PEI/2MPA indicates an efficient cell internalization and endosomal localization of QDs with strong luminescence (Figure 2. 20), proving potential as an optical probe. This optical signal originating from NIRQDs was dramatically stronger than the weak autofluorescence seen at this excitation wavelength (532 nm) (Figure 2. 21).

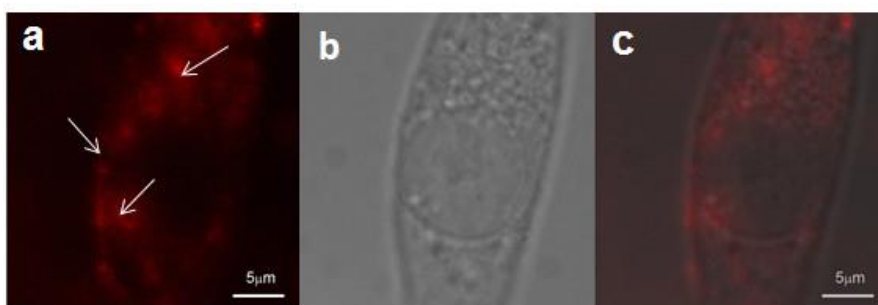


Figure 2. 20 Cellular uptake and localization of PEI/2MPA coated Ag₂S NIRQDs by HeLa cells. Near IR (a), transmission (b) merged image (c) of an individual cell. Red color shows the quantum dots. Arrows show some of the QDs in the cell.

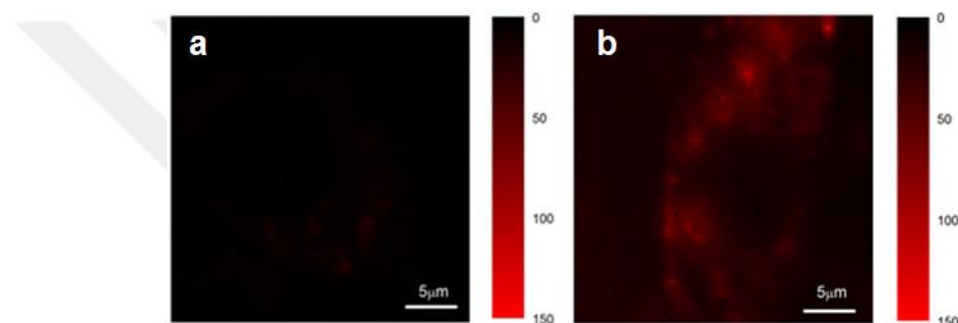


Figure 2. 21 Confocal images of HeLa cells. Cells untreated with QDs (a), cells with QDs (b). Red color shows the quantum dots. The scale means the intensity of QD emission.

2.3.6 *In vivo* imaging

In order to evaluate PEI/2MPA Ag₂S QDs as an optical probe, a model organism, *Caenorhabditis elegans* (*C. elegans*), was also studied. *C. elegans* has 35 % homology with human genes, are quite transparent and resistant to extreme conditions [177]. Therefore, they are very good model organisms for biological studies to be studied as well as for *in vivo* imaging. For this purpose, worms were incubated with PEI/2MPA Ag₂S QD solutions at a concentration of 200 μg/mL for 2 hours and the nanoparticles were allowed to be eaten by worms like food. The images were taken by an inverted fluorescence microscope using NIR filters. As shown in Figure 2. 23, the nanoparticles were efficiently internalized by *C. elegans* and concentrated especially in pharynx and anus parts of the worms according to the body plan of *C. elegans* seen in Figure 2. 22, as evident from the strong luminescence of Ag₂S QDs. Detection of no luminescence from the control group both confirms suppression of autofluorescence and indicates that the

source of this optical signal is Ag₂S QDs. These imply that these NIRQDs are promising optical imaging agent for biological applications. The closer images in Figure 2. 24 illustrate more detailed analyses of QD–worm interaction. Generally, drugs enter *C. elegans* through three distinct ways: uptake by exposed sensory neuronal endings, diffusioin through the skin and ingestion [178-180]. The strong luminescence in pharynx, intestine and anus parts of the worms demonstrates that the uptake of QDs were through ingestion.

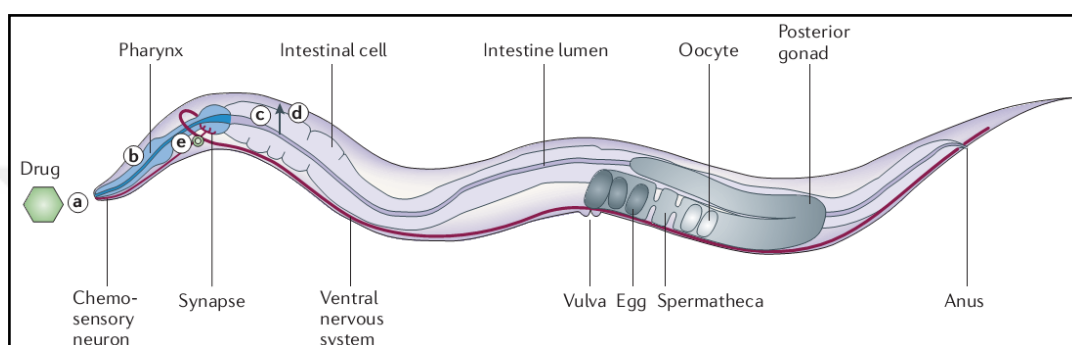


Figure 2. 22 Simplified body plan of a *C. elegans* adult hermaphrodite.

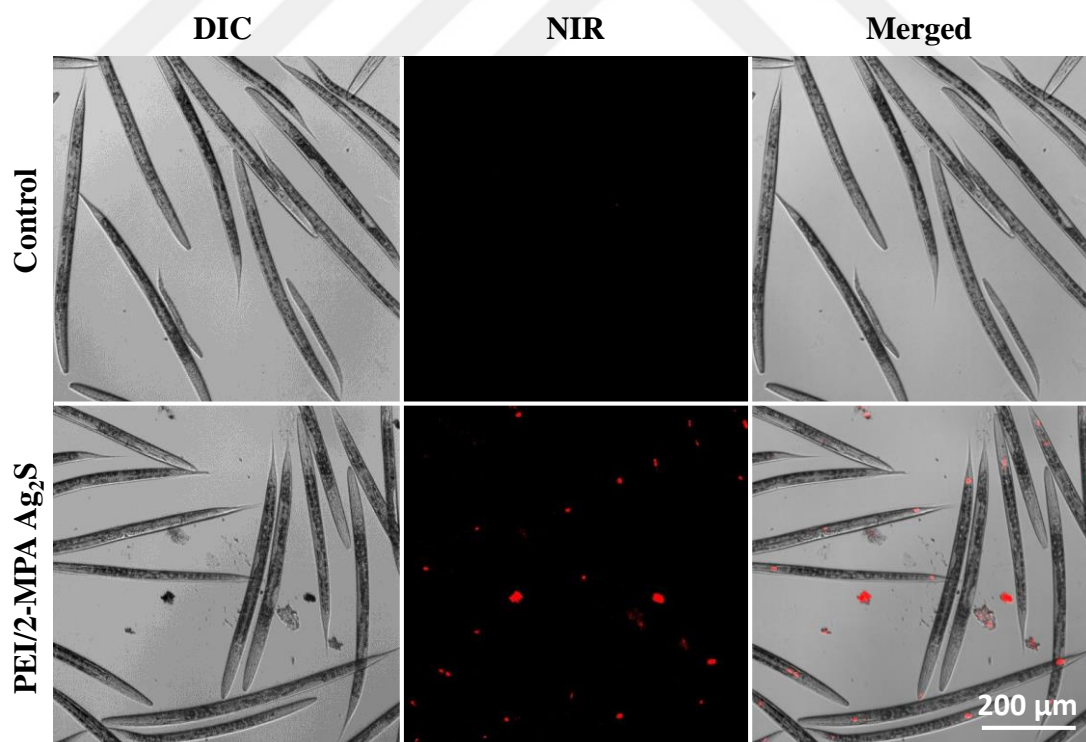


Figure 2. 23 Inverted fluorescence microscopy images of *C. elegans* incubated with 200 µg/mL of PEI/2MPA Ag₂S QDs (80/20 PEI-25kDa/2MPA). Top line shows control group without QDs and bottom line shows DIC, NIR and merged images of Ag₂S QDs

introduced worms. Images were taken with a 10x objective. Excitation at 550 nm and NIR filter was used in the emission.

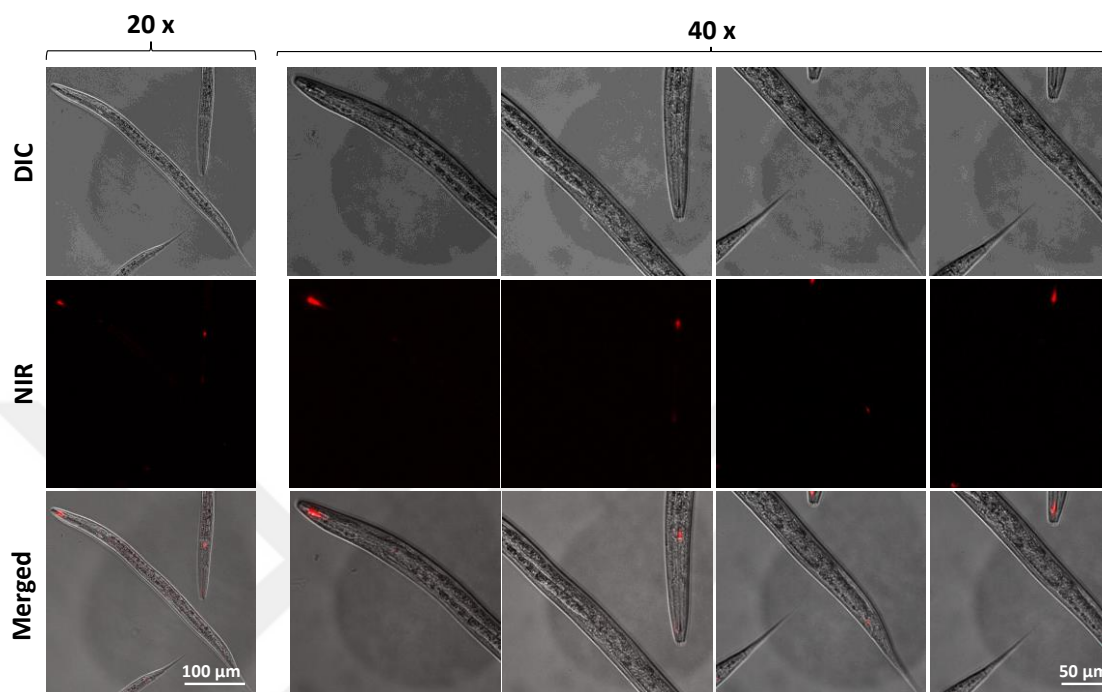


Figure 2. 24 Microscope images of *C. elegans* incubated with PEI/2MPA Ag₂S QDs (80/20 PEI/2MPA) at a concentration of 200 $\mu\text{g/mL}$. The images were taken using 20x and 40x objectives.

2.3.7 Use of Ag₂S-PEI/2MPA NIRQDs as *in vitro* transfection agents

To evaluate the potential of Ag₂S NIRQDs coated with PEI/2MPA mixture as gene delivery agents, a series of *in vitro* green fluorescence protein (pMax-GFP) transfection experiments were performed with MCF-7 and HeLa cells. Commercial cell culture grade PEI (linear, 25 kDa) was used as a control. QDs were studied in a concentration range where no significant toxicity was detected ($[\text{Ag}^+] = 1\text{-}2.5 \mu\text{g/mL}$, $[\text{QD}] = 1\text{-}2.5 \mu\text{g/mL}$) (Figure 2. 18). As shown in Figure 2. 25 and Figure 2. 26, GFP transfection efficiency and expression levels were similar or higher than the commercial PEI (used at a standard, non-toxic dose) when the GFP vector was delivered using the Ag₂S NIRQD above 1.5 $\mu\text{g/ml Ag}^+$ (6.9 $\mu\text{g/ml QD}$) concentration both in MCF-7 cells and HeLa cells (Figure 2. 26), respectively.

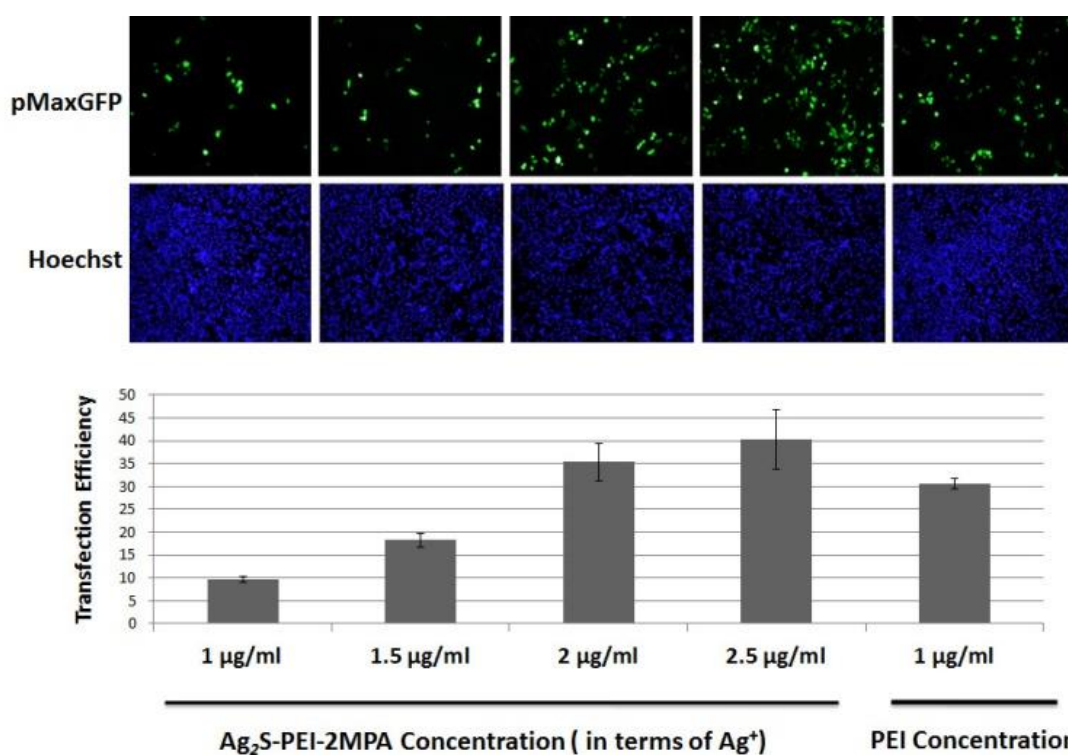


Figure 2. 25 Transfection of MCF-7 cells: (Top) Cells were transfected with pMax-GFP plasmid using Ag₂S-PEI/2MPA NIRQD or control PEI (1 µg/ml). Transfection efficiency was assessed under a fluorescent microscope. Hoechst staining was used to show the nuclei of all cells in the field. (Bottom) Quantitative analysis of GFP positive cells in (Top) (mean ± SD of independent experiments, $n = 3$).

Highest transfection efficiencies achieved with Ag₂S NIRQD were as 41 % for HeLa and 40 % for MCF-7 cells. Under similar conditions, transfection efficiency of commercial PEI was around 30 % for both cell lines. Considering that the actual PEI content of the QD may be lower than anticipated, and free PEI at the corresponding doses would be too toxic to be used, this improvement over free PEI may be more significant than it seems.

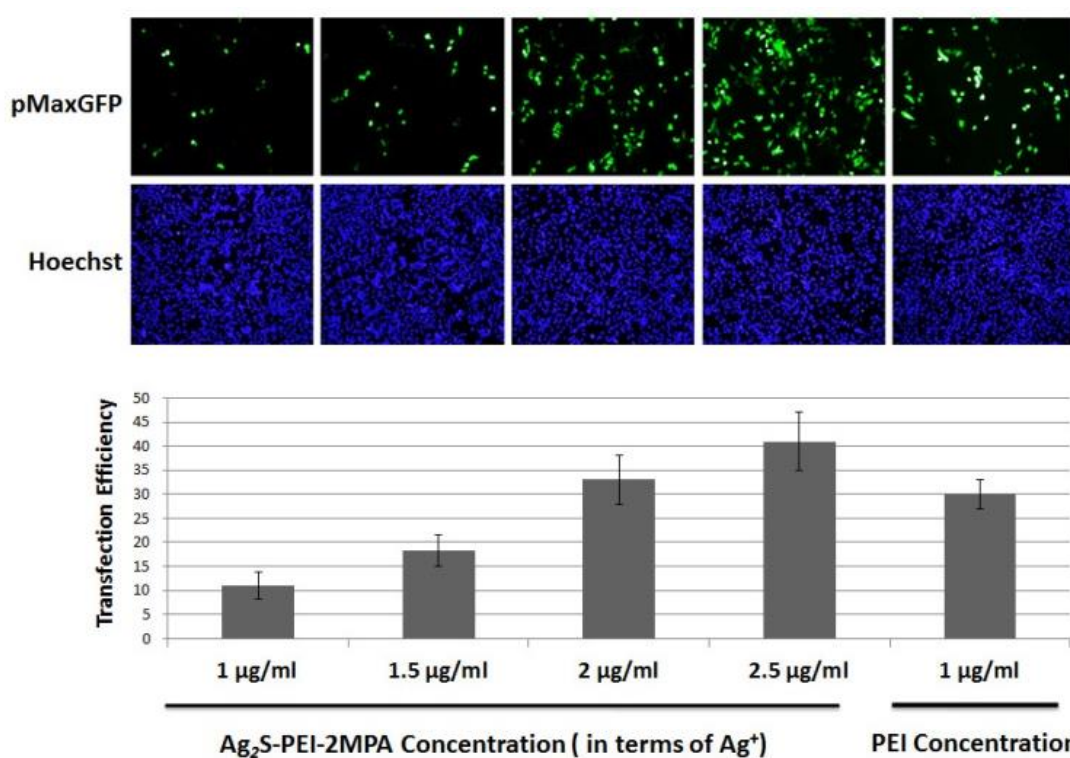


Figure 2. 26 Transfection of HeLa cells. (Top) Cells were transfected with pMax-GFP plasmid using Ag₂S-PEI/2MPA NIRQDs or control PEI (1 μg/ml). Transfection efficiency was assessed under a fluorescent microscope. Hoechst staining was used to show the nuclei of all cells in the field. (Bottom) Quantitative analysis of GFP positive cells in (Top) (mean ± SD of independent experiments, $n = 3$).

The CLM images of the transfected MCF-7 cells with QDs (Figure 2. 27) demonstrate a strong optical signal originating from Ag₂S-PEI/2MPA NIRQDs proving internalization of particles conjugated with pMax-GFP by the cells. These images prove the efficient uptake of QDs with and without the plasmid. These results confirmed that both DNA binding and intact DNA delivery capabilities of Ag₂S-PEI/2MPA QDs are better than that of commercial PEI 25 kDa, promoting these QDs as biocompatible theranostic nanoparticles.

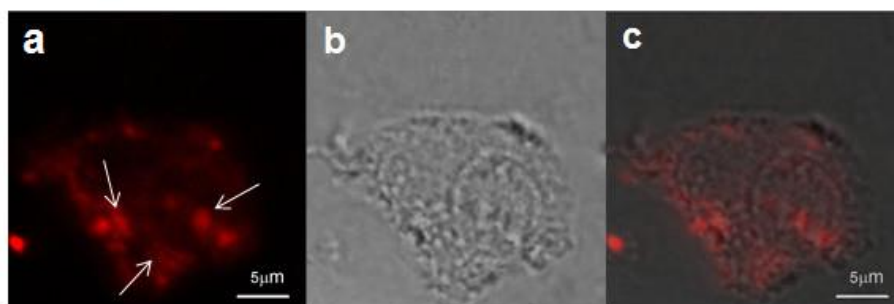


Figure 2. 27 Cellular uptake and localization of GFP loaded PEI/2MPA coated Ag₂S NIRQDs in MCF-7 cells. Near IR (a), transmission (b) and merged images (c) of an individual cell. Arrows show QDs in the cell.

2.4 Conclusions

Theranostics have been very popular for the last decade, especially with the development of nanoparticles as drug carriers and imaging agents. Combined action of gene delivery and optical imaging is one of the most valuable capabilities in medicine and is moving towards near-infrared emitting quantum dots due to many advantages described herein. The present study demonstrated a simple, aqueous preparation of cationic, cytocompatible Ag₂S quantum dots with utilization of PEI and 2MPA mixed coatings and their potential as optical probes and gene delivery vehicles *in vitro*. Advantages of these NIRQDs are numerous: Highest quantum yield reported until now (150 %) may allow reduction of necessary dose for signal detection. Strong luminescence in the NIR-I window eliminates autofluorescence for better signal-to-noise ratio and allows strong optical signal. Although PEI coating provided poorly luminescent particles, incorporation of 2MPA as a co-stabilizer, provided a synergy and produced colloidally stable particles with strong luminescence and smaller size crystals compared to PEI or 2MPA coated particles. Although a polymeric coating usually provides colloidal stability, it leaves defects on crystal surface and causes poor luminescence due to the lack of dense packing restricted by the polymer backbone. Hence, addition of small strongly binding 2MPA, both decreases the crystal size due to such strong Ag-thiol binding and passivates uncoordinated sites, increasing QY. Silver chalcogenides are being demonstrated as great alternatives to heavy metal containing quantum dots also in terms of biocompatibility. PEI/2MPA coated Ag₂S NIRQDs therefore, brings together an ideal quantum dot core with an ideal coating. Although not as cytocompatible as 2MPA coated Ag₂S NIRQDs,

PEI/2MPA coated Ag₂S NIRQDs are cytocompatible below 5 $\mu\text{g Ag}^+/\text{mL}$ (23 $\mu\text{g} /\text{mL}$ QD). One of the most important findings is that binding PEI to particle surface decreases the toxicity with respect to free PEI, possibly due to the loss of some amines upon surface binding. Achieving cytocompatibility without PEGylation of the cationic particles are very important since PEGylation does interfere with gene delivery potential and endosomal escape of the nanoparticles.

These NIRQDs were internalized effectively by HeLa and MCF-7 cells as well as *C. elegans* and generated strong optical signal in the NIR-I region suppressing the tissue autofluorescence, which is highly desirable for optical detection of the particles.

These cationic Ag₂S NIRQDs successfully transfected GFP to both of these cell lines . Transfection efficiency was about 40 % following a standard protocol which was adapted from standard PEI (linear, 25 kDa) experiments which had 30 % transfection efficiency. Possibly this can be optimized further and even better efficiencies can be obtained via a N/P ratio study.

In the rise of Ag₂S NIRQDs, we demonstrate the synthesis of highly luminescent, cationic QDs with the best known polymeric transfection agent, PEI, and point out the promise of Ag₂S as valuable new theranostic nanoparticles.

Chapter 3

3. PEGYLATION OF CATIONIC Ag₂S NIRQDs FOR DRUG AND GENE DELIVERY IN CANCER TREATMENT

3.1 Introduction

In the previous chapter, cationic polyethyleneimine (PEI)-25 kDa and 2MPA coated Ag₂S QDs were developed with excellent quantum yield, colloidal stability and transfection efficiency [181]. Positively charged particles easily enter cells by interaction with negatively charged cell membrane [182, 183]. However, cationic QDs can induce some toxicity via interacting with blood components depending on the surface charge. Moreover, their sizes increase by the formation of protein corona on the surface of the particles due to large surface to volume ratio. This results with rapid clearance of nanoparticles from circulation system by macrophage engulfment and accumulation of the structures in the reticuloendothelial system (RES) [184, 185]. To reduce all of these negative effects, particles are usually functionalized with PEG. PEG coating increases biocompatibility, colloidal stability in water and prolongs circulation half-life by masking the surface and nonspecific protein interaction [186].

In this chapter, PEGylation of the cationic Ag₂S QDs, and its use as a drug/gene delivery agent with optical imaging modality are discussed.

Doxorubicin (DOX), one of the most widely used chemotherapeutic agents with antitumor activity against a variety of solid tumors [187], was loaded to PEGylated QDs. In clinical applications, the drug has several undesirable side effects which restrict its clinical usage. Direct administration of the drug causes toxicity to healthy tissues. Therefore, nanoparticle mediated DOX delivery systems may reduce the side effects and improve drug efficacy. Liposomal structures, polymeric carriers, nano-micelles and

dendrimers have been used for this purpose [188-191]. A remarkable common feature of these nanocarriers is that their surfaces are usually functionalized with poly(ethylene glycol) (PEG) polymers because PEGylation enhances the dispersion and circulation time of nanoparticle in blood and facilitate the accumulation of the drug at the tumor sites by enhanced permeability and retention (EPR) effect [192, 193]. Most cancer therapies exploit the EPR effect which is a passive way of targeting drugs to the tumor.

EPR effect is a result of anatomical defects of blood vessels in the tumor region. The neovasculature of cancer tissues differs from normal tissues in microscopic scale [194]. The blood vessels in tumor area are leaky, defective and irregular in shape. In addition, the surrounding cells such as perivascular cells, smooth-muscle layer or basement membrane are usually absent or abnormal in the vascular wall. These abnormalities cause high amounts of accumulation of nanoparticles as well as blood plasma components in the tumor tissue. In addition, poor lymphatic drainage and slow venous return in tumor region result in retention and slow clearance of the macromolecules from the tissues [195, 196]. Macromolecules are selectively accumulated in the area according to their size. Generally, the structures up to 400 nm can enter to the tumor area. On the other hand, low-molecular-weight molecules, such as small molecule drugs, undergo rapid diffusion in the circulating blood and filtrated by kidneys, subjecting to renal clearance [137]. Hence, loading drugs to nanocarriers do enhance their efficacy.

In this study, combination therapy, namely simultaneous delivery of gene and DOX, has been attempted with PEGylated cationic Ag₂S QDs. For cancer therapy, *p53* tumor suppressor gene which is mutated in over 50 % of human cancers was chosen. *P53* regulates cell cycle and protect DNA against mutations (Figure 3. 1). During DNA damage, the gene mediates apoptosis by activating multiple genes involved in apoptosis. Mutations on *p53* lead to loss of the tumor suppressor function and become cancerous of the cells [197-199]. Therefore, delivery of healthy *p53* gene by nanocarriers can be promising approach to cancer therapy. In this chapter, PEGylated Ag₂S QDs were designed as drug and gene carrier systems besides the optical imaging function. DOX as anticancer drug and *p53* as apoptosis inducing gene were loaded to QDs and the cell death levels were measured in addition to characterization of PEGylated Ag₂S QDs.

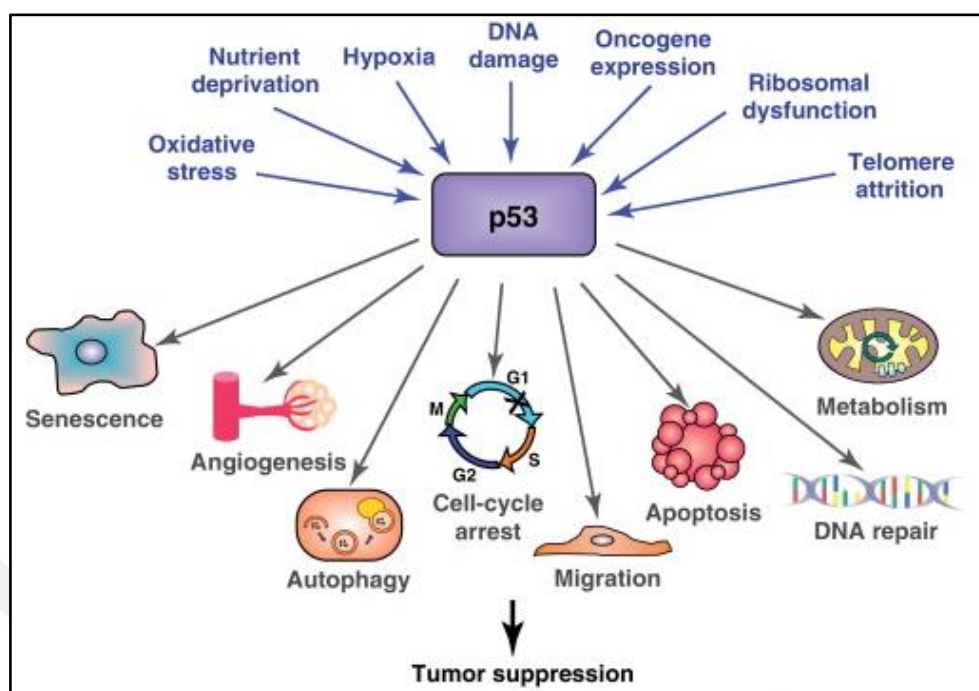


Figure 3. 1 Cellular response to stress signals by *p53* activation [200].

3.2 Materials and Methods

3.2.1 Materials

Silver nitrate (AgNO₃) was purchased from Sigma-Aldrich . Sodium sulfide (Na₂S) was purchased from Alfa-Aesar. Branched polyethyleneimine (PEI) (25 kDa molecular weight (MW)) and N,N'-carbonyldiimidazole (CDI) were obtained from Aldrich (Germany). Methoxy (polyethylene glycol) (mPEG-OH, 2 kD) was purchased from Rapp Polymere, Germany) and chloroform and tetrahydrofuran were obtained from Merck Millipore. Doxorubicin hydrochloride (DOX·HCl) was purchased from SABA pharmaceuticals (Turkey). p53-GFP plasmid was obtained from Addgene (plasmid 11770, USA). Only Milli-Q water (18.2 MΩm) was used when necessary.

Roswell Park Memorial Institute (RPMI) 1640 mediums (with l-glutamine and 25 mM HEPES), trypsin-EDTA and penicillin-streptomycin solutions were provided by Multicell, Wisent Inc. (Canada). Fetal bovine serum (FBS) was obtained from Capricorn Scientific GmbH (Germany). Thiazolyl blue tetrazolium bromide (MTT) and phosphate buffered saline (PBS) tablets were purchased from Biomatik Corp. (Canada). Dimethyl sulfoxide Hybri-Max™, 4',6-diamidino-2-phenylindole (DAPI) was obtained from Sigma (USA) and 4 % paraformaldehyde solution in PBS was purchased from Santa Cruz

Biotechnology, Inc. (USA). All 12, 24 and 96-well plates were purchased from Nest Biotechnology Co. Ltd. (China).

All reagents were of analytical grade or of the highest purity.

HCT 116 (wt) and HCT 116 p53 -/- (Human colon cancer cell lines) were purchased from the American Type Culture Collection (ATCC, Manassas, VA, USA). HeLa (human cervical carcinoma) and MCF-7 (human breast adenocarcinoma) cell lines were given as a gift from the Devrim Gozuacik Lab (Sabanci University, Istanbul, Turkey) for this study.

3.2.2 Preparation of PEI/2MPA coated Ag₂S (Ag₂S) NIRQDs

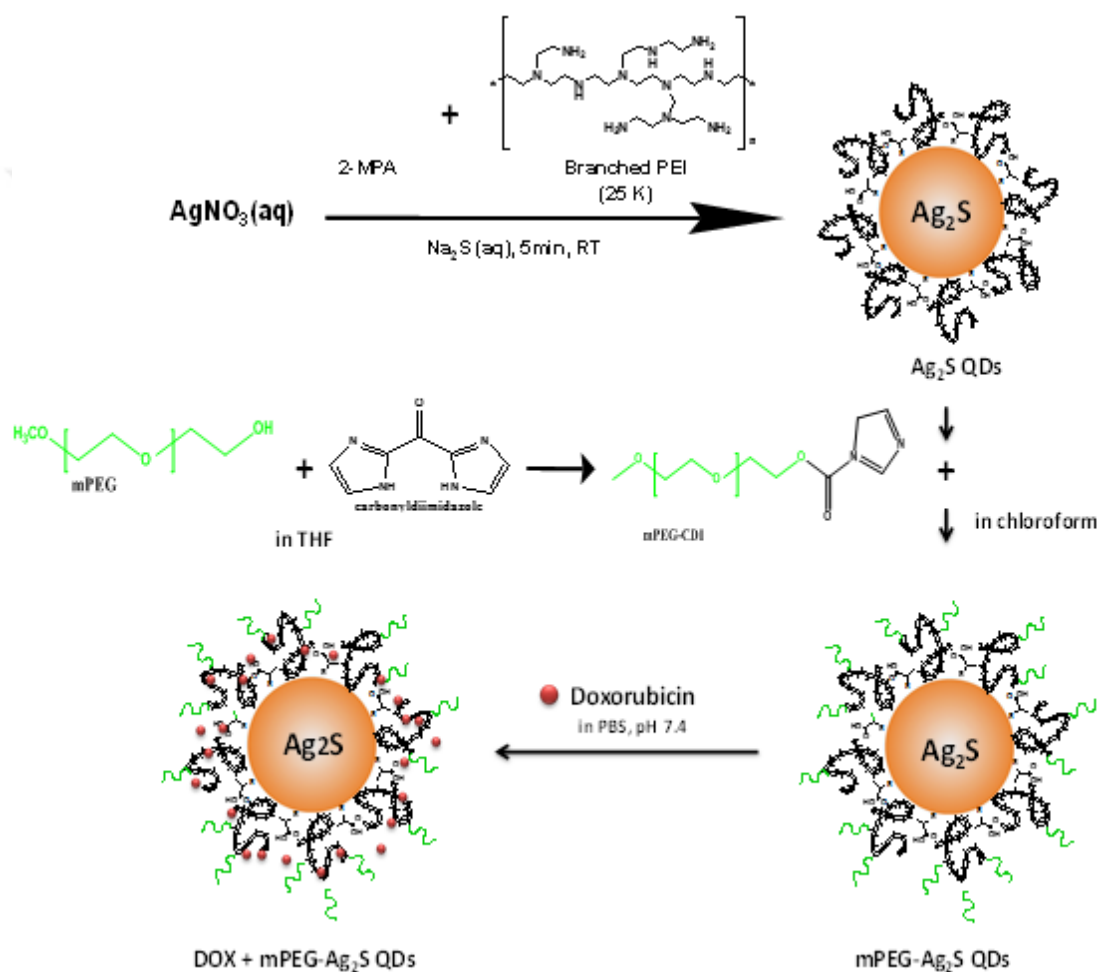
Ag₂S QDs were prepared according to the previous chapter. In details, 0.25 mmol of AgNO₃ was dissolved in 75 ml of deionized water under an inert atmosphere. The reaction was performed under vigorous mechanical stirring (5000 rpm) at room temperature (RT). 2.85x10⁻³ mmol of PEI (25 kDa MW) and 0.25 mmol of 2MPA were added into the solution. The pH of the mixture was adjusted to 9 using NaOH (1M) and acetic acid (1 M) solutions. Finally, 0.0625 mmol of Na₂S, dissolved in a separate round bottom flask with 25 mL of deoxygenated water, was injected to the mixture and stirred for 5 min (Scheme 3. 1). The obtained brown solution was washed through Amicon-Ultra centrifugal filters (30000 Da cut off) to remove unbound chemicals and lyophilized for further applications. All powder samples was stored at -20 °C, whereas liquids stored at 4 °C.

3.2.3 Preparation of CDI-activated methoxy-PEG (mPEG-CDI)

Firstly, the methoxy (polyethylene glycol) (mPEG, 2 kDa) was activated by N³-carbonyldiimidazole (CDI) in order to conjugate the hydroxyl terminal groups to amine groups of branched PEI on Ag₂S QDs (Scheme 3. 1). For this purpose, the procedure of Guihua et al. was followed [201]. According to the procedure, mPEG-OH (4.0 g) was dissolved in anhydrous THF (30 mL) after vacuum-dried at 60 °C for 8 h. Meanwhile, CDI (3.2 g) was dissolved in THF (20 mL), separately, and mPEG-OH solution was added dropwise to this solution. The mixture was allowed to stir under argon atmosphere and finally, the reaction was terminated by addition of 200 µL of distilled water. The reaction solution was subjected to a large amount of cold diethyl ether under vigorous agitation. The precipitate was collected by centrifugation and dried in vacuum.

3.2.4 PEGylation of Ag₂S NIRQDs

PEI/2MPA coated Ag₂S NIRQDs was PEGylated as shown in Scheme 3. 1. Briefly, PEI/2MPA Ag₂S QDs (11 mg) and CDI activated mPEG (80 mg) were dissolved in 10 mL of chloroform and the mixture was stirred at room temperature for 24 h. The resulting product was again added to a large amount of cold diethyl ether under vigorous agitation and centrifuged. The collected precipitate was dried under vacuum atmosphere and washed with deionized water using Amicon-Ultra centrifugal filters (30000 Da cut off).



Scheme 3. 1 Synthesis of PEGylated-Ag₂S NIRQDs and DOX loading via non-covalent complexation.

3.2.5 DOX loading on PEGylated Ag₂S QDs

20 mg of PEGylated Ag₂S QDs and DOX.HCl (1mg) were suspended in 50 mL deionized water under vigorous stirring for 36 h at RT and the solution was dialyzed against 1L PBS (pH 7.4) for 2 × 1.5 hours using a 3500 Da-MWCO cellulose dialysis

membrane to remove unloaded DOX. PBS was refreshed at each 1.5 hour-dialysis. The unloaded DOX was measured from a concentration dependent absorbance calibration curve of DOX based on the DOX absorbance at 485 nm (Figure 3. 2) by the following equation:

$$\text{DOX loading efficiency \%} = \frac{W_{\text{total}} - W_{\text{free}}}{W_{\text{total}}} \times 100\% \quad (1)$$

where W_{total} is DOX added initially, W_{free} is the unloaded DOX.

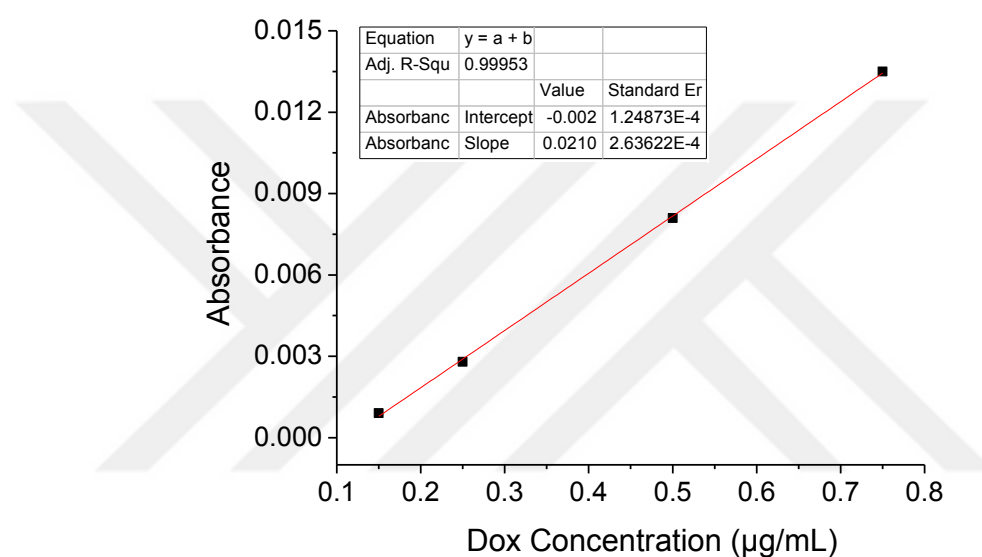


Figure 3. 2 Concentration dependent absorbance calibration curve for free DOX plotted with absorbance intensity of known concentrations of DOX at 485 nm.

3.2.6 Characterization methods

The luminescence in NIR region was recorded with a homemade setup equipped with a 1/8 Newport Cornerstone 130 monochromator which has 600 L per mm grating and operates in the 400–1000 nm. The samples were excited with a frequency doubled output of a DPSS laser (532 nm) and the luminescence was filtered through a 590-nm long pass filter. The signals were detected using a femtowatt sensitive Si detector (Thorlabs PDF10A, 1.4×10^{-15} W Hz^{-1/2}). The slit width was fixed at 0.2 mm. The fluorescence in visible region was measured by a Horiba Yvon FluoroMax-3 spectrofluorometer. Absorbance in the 300–1100 nm region was recorded by a Shimadzu 3101 PC UV-Vis-NIR spectrophotometer. The hydrodynamic size and zeta potential of QDs were recorded on a Malvern Zetasizer Nano-ZS in aqueous solution. Ag content in

QD solutions was analysed with an Agilent 7700x Inductively Coupled Plasma Mass Spectrometry (ICP-MS) according to previous chapter. FTIR spectrum was conducted by a ThermoScientific Nicolet iS10 instrument (ATR-FTIR) in the wavenumber region from 500 to 4000 cm⁻¹.

3.2.7 Cell culture

HeLa human cervical cancer cells and MCF-7 human breast adenocarcinoma cells were grown in an incubator at 37°C in 5 % CO₂, in RPMI medium supplemented with 10 % FBS and 1 % penicillin-streptomycin.

HCT 116 and HCT 116 p53 -/- (Human colon cancer cell lines) were cultured in McCoy's 5A media (*PAN Biotech*, Aidenbach, Germany) supplemented with 10 % fetal calf serum (*Pan Biotech*, Aidenbach, Germany), l-glutamine (*Biological Industries*, 03-020-1B) and 100 U/100 mg/ml penicillin/streptomycin (*Biological Industries*, 03-031-1B) and grown in a 37°C tissue culture incubator under 5% CO₂.

3.2.8 *In vitro* cytotoxicity studies

In vitro cytotoxicity studies were performed using 3-(4,5-dimethylthiazol-2-yl)-2,5-diphenyl tetrazolium bromide (MTT) viability assay. HeLa, MCF-7 and HCT 116 cells were seeded at a concentration of 1 x 10⁴ cells per well into 96-well plates and incubated at 37 °C under 5 % CO₂ for one day. The second day, cells were subjected to samples in different Ag concentrations with fresh culture medium and incubated for additional 48 h. Cells without any treatment were employed as positive controls. At the end of incubation, 50 μL of MTT solution (5 mg/mL in PBS, pH 7.4) was introduced to each well with 150 μL of fresh culture medium. After incubated 4 more hours at 37 °C in 5 % CO₂, DMSO/EtOH (1:1 v/v) solution was added to each well to dissolve purple formazan crystals that appear in the mitochondria of living cells. The absorbance intensities were recorded at 600 nm with a reference wavelength of 630 nm using a microplate reader (*BioTek ELx800 Absorbance Microplate Reader*). Treated cells without MTT solution were considered to correct the absorbance intensities. Each trial was repeated three times. The relative cell viability was calculated in reference to using following equation:

$$\text{cell viability (\%)} = [\text{Absorbance}_{\text{treated cells}} / \text{Absorbance}_{\text{control}}] \times 100. \quad (2)$$

3.2.9 *In vitro* cell imaging

HeLa and MCF-7 cells were cultured on a 6-well plate at a density of 2.5×10^5 cell/well in RPMI complete medium and incubated for one day at 37 °C in 5 % CO₂. The growing cells were treated with the samples at 2.5 µg/mL Ag concentration for 4 h. After incubation, the cells were washed with PBS to remove untaken QD samples and fixed with 4 % paraformaldehyde solution for 20 min at RT. Washing step with PBS was repeated and DAPI staining was performed in order to reveal cell nucleus. The cells were washed again and 2 mL PBS was left in each well to protect cells against drying. Cells without QD were used as controls. Finally, cells were visualized under an Inverted Life Science Microscope (Olympus-Xcellence RT Life Science Microscopy) by employing filter sets for DAPI (λ_{exc} : 352-402 nm and λ_{em} : 417-477 nm), DOX (cy3: λ_{exc} : 530-560 nm and λ_{em} : 573-648 nm) and NIR region (λ_{exc} : 550 nm and λ_{em} : 650 nm long pass), respectively. The recorded images were processed by ImageJ software (version 1.46r, NIH, USA) [202].

3.2.10 PI cell cycle analysis

Cell cycle analysis by quantification of cellular DNA is one of the mostly used techniques to determine apoptosis in the cells. By the help of a DNA binding dye, Propidium Iodide (PI), highly condensed or fragmented nuclei can be determined. For PI analysis, HCT 116 cells were collected and fixed with 70 % ethanol for 16 h at 4 °C after washed twice with ice-cold 1X-PBS. Then, samples were centrifuged at 1200 rpm for 5 min to remove ethanol. The pellet was dissolved in 100 µl of 1X-PBS, RNase (100 µg/ml) and PI (40 µg/ml) (P3566, Invitrogen, Eugene, Oregon, USA) solution and subsequently incubated for 30 min at 37°C in dark. Fluorescent PI dye which stains DNA was measured by BD FACS Canto Flow Cytometry System (BD, San Jose, CA) within 1hr. At least 10,000 events were analyzed for each measurement.

3.2.11 Immunoblotting

Proteins extraction of HCT 116 cells was conducted using RIPA buffer (50 mM TRIS-HCl pH 7.4, 150 mM NaCl, 1% NP40, 0.25% Na-deoxycholate) supplemented with complete protease inhibitor cocktail (Roche, 04-693-131-001) and 1mM phenylmethylsulfonyl fluoride (PMSF; Sigma-Aldrich, P7626). Then, cell extracts (50

µg) were separated in 15 % or 10 % SDS-polyacrylamide gels and transferred to a nitrocellulose membrane. Blockage was performed in 5 % nonfat milk in PBST (3.2 mM Na₂HPO₄, 0.5 mM KH₂PO₄, 1.3 mM KCl, 135 mM NaCl and 0.05 % Tween 20, pH 7.4) or TBST (for phosphorylated protein analysis) for 1 h at RT and membranes were incubated in 3% BSA-PBST solutions containing primary antibodies (ab): anti-PARP ab (CST, #9542S, 1:1000), anti-cleaved Caspase-3 (Asp175) ab and anti-β-actin ab (Sigma-Aldrich, A5441, 1:10000). Finally, secondary mouse or rabbit antibodies coupled to horseradish peroxidase (anti-mouse: Jackson Immunoresearch Laboratories, 115035003; anti-rabbit: Jackson Immunoresearch laboratories, 111035144, 1:10,000) were introduced in 5 % milk/PBST for 1 h at RT and protein bands were detected with chemiluminescence.

3.2.12 *In vitro* transfection studies

Transfection studies were performed with HCT 116 (wt) and HCT 116 p53^{-/-} cells using p53-GFP plasmid that the structure shown in Figure 3. 3.

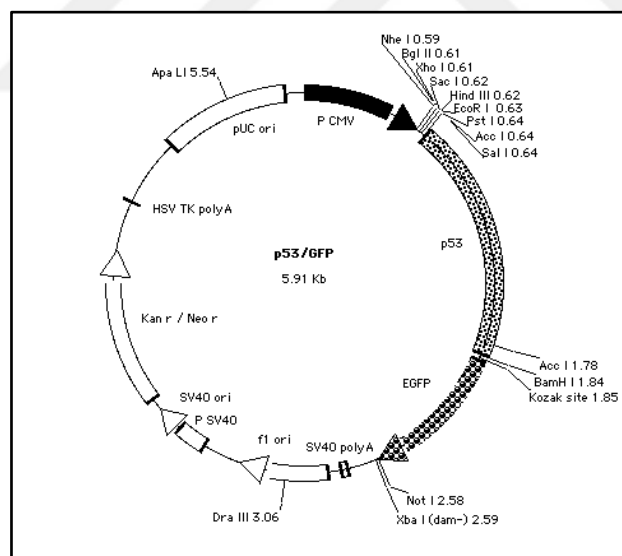


Figure 3. 3 The structure of p53/GFP plasmid used in the study, which was inserted in DH5-alpha *E. coli*.

To obtain p53-GFP plasmid, standard microbiology protocols were applied. *E. coli*, containing p53-GFP plasmid (Addgene plasmid 11770) were amplified on a Luria Bertani (LB) agar plate and a single colony was grown in LB Broth liquid medium for 18 hours (until the log phase). Finally, plasmid DNA was purified with Qiagen Plasmid Plus

Maxi Kit (Cat No./ID: 12965) and quantified with a Nanodrop Spectrophotometer (Figure 3. 4). QD and pDNA complexes were prepared at N/P ratio of 40/1 using 3 μ g fixed amount of pDNA for each experiment. N/P ratio of of 20/1 and 60/1 were also studied to optimize the transfection efficiency. Transfection efficiency was measured by a BD FACS Canto Flow Cytometry System (BD, San Jose, CA). At least 10000 events were analyzed for each case.

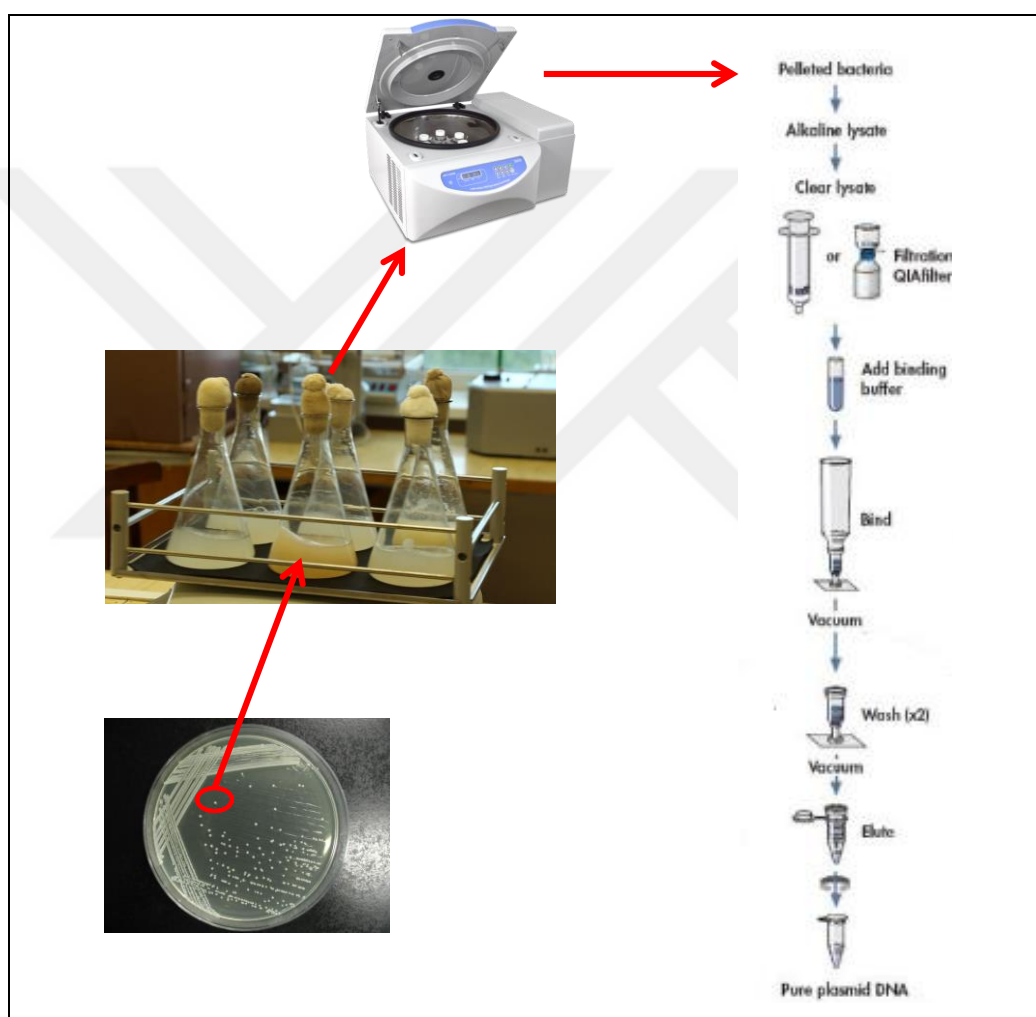


Figure 3. 4 Simple illustration of cultivation steps of *E. coli* and plasmid DNA purification.

3.2.13 Statistical analysis

Statistical analysis was performed by application of analysis of variance (ANOVA) with Bonferroni's multiple comparisons test using Graph Pad 4.04 version software (GraphPad Software, Inc., USA). All quantitative data were obtained from the averages

of at least three independent experiments ($n = 3$) and expressed as mean \pm standard deviation (SD). p -value < 0.05 was accepted as statistically significant.

3.3 Results and Discussion

3.3.1 Characterization of mPEG-Ag₂S QDs

In this study, cationic Ag₂S NIR emitting QDs developed in previous chapter were PEGylated using a methoxy-polyethylene glycol (mPEG-OH, 2 kD) and loaded with DOX, an anticancer drug, for simultaneous tumor chemotherapy and optical imaging. To prepare the samples, the procedure illustrated in Scheme 3. 1 was followed. In this procedure, first of all, Ag₂S QDs were synthesized in a mixture of PEI-25 kDa MW and 2MPA using AgNO₃ as a silver source and Na₂S as a sulphur source. mPEG-OH, activated with CDI, was then conjugated to the free amine groups of the PEI/2MPA coated Ag₂S QDs. PEGylated Ag₂S QDs were loaded with DOX via hydrophobic and electrostatic interactions. Unloaded drug was removed by dialysis against PBS and DOX loading efficiency was calculated as 88 % from its absorbance at 485 nm (Scheme 3. 1). This is equal to 0.044 mg DOX per 1 mg PEGylated Ag₂S.

After PEGylation, the emission wavelength of Ag₂S QDs showed a slight blue shift from 817 nm to 807 nm and emission intensity decreased (Figure 3. 5). However, QDs still have strong emission intensity for diagnostic applications.

DLS and zeta potential analysis proved colloidal stability of QDs after PEGylation and DOX loading steps, as well. As shown in Table 3. 1, the average number based hydrodynamic size of Ag₂S QDs was 5.01 ± 1.6 nm with a zeta potential of 60 ± 1.2 mV. When the nanoparticles were PEGylated, the hydrodynamic size increased to 8.4 ± 0.9 nm, whereas the zeta potential decreased to 37.5 ± 2.9 mV. This was expected, since PEG should increase the hydrated shell thickness and should reduce the overall net cationic charge due to its anionic contribution. Drug loading was further increased the average size with a decrease in surface charge. Hydrodynamic size of DOX loaded particles appeared as 15.52 ± 0.72 nm which implies that these nanoparticles are still ultrasmall and under 50 nm. Decrease in zeta potential proves successful drug loading on QDs, as well.

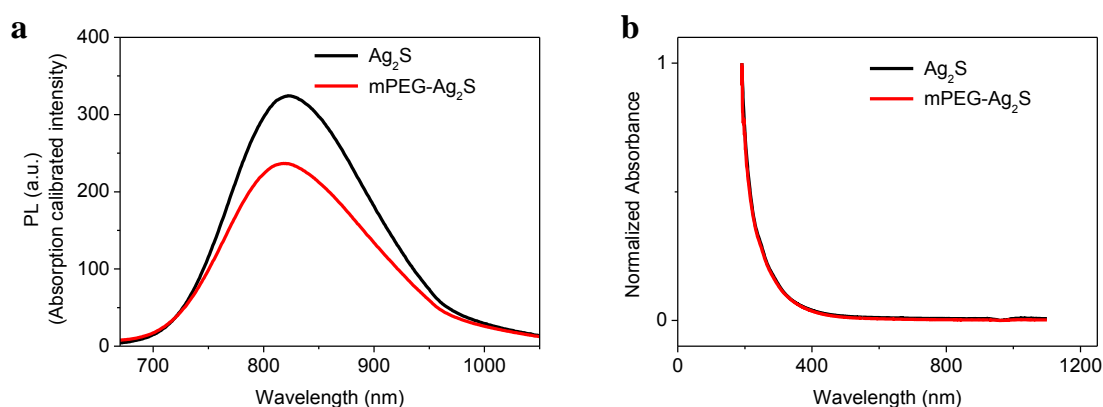


Figure 3. 5 Photoluminescence and corresponding absorbance spectra of PEI/2MPA coated Ag₂S QDs (Ag₂S QDs) and the PEGylated formulations.

Table 3. 1 Number-average size distribution and zeta potential of NIRQDs.

Sample	Ag ₂ S	mPEG-Ag ₂ S	DOX + mPEG-Ag ₂ S
Size (nm)	5.01 ± 1.6	8.4 ± 0.9	15.52 ± 0.72
Zeta Potential (mV)	60 ± 1.2	37.5 ± 2.9	11.3 ± 1.8

3.3.2 Assessment of *in vitro* cytotoxicity

The cytotoxicity of Ag₂S, PEGylated Ag₂S and DOX loaded PEGylated Ag₂S QDs to HeLa and MCF-7 cells were evaluated by MTT cytotoxicity assay. Concentrations of the particles were adjusted according to their Ag content measured by ICP-MS to keep the number of particles constant at each formulation. As shown in Figure 3. 6 and Figure 3. 7, the cell viability seems to increase after PEGylation and decreased dramatically after DOX loading in both cell lines, as expected. It seems like MCF-7 cells are more vulnerable and viability fell below 50 % at 2.5 µg Ag/mL dose, yet in HeLa cells viability stayed around 60-40 % in the 0.5-5 µg Ag/ml range.

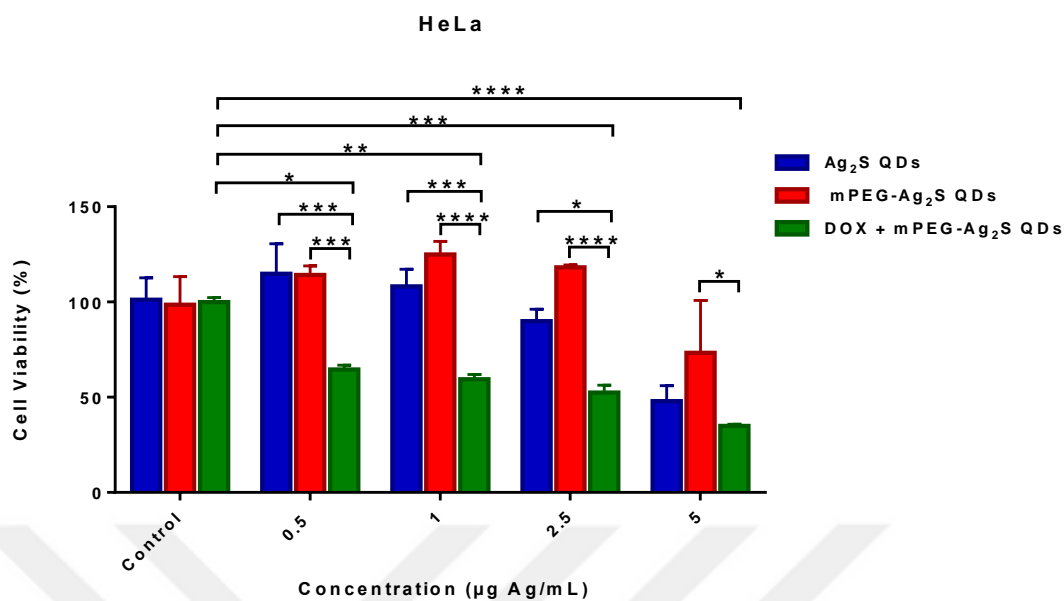


Figure 3. 6 Cell viability of HeLa cells treated with Ag₂S, mPEG-Ag₂S and DOX loaded PEG-Ag₂S for 48 hours, performed by MTT assay. Untreated cells were accepted as positive control. The data were expressed as mean \pm S.D. (n=3), ($p < 0.05$ (*), $p < 0.01$ (**), $p < 0.001$ (***) and $p < 0.0001$ (****)).

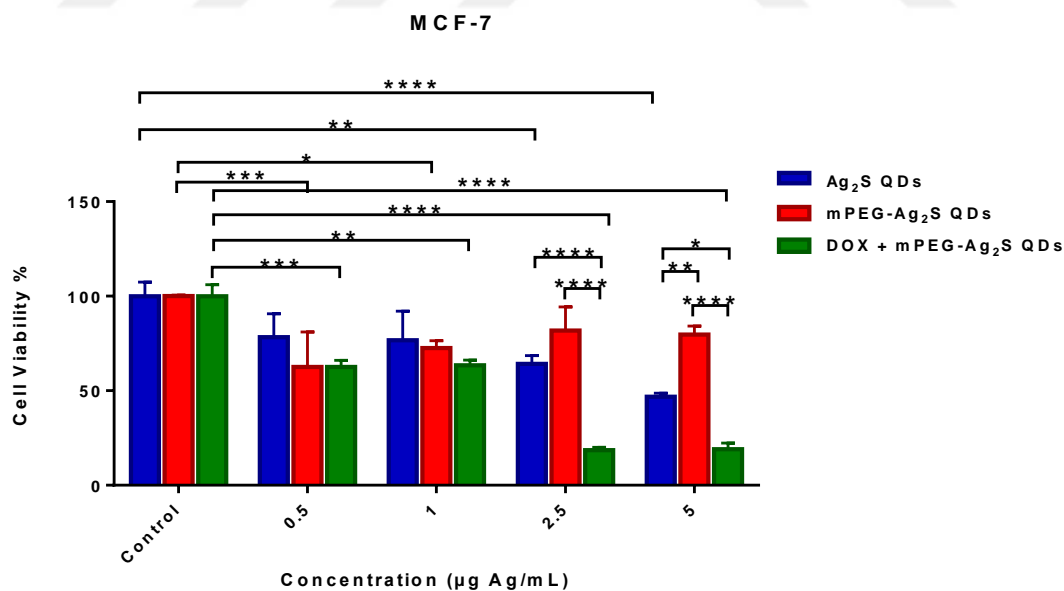


Figure 3. 7 Cell viability of MCF-7 cells treated with Ag₂S, mPEG-Ag₂S and DOX loaded PEG-Ag₂S for 48 hours, performed by MTT assay. Untreated cells were accepted as positive control. The data were expressed as mean \pm S.D. (n=3), ($p < 0.05$ (*), $p < 0.01$ (**), $p < 0.001$ (***) and $p < 0.0001$ (****)).

The cytotoxicity assay was repeated with HCT 116 cells. DOX loaded particles were compared with free DOX in equivalent concentrations with DOX loaded particles. As shown in Figure 3. 8, the cell viability of the particles is relatively higher than free DOX. However, there is no statistical significance between free drug and the drug loaded Ag₂S QDs. This implies that DOX loaded PEG-Ag₂S QDs are as effective as free DOX although PEGylation should decrease cellular uptake of the nanoparticles.

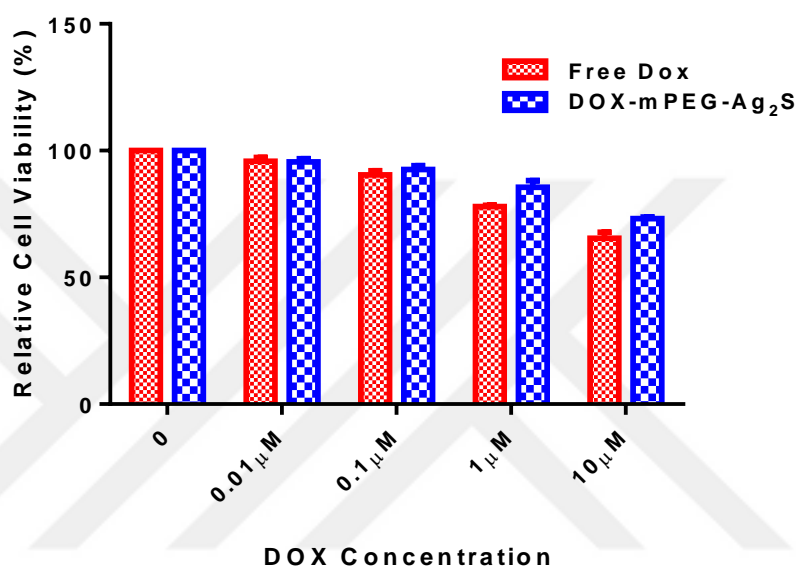


Figure 3. 8 Cell viability of HCT 116 cells treated with free DOX and DOX loaded PEG-Ag₂S for 48 hours, performed by MTT assay. Untreated cells were accepted as positive control. The data were expressed as mean \pm S.D. (n=3), ($p < 0.05$ (*), $p < 0.01$ (**), $p < 0.001$ (***) and $p < 0.0001$ (****)).

3.3.3 Microscopy Studies

To evaluate the intracellular uptake of QDs, HeLa cells were incubated with mPEG-Ag₂S and DOX loaded mPEG-Ag₂S NIR emitting QDs, at 2.5 $\mu\text{g Ag}/\text{mL}$ dose for 4 h (containing 1.05 $\mu\text{g}/\text{mL}$ DOX). Both NIR and DOX emission signals were indicated in red colour due to emission scale as seen in Figure 3. 9. Strong intracellular signals originating from QD (Figure 3. 9b and Figure 3. 9e) and DOX (Figure 3. 9c and Figure 3. 9f) reveal that mPEG-Ag₂S QDs are promising optical agent and favourable drug delivery systems for biomedical applications. Also, migration of DOX to the nuclei is also visible in the images, indicating effective release of the DOX in the endosome.

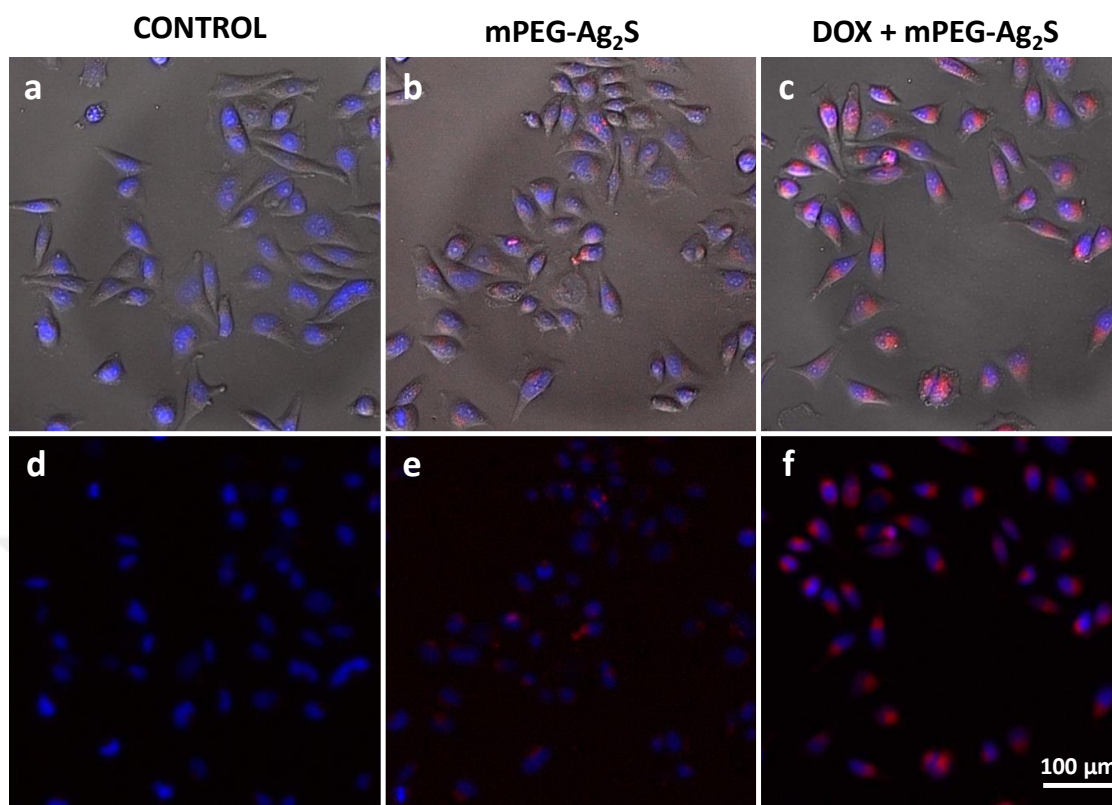


Figure 3. 9 Fluorescence microscopy images of HeLa cells treated with mPEG-Ag₂S and DOX loaded mPEG-Ag₂S QDs at 2.5 μg/mL Ag concentration. Untreated cells were used as controls. (a, d) Control cells. (b,e) mPEG -Ag₂S. (c,f) DOX loaded mPEG-Ag₂S. (a) is merged image from the bright field, DAPI, CY3 and NIR filters. (b) is merged image from the bright field, DAPI and NIR filters. (c) is merged image from the bright field, DAPI and CY3 filters. (d, e and f) is the corresponding fluorescence images without bright field. Blue signal shows DAPI staining for cell nuclei. Red signals in (b and e) indicate QD emission; in (c and f) DOX emission.

3.3.4 Evaluation of Cell Cycle Analysis

Propidium iodide (PI) flow cytometric assay is a commonly used technique for evaluation of apoptosis via checking cell cycle arrest [203]. PI is an intercalating fluorescent agent that binds to DNA. The dye is membrane impermeable and excluded from the viable cells. Cells with the dye corresponds to dead cells.

Doxorubicin is a topoisomerase II inhibitor which is responsible from overwinding or underwinding of DNA during DNA replication and transcription (Figure 3. 10) [204]. DOX treatment of cell induces G₂/M arrest because of inhibition of topoisomerase II

[205]. To evaluate the DOX effect, DOX loaded mPEG-Ag₂S QDs were compared with corresponding amount of free DOX. As shown in Figure 3. 11, control cells present a high level of stained DNA in G1 phase. However, DOX and DOX loaded QD exposure increases the DNA level in G2-M phase due to topoisomerase inhibition of DOX. This difference is more clear with free DOX.

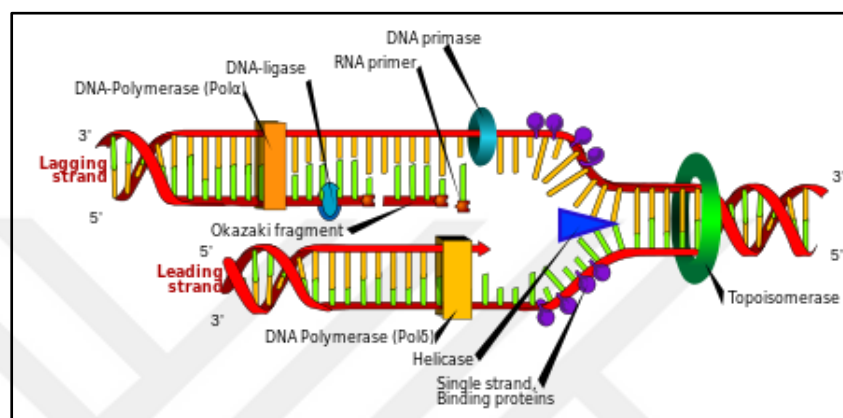


Figure 3. 10 Topoisomerase function during DNA replication [206].

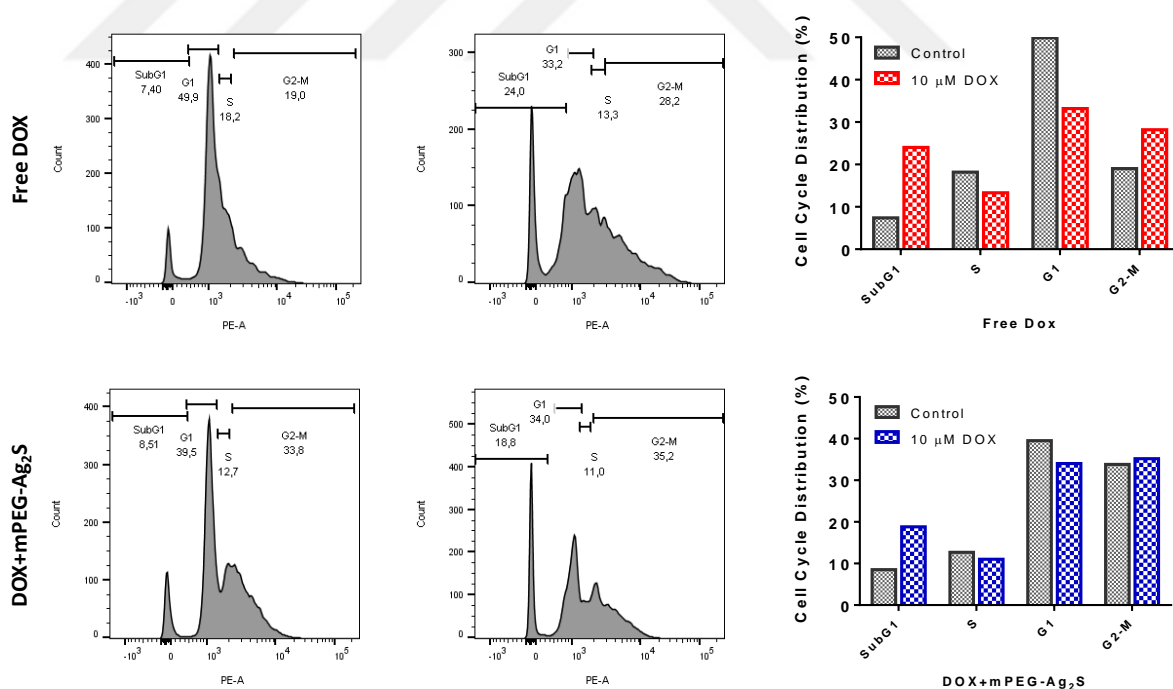


Figure 3. 11 Flow cytometric analysis of cell cycle with propidium iodide fluorescent staining. Free DOX and DOX loaded mPEG-Ag₂S QDs were used in 10 μM DOX concentration.

3.3.5 Evaluation of immunoblotting

Apoptosis event in HCT 116 cells after treatment with free DOX and DOX loaded Ag₂S QDs were detected using western blot analysis. As shown in Figure 3. 12, external stress can start the apoptosis. One of the possible pathways of apoptosis is DNA fragmentation by PARP cleavage as a result of activation of caspases. Caspase 3 is also induce PARP cleavage. Therefore, cleaved PARP (c-PARP) and cleaved caspase-3 (c-C3) proteins are important markers of apoptosis. For this reason, PARP, c-PARP and c-C3 antibodies were used to reveal apoptosis in HCT 116 cells treated with the samples. DOX induces the apoptosis in cells. To evaluate the effects of DOX loaded nanoparticles in molecular level, western blot analysis was done. Protein extracts of treated HCT 116 cells were incubated with antibodies of PARP, c-PARP and c-C3. As shown in Figure 3. 13, 10 μ M concentration of free DOX leads to formation of cleaved PARP and cleaved caspase 3. DOX loaded mPEG-Ag₂S QDs at the same DOX concentration were also effectively induced apoptotic pathways in the cells. Inactivated PARP was found in all cell lines, as expected. β -actin, an housekeeping gene, was used as loading control. Study was repeated for 0.1 μ M DOX, but no significant effect was detected.

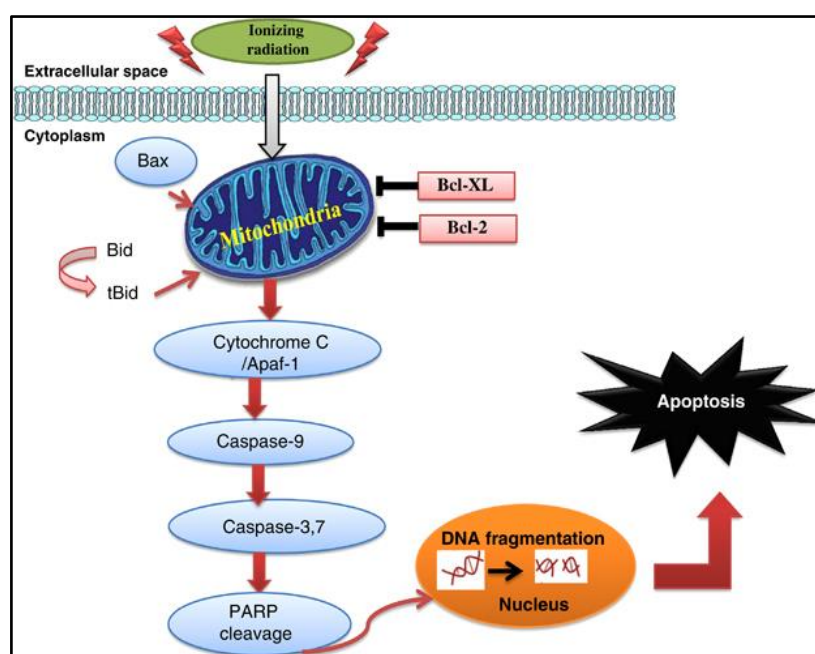


Figure 3. 12 Apoptosis pathway by caspase activity and PARP cleavage [207].

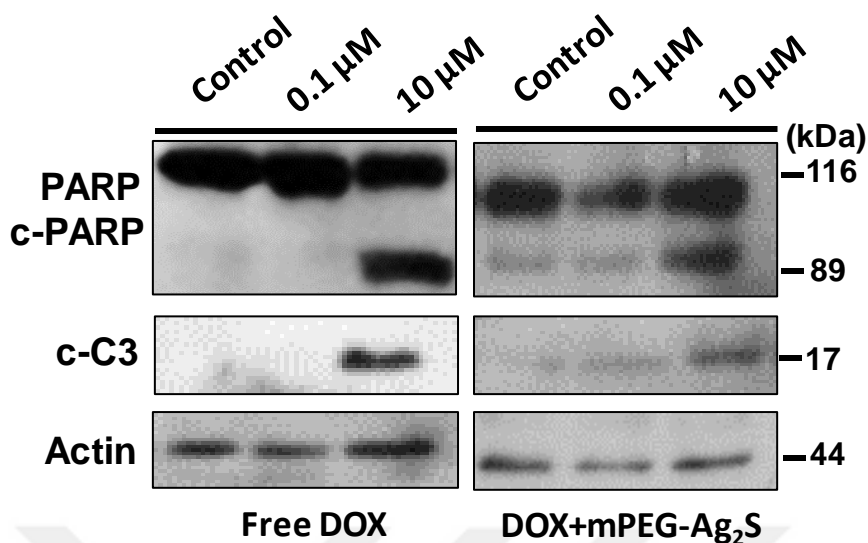


Figure 3. 13 Western blot analysis of protein extracts of HCT 116 cells treated with free DOX and DOX-mPEG-Ag₂S QDs. The samples were used in equivalent DOX concentrations. The bands of c-C3 (cleaved caspase-3) and c-PARP (cleaved PARP) are clearly seen at 10 μM DOX and 10 μM DOX including mPEG-Ag₂S QD concentrations.

3.3.6 Transfection Studies

In the previous chapter, transfection ability of cationic Ag₂S QDs were shown using a model gene, GFP. PEGylated-Ag₂S QDs have still enough cationic charge even after DOX loading, hence can be utilized as a transfection agent or for the delivery of combination therapy. For an effective cancer therapy, combination of drug and gene in a single particle is one of the most attractive approaches. PEGylated Ag₂S QDs with their cationic nature and high drug loading capacity are very appropriate candidates for such duty. For this purpose, *p53* gene, tumor suppressor gene which has many tasks within living cells (Figure 3. 1), was loaded to mPEG-Ag₂S and DOX-mPEG-Ag₂S QDs. Most of the cancer cells (~ 50 % of cancer cases) have *p53* mutations. Delivery of the healthy gene from outside by nanocarriers can start *p53* function again in *p53* mutated cancer cells and so, induce apoptotic cell killing. So, these QDs were loaded with *p53*-GFP plasmid at N/P ratio of 40/1. We know from our previous studies that the plasmid can completely bind to these QDs (before and after PEGylation) at and above the N/P ratio of 5/1. HCT 116 wild type (wt) and a *p53* knock out type of HCT 116 (HCT 116 *p53* -/-

) were transfected with p53-GFP plasmid using these QDs. Transfection efficiencies were recorded by flow cytometry, measuring the GFP signal. As shown in Figure 3. 14, the transfection level of the nanoparticles were quite low. HCT 116 wt cells have 3 % transfection efficiency both with mPEG-Ag₂S and DOX-mPEG-Ag₂S QDs. This situation is not dramatically different in HCT 116 p53^{-/-} cells, but there is a very slight increase with mPEG-Ag₂S QDs (3.3 %). The DOX loaded nanoparticles are ineffective in transfection. Using N/P ratio of 20/1 and 60/1 did not cause a remarkable increase in the transfection efficiency (Figure 3. 15).

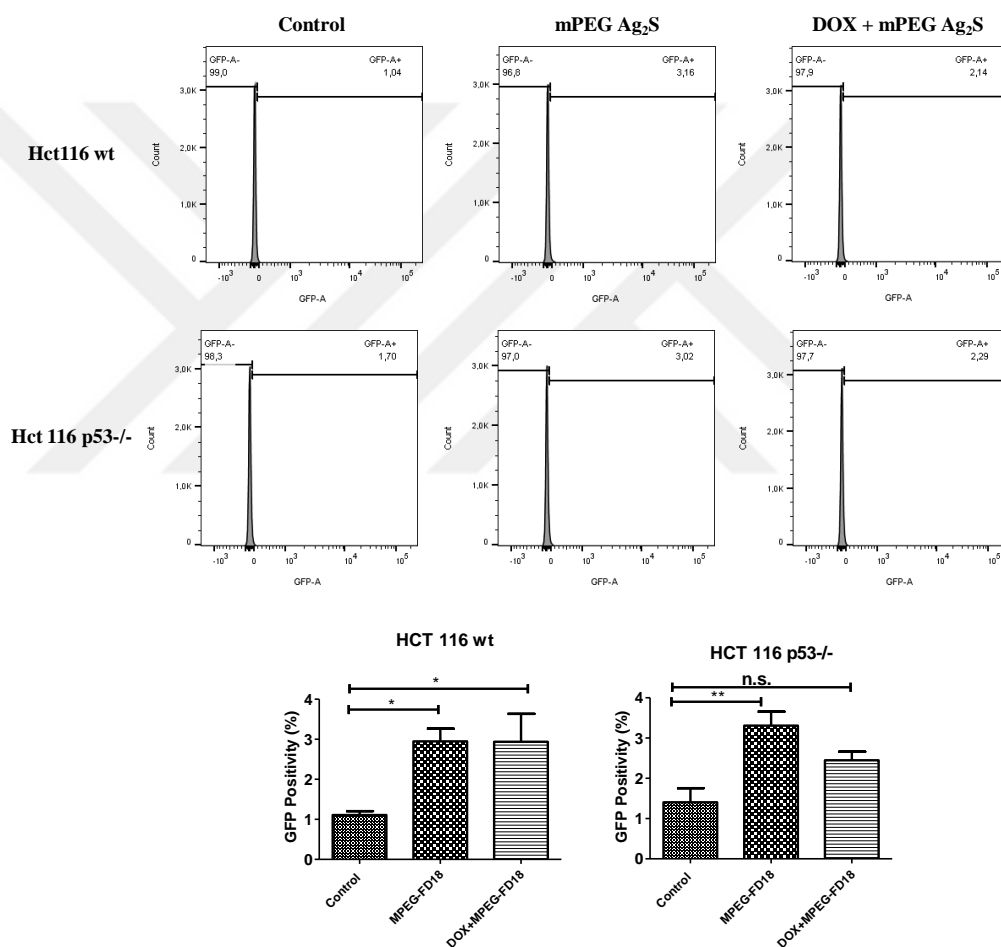


Figure 3. 14 Flow cytometry evaluations of transfection efficiencies of HCT 116 wt and HCT 116 p53^{-/-} cells treated with p53-GFP/mPEG-Ag₂S or p53-GFP /DOX-mPEG-Ag₂S QDs in N/P ratio of 40/1. Values are means mean \pm S.D. ($n=3$), ($p < 0.05$ (*), $p < 0.01$ (**)).

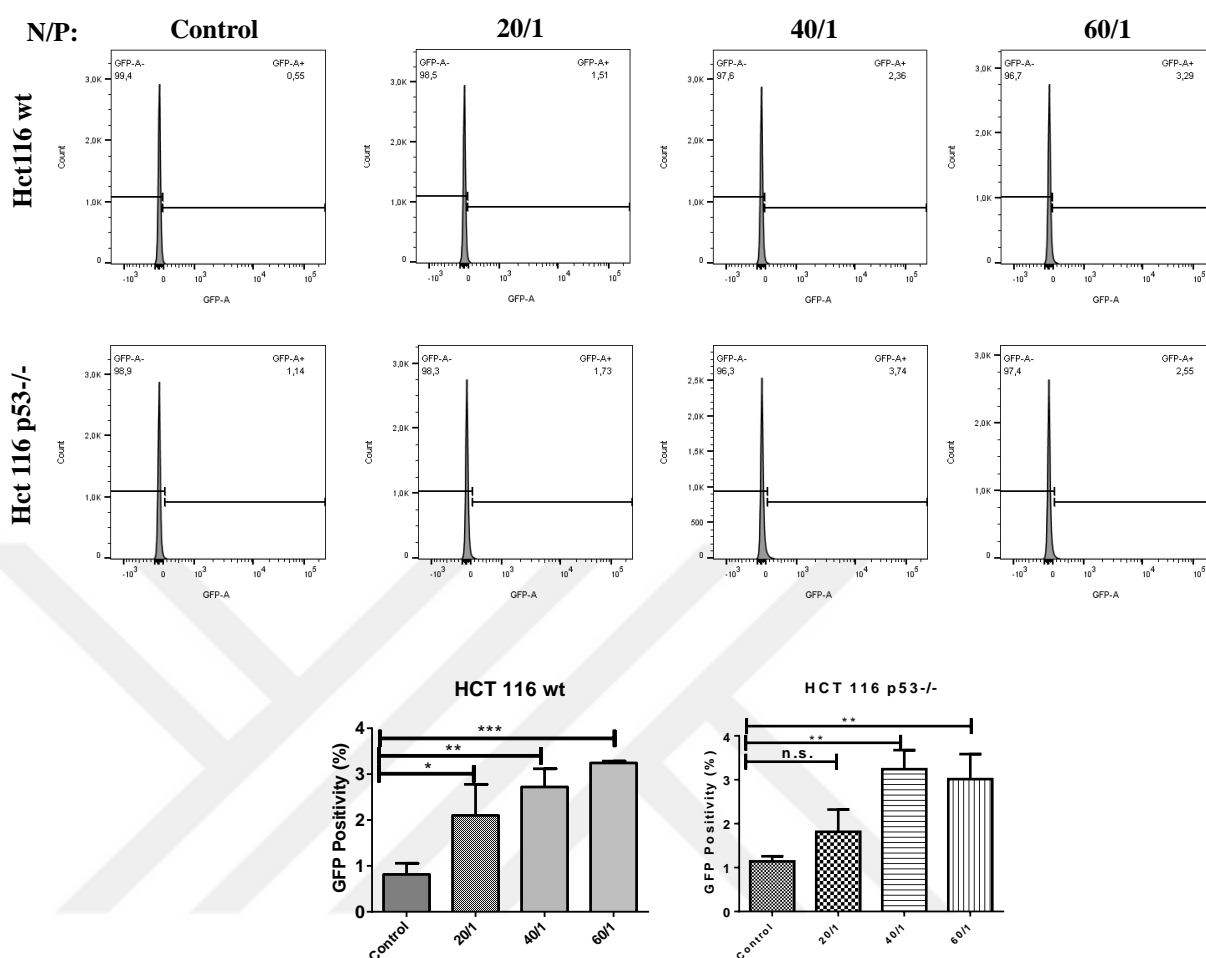


Figure 3. 15 Flow cytometry evaluations of transfection efficiencies of HCT 116 wt and HCT 116 p53^{-/-} cells treated with p53-GFP /mPEG-Ag₂S QDs in different N/P ratios. Values are means mean \pm S.D. ($n=3$), ($p < 0.05$ (*), $p < 0.01$ (**)).

3.4 Conclusion

In this study, PEI/2MPA coated cationic Ag₂S QDs were PEGylated to increase their biocompatibility and blood half-life. The characterization studies revealed that the nanoparticles have high colloidal stability in aqueous medium and strong luminescence in the medical window. Doxorubicin which is one of the mostly used cancer drug was loaded to the PEGylated particles to evaluate the QDs as a cancer drug delivery agent. The biological applications showed a remarkable increase in biocompatibility of particles after PEGylation and high internalization by HeLa cells. In addition, toxicity studies performed with free DOX in HCT 116 cells demonstrated that DOX loaded mPEG-Ag₂S

QDs were as effective as free drug. PI cell cycle and western blot analyses showed that these DOX loaded nanocarriers induce apoptosis in the cells. DOX-loaded QDs had an IC₅₀ around 2.5 $\mu\text{g Ag/mL}$ (containing 1.05 $\mu\text{g/mL DOX}$) in HeLa but about 25 % viability at the same dose in MCF-7. The transfection studies indicated low transfection level with QDs. This decrease is a result of PEGylation of the nanoparticles, although their biocompatibilities increase after PEG. This study is a part of an ongoing project and in the next steps, the PEG amount of particles will be decreased without causing any significant decrease in biocompatibility of the nanoparticles and a targeting ligand will be conjugated to QDs to increase drug accumulation in cancer cells.



Chapter 4

4. EVALUATION OF PEI/AMINO ACID COMBINATIONS AS A COATING AND DEVELOPMENT OF PEI/L-CYSTEINE COATED CATIONIC Ag₂S QUANTUM DOTS AS THERANOSTIC NANOPARTICLES

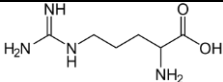
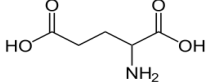
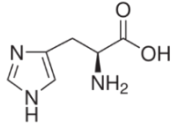
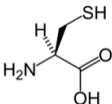
4.1 Introduction

In an effort to combine imaging and therapy, cationic QDs that can effectively condense and carry genes, and allow tracking the destiny of the transfection vehicle and the outcome of the therapy, are desired. Polyethyleneimine (PEI) (25 kDa, branched) is the most efficient and widely used cationic polymer in gene transfection, but has significant toxicity [208, 209]. As shown in Chapter 2, Ag₂S NIRQDs with PEI (25 kDa, branched) and 2MPA mixed coating have the highest reported QY in the literature for Ag₂S QDs. They generated strong intracellular optical signal and provided efficient transfection of green fluorescence protein (GFP) [181]. Hence, proposed strategy has worked successfully. PEI in the coating provides gene binding and delivery potential and 2MPA provides the strong luminescence in such a composition. As the 2MPA amount increased, the luminescence intensity increased. Without 2MPA, PEI coated Ag₂S did not show any luminescence, most probably due to crystal surface defects. But, the Ag₂S NIRQDs with the mixed coating had stronger emission than Ag₂S coated only with 2MPA, and improved cytocompatibility compared to PEI, indicating a synergy.

Yet, a broad range of coating compositions could not be studied due to limitations in stability above 40 mol % 2MPA.

Here, we aimed to decrease the toxicity of PEI coated Ag₂S QDs by using lower molecular weight (25kDa to 1.8 kDa MW) branched PEI and aminoacids (aa) instead of 2MPA. High molecular weight PEI (above 25 kDa) is an effective transfection agent however suffer from toxicity. As the molecular weight decreases, toxicity but also transfection efficiency decreases. When attached on particle surface, short PEI chains may act like a high molecular weight polymer providing a good transfection efficiency with low toxicity. Application of amino acids as a coating material may also be useful on tunability of the surface charge, toxicity and optical properties of quantum dots. In order to achieve this task, Ag₂S QDs were synthesized with different molecular weight of PEI using various types of aminoacids such as l-arginine, l-cysteine, l-histidine and l-glutamic acid. These amino acids differ from each other in terms of their functional groups and particle binding sites (Table 4. 1). So, in this chapter, influence of the PEI MW, amino acid type, the ratio of the two as well as reaction parameters on the final properties of cationic Ag₂S QDs are discussed with an ultimate goal of size tunability, strong NIR emission with improved cytocompatibility and transfection efficiency over that of PEI/2MPA Ag₂S. For gene transfection, GFP and GFP-p53 were used. *In vitro* and *in vivo* imaging properties were also investigated.

Table 4. 1 Structures and pKa values of amino acids used as coating in the study [210].

Amino acids	Chemical Structure	pKa			Isoelectric point
		α - carboxylic acid	α -amino	α -side chain	
L-arginine		2.01	9.04	12.48	10.76
L-glutamic acid		2.10	9.47	4.07	3.22
L-histidine		1.82	9.17	6	7.59
L-cysteine		1.96	10.2	8.15	5.07

4.2 Materials and methods

4.2.1 Materials

Silver nitrate (AgNO₃) and Cys, were obtained from Sigma-Aldrich (USA). L-histidine was obtained from TCI. L-arginine, l-glutamic acid, thioacetamide (TAA), sodium hydroxide (NaOH), ethanol and acetic acid (CH₃COOH) were purchased from Merck. Branched polyethylenimine (PEI) (Mw 25 kDa) was provided by Aldrich (Germany). 1.8 kDa and 10 kDa PEI were obtained from Polysciences, Inc. (Germany). LDS 798 Near-IR laser dye was provided from Exciton Inc. Ultra-pure water (MilliQ, Millipore, 18.2 MΩ cm) was used for the preparation of all aqueous solutions.

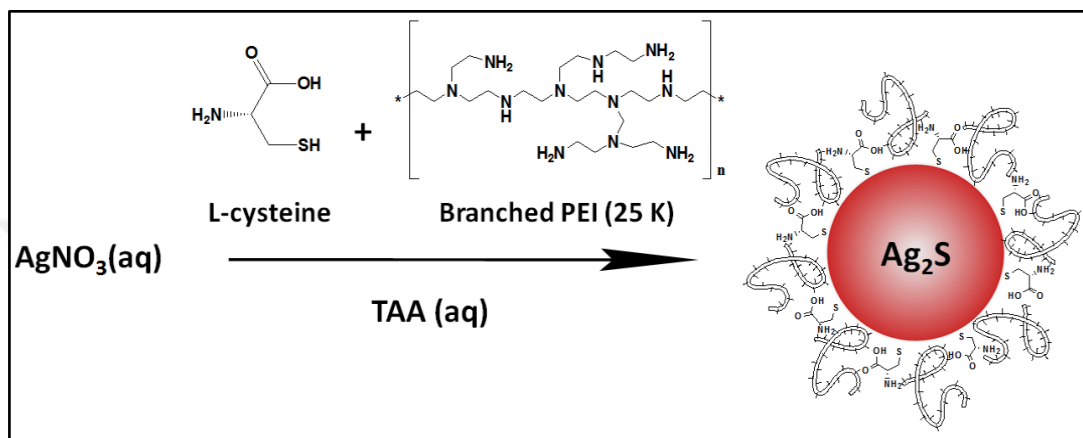
Roswell Park Memorial Institute (RPMI) 1640 medium (with l-glutamine and 25 mM HEPES) was obtained from Multicell, Wisent Inc. (Canada). Fetal bovine serum was purchased from Capricorn Scientific GmbH (Germany). Trypsin-EDTA and penicillin-streptomycin solutions were provided from Wisent Inc. (Canada). Thiazolyl blue tetrazolium bromide (MTT) and phosphate buffered saline (PBS) tablets were obtained from Biomatik Corp. (Canada). Paraformaldehyde solution 4 % in PBS was purchased from Santa Cruz Biotechnology, Inc. (USA). 6-well and 96-well plates were purchased from Nest Biotechnology Co. Ltd. (China). Dimethyl sulfoxide Hybri-Max™ and 4',6-diamidino-2-phenylindole (DAPI) were provided by Sigma (USA). HeLa (human epithelial carcinoma cell line) cells were given as a gift from the Gozuacik Lab (Sabanci University, Istanbul, Turkey) for this study. Mice were purchased from Koç University Animal Research Facility (Istanbul, Turkey). All chemicals were analytical grade and used without any purification.

4.2.2 Preparation of PEI and amino acid coated Ag₂S QDs

For a typical synthetic procedure, desired amounts of PEI and aminoacids were dissolved in the 75 ml of deoxygenated water, under argon flow, then 42.5 mg of AgNO₃ (0.25 mmol) was added to this solution (*e.g.* Scheme 4. 1). The pH of the solution was adjusted to the point where the solution is clear, using NaOH (2 M). Thioacetamide (TAA) in an amount appropriate for the desired Ag/S ratio (*e.g.* 4.7 mg, 0.0625 mmol for Ag/S ratio=4/1) was dissolved in 25 ml of deoxygenated water, separately and added to the initial solution under vigorous mechanical stirring (5000 rpm). The particle growth

was followed by absorption and emission spectrum of the aliquots taken from the reaction at different time points.

This reaction procedure was repeated with 25kDa, 10 kDa and 1.8 kDa MW of PEI and aminoacids such as l-arginine, l-histidine, l-glutamic acid and l-cysteine (Cys) in different reaction conditions to obtain stable and luminescing particles.



Scheme 4. 1 Aqueous synthesis of PEI/Cys Ag₂S NIRQDs.

4.2.3 Preparation of PEI and Cys coated Ag₂S QDs

The detailed characterization studies were performed with PEI-25 kDa/Cys coated Ag₂S QDs depending on the results obtained with PEI in different MWs and aminoacids in various types as shown in results and discussion section of this chapter.

The synthetic procedure is as explained above and shown in Scheme 4. 1. Here, the impact of reaction variables such as PEI/Cys, coating (PEI and Cys)/Ag, Ag/S, reaction temperature and reaction duration on the optical properties and stability of the Ag₂S QDs was studied. Table 4. 10 lists all PEI/Cys ratios used for the synthesis of Ag₂S QDs at fixed Ag/S (=4), coating (PEI/Cys)/Ag (=5), reaction pH (=10.5) at 70°C in 1h reaction. Here, moles of coating is equal to the total number of moles of 1° and 2° amines coming from PEI and thiol coming from Cys. This is based on the stronger affinity of the thiol to Ag₂S than the amine in Cys and the assumption that primary and secondary amines of PEI would be more effective in binding to Ag₂S surface. Hence, the PEI/Cys mol ratio is equal to the total number of moles of primary and secondary amines of the branched PEI (25kDa)/moles of thiol coming from Cys. So, when 100 % PEI was used as a coating

at the coating/Ag ratio of 5, the amount of PEI used brought in total of 1.25 mmol primary and secondary amines in total. In a mixed coating, such as 60 % PEI and 40 % Cys, amounts of each material was adjusted to provide 0.75 mmol amine (primary and secondary) coming only from PEI and 0.50 mmol thiol coming from Cys. To study the effect of coating/Ag ratio independently, other parameters were fixed at Ag/S=4, pH=10.5 at 70 °C for 1h reactions. Studied ratios were listed in Table 4. 11. The effect of the Ag/S ratio on the properties of Ag₂S QDs were studied at fixed Ag⁺ concentration (0.25 mmol) by changing the number of moles of thioacetamide between 0.025 mmol (for Ag/S, 10/1) and 0.50 mmol (for Ag/S, 1/2) keeping all other parameters identical as summarized in Table 4. 12. In order to study the impact of reaction temperature, QD60 synthesis was repeated at different reaction temperatures as listed in Table 4. 13, keeping all other parameters unchanged. QD50 and QD80 was also synthesized at room temperature. The obtained brown quantum dot solutions were washed using Amicon-Ultra centrifugal filters (30000 Da cut off) with deionized water and kept in the dark at 4 °C.

4.2.4 Characterization methods

Absorbance spectra of the quantum dots were measured by a Shimadzu 3101 PC UV-Vis-NIR spectrometer in the 300-1100 nm range. Brus equation was used for the calculation of crystal sizes of the QDs from the absorption edge determined from absorption spectra of the particles (Eq. (1)).

$$\Delta E = \frac{\hbar^2 \pi^2}{8R^2} \left[\frac{1}{m_e} + \frac{1}{m_h} \right] - 1.8 \frac{e^2}{\epsilon_{Ag_2S} 4\pi \epsilon_0 R} \quad (1)$$

R symbolizes the radius of the nanocrystal, m_e (0.286 m_0) and m_h (1.096) show the respective effective electron and hole masses, ϵ_{Ag_2S} (5.95) is the dielectric constant for bulk Ag₂S and ΔE is the band gap energy difference between the nanocrystal and the bulk semiconductor.

Photoluminescence measurements in near-infrared region were performed with a homemade set up composed of a 1/8 Newport Cornerstone 130 monochromator equipped with a 600 L/mm grating that functions in the 400-1100 nm range, a femtowatt sensitive

Si detector (Thorlabs PDF10A, 1.4×10^{-15} W/Hz^{1/2}) and a frequency doubled output of a DPSS laser (532 nm). The slit width was adjusted to 0.2 mm and a 590 nm long pass filter was used in data acquisition.

The microstructure of QDs (QD60-RT) was examined with a transmission electron microscope (TEM, Philips-FEI-Tecnai G2 F30) operating at an accelerating voltage of 200 kV. The hydrodynamic size and zeta potential of the QDs were conducted in water using a Malvern Zetasizer Nano-ZS.

Lifetime of Ag₂S QDs (QD60-RT) in chloroform was measured using Horiba Fluorolog equipped with TCSPC Triple Illuminator. 456 nm Horiba Nanoled pulsed diode light source (pulse duration 1.2 ns) was used.

Ag amount in QD solutions was quantified by Agilent 7700x Inductively Coupled Plasma Mass Spectrometry (ICP-MS) after digestion of QDs with suprapur nitric acid 65 % and suprapure sulphuric acid 96 %. Amount of the organic content of QDs was measured on a TG/DTA (SII EXSTAR 6300) under argon gas flow from room temperature to 600 °C at the heating rate of 10 °C/min. Organic elemental analyses of QDs were conducted with a CHNS/O Analyzer (Thermo Scientific Flash 2000 Organic Elemental Analyzer) to determine the S and N content of the coating. In each test 2-3 mg dried sample was loaded in to a tin capsule with the addition of vanadium pentoxide which is a typical “oxygen donor” that allows the total conversion of sulphur. Then, the capsules were placed on the combustion reactor via the Thermo Scientific MAS 200R autosampler. The standard 2,5-bis-(5-tert-butyl-2-benzooxazol-2-yl) thiophene (BBOT) was used to draw calibration curve.

FTIR spectrum was recorded on a Thermoscientific Nicolet iS10 instrument (ATR-FTIR) in the wavenumber region from 650 to 4000 cm⁻¹ with resolution 1 cm⁻¹. For XPS measurements Thermo Scientific K-Alpha XPS with Al K-alpha monochromatic radiation (1486.3 eV) was used. Dried samples (QD60-RT) were placed on an adhesive carbon tape and exposed to 400 μm X-ray spot size with 50.0 eV pass energy corresponding to a resolution of roughly 0.5 eV. The experimental pressure and the base pressure were kept below about 1×10^{-7} mbar and 9×10^{-9} mbar, respectively. All spectra were corrected with respect to C1s peak at 284.5 eV.

4.2.5 Cell culture

All culture media were supplemented with 10 % fetal bovine serum and 1 % penicillin-streptomycin. HeLa cells were cultured in RPMI 1640 complete medium, supplemented with 10 % FBS and 1 % penicillin–streptomycin antibiotic solution, in a 5 % CO₂-humidified incubator at 37 °C.

4.2.6 Cytotoxicity assay

Cytotoxicity of the bPEI (25kD)/Cys was evaluated using the colorimetric MTT metabolic activity assay. HeLa cells growing in log phase were seeded into a 96-well plate at a density of 7500 cells/well and cultured at 37 °C in an atmosphere of 5 % CO₂. After overnight incubation, the medium was replaced with a fresh medium containing Ag₂S quantum dots in concentrations of 0.8-10 µg/mL Ag as determined by the ICP analysis of the particles. Cells with no treatment were used as controls. After 24 h incubation, the medium was discarded and cells were washed with 1× PBS, pH 7.4. 50 µL of MTT reagent (5 mg/mL) and 150 µL medium were added to each well. Purple formazan crystals formed after 4 hours in each well were dissolved with ethanol:DMSO (1:1 v/v) solution shaking gently for 15 min. A microplate reader (BioTek ELx800 Absorbance Microplate Reader) was used to record the absorbance intensity at 600 nm with a reference wavelength of 630 nm. Untreated cells were taken as positive controls under the assumption of 100 % viability and treated cells without MTT reagent were used for the correction of absorbance intensities ($n = 8$). The relative cell viability was calculated as $[A_{\text{sample}}/A_{\text{control}}] \times 100$.

4.2.7 *In vitro* cell imaging

The *in vitro* cell imaging of Ag₂S QDs was performed on an Inverted Life Science Microscope (Olympus-Xcellence RT Life Science Microscopy). HeLa cells were grown on a 6-well plate at a density of 1.5×10^5 cell/ well in complete RPMI 1640 medium, incubated at 37 °C under 5 % CO₂ for 12 hours. Ag₂S QDs at 10 µg/mL Ag dose were introduced to the cells and after 1 hour incubation, the cells were washed with 1× PBS three times to remove QDs in the medium. Then, the cells were fixed using paraformaldehyde solution (4 % in PBS) for 20 min, and

after being washed three times, the nuclei were stained with a fluorescent dye, DAPI. The washing step was repeated for three times and 2 mL PBS was left in each well to protect the cells against drying. The fixed cells were visualized by inverted Life Science Microscope using specific filters for nuclei and NIR emitting QDs: DAPI region (λ_{exc} : 352-402 nm and λ_{em} : 417-477 nm) and NIR region (λ_{exc} : 550 nm and λ_{em} : 650 nm long pass), respectively. Same experimental process was performed with control cells. Images were processed and merged using ImageJ analysis program [202].

4.2.8 *In vivo* imaging

The *in vivo* imaging of Ag₂S QDs in NIR region were performed using BALB/c mouse purchased from Animal Research Laboratory of Koc University. All experiments were performed according to the protocols approved by Koc University Animal Research Local Ethics Committee. 2.25 mg of PEI/Cys coated Ag₂S QDs (QD60-RT) (15 mg/ml in PBS) were administered to the mouse (27 g) by intraperitoneal injection. 1 h after injection, mouse was anesthetized with 2.5 % isofluorane in oxygen and transferred to a Perkin Elmer IVIS[®] Lumina III In Vivo Imaging System (excitation: 740 nm, emission filter: 840 nm long-pass). An untreated mouse weighting 25 g was also imaged to determine the background signal.

4.2.9 *In vitro* transfection studies

GFP and p53-GFP plasmids were obtained using standard microbiology protocols as shown Figure 3. 4. pDNA and QD complexes were prepared at different N/P ratios and different concentrations in OPTI-MEM serum reduced medium for 20 min at room temperature and introduced into the cells. HeLa, MEF p53^{-/-} and MEF p53 wt cells were used in the study. Images were recorded using an inverted fluorescence microscope equipped with appropriate filters for NIR, DAPI and GFP signals.

HeLa cells were seeded at a density of 25000 cells per well in a 24-well plate in RPMI 1640 complete medium, supplemented with 10 % FBS and 1 % pen-strep. After incubation of the cells at 37 °C in 5 % CO₂ for one day, HeLa cells were treated with

different concentrations of QD/pGFP complexes prepared at 15/1 N/P (nitrogen/phosphorus) ratio for 48 hours and transfection efficiency was followed by fluorescence microscopy of fixed cells. Table 4. 2 shows the formulation of plasmid-nanoparticle complexes used for transfection studies.

Table 4. 2 QD and plasmid DNA concentrations used in the transfection studies.

Concentrations	PEI/cys Ag ₂ S (µg/mL)	pDNA (µg/mL)
Conc 1	2.36	0.5
Conc 2	4.71	1
Conc 3	7.07	1.5
Conc 4	9.42	2

For transfection of MEF cells, cells were seeded at a concentration of 30000 cell per well in 24-well plate, first day, as explained above and the images were recorded after the cells were incubated with the complexes for 48 h. The transfection in MEF cells was repeated with different N/P ratio keeping nanoparticle amount as 2.36 µg/mL.

4.2.10 Statistical analysis

For statistical analysis, one-way ANOVA with Tukey's multiple comparison test of GraphPad Prism 6 software package from GraphPad Software, Inc., USA was used. All data expressed as mean ± standard deviation (SD), and p<0.05 was considered statistically significant.

4.3 Results and Discussion

4.3.1 Influence of PEI molecular weight and amino acids on Ag₂S QDs

To investigate the influence of molecular weight of PEI and types of amino acids on the optical properties and colloidal stability of Ag₂S QDs, 25-10-1.8 kDa PEI and amino acids such as l-arginine, l-glutamic acid, l-histidine and l-cysteine were used. Each combination with the details of the reaction parameters is listed below.

4.3.1.1 PEI-25 kDa Ag₂S QDs

4.3.1.1.a L-arginine and l-arginine/PEI (branched, 25 kDa) Ag₂S QDs

Arginine was used as coating material to synthesize Ag₂S QDs. However, the results showed that Ag₂S QDs precipitate in these conditions. This means that use of only arginine for coating is not enough to stabilize the surface and can not provide colloidal stability to particles. Then, the same conditions were repeated with CdS QDs to control reaction parameters but again the results were same. Mixed coating composed of PEI-25 kDa and l-arginine, was successful but the luminescence intensity of obtained Ag₂S QDs were quite low (Table 4. 3).

Table 4. 3 Synthesis conditions of l-arginine and l-arginine/branched PEI-25 kDa coated Ag₂S QDs.

Rxn Code	Coating/Ag/S mol ratio	Sulphur source	PEI-25 kDa / Arg (mol/mol)	pH _i ^a	pH _f ^b	Temperature (°C)	Result
DAA_01	20/4/1	Na ₂ S	0/100	9.5	10	RT	Precipitation
DAA_05	20/4/1	TAA	0/100	9.50	9.50	70	
DAA_06	20/4/1	TAA	80/20	9.60	10.5	70	Colloidally stable particles with low luminescence
DAA_08	5/1/2	TAA	8/20	9.50	9.50	70	

^a pH before sulphur source. ^b pH after sulphur source. RT : Room temperature.

4.3.1.1.b L-Glutamic acid and l-glutamic acid /PEI (branched, 25 kDa) Ag₂S QDs

After arginine, glutamic acid was used to stabilize Ag₂S QDs. The reaction parameters are listed in Table 4. 4 were studied, separately. Similar to l-arginine, l-glutamic acid needed PEI to form stable colloids but no luminescence was detected.

Table 4. 4 Synthesis conditions of glutamic acid and glutamic acid/branched PEI-25 kDa coated Ag₂S QDs.

Rxn Code	Coating/Ag/S mol ratio	Sulphur source	PEI-25 kDa / Glu (mol/mol)	pH _i ^a	pH _f ^b	Temperature (°C)	Result
DAA_09	20/4/13	TAA	0/100	3.50	8.00	60	Precipitation
DAA_10	20/4/1	TAA	0/100	3.50	8.00	70	Precipitation
DAA_11	20/4/1	TAA	80/20	6.50	10.50	50	Colloidally stable particles with low luminescence
DAA_12	20/4/1	Na ₂ S	80/20	6.50	10.50	RT	
DAA_13	20/4/1	Na ₂ S	0/100	3.50	10.20	RT	
DAA_14	20/4/1	Na ₂ S	60/40	5.20	10.00	RT	
DAA_18	9.6/4/1	Na ₂ S	60/40	6.50	10.00	RT	
DAA_19	20/4/1	Na ₂ S	80/20	6.90	10.00	RT	
DAA_20	20/4/1	TAA	80/20	6.60	10.00	RT	
DAA_31	20/4/1	TAA	0/100	3.50	10.00	RT	
DAA_32	20/4/1	TAA	60/40	5.20	10.00	RT	

^a pH before sulphur source. ^b pH after sulphur source. RT : Room temperature. TAA: Thioacetamide.

4.3.1.1.c L-histidine and l-histidine/PEI (branched, 25 kDa) Ag₂S QDs

L-histidine has an imidazole side chain. Its reactions were performed in different pH conditions considering the pK_a value and isoelectric point of the amino acid (Table 4. 5). However, all conditions resulted in precipitation.

Table 4. 5 Synthesis conditions of l-histidine and l-histidine/branched PEI-25 kDa coated Ag₂S QDs.

Rxn Code	Coating/Ag/S mol ratio	Sulphur source	PEI-25 kDa / Histidine (mol/mol)	Rxn pH*	Temperature (°C)	Result
fd58	20/4/1	TAA	100/0	9.5	RT	Precipitation
fd59	20/4/1	TAA	100/0	7.4	RT	
fd60	24/4/1	TAA	100/0	5.5	RT	
fd61	20/4/1	TAA	60/40	9.5	RT	
fd62	20/4/1	TAA	80/20	5.5	RT	
fd63	20/4/1	TAA	60/40	11.0	RT	

*Reaction pH was adjusted before sulphur addition. TAA: Thioacetamide. RT: Room temperature.

4.3.1.1.d L-cysteine and l-cysteine/PEI (branched, 25 kDa) Ag₂S QDs

This formulation produced colloiddally stable and highly luminescing QDs. The details were explained in the following sections of this chapter.

4.3.1.2 PEI-10 kDa Ag₂S QDs

4.3.1.2.a PEI (branched, 10 kDa) coated Ag₂S

To investigate the influence of PEI-10 kDa coating and obtain optimum conditions before amino acid addition, the reactions were performed only with the polymer (Table 4. 6). At the synthesis conditions where different coating and core ratios were used, particles gave no emission, but they were colloiddally stable.

Table 4. 6 Synthesis conditions of branched PEI-10 kDa coated Ag₂S QDs.

Rxn Code	Coating/Ag/S mol ratio	Sulphur source	pH*	Temperature (°C)	Result
fd74	25/2.5/1	TAA	9.5	RT	Colloidally stable particles with no luminescence
fd75	12.5/2.5/1	TAA	9.5	RT	
fd76	20/4/1	TAA	9.5	RT	
fd77	30/6/1	TAA	9.5	RT	

*Reaction pH was adjusted before sulphur addition. TAA: Thioacetamide. RT: Room temperature.

4.3.1.2.b PEI (branched, 10 kDa)/l-cysteine Ag₂S QDs

Particles were synthesized with PEI-10 kDa and l-cysteine mixed coating at different conditions as summarized in Table 4. 7. However, colloidally stable particles were not obtained.

Table 4. 7 Synthesis conditions of branched PEI-10 kDa/l-cysteine Ag₂S QDs.

Rxn Code	Coating/Ag/S mol ratio	Sulphur source	PEI-10 kDa / Cys (mol/mol)	pH*	Temperature (°C)	Result
fd68	20/4/1	TAA	60/40	10.5	RT	Precipitation
fd69	44/4/1	TAA	82/18	8.5	RT	
fd70	40/4/2	TAA	90/10	8.5	RT	
fd71	27.8/2.6/1	TAA	94.6/5.4	9.5	RT	
fd72 (at open air)	27.8/2.6/1	TAA	94.6/5.4	9.5	RT	
fd73	25/2.5/1	TAA	80/20	9.5	RT	

*Reaction pH was adjusted before sulphur addition. TAA: Thioacetamide. RT: Room temperature.

4.3.1.2.c PEI (branched, 10 kDa)/2MPA Ag₂S QDs

As explained above, arginine, glutamic acid and histidine were not successful in stabilizing Ag₂S QDs alone. Hence, the reactions were repeated with 2MPA instead of these amino acids because of the excellent properties of PEI-25 kDa/2MPA coated Ag₂S QDs (Chapter 2). Next, the influence of PEI MW was studied. Reactions are summarized in Table 4. 8. Again, colloiddally stable but non-luminescing particles were obtained. The results are significant to understand the effect of molecular weight of PEI. Capturing of the Ag₂S surface with 10 kDa PEI was sufficient to suspend particles in water but a dense packing resulting in complete passivation of the crystal surface was not achieved, hence no luminescence was obtained. Yet, PEI 25 kDa effectively passivate the surface and provide colloidal stability.

Table 4. 8 Synthesis conditions of branched PEI-10 kDa/2MPA Ag₂S QDs.

Rxn Code	Coating/Ag/S mol ratio	Sulphur source	PEI-10 kDa / 2MPA (mol/mol)	pH*	Temperature (°C)	Result
fd78	20/4/1	TAA	60/40	10.5	RT	Colloiddally stable particles with no luminescence
fd79	20/4/1	TAA	80/20	11.0	RT	
fd81	20/4/1	Na ₂ S	60/40	10.5	RT	
fd82	20/4/1	TAA	60/40	10.5	50	

*Reaction pH was adjusted before sulphur addition. TAA: Thioacetamide. RT: Room temperature.

4.3.1.3 PEI-1.8 kDa Ag₂S QDs

4.3.1.3.a PEI (branched, 1.8 kDa)/cysteine Ag₂S QDs

To further investigate the effect of MW on Ag₂S QDs, the reactions were repeated with PEI 1.8 kDa using l-cysteine as a co-coating at different conditions (Table 4. 9). However, all particles were precipitated.

Table 4. 9 Synthesis conditions of branched PEI-1.8 kDa/l-cysteine Ag₂S QDs.

Rxn Code	Coating/Ag/S mol ratio	Sulphur source	PEI-1.8 kDa / l-cys (mol/mol)	pH*	Temperature (°C)	Result
fd51	20/4/1	TAA	60/40	10.5	RT	Precipitation
fd52	20/4/1	TAA	60/40	10.5	50	
fd53	20/4/1	TAA	60/40	10.5	70	
fd54	20/4/1	TAA	60/40	10.5	90	
fd55	20/4/1	Na ₂ S	60/40	10.5	RT	

*Reaction pH was adjusted before sulphur addition. TAA: Thioacetamide. RT: Room temperature.

4.3.1.3.b PEI (branched, 1.8 kDa)/2MPA Ag₂S QDs

The reaction was also repeated with 2MPA, but the results were indifferent.

4.3.2 Synthesis and optical characterization of PEI/Cys Ag₂S QDs

L-cysteine/PEI (branched, 25 kDa) coated Ag₂S QDs were demonstrated colloiddally stable particles with excellent luminescence quality and cationic structure. These near IR emitting Ag₂S QDs were prepared directly in water from AgNO₃ and TAA using branched 25 kDa PEI and Cys as a mixed coating. The reaction variables were studied to evaluate the emission tunability and the effects on particle properties with a motivation to find the best composition and size for high cytocompatibility and strong emission. All reaction mixtures were set to pH 10.5 before the addition of TAA, in order to deprotonate the amine groups of PEI and Cys and obtain a clear solution. However, after the purification steps, all aqueous QD solutions were adjusted to pH 7.4 to prevent any pH effect on the photoluminescence of QDs, for the purpose of comparison.

The organic coating passivates the surface of the growing crystal and often is effective in controlling the crystal size. Yet, it is also responsible from colloidal stability and surface quality. The later impacts the luminescence intensity and quantum yield dramatically. PEI coated Ag₂S QDs were colloiddally stable but did not luminesce in near IR region (Figure 4. 2e). Polymeric coatings are usually

inferior to small thiolated molecules since they lack dense packing on the crystal surface leaving uncoordinated sites, hence do not provide strong luminescence. On the other hand, polymers provide enhanced colloidal stability due to multidentate binding [181]. However, addition of Cys along with PEI provided both strong luminescence and colloidal stability as in the case of PEI/cys (Figure 4. 1a). Cys binds to crystal surface strongly with the thiol and since it is a small molecule, it can diffuse to the crystal surface and passivate the uncoordinated sites left behind by PEI.

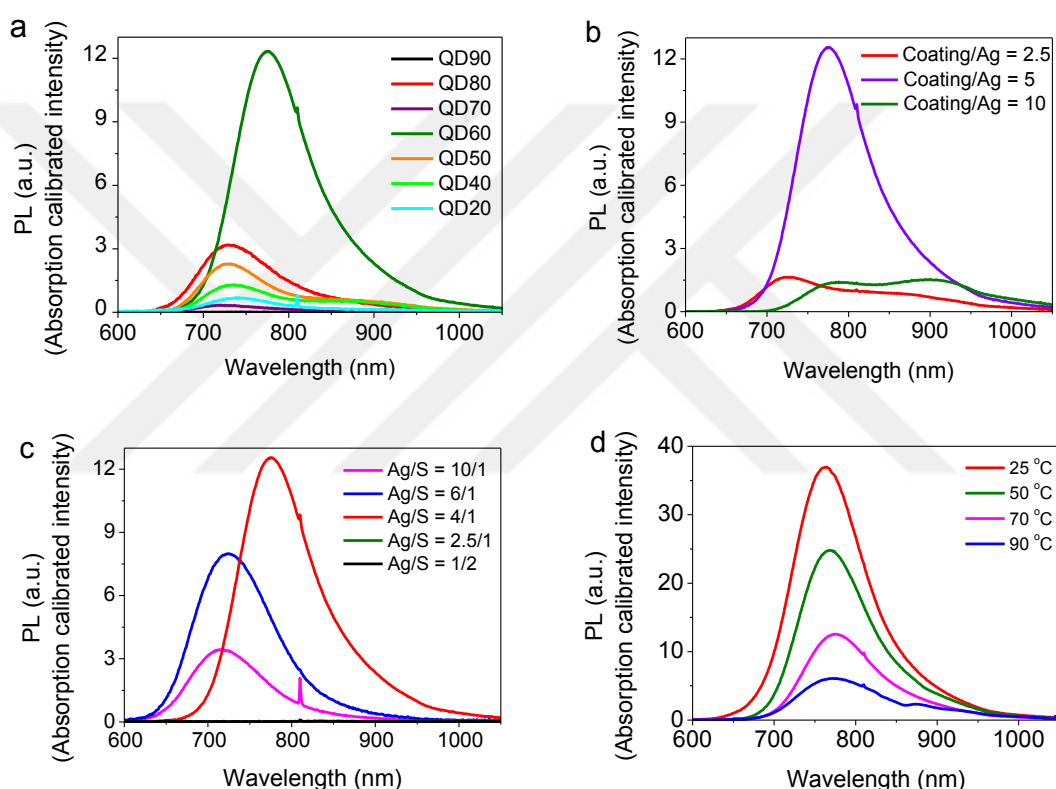


Figure 4. 1 Photoluminescence spectra of PEI/Cys coated Ag₂S QDs synthesized at (a) different PEI/Cys ratios, (b) Ag/coating (PEI + Cys), (c) Ag/S mole ratios and (d) at different temperatures.

To investigate the effect of coating composition, PEI/Cys ratio was varied keeping the total Ag/coating ratio constant at 1/5. Cys was effective in generating different compositions and incorporated between 10-80 mol %. Overall, all particles with the mixed coating had absorption onset at shorter wavelengths than PEI coated Ag₂S QD, indicating smaller crystal size possibly due to the presence

of strongly binding small Cys which prevented crystal growth and strong luminescence due to better surface passivation (Table 4. 10). 10 mol % Cys in the coating formulation shifted the absorption onset to shorter wavelength indicating smaller crystals but was not sufficient enough to provide detectable luminescence.

All other mixed coatings provided luminescent QDs. By changing the coating composition it was possible to tune the emission between 725 to 775 nm with a full-width at half-maximum (FWHM) of around 100 nm which is relatively narrow compared to other aqueous Ag₂S QDs. With increasing Cys amount up to 30 mol %, crystal size decreased from 3.12 to 2.50 nm shifting the emission maxima to shorter wavelengths. Beyond 40 mol %, emission peaks shifted slightly to longer wavelengths again. For the comparison, Ag₂S coated only with Cys was prepared under identical conditions. Interestingly, Cys-Ag₂S QDs synthesized under these conditions are the largest ones with no significant luminescence (Table 4. 11e). Thus, there is a clear synergy in the combination of these two coating materials which results from different growth kinetics and different binding types. From a broader perspective, all Ag₂S QDs had emission maxima between 725-740 nm. QD60-70 with emission max at 775 nm showed more than four times stronger intensity than the others. Interestingly, excluding the 60/40 ratio, in general the luminescence intensity decreased with the increasing amount of Cys which is opposite to what was seen with PEI/2MPA coating [181]. Cys coated Ag₂S has a featureless absorption profile, whereas all QDs with mixed coatings have a clear first excitonic peak (Figure 4. 2) and significant luminescence with Stoke's shift which is about 100 nm or less.

All Ag₂S QDs with PEI in the coating had positive zeta potential, between +28-63 meV (Table 4. 10), which is good for binding negatively charged species such as drugs and oligonucleotides and for colloidal stability due to charge repulsion [211, 212].

Hydrodynamic sizes of these Ag₂S QDs are all below 100 nm and mostly below 50 nm which is very valuable for long blood circulation time and molecular targeting in the *in vivo* use of such particles. Several studies have reported that optimal size range should be in between 10-100 nm for *in vivo* applications of a particle [213]. Larger particles (>

200 nm) accumulate in the spleen and are processed by the phagocytic cells or by the macrophages in blood [214], while smaller particles (< 10 nm) undergo a rapid renal clearance [215].

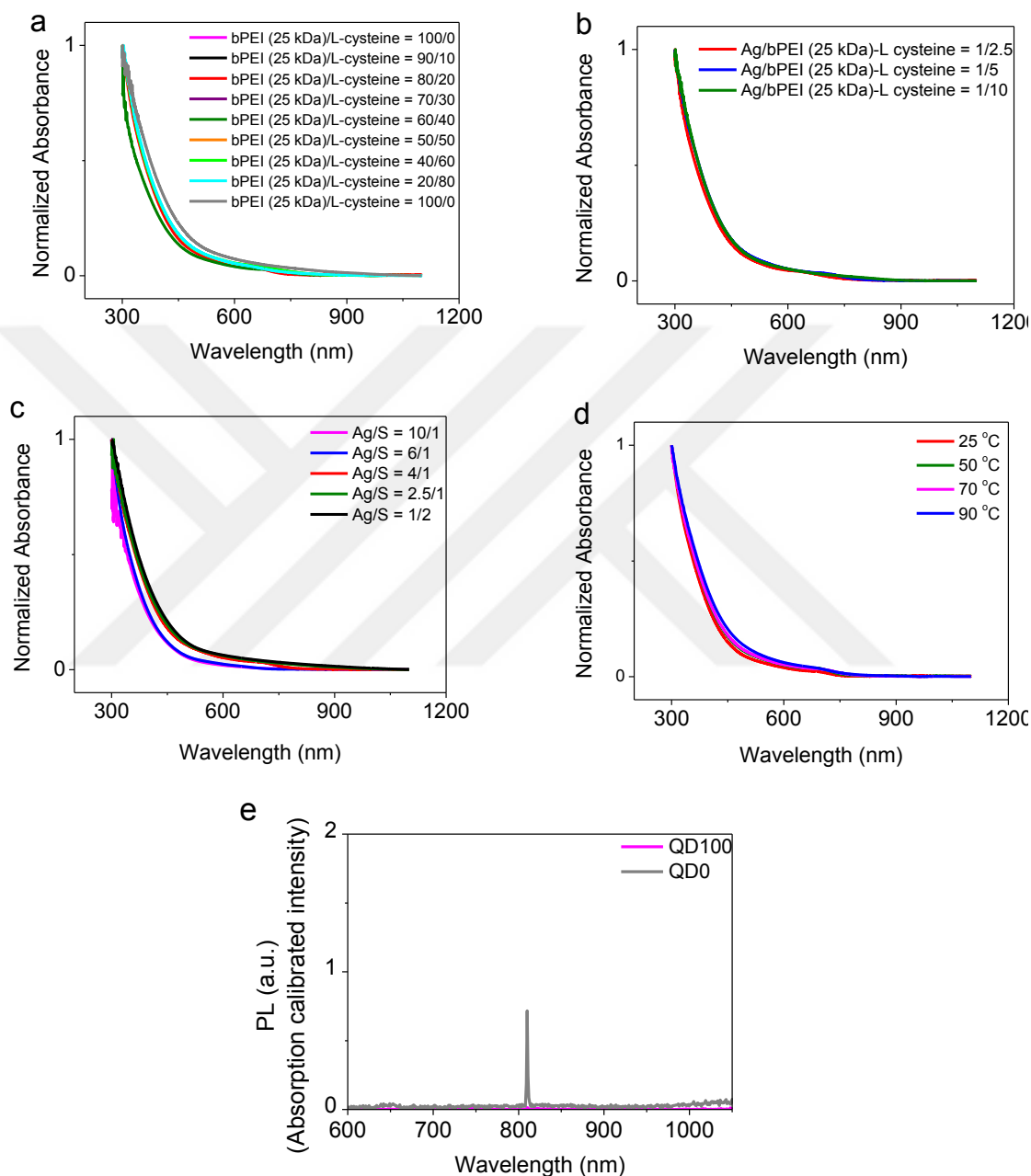


Figure 4. 2 Absorbance spectra of PEI/Cys coated Ag₂S QDs synthesized at different PEI/Cys (a), Ag/coating (PEI and Cys) (b) Ag/S mole ratios (c), temperature (d) and photoluminescence spectra of QD100 and QD0 (e).

Table 4. 10 Effect of the PEI/Cys ratio on the properties of Ag₂S QDs.

Rxn Code	PEI/Cys (mol %)	λ_{em} (_{max}) (nm)	Size ^a (nm)	Band gap (eV)	λ_{abs} (_{cutoff}) ^b (nm)	FWHM (nm)	Dh ^c (nm)	Zeta pot. (mV)
QD100-70	100/0	-	3.12	1.30	955	-	26.5 ± 4.1	41.2 ± 1.2
QD90-70	90/10	-	2.70	1.48	837	-	9.2 ± 0.8	41.2 ± 2.0
QD80-70	80/20	731	2.52	1.60	779	106	10.6 ± 1.2	45.8 ± 1.7
QD70-70	70/30	725	2.50	1.62	768	101	11.1 ± 1.3	41.9 ± 0.7
QD60-70	60/40	775	2.64	1.52	816	105	49.3 ± 14.1	63.6 ± 4.9
QD50-70	50/50	730	2.74	1.47	846	91	10.4 ± 2.7	28.4 ± 1.1
QD40-70	40/60	734	2.73	1.47	844	98	72.6 ± 11.1	44.7 ± 2.2
QD20-70	20/80	740	2.74	1.47	846	93	38.8 ± 6.7	47.3 ± 1.2
QD0-70	0/100	-	3.18	1.28	968	-	69.8 ± 16.7	-31.5 ± 0.8

^a Calculated by Brus equation. ^b Absorbance onset determined from the absorbance spectrum (Fig. S1a). ^c Hydrodynamic diameter measured by DLS and reported as the number average. *Reaction conditions: Ag:S = 4, coating (PEI/Cys):Ag = 5, reaction pH=10.5, T=70 °C, 1h reaction.

Ag₂S QDs prepared with 60/40 PEI/Cys (QD60-70) coating formulation stood out as the most luminescent particle with a strongly cationic nature (+63.6 meV) and small hydrodynamic size (about 50 nm). Hence, keeping PEI/Cys ratio constant at 60/40, the effect of coating amount on particle properties was studied. Total coating/Ag ratio which was initially 5 was changed to 2.5 and 10 (Table 4. 11). Absorption spectra of these three particles indicate (Figure 4. 2b) decreasing band gap with the increasing coating amount and hence, the inorganic core size increases. However, photoluminescence spectra of the QDs with coating/Ag ratio of 2.5 and 10 showed two peak maxima: one in 700-800 nm region and another one around 900 nm which is possibly defect-related emission (Figure 4. 1b) [216]. But, the QD prepared with coating/Ag ratio of 5, has relatively sharper peak centred at 775 nm with dramatically better intensity.

In terms of the hydrodynamic size and zeta potential, all of these three Ag₂S NIRQDs are colloiddally stable and in appropriate size range for *in vivo* applications (Table 4. 11).

Table 4. 11 Effect of coating/Ag ratio on the properties of Ag₂S QD (QD60).*

Coating/Ag (mol/mol)	$\lambda_{em(max)}$ (nm)	Size ^a (nm)	Band gap (eV)	λ_{abs} (cutoff) ^b (nm)	FWHM (nm)	Dh ^c (nm)	Zeta pot. (mV)
2.5	-	2.59	1.55	799	-	48.1 ± 11.1	49.3 ± 2.5
5	775	2.64	1.52	816	105	49.3 ± 14.1	63.6 ± 4.9
10	-	2.87	1.40	886	-	13.2 ± 1.8	46.7 ± 4.0

* Formulation: PEI/Cys=60/40 mol/mol, Ag:S = 4, reaction pH = 10.5, 1h reaction. ^aCalculated by Brus equation. ^b Absorbance onset. ^c Hydrodynamic diameter measured by DLS and reported as the number average.

To tune the crystal size, and therefore emission wavelength of Ag₂S QDs further, different Ag/S ratios between 10/1 and 1/4 were studied using PEI/Cys ratio of 60/40 (QD60-70), at coating/Ag ratio of 5. As shown in Figure 4. 1c and Table 4. 12, decreasing Ag/S ratio causes a red shift in emission maxima from 716 (10/1 Ag/S) to 775 nm (4/1 Ag/S) with enhanced luminescence intensity. At the lower ratios, no detectable luminescence was observed.

Table 4. 12 Effect of the Ag/S on the properties of Ag₂S QDs (QD60)*

Ag	S	$\lambda_{em(max)}$ (nm)	Size ^a (nm)	Band gap (eV)	λ _{abs(cutoff)} ^b (nm)	FWHM (nm)	Dh ^c (nm)	Zeta pot. (mV)
10	1	716	2.30	1.78	698	104	54.0 ± 15.4	68.1 ± 1.5
6	1	724	2.40	1.69	736	108	23.2 ± 3.1	54.3 ± 5.2
4	1	775	2.64	1.52	816	105	49.3 ± 14.1	63.6 ± 4.9
2.5	1	-	3.04	1.33	932	-	13.3 ± 0.8	47.7 ± 3.9
1	2	-	3.13	1.30	955	-	26.2 ± 10.2	41.7 ± 5.1

* Formulation: PEI/Cys=60/40 mol/mol, Ag:S = 4, reaction pH = 10.5, 1h reaction. ^aCalculated by Brus equation. ^b Absorbance onset. ^c Hydrodynamic diameter measured by DLS and reported as the number average.

Reaction temperature is usually a significant factor affecting the growth kinetics and hence the particle size. Particles were tried to be grown to a similar size at different temperatures (keeping the formulation constant). It is clearly seen in Table 4. 13 that as the temperature increased from 25 to 90 °C, crystals grew to relatively similar sizes at shorter times but in the expense of emission intensity (Figure 4. 1d). The quantum yield of QD60-RT, for instance, is 157 % (with respect to LDS-798 NIR dye) (Figure 4. 4) which is the highest value reported for Ag₂S QD until now. Thioacetamide (TAA) is a slow sulphur releasing agent. It decomposes faster at high temperatures into H₂S and acetamide, hence causes faster particle growth. This may produce larger number of defects responsible from non-radiative relaxation processes of the excited photons causing the observed reduction in the emission intensity. At low temperatures, nucleation and growth of the crystals may be slow but are more defect free [217]. Emission peak of the QD prepared at 90 °C is also much broader, may be indicating a broader size distribution and defect related emissions, as well [218].

Table 4. 13 Effect of reaction temperature on the properties of PEI/Cys - Ag₂S QDs.

Rxn Code	(°C)	Reaction Time	λ_{em} (_{max}) (nm)	Size ^a (nm)	Band gap (eV)	λ _{abs(cutoff)} ^b (nm)	FWHM (nm)	Dh ^c (nm)	Zeta pot. (mV)	QY (%)
QD60-RT	25	3 h	763	2.56	1.57	790	104	41.7 ± 3.0	68.6 ± 2.0	157
QD60-50	50	2 h	769	2.58	1.56	795	102	21.8 ± 8.6	38.6 ± 2.4	136
QD60-70	70	1 h	775	2.64	1.52	816	105	49.3 ± 14.1	63.6 ± 4.9	NC ^d
QD60-90	90	30 min	773	2.73	1.47	845	116	40.6 ± 3.8	40.6 ± 1.2	NC ^d

^a Calculated by Brus equation. ^b Absorbance onset determined from the absorbance spectrum (Fig. S1d). ^c Hydrodynamic diameter measured by DLS and reported as the number average. ^d Not calculated *Reaction conditions: Ag:S=4, coating:Ag=5, PEI:Cys=60:40, reaction pH=10.5.

Based on the dramatic increase in the luminescence intensity of QD60 at RT, QD80-70 and QD50-70 were also prepared at RT. Low reaction temperature improved the emission intensity of QD50 as well, but the opposite was seen with QD80. This may be due to slower diffusion of polymeric component at lower temperature, which is critical for growth and adsorption to crystal surface. This may cause more defects on crystal surface hence decrease the amount of radiative coupling. In the final case, three particles (QD80-70, QD60-RT, QD50-RT) with different composition but with strong luminescence at similar wavelengths (Figure 4. 3) were subjected to *in vitro* studies to evaluate the effect of composition on particle toxicity. Their properties are summarized in Table 4. 10, Table 4. 13 and Table 4. 14.

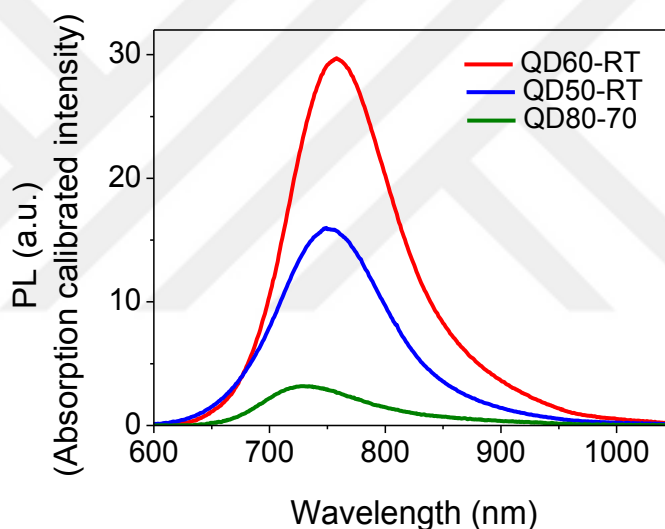


Figure 4. 3 Photoluminescence spectra of the best luminescing PEI/Cys coated Ag₂S QDs.

Table 4. 14 Properties of QD50-RT Ag₂S QDs. *

Rxn Code	T (°C)	Rxn Time	$\lambda_{em(max)}$ (nm)	Size ^a (nm)	Band gap (eV)	λ abs(cutoff) ^b (nm)	FWHM (nm)	Dh ^c (nm)	Zeta pot. (mV)
QD50-RT	25	3h	749	2.73	1.47	843	110	28.2 ± 11.7	48.8 ± 0.2

* Formulation: PEI/Cys=50/50 mol/mol, Ag:S = 4, reaction pH = 10.5. ^aCalculated by Brus equation. ^b Absorbance onset. ^cHydrodynamic diameter measured by DLS and reported as the number average.

In addition, the reactions were repeated with 1.8 kDa and 10 kDa branched PEI, again in combination with Cys, to investigate the molecular weight effect of the polymer on the QD properties. However, no colloiddally stable and luminescent particles were obtained.

Quantum yield calculation: Quantum yield (QY) of the QDs was calculated by comparing the integrated emission of QD solution (in water) with that of a NIR dye (LDS 798 in methanol solution, quantum yield reported as 14 % by the producer). Four different concentrations of QD and the dye solution were prepared with similar absorption (below 0.1) at the excitation wavelength and integrated areas of the emission curves were plotted against the absorbance (Table 4. 13). The ratio of the slope of these plots with the refractive index of water and MeOH based on Eq. (2) gave the QY of the prepared QDs [219, 220].

$$\Phi_{\text{QD}} = \left(\frac{\text{Grad}_{\text{QD}}}{\text{Grad}_{\text{REF}}} \right) \left(\frac{\eta_{\text{water}}^2}{\eta_{\text{MeOH}}^2} \right) \times 100 \quad (2)$$

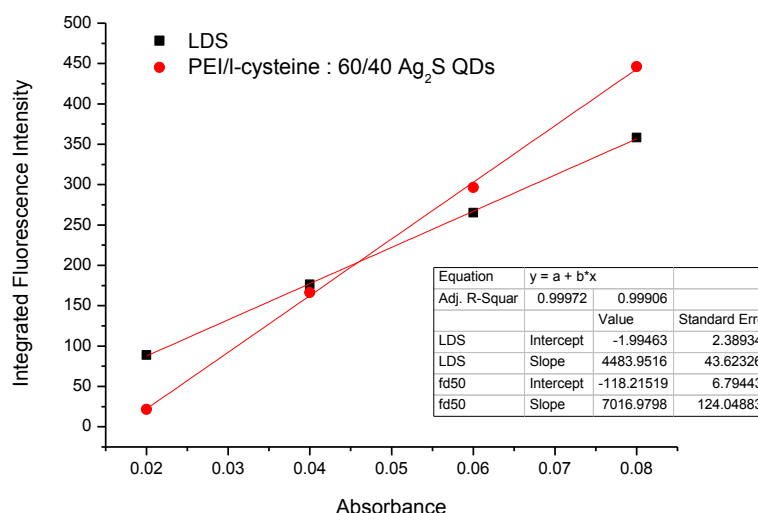


Figure 4. 4 Plot of the the integrated luminescence intensities of the reference dye and Ag₂S QDs against the absorbance. Inset shows the slope of each line corresponding to Ag₂S and dye samples.

4.3.3 Characterization of PEI/Cys coated Ag₂S QDs

Photoluminescent lifetime measurements were performed on QD60-RT, which showed the strongest luminescence. The decay curve found to be multiexponential with an average lifetime calculated as 75.78 ns with 1.096 value of chi-square (Figure 4. 5 and Table 4. 15). This is somewhat similar to literature values [110, 221]. Actually, the fit of the decay curve indicates four different events with 1.55 (1.60 %), 11.66 (17.54 %), 42.17 (45.69 %) and 154.79 (35.17 %) ns lifetimes. Usually, 1 ns and faster decays may be attributed to non-radiative decay [222]. For a 4.5 nm Ag₂S (3-6.5 nm) with emission at 850 nm, biexponential decay with 1 and 11 ns was reported and the later was attributed to the excitonic recombination [222]. In another study, 1.5 nm Ag₂S with emission maxima at 813 nm was reported to have an average lifetime of 57 ns, which was attributed to the radiative decay related to surface inhomogeneities [221]. Zhang et al. reported increasing lifetimes for Ag₂S-dodecanethiol with increasing crystal size [110]. Actually, they have mostly focused on the long lifetime component increasing from 57 to 181 ns as the crystal size increased from 2.4 to 7.0 nm, may be because that was the major component in each case, but they have seen a slow component which was between 11-14 ns for 2.4-3.7 nm and 26-31 ns for 3.6-7.0 nm size Ag₂S. Looking at all of these data, we may suggest that the relatively fast component (around 11 ns) may be due to radiative excitonic coupling in each of these cases. Slower components, which is around 42 ns, may be due to the lattice defects which creates mid-gap absorption [222], and the slowest component may be related to surface defects. Of course, considering the values reported for different sized particles [110] and the size distribution of these particles, such multicomponent decay may be at least partially due to the size distribution. Detailed studies are underway.

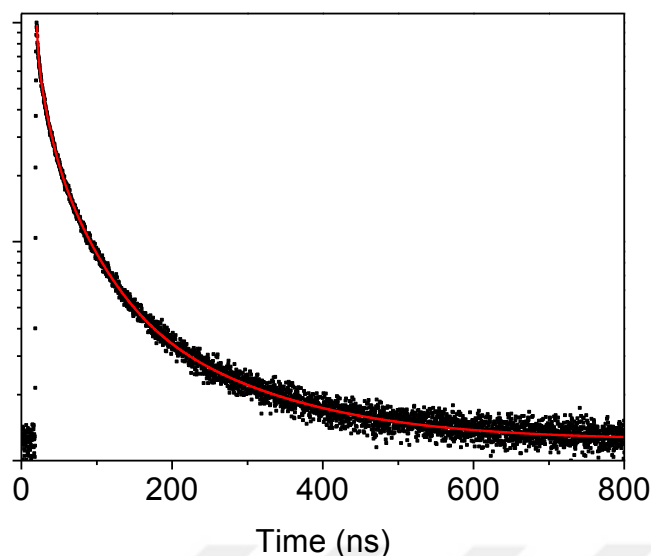


Figure 4. 5 Time resolved photoluminescence decay curve of QD60-RT. Black dots are scattered and red line is fitted data.

Table 4. 15 Fluorescence lifetime analysis of QD60-RT*

T1 (ns)	T2 (ns)	T3 (ns)	T4 (ns)	B1 (%)	B2 (%)	B3 (%)	B4 (%)	Weight Average (ns)
11.66	42.17	154.79	1.55	17.54	45.69	35.17	1.60	75.78

*Components of PL decay of Ag₂S QDs were identified to be multiexponential in the form of;

$$A + B1 \exp(-i/\tau1) + B2 \exp(-i/\tau2) + B3 \exp(-i/\tau3) + B4 \exp(-i/\tau4)$$

where τ_1 , τ_2 , τ_3 , τ_4 are decay components and B1, B2, B3 and B4 are percentage of related decay component.

XPS analysis confirmed the suggested Ag₂S structure as well (Figure 4. 6). Ag 3d peaks at the binding energies (BE) of 366.45 (3d_{5/2}) and 372.44 (3d_{3/2}) eV fit to Ag-S of Ag₂S (Figure 4. 6a). Typically S 2p comes out as a doublet, and there are two different S in these QDs (Figure 4. 6b). The doublet at BE of 159.98 eV and 161.18 eV fits to the 2p_{3/2} and 2p_{1/2} of S-Ag, respectively. The other doublet at 166.84 eV and 168.04 eV belongs to the S of Cys. Two peaks of N1s at BE of

397.73 and 399.29 eV originates from the secondary and primary nitrogens of PEI (Figure 4. 6c). The tertiary nitrogen peak is hindered by the peak of secondary N.

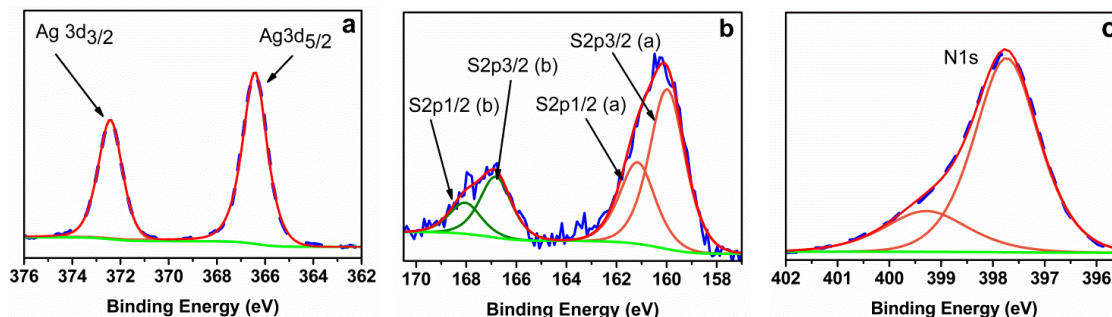


Figure 4. 6 XPS spectra of Ag₂S (QD60-RT) QDs. (a) Ag 3d, (b) S 2p and (c) N 1s.

TEM images of Ag₂S QDs revealed well dispersed spherical structures with broad size distribution (1-7 nm) (Figure 4. 7). Focused images (Figure 4. 7c) clearly showed crystalline structure with 0.220 nm interplanar distance, which fits well to the reported values for the [031] plane of monoclinic Ag₂S [223, 224].

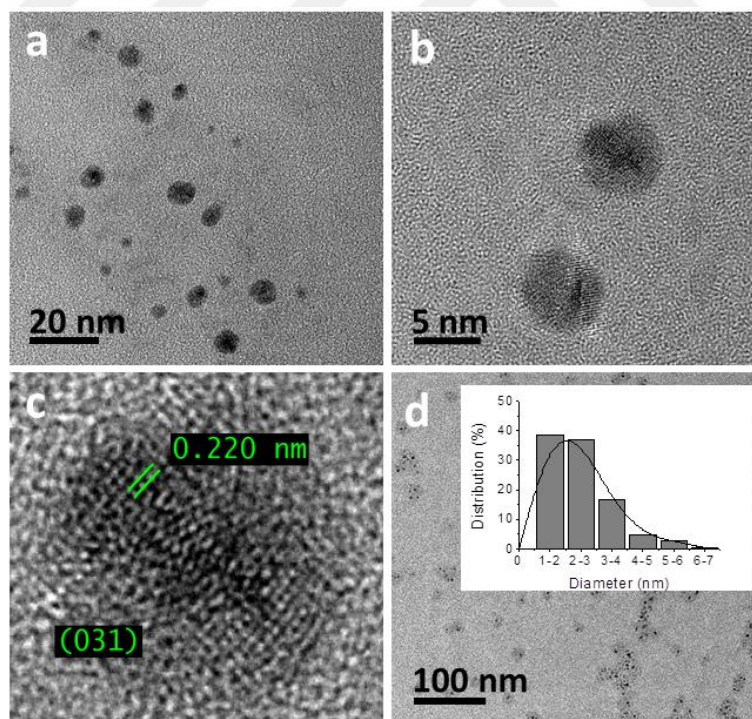


Figure 4. 7 TEM analyses of PEI/Cys coated Ag₂S QDs (QD60-RT). (a) and (b) TEM images of nanoparticles at different magnifications, (c) interplanar spacing and corresponding plane and (d) size distribution of nanoparticles.

The IR spectrum of PEI/Cys coated Ag₂S QDs (QD60-RT) confirms the coexistence of Cys and PEI in the particle coating (Figure 4. 8). Strong bands at 1551 and 1386 cm⁻¹ are typical for asymmetric and symmetric carboxylate stretching modes of Cys and the bands at 3276 cm⁻¹ and 2940-2827 cm⁻¹ point out the presence of N-H and C-H stretching modes of PEI, respectively. In addition, the disappearance of S-H stretching band which is around 2560 cm⁻¹ confirms the binding of Cys to Ag₂S core from the thiol.

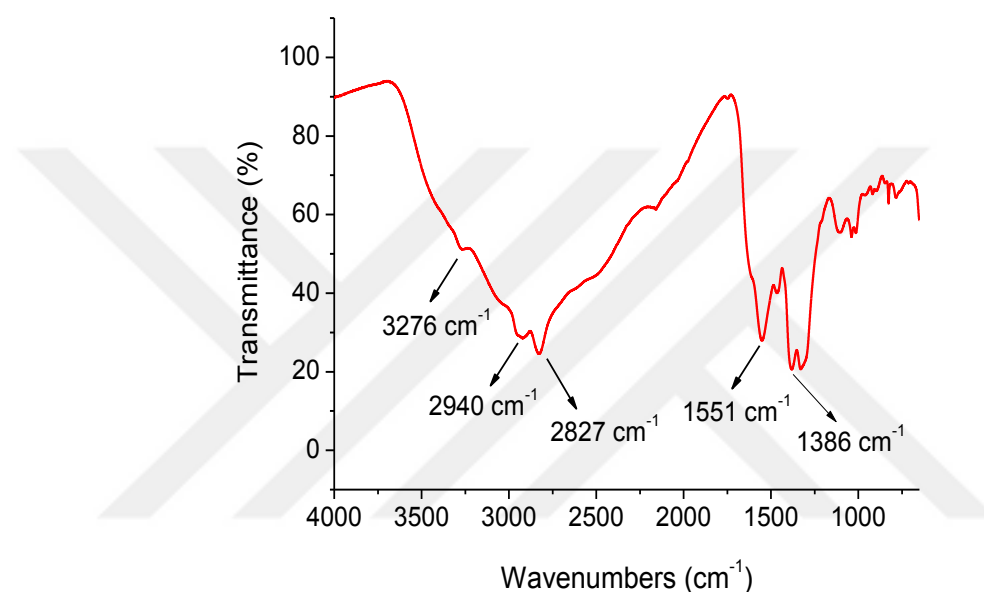


Figure 4. 8 IR spectrum of PEI/l-cysteine coated Ag₂S QDs (QD60-RT).

The organic content of the best emitting QDs which is QD60-RT was determined as 55.6 % by TGA (Figure 4. 9).

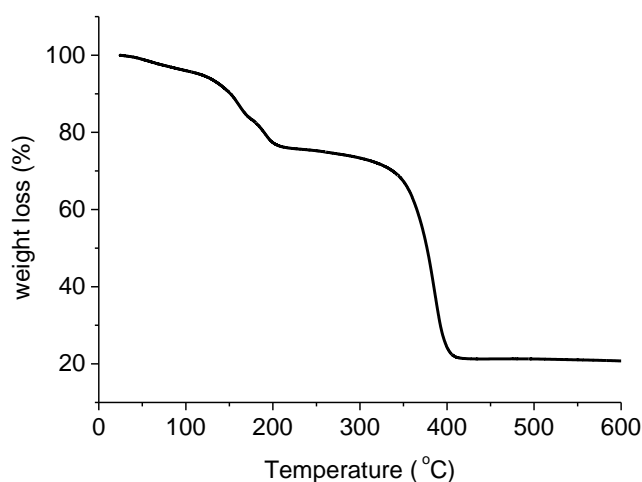


Figure 4. 9 Thermogravimetric analysis of PEI/Cys coated Ag₂S (QD60-RT).

4.3.4 Evaluation of *in vitro* cytotoxicity of Ag₂S QDs

The cytotoxicity of Ag₂S QDs on HeLa cervical carcinoma cell line was determined with MTT assay. Three strongly luminescing QDs with different ratio of PEI/Cys (QD80-70, QD60-RT, QD50-RT: the first number indicates the PEI mol % in feed and the second indicates the synthesis temperature) with emission maxima around 750 nm and the one coated only with PEI (QD100-70) were studied. The emission wavelength and the size were tried to be kept similar in order to study mainly the effect of coating composition. Figure 4. 10 shows the viability of HeLa cells after 24 h incubation with these Ag₂S QDs. Incubation dose was based on the Ag concentration determined with ICP-MS (Table 4. 16) and was studied in 0.8-10 µg/mL range. As seen in Figure 4. 10 and Figure 4. 11, the most toxic QD (viability at and below 50 %) at all concentrations is the one coated only with PEI. However, addition of Cys to the coating improved cytocompatibility, dramatically. All Ag₂S with the mixed coating compositions are weakly toxic below 2.4 µg/mL. Ag₂S QDs with 50/50 PEI/Cys (QD50-RT) emerged as the most cytocompatible formulation with no significant cytotoxicity upto 3.2 µg/mL and become strongly cytotoxic above 5.6 µg/mL Ag dose (Figure 4. 11). Ag₂S QD with 80/20 PEI/Cys (QD80-70) is weakly toxic and the major difference between QD80-70 and QD50-RT starts at 3.2 mg Ag/mL dose. The high cytocompatibility of QD50 may be related to low zeta potential, low PEI content (Table 4. 14 and Table 4. 16) and small hydrodynamic size. QD80-70 and QD50-RT have the highest and the lowest PEI content in the final particle as determined by the elemental analysis (Table 4. 16) of the four particles studied for toxicity evaluation. Surface charge increased with the PEI content, rendering particles slightly more toxic even at similar particle sizes. Surprisingly, Ag₂S QDs with 60/40 PEI/Cys (QD60-RT) which is the best luminescing particle, is the most toxic among the three mixed coating composition studied here. It may be due to high surface positive charge compared to the other two. It was weakly toxic at and below 2.4 µg Ag/mL dose and significantly less cytocompatible than the other two QDs with mixed coatings at all concentrations. All were toxic at and above 5.6 µg Ag/mL dose.

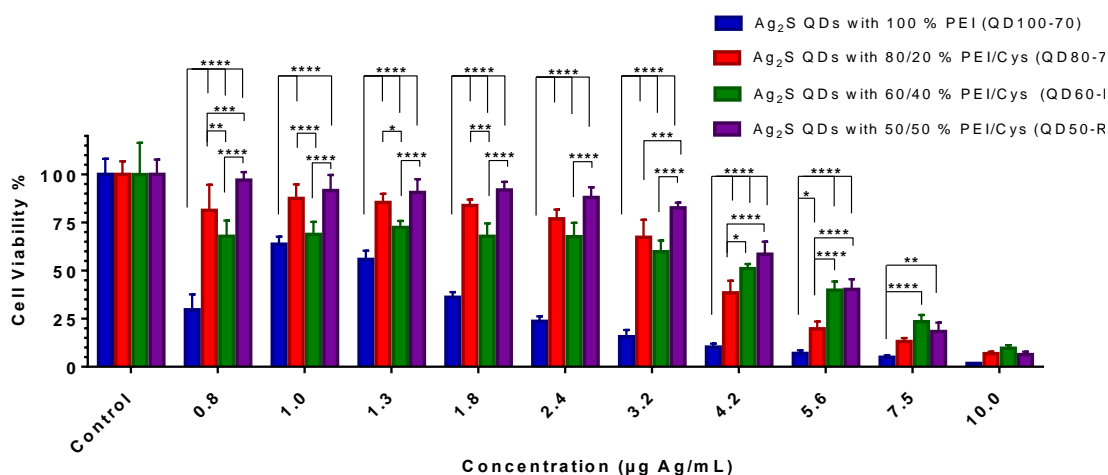


Figure 4. 10 Viability of HeLa cells treated with PEI/Cys coated Ag₂S QDs after 24 hours incubation measured by MTT assay compared to untreated HeLa cells. The data are expressed as mean \pm S.D. ($n = 8$).

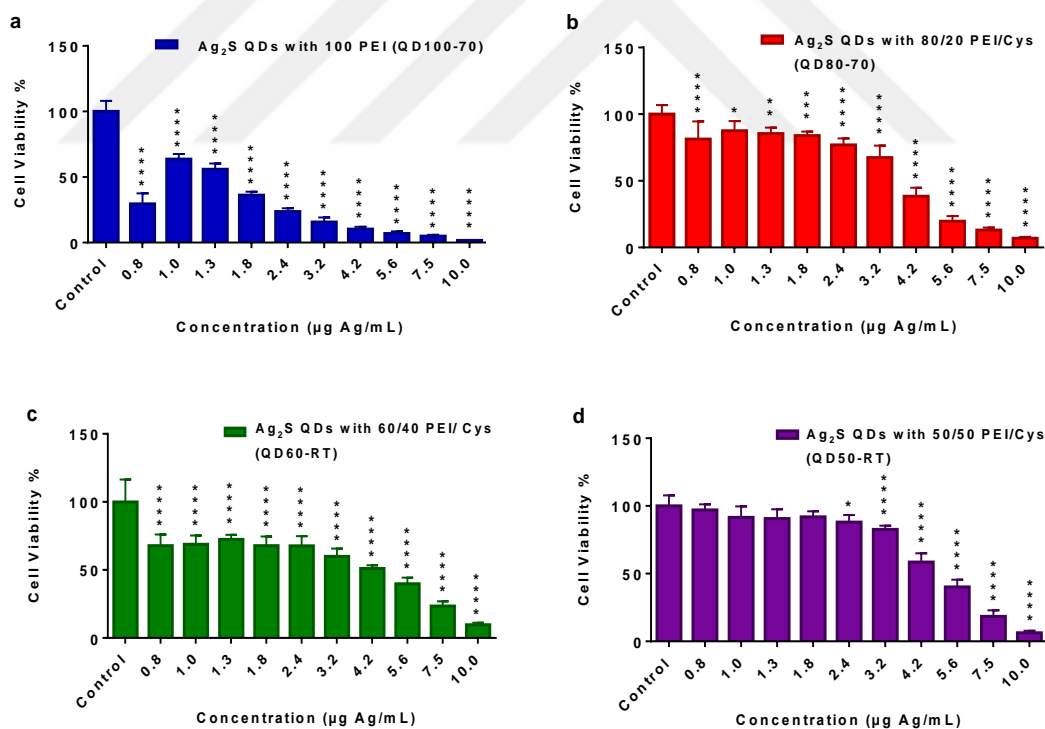


Figure 4. 11 Viability of HeLa cells treated with QD100-70 (QD100) (a), QD80-70 (b), QD60-RT (c) and QD50-RT (d) after 24 hours incubation measured by MTT assay compared to untreated HeLa cells. The data are expressed as mean \pm S.D. ($n = 8$). ($p < 0.05$).

Table 4. 16 Composition analysis of Ag₂S QDs.

PEI/Cys (mol/mol) ^a	Ag (wt %) ^b	N/S (mol/mol) ^c (Experimental) ^d	N/S (mol/mol) ^c (Theoretical) ^e
80/20	21.5	7.24	7.30
60/40	28.4	5.29	3.39
50/50	24.6	4.71	2.58

^a Mol ratio was originally calculated as the total number of moles of primary and secondary amines of the branched PEI (25kDa) / moles of thiol coming from Cys. ^b Measured by ICP OES. ^c N = (moles of N coming from PEI) + (moles of N coming from Cys). S = moles of S coming from Cys. ^d Measured by CHNS/O Analyzer. ^e Based on feed ratio provided in first column.

4.3.5 *In vitro* and *in vivo* optical imaging

HeLa cells were incubated with the Ag₂S QDs (QD60-RT) to evaluate their potential as NIR imaging agents. Microscopy images of the HeLa cells treated with PEI/Cys Ag₂S QDs revealed high uptake and endosomal localization of QDs in the cells (Figure 4. 12). Such a strong signal from the QD with almost no autofluorescence is very critical for biomedical applications. This was further shown with the strong optical signal detected from a BALB/c mouse which was subjected to an intraperitoneal injection of QD60-RT (Figure 4. 13). With QDs emitting in the visible region autofluorescence of the tissue is a very serious handicap and most of the time animals should be subjected to a special diet to reduce the autofluorescence. Provided *in vitro* and *in vivo* images indicate a strong potential for these QDs as an *in vivo* imaging agents. Considering that the peak maximum of this QD at 775 nm and the longpass filter used which allows signals above 840 nm reach to detector, indicates that such a strong luminescence signal is detected with only a small portion of the possible emission that can be obtained by these QDs.

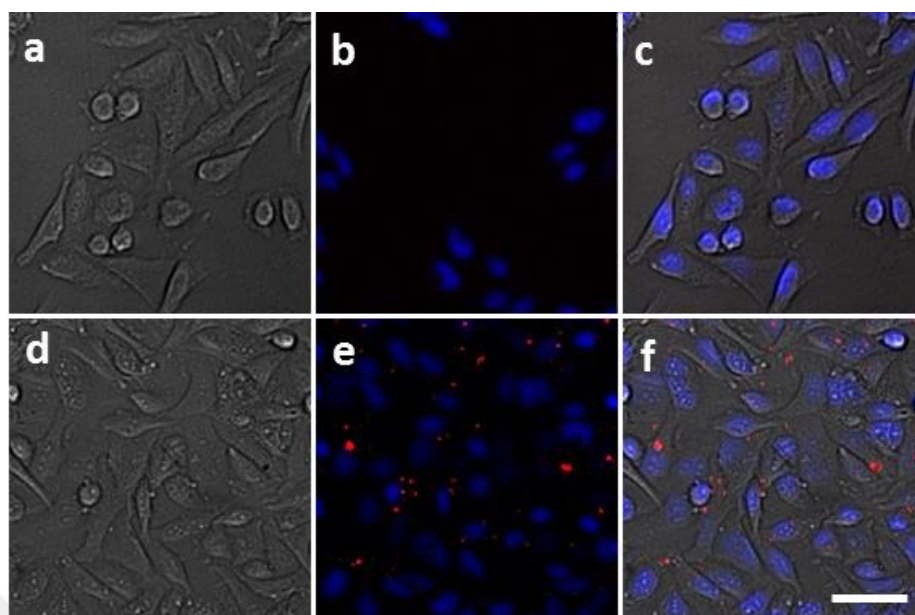


Figure 4. 12 Cellular localization of PEI/Cys coated Ag₂S NIRQDs (QD60-RT) by HeLa cells. DIC (a), DAPI and NIR (b), and merged (c) images of control cells and DIC (d), DAPI and NIR (e), and merged (f) images of QD treated cells. The scale bar shows 100 μ m.

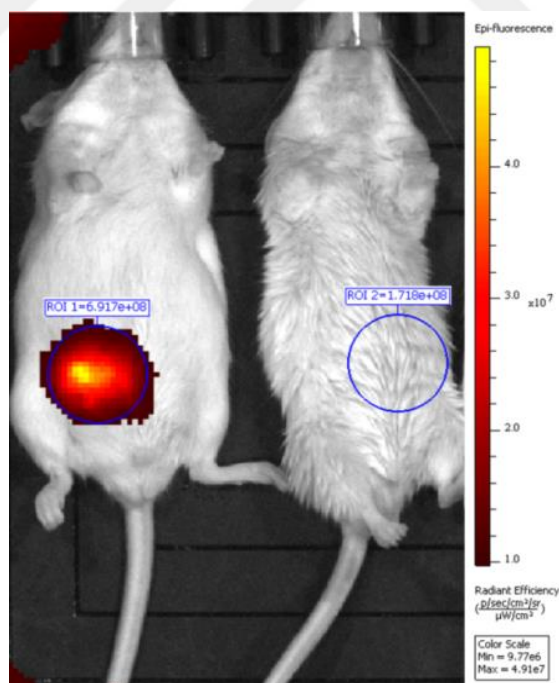


Figure 4. 13 *In vivo* fluorescence image of a BALB/c mice (left image) 1 h after intraperitoneal injection of the QD60-RT and (right image) the control mice with no QD injection (Excitation at 740 nm. Emission filter: 840 nm long-pass).

4.3.6 *In vitro* transfection studies

Here, to evaluate the transfection efficiency of PEI coated Ag₂S QDs, GFP (green fluorescent protein) plasmid DNA and p53-GFP (tumor suppressor gene) were loaded to PEI/Cys cationic Ag₂S QDs. Transfection efficiency was assessed following the expression of GFP via a fluorescence microscope. Different cell types were used in the study. HeLa cells were chosen because it is one of the frequently used cell lines in biomaterial evaluation and a p53 knock out (mouse embryonic fibroblasts, MEF p53^{-/-}) and a wild type (MEF wt) cells were employed to see p53 expression.

4.3.6.1 GFP/PEI/Cys Ag₂S QDs

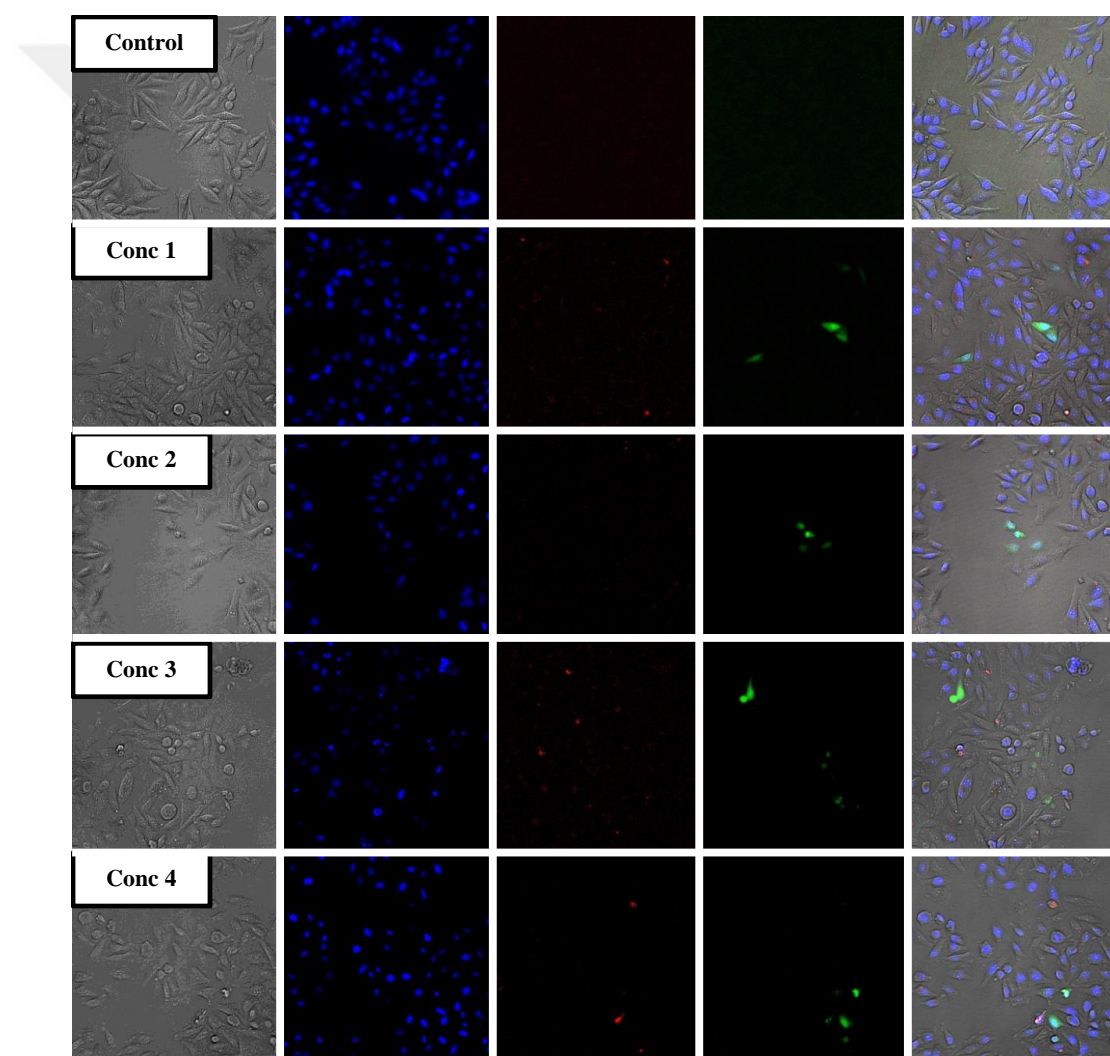


Figure 4. 14 Transfection of HeLa cells with GFP plasmid using PEI/Cys Ag₂S NIRQDs. QD/pDNA complexes prepared at 15/1 N/P ratio were introduced into the cells in

different concentrations. Cells without any treatments were used as control. Images were taken with an inverted fluorescence microscope. DAPI staining was used to show nuclei of all cells in the field (blue color). Red signals indicate QD internalization into the cells. Green signals show GFP transfection.

The transfection ability of PEI/Cys coated Ag₂S QDs was evaluated first in HeLa cells using pGFP. Cells were subjected to different concentrations of QD/pGFP complexes shown in Table 4. 2 which were prepared at 15/1 N/P (nitrogen/phosphorus) ratio in Opti-MEM reduced-serum medium and allowed for transfection for 48 hours. Figure 4. 14 clearly shows internalization of nanoparticles and transfection of GFP in all concentrations applied. However, the transfection efficiency was quite low as seen in the images.

4.3.6.2 p53-GFP / PEI/cys Ag₂S QDs

p53-GFP plasmid also loaded to PEI/Cys Ag₂S QD due to its promise in cancer gene therapy. HeLa, MEF p53 ^{-/-} and MEF wt cells were transfected with these QDs in different concentrations.

As seen in Figure 4. 15, the expression of p53-GFP is quite low. HeLa cells have healthy *p53* gene, so the delivered plasmid may be digested in the cell since it is not needed.

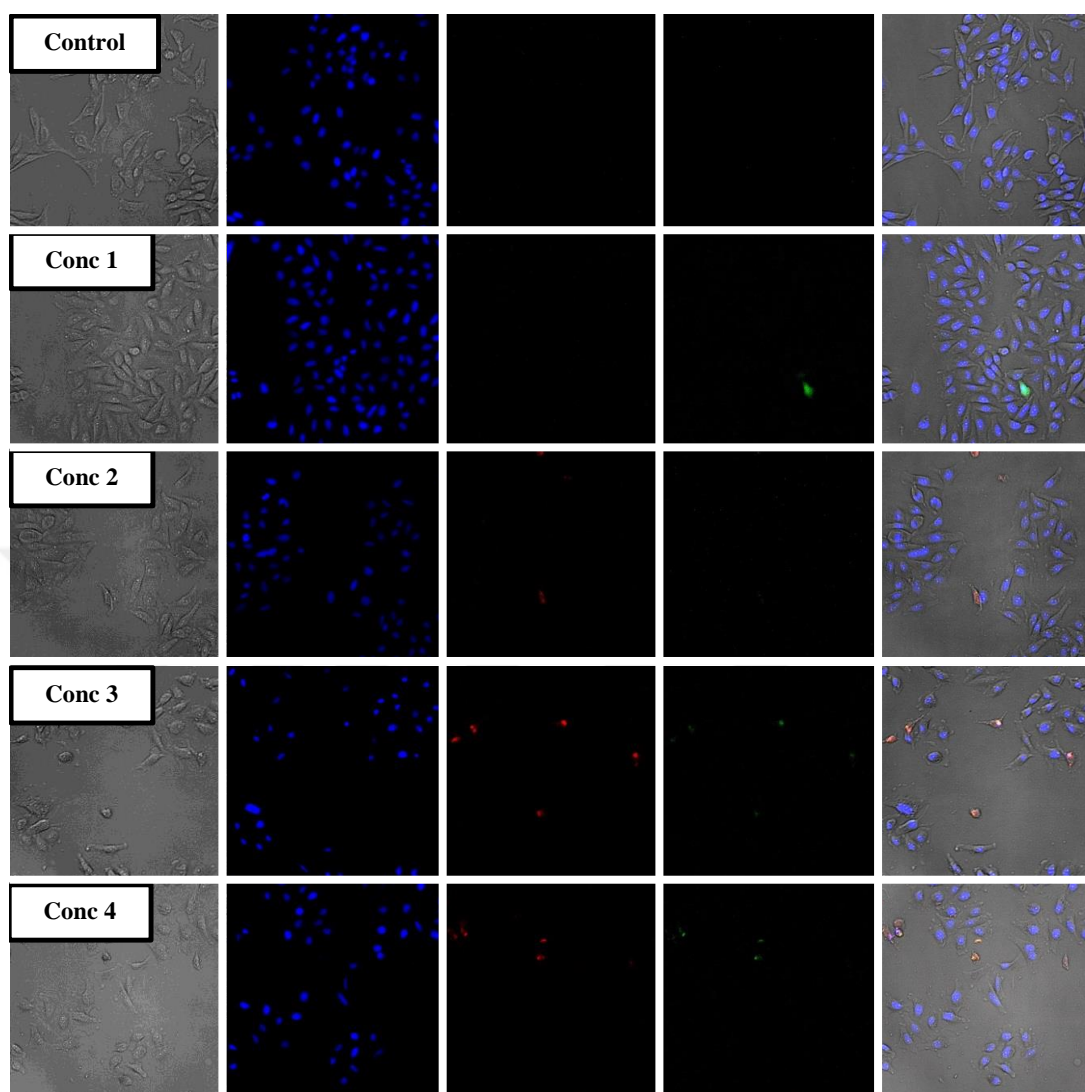


Figure 4. 15 Transfection of HeLa cells with p53-GFP plasmid using PEI/Cys Ag₂S QDs. QD/pDNA complexes prepared at 15/1 N/P ratio (Table 4. 2) were introduced into the cells in different concentrations. Cells without any treatments were used as control. Images were taken with an inverted fluorescence microscope. DAPI staining was used to show nuclei of all cells in the field (blue color). Red signals indicate QD internalization into the cells. Green signals show GFP transfection.

With this motivation, p53 knock out and wild type of mouse embryonic fibroblasts cells were exposed to QD/p53-GFP complexes at the concentrations summarized in Table 4. 2. Cells were treated with the complex for 48 h. As seen from Figure 4. 16A and Figure 4. 16B, uptake of the nanoparticles are limited and GFP expression is extremely low, with

a small amount of transfection at high concentrations in MEF p53 ^{-/-} cells since these cells were p53 deficient. The reason may be the low transfection ability of MEF cells, non-efficient release of DNA from QDs. This needs further investigation.

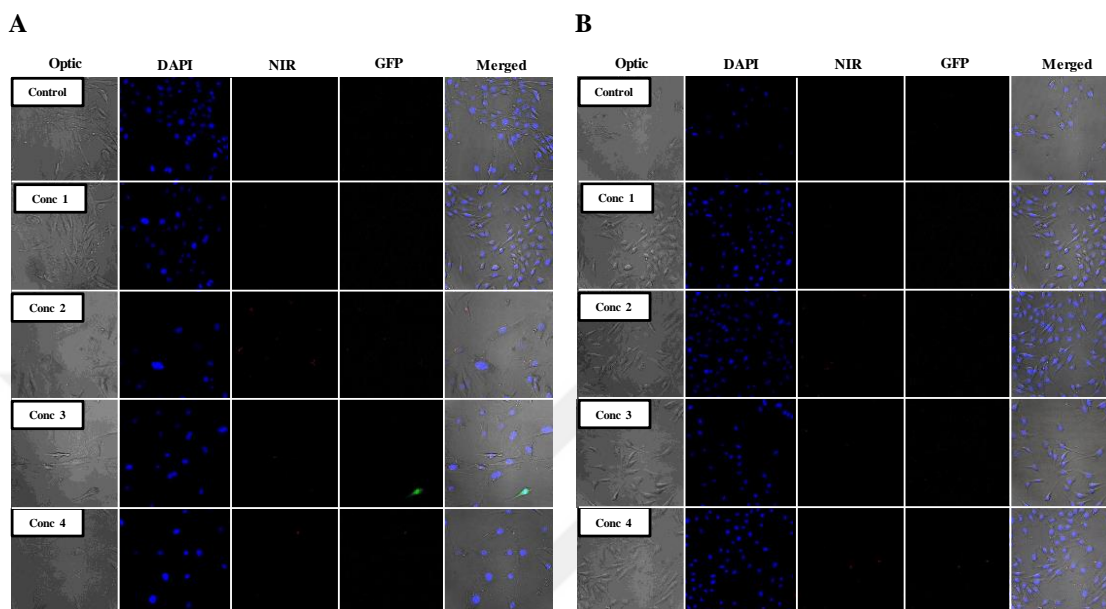


Figure 4. 16 Transfection of (A) MEF p53 ^{-/-} and (B) MEF wt cells with p53-GFP plasmid using PEI/Cys Ag₂S NIRQDs. QD/pDNA complexes prepared at 15/1 N/P ratio were used in different concentrations. Cells without any treatments were employed as control. Images were taken with an inverted fluorescence microscope. DAPI staining was used to show nuclei of all cells in the field (blue color). Red signals indicate QD internalization into the cells. Green signals show GFP transfection.

All transfection studies mentioned above was done with complexes prepared at N/P ratio of 15/1, because both our previous studies and literature indicates that at 5/1 N/P ratio complete complexation of plasmid with PEI or PEI coated nanoparticles is achieved. However, at 5/1 ratio, the positive zeta potential of complexes decreases and this complicates the uptake of the complexes into the cells. To confirm this phenomenon, different N/P ratios were checked (from 5/1 to 15/1). The results shown in Figure 4. 17 also proved this hypothesis. Although no significant GFP signal was detected with complex produced with in 5/1 N/P ratio, strong GFP signal could be seen at and mostly above, 10/1 ratio.

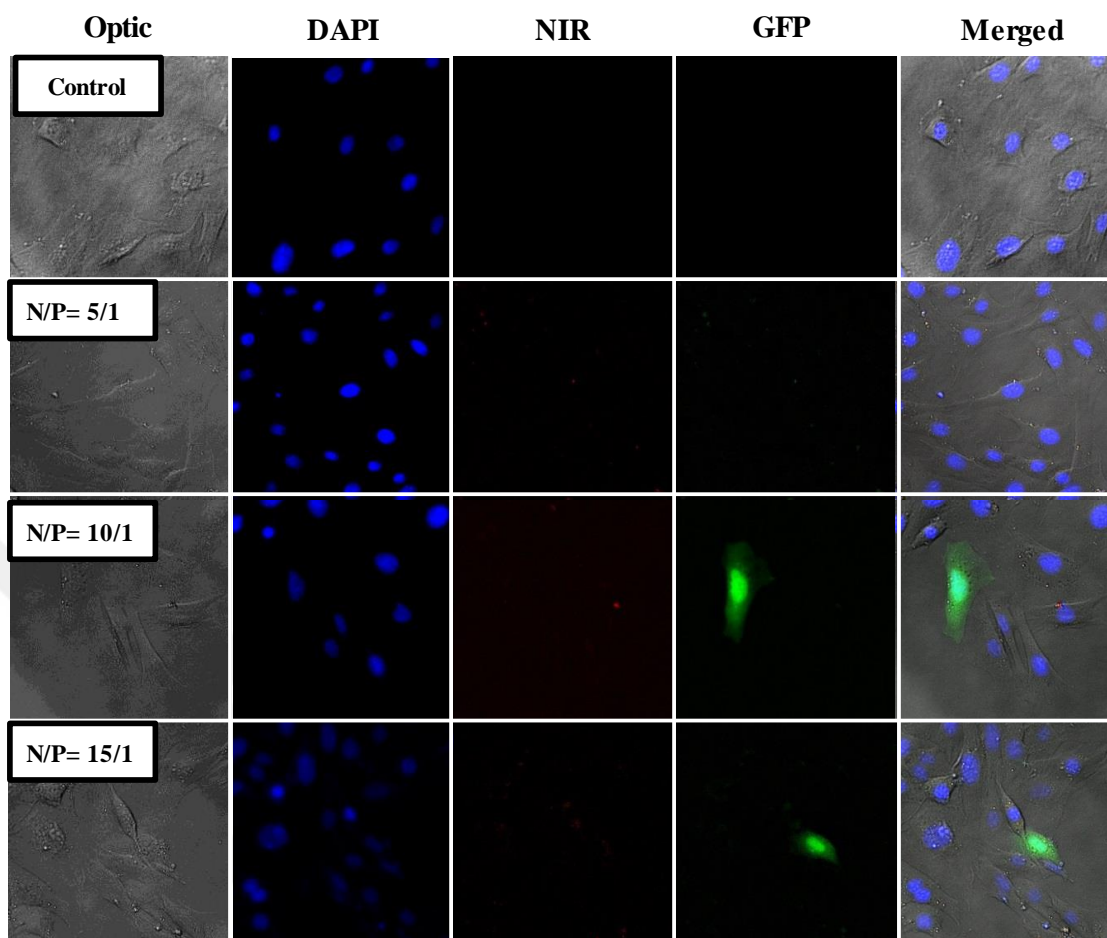


Figure 4. 17 Transfection of MEF p53 ^{-/-} cells with p53-GFP plasmid using PEI/Cys Ag₂S QDs. Different N/P ratios were employed at a concentration of 2.36 μg/mL. Cells without any treatments were used as control. Images were taken with an inverted fluorescence microscope. DAPI staining was used to show nuclei of all cells in the field (blue color). Red signals indicate QD internalization into the cells. Green signals show GFP transfection.

4.4 Conclusions

Cationic NIR emitting Ag₂S quantum dots were prepared successfully with PEI/Cys mixed coating approach, using 25 kDa branched PEI. It was shown here that lower molecular weight PEI even with the mixed coating approach and other amino acids do not provide luminescent QDs, at least under the studied conditions. The reason is probably due to the high complexation of high molecular weight-PEI with Ag₂S and binding of l-cysteine on QD surfaces with thiol bonds. Hence, sufficiently well passivated surface of QD to provide luminescence could be

achieved. On the contrary to the Ag₂S NIRQDs coated with PEI/2MPA [225] where the highest 2MPA amount was 40 mol % to ensure stability, a broad range of PEI/Cys compositions could be studied here. This provided an opportunity to produce smaller particles with emission maxima below 800 nm and to tune the emission in a slightly broader range with a narrower particle size distribution and FWHM. This is desirable with the current imaging instruments which usually lose sensitivity dramatically above 800 nm. Additional amine units contributed by Cys provided a stronger positive charge on the particle surface, as well. Increasing amount of Cys, reduced the luminescence intensity without affecting the emission maxima dramatically. Interestingly, PEI/Cys ratio of 60/40 (QD60-RT) produced the particle with the dramatically increased emission intensity (QY 157 %) and at a significantly longer wavelength (775 nm) than others (725-740 nm). To the best of our knowledge, this unique combination of the coating molecules provided the first examples of Ag₂S NIR QDs with the emission at the low wavelength range of NIR (below 800 nm) with an exceptionally high QY.

The reaction conditions like PEI/Cys, Ag/S, Ag/coating ratios and temperature played key roles in obtaining strong emission and colloidal stability. All compositions were colloidally stable. Other than the QD60 case, Ag/S ratio was the only effective parameter to tune the emission wavelength further. Temperature of the synthesis showed its influence mostly on the emission intensity. Particle growth and stabilization was influenced by the composition and hence for each composition the strong emission was obtained at different temperatures. Higher polymer content required higher reaction temperature for better passivation and stronger luminescence.

Source of the luminescence was explored with time resolved luminescence. Multiexponential decay curves indicated four different life times between 1.55 and 154.79 ns which gives an average lifetime of 75.78 ns. These values indicate non-radiative, excitonic, lattice and surface defect related decays. Effect of size distribution may be also considered for such variety in luminescence lifetimes.

The cytotoxicity analysis indicated dramatically better cytocompatibility of QDs with the mixed coating over pure PEI coating, in agreement with our previous findings [181]. At and below 2.4 µg/mL Ag dose these QDs did not show much

dose dependent toxicity. Yet, there is clear difference between the toxicity of QDs with about similar emission wavelengths but different coating compositions, favouring 50, 20, 60 mol % Cys in the coating composition in the decreasing order. It seems like size and surface charge has an important impact on this outcome.

Strong NIR signals obtained from the endosomes of HeLa cells and from the mice injected with QDs intraperitoneally, signify a great and effective contrast enhancement and hence potential as optical imaging agents. Strong cationic nature of these particles was exploited for gene delivery. GFP and p53-GFP plasmids were loaded to PEI/Cys Ag₂S QDs and HeLa, MEF p53 ^{-/-} and MEF wt cells were transfected. However, the transfection results were quite poor. The efficiencies can be improved in future works. Internalization efficiency of QDs and release rate of the plasmid *in vitro* should be studied further.

Overall, these new cationic Ag₂S NIR QDs with a high quantum yield and strong imaging efficiency are new promising theranostic nanoparticles designed specifically for gene delivery but also suitable for drug delivery.

Chapter 5

5. TUMOR-TARGETED THERAPY OF FOLIC ACID CONJUGATED DOX LOADED Ag₂S NIRQDS

5.1 Introduction

In the previous chapters, synthesis of cationic Ag₂S NIRQDs, their concentration dependent cytotoxicity in different cell lines, exceptionally high quantum yields, and hence potential as optical imaging agent in cell lines, in *C.elegans* and mice have been demonstrated. Their potential as theranostic nanoparticles have been presented with GFP transfection (Chapter 2 and 4) and DOX delivery to cancer cell lines (Chapter 3) coupled with strong intracellular NIR optical contrast. Since, optical imaging does not involve any harmful radiation, is quite sensitive, can be performed frequently and relatively more economic than the alternative imaging techniques, a highly luminescent heavy-metal free NIRQD would be very valuable in optical diagnostics. Also, ability to deliver genes and drugs more effectively to the diseased site is very important especially in chemotherapy of cancer, since drugs usually have serious side effects. So, next step in the cationic Ag₂S theranostic quantum dots, is the site specific delivery of QDs, to reduce the side effects and increase the efficacy of therapy.

High surface to volume ratio of QDs and functional coating materials allow loading of therapeutic agents such as drugs, oligonucleotides, peptides to the coating as well as decoration with targeting ligands for site specific delivery [113, 117, 226-230]. Tan et al. demonstrated targeted delivery of Ag₂S QDs to Rvβ3 integrin receptor overexpressed on tumor cells by conjugation of a cyclic peptide, arginine-glycine-aspartic acid-

(D)phenylalanine-lysine (cRGDFk) to the QDs [116]. Wang and Yan, showed high accumulation of antiVEGF conjugated Ag₂S QDs in the tumor of the mice following intravenous administration [113].

Folate receptors which is a glycosyl-phosphatidylinositol-linked membrane glycoprotein is one of the highly expressed receptors in several cancer cells including brain, lung, neck, breast, nasopharyngeal, colorectal and ovarian cancers [231-233]. Folic acid, an oxidized form of folate has high binding affinity to folate receptors ($K_d \sim 10^{-10}$ M). The ligand is internalized into cells through receptor mediated endocytosis [232, 234]. These properties make the folic acid a popular ligand for the use of quantum dots as tumor targeting systems. This can be exploited for tumor specific imaging but also can be coupled with therapeutic effect, if QDs are loaded with anticancer drugs. Doxorubicin (DOX) is a commonly used chemotherapy drug. It binds to DNA by intercalation and induces apoptosis in cancer cells [235]. However, direct administration of the drug causes its accumulation both in malignant and non-malignant cells in the body and decrease the quality of patients' life due to its undesired side effects [236]. Therefore, delivery of the drug selectively to the cancerous tissues is an urgent demand. This is a common need with almost all chemotherapy drugs. [237, 238].

Here, we demonstrate high drug efficacy via selective delivery of DOX loaded Ag₂S NIR QDs decorated with FA to HeLa cells (folate receptor +) in a comparative study where A549 cells (folate receptor -) were used as control. Cationic Ag₂S NIR QDs with PEI/Cys coating which has strong emission in the medical-optical window, with one of the highest quantum yields reported in the literature [239], was used in this study. Overall cationic nature of the particles assumed to enhance cell surface interaction and internalization. For the active targeting, QDs were decorated with FA using a PEG linker. *In vitro* cytotoxicity, cellular uptake and apoptosis/necrosis studies were performed to evaluate the potential biological uses of the particles. The effectiveness of folate targeting QDs have been reported by NIR emitting QDs having heavy metals [240-242] but the targeting of Ag₂S QDs by folic acid, highly expressed in most of the cancer cells, presented only in our previous work [118] and in this study.

5.2 Materials and Methods

5.2.1 Materials

Silver nitrate (AgNO₃), l-cysteine (Cys), folic acid and 2-(N-morpholino) ethanesulfonic acid (MES) were purchased from Sigma-Aldrich (USA). Thioacetamide (TAA), N-hydroxysuccinimide (NHS), sodium hydroxide (NaOH), ethanol and acetic acid (CH₃COOH) were obtained from Merck Millipore (USA). 1-Ethyl-3-(3-dimethylaminopropyl) carbodiimide (EDC) was purchased from Alfa Aesar (UK). Branched polyethylenimine (PEI) (Mw 25 kDa) was purchased from Aldrich (Germany). Amine-polyethylene glycol-valeric acid (NH₂-PEG-VA) (3400 MW) was provided by Laysan Bio Inc. (Alabama). Doxorubicin hydrochloride (DOX·HCl) was obtained from SABA pharmaceuticals (Turkey). LDS 798 Near-IR laser dye was purchased from Exciton Inc. Dialysis membrane (Cellu-Sep T1, MWCO 3500 Da) was provided by Membrane Filtration Products, Inc. (USA). Ultra-pure water (MilliQ, Millipore, 18.2 MΩ cm) was used in all experiments.

Both folic acid containing and folic acid free Roswell Park Memorial Institute (RPMI) 1640 mediums (with l-glutamine and 25 mM HEPES), trypsin-EDTA and penicillin-streptomycin solutions were provided by Multicell, Wisent Inc. (Canada). Fetal bovine serum (FBS) was obtained from Capricorn Scientific GmbH (Germany). Thiazolyl blue tetrazolium bromide (MTT) and phosphate buffered saline (PBS) tablets were purchased from Biomatik Corp. (Canada). Dimethyl sulfoxide Hybri-Max™, 4',6-diamidino-2-phenylindole (DAPI) and adenosine 5'-triphosphate (ATP) bioluminescent assay kit were obtained from Sigma (USA) and 4 % paraformaldehyde solution in PBS was purchased from Santa Cruz Biotechnology, Inc. (USA). Propidium iodide was purchased from Sigma-Aldrich (USA). Annexin-V-FLUOS was obtained from Roche (Germany). Hoechst 33342 was obtained from Thermo Scientific (Germany). M30 Apoptosense ELISA kit was provided by Peviva (Sweden). JC-1 mitochondrial membrane potential assay kit was obtained from Cayman Chemicals (USA). All 12, 24 and 96-well plates were purchased from Nest Biotechnology Co. Ltd. (China).

HeLa (human cervical carcinoma cell line) and A549 (adenocarcinomic human alveolar basal epithelial cell line) cells are gifts of Devrim Gozuacik (Sabanci University, Istanbul, Turkey) and Ferda Ari (Uludag University, Bursa, Turkey), respectively.

5.2.2 Synthesis of Ag₂S NIRQDs

Ag₂S QDs were prepared according to the previous report [239]. Briefly 0.25 mmol of AgNO₃ was dissolved in 75 ml of deoxygenated water under vigorous mechanical stirring (5000 rpm) at room temperature and 2.14x10⁻³ mmol of PEI and 0.50 mmol of l-cysteine (Cys) were added into the solution. Using NaOH (1 M) and acetic acid (1 M) solutions, the pH of the solution was kept at 10.5. Thioacetamide (TAA, 0.0625 mmol), dissolved in 25 ml of deoxygenated water, was injected to this solution and stirred for 3 h under argon atmosphere (Scheme 5. 1). The resulting brown solution was washed by Amicon-Ultra centrifugal filters (30000 Da cut off) and stored in the dark at 4 °C after its pH was adjusted to 7.4.

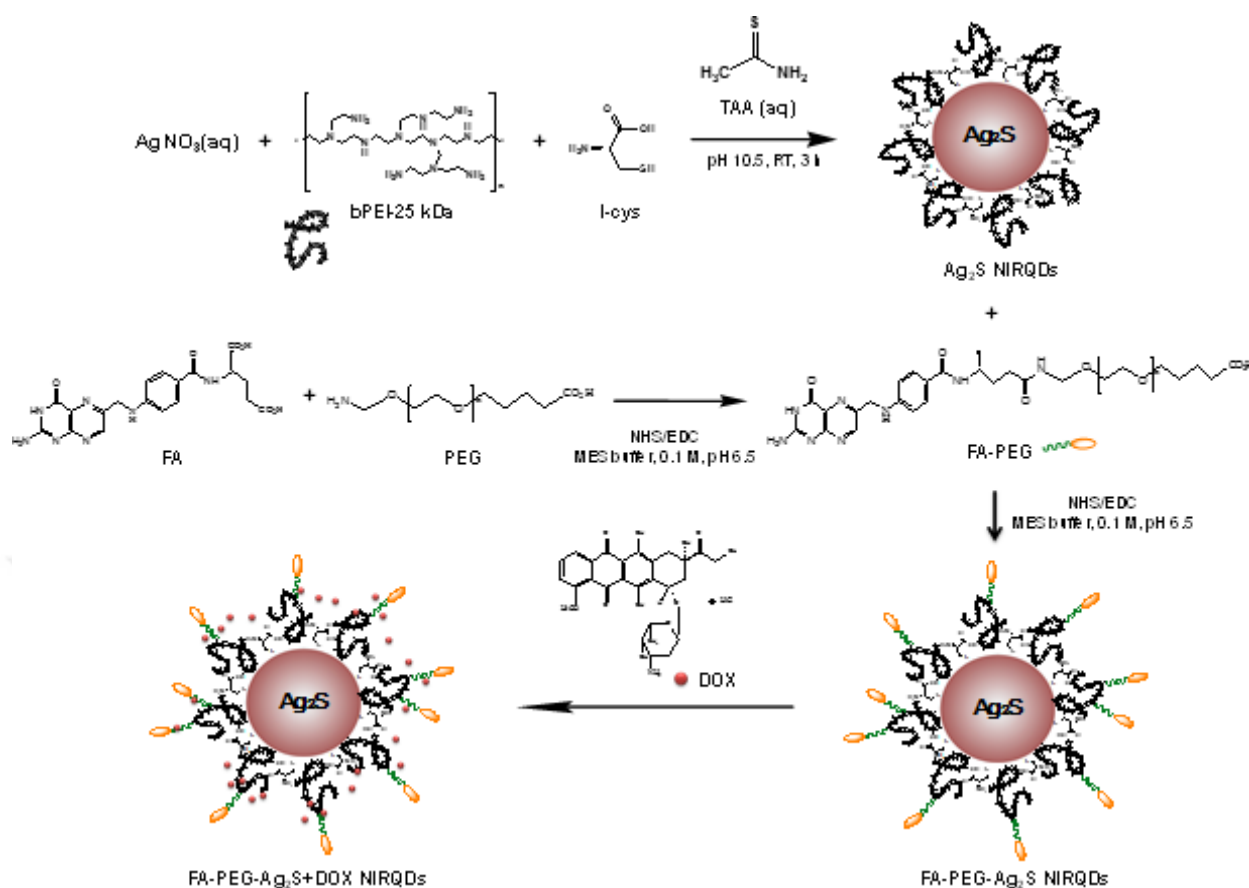
5.2.3 Preparation of FA-PEG-COOH conjugate

Folic acid tagged PEG (FA-PEG-COOH) was prepared via amidation reaction using NH₂-PEG-VA (MW 3400 Da) [243]. According to the procedure, firstly, folic acid (1.5 mmol) was dissolved in 30 mL of MES buffer (0.1 M, pH 6.5) and activated with NHS (6 mmol) and EDC (6 mmol) for 30 minutes. NH₂-PEG-VA was added to this mixture (0.075 mmol) and was stirred for 24 h at room temperature (Scheme 5. 1). Finally, the reaction mixture was washed with deionized water via Amicon-Ultra centrifugal filters (30000 Da cut off) and stored at -20 °C after being lyophilized.

5.2.4 Preparation of FA-PEG-Ag₂S NIRQDs

FA-PEG-COOH conjugate was attached to Ag₂S QDs via a standard amidation reaction (Scheme 5. 1). FA-PEG-COOH (0.02 mmol) was activated with NHS (0.2 mmol) and EDC (0.2 mmol) in 10 mL of MES buffer (0.1 M, pH 6.5) for 30 minutes. Ag₂S QDs (1 gram) were added to the solution and the reaction was stirred at RT for 24 h. Then, the resulting particles were washed with deionized water using Amicon-Ultra centrifugal filters (30000 Da cut off).

Folic acid amount bound to nanoparticles were calculated from the absorbance of FA at 320 nm using a concentration dependent absorbance calibration curve for folic acid (Scheme 5. 1).



Scheme 5. 1 Schematic representation of aqueous synthesis of FA-PEG-conjugated Ag₂S NIRQDs and DOX loading via non-covalent complexation.

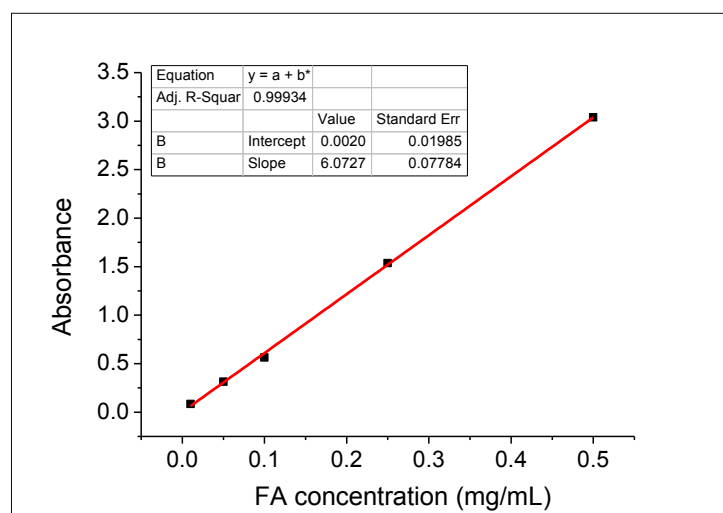


Figure 5. 1 Concentration dependent absorbance (at 320 nm) calibration curve for free folic acid .

5.2.5 DOX loading on FA-PEG-Ag₂S NIRQDs

Lyophilized FA-PEG-Ag₂S QDs (20 mg) were suspended in 50 mL deionized water with DOX·HCl (1 mg) under vigorous stirring for 36 h at room temperature. Then, DOX loaded particles were dialyzed in 1L PBS (pH 7.4, 1x) for 1.5 h using 3500 Da molecular weight cut-off cellulose dialysis membrane to remove free DOX. The purification was repeated one more time to confirm that all free DOX in the solution was removed. The amount of unloaded drug was calculated from a standard absorbance (485 nm) concentration calibration curve of DOX using the following equation (Figure 5. 2):

$$LE \% = \frac{W_{total} - W_{free}}{W_{total}} \times 100\% \quad (1)$$

where in LE is loading efficiency, W_{total} is the amount of DOX used initially, W_{free} is the amount of unbound DOX.

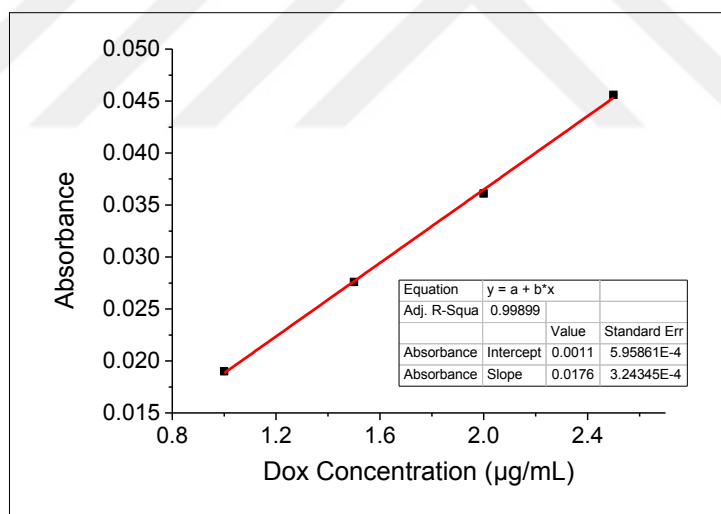


Figure 5. 2 Concentration dependent absorbance (at 485 nm) calibration curve for free DOX.

5.2.6 Characterization Methods

Photoluminescence (PL) spectra were recorded on a Horiba Yvon FluoroMax-3 spectrofluorometer (λ_{ex} : 350 nm and λ_{em} : 370 nm long pass filter). Absorbance measurements in the 205-750 nm range were recorded on a Shimadzu 3101 PC UV-Vis-NIR spectrophotometer. Crystal size and the morphology of QDs was studied with a transmission electron microscope (TEM, Philips-FEI-Tecnaï G2 F30) functioning at an

accelerating voltage of 200 kV. Aqueous solutions of QDs were dropped on a carbon coated Cu-grid and dried. The hydrodynamic size and zeta potential of the particles in water were determined with a Malvern Zetasizer Nano-ZS. Content of the Ag in the QD solutions was determined using Agilent 7700x Inductively Coupled Plasma Mass Spectrometry (ICP-MS). QD samples were digested with an acid treatment procedure (suprapur nitric acid 65 % and suprapur sulphuric acid 96 %) for the measurement. Ag ion concentration was calculated from a standard curve created and measured with Ag ICP solution on the same day of experiments. All measurements were performed at fixed pH (7.4) value of QD solutions.

5.2.7 Cell culture

HeLa human cervical cancer cells and A549 adenocarcinomic human alveolar basal epithelial cells were grown at 37°C under 5 % CO₂ in RPMI medium with folic acid supplemented with 10 % FBS and 1 % penicillin-streptomycin.

5.2.8 *In vitro* cytotoxicity studies

5.2.8.1 MTT assay

In vitro cytotoxicity of QDs was assessed by 3-(4,5-dimethylthiazol-2-yl)-2,5-diphenyl tetrazolium bromide (MTT) viability assay. HeLa and A549 cells were seeded in 200 µL of FA-free culture medium at a density of 1 x 10⁴ cells/well in 96-well plates, and incubated at 37 °C in a 5 % CO₂ atmosphere. In the next day, the growing cells were treated with QDs in fresh culture medium. After 48 h incubation, 50 µL of MTT solution (5 mg/mL in PBS, pH 7.4) was added to each well with 150 µL of culture medium containing folic acid and incubated 4 more hours. Purple formazan crystals that appear in the mitochondria of living cells were dissolved with DMSO/EtOH (1:1 v/v) solution. The absorbance intensity was read by a microplate reader (BioTek ELx800 Absorbance Microplate Reader) at 600 nm with a reference wavelength of 630 nm. Treated cells without MTT reagent were used to correct the absorbance intensities. The relative cell viability of treated cells was calculated in reference to the untreated control cells using the formula:

$$\text{cell viability (\%)} = [\text{sample absorbance/control absorbance}] \times 100 \quad (n = 3). \quad (2)$$

QD doses were based on the Ag content of the samples which is measured by ICP-MS to keep the number of particles constant between different formulations. The toxicity of free DOX in equivalent concentrations to DOX content of QDs was also studied. Untreated cells were used as positive controls.

5.2.8.2 ATP assay

HeLa and A549 cells were seeded in 100 μ L of FA-free culture medium at a density of 5×10^3 cells/well in a 96-well plate and incubated for 24 h at 37 °C in 5 % CO₂. Next day, QDs and free DOX (at equivalent concentrations of DOX-FA-PEG-Ag₂S) were added into cells separately with fresh culture medium. After 48 h incubation, ATP content in the living cells was determined according to manufacturer's protocol (ATP Bioluminescence Assay, Sigma, USA). Briefly, the intracellular ATP was extracted from the cells using the ATP-releasing reagent of the kit and the luciferin-luciferase mixture was added. Luminescence signal was recorded using a luminometer (FLx800 Microplate Fluorescent Reader, Bio-Tek, USA) with a count integration time of 1 s. Cells without treatment were used as control and the percentage of cell viability was calculated using equation (2) ($n = 3$).

5.2.9 Intracellular uptake of QDs

HeLa and A549 cells were seeded on a 6-well plate at a density of 2.5×10^5 cells/well in FA-free complete medium and grown for 24 h at 37 °C and 5 % CO₂. Next day, the growing cells were incubated with QD samples at 2 μ g/mL Ag concentration for 1 h. Then, the medium was removed and cells were fixed with paraformaldehyde solution (4 % in PBS) for 20 min. After being washed with PBS, cells were incubated for an additional 15 min with 1 μ g/mL of DAPI nucleus dye. The cells were rewashed three times with PBS to remove unbound dye, and left in 2 mL PBS to prevent drying. Cells without any QD treatment were used as controls. These fixed and washed cells were imaged under an Inverted Life Science Microscope (Olympus-Xcellence RT Life Science Microscopy) using filters for DAPI (λ_{exc} : 352-402 nm and λ_{em} : 417-477 nm), DOX (cy3: λ_{exc} : 530-560 nm and λ_{em} : 573-648 nm) and NIR region (λ_{exc} : 550 nm and λ_{em} : 650 nm long pass), respectively. The obtained images were processed and merged using ImageJ software (version 1.46r, NIH, USA) [202].

The quantitative analysis of QD uptake was performed by the determination of Ag content in cells after incubation of cells with the samples. HeLa and A549 cells were prepared as in microscopy image analysis and incubated with QD samples for 1 h. Then, the cells were washed with PBS to remove un-internalized nanoparticles by the cells and were collected after trypsinized. Acid digestion procedure was applied and Ag content was determined by ICP-MS ($n=3$). All experiments were repeated three times.

5.2.10 Apoptosis and Necrosis

5.2.10.1 Annexin V-FITC/PI apoptosis assay

Annexin V-FITC/PI apoptosis assay was used to determine the apoptosis and necrosis that takes place in treated cells after treatment with the QDs and free DOX. HeLa and A549 cells were prepared at a density of 5×10^3 cells/well in a 96-well plate using 100 μ L of FA-free culture medium for each well and subjected to QDs (1.5 μ g Ag/ml) and free DOX (0.27 μ g/ml) in triplicate after incubated for 24 h at 37 °C in 5 % CO₂. The cells were left for another 24 h incubation in 5 % CO₂ at 37 °C. Untreated cells were used as control. Finally, cells were stained using Annexin V-FLUOS Staining Kit according to the protocol provided by the manufacturer (Roche, Germany) and using Hoechst 33342 (Thermo Scientific (Germany), 5 μ g/mL). The stained cells were visualized under fluorescent microscope (CKX41; Olympus Corporation Tokyo, Japan).

5.2.10.2 M30 Assay

Apoptotic effect of QDs and free DOX was also measured using M30 Assay. Cells were prepared as in Annexin V-FITC/PI apoptosis assay and incubated with samples for 48 h in a 5 % CO₂-humidified atmosphere at 37 °C ($n=2$). Apoptosis level was determined by a commercially available immunoassay kit (M30-Cytodeath ELISA kit, Peviva AB, Sweden), according to the manufacturer's instructions and the absorbance was recorded with an ELISA microplate reader at 450 nm (FLASH Scan S12, Germany).

5.2.10.3 Mitochondrial membrane potential ($\Delta\psi_m$) analysis

Apoptosis level in the HeLa and A549 cells after incubation with Ag₂S, FA-PEG-Ag₂S, DOX loaded FA-PEG-Ag₂S and free DOX was also confirmed by mitochondrial membrane potential ($\Delta\psi_m$) assay. The cells were prepared and incubated with the QDs

and free DOX for 24 h in 5 % CO₂ at 37 °C as in Annexin V-FITC/PI apoptosis assay. JC-1 mitochondrial membrane potential assay kit (Cayman Chemicals, USA) was used according to the protocol provided by the manufacturer. The stained cells were visualized by a fluorescence microscopy (CKX41; Olympus Corporation Tokyo, Japan).

5.2.11 Statistical Analysis

Statistical evaluation of data was carried out using non-parametric Kruskal–Wallis one-way analysis of variance followed by multiple Dunn’s comparison test and Mann-Whitney test of GraphPad Prism 6 software package (GraphPad Software, Inc., USA). P-value < 0.05 was accepted for statistically significance. All quantitative data was expressed as mean standard deviation (S.D.). All tests were two-tailed.

5.3 Results and Discussion

5.3.1 Preparation and characterization of Ag₂S, FA-PEG-Ag₂S and DOX loaded

FA-PEG-Ag₂S NIRQDs

In this study, we developed FA tagged and DOX loaded NIR emitting cationic Ag₂S QDs for tumor targeted chemotherapy and optical imaging. These theranostic QDs were prepared according to the method outlined in Scheme 5. 1. Initially, cationic Ag₂S QDs were prepared directly in water with PEI and l-cysteine mixed coating in a single step using AgNO₃ and TAA precursors as described previously [239]. For FA conjugation, carboxylic acid of folic acid was activated by EDC /NHS in MES buffer (0.1 M, pH 6.5) and reacted with amine groups of NH₂-PEG-VA (MW 3400 Da). Later, FA-PEG-VA was conjugated to Ag₂S QDs via amidation using the same synthetic procedure. Finally, DOX was loaded to FA-PEG-Ag₂S QDs via hydrophobic and electrostatic interactions between DOX, PEG and PEI. PEG bridge between the nanoparticle and FA, increases the accessibility of folic acid to folate receptors and means to load DOX to QDs.

Folic acid conjugation and drug loading were confirmed with photoluminescence (PL) and absorbance spectroscopy. Emission peak maxima at 450 nm of FA-PEG-Ag₂S and FA-PEG-Ag₂S-DOX indicates the presence of FA (Figure 5. 3a). The absorbance spectra also confirmed FA conjugation to nanoparticles with typical peaks at around 300 nm and 375 nm with a slight red shift compared to free FA (Figure 5. 3b). Based on a calibration curve prepared from the concentration dependent absorption or emission of

FA, a 94.8 % binding efficiency (0.0354 mg (8.02 μ mol) FA/mg nanoparticles) was obtained (Figure 5. 1). DOX has emission maxima at 560 nm and 590 nm (Figure 5. 3a) and strong absorption at 485 nm (Figure 5. 3b). FA-PEG-Ag₂S-DOX clearly indicates the presence of DOX based on these typical emission peaks. In addition, DOX loading was shifted the emission peak maximum of NIR emitting QDs to 745 nm (Figure 5. 3a). DOX loading efficiency of FA-PEG-Ag₂S QDs was determined based on the DOX absorbance at 485 nm using a calibration curve for DOX (Figure 5. 2). The results showed that 73.4 % drug loading efficiency was achieved, meaning 0.0367 mg DOX/mg nanoparticle composition was obtained.

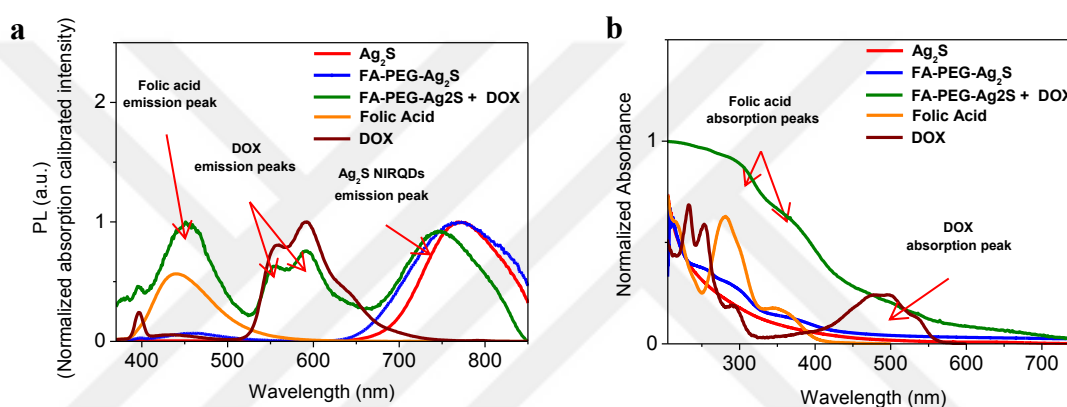


Figure 5. 3 Normalized photoluminescence (excitation at 360 nm) (a) and normalized absorbance spectra (b) of Ag₂S, FA-PEG-Ag₂S, DOX loaded FA-PEG-Ag₂S NIRQDs and free folic acid and DOX as references.

Table 5. 1 summarizes the average particle sizes (by number) with PDI and zeta potential of all compositions. Ag₂S QDs have an average hydrodynamic size of 41.7 ± 3.0 nm and zeta potential of 68.6 ± 2.0 mV confirming strong cationic nature. Such high surface charge provides good colloidal stability in aqueous media and should enhance the cellular uptake considering the large number of negatively charged domains in cell membrane [244]. Conjugation of FA-PEG-VA to Ag₂S, increased the average hydrodynamic size slightly to 51.4 ± 1.4 nm with a lower PDI indicating just increase in the corona thickness associated with some steric stabilization due to PEG chains as well with no significant agglomeration during conjugation chemistry. FA-PEG-Ag₂S has lower zeta potential, 47.4 ± 0.9 mV, than Ag₂S QDs since some of the amine groups were consumed during FA-PEG conjugation. After DOX loading, hydrodynamic size decreased significantly to 27.0 ± 2.9 nm, possibly due to some collapse of corona as a

result of DOX-coating interaction. This decreased the zeta potential to 30.2 ± 2.0 mV, but this is high enough surface charge to ensure colloidal stability and favourable interaction with cell membrane. Overall, the target composition, FA-PEG-Ag₂S-DOX, was synthesized with 0.0354 mg (8.02 μ mol) FA and 0.0367 mg DOX per mg nanoparticle in ultrasmall sized regime with a strong cationic nature (Table 5. 2).

Table 5. 1 Hydrodynamic size and surface charge of Ag₂S QD compositions.

Sample Name	Size (nm)	PDI	Zeta (mV)
Ag ₂ S	41.7 ± 3.0	0.205	68.6 ± 2.0
FA-PEG-Ag ₂ S	51.4 ± 1.4	0.122	47.4 ± 0.9
FA-PEG-Ag ₂ S + DOX	27.0 ± 2.9	0.291	30.2 ± 2.0

FA-PEG-Ag₂S QDs have spherical morphology with crystal sizes in the range of 3.6 to 7.4 nm (Figure 5. 4). Considering relatively broad emission peak of Ag₂S, a large crystal size distribution is reasonable.

Table 5. 2 Ag and DOX content in the nanoparticles

Sample Name	Ag content (mg %)	DOX (mg %)
Ag ₂ S	28.4	-
FA-PEG-Ag ₂ S	21.1	-
FA-PEG-Ag ₂ S + DOX	17.8	3.67

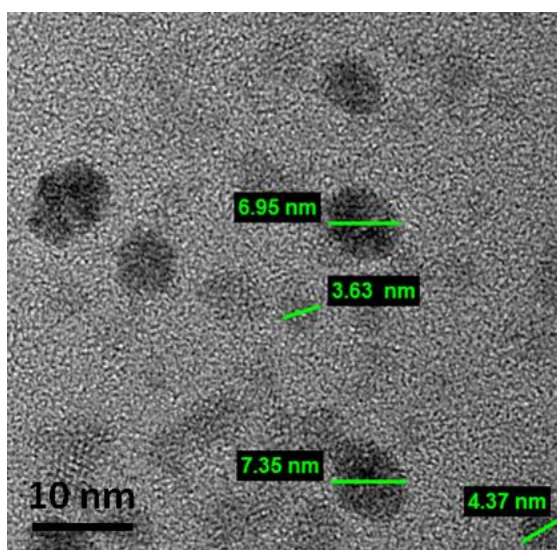


Figure 5. 4 TEM image of FA-PEG-Ag₂S.

5.3.2 *In vitro* cytotoxicity studies

In the *in vitro* studies, folate receptor positive HeLa human cervical carcinoma cells [245] and folate receptor negative A549 adenocarcinomic human alveolar basal epithelial cells were used. Cytotoxicity of Ag₂S compositions were evaluated by MTT and ATP assays. Dose of QDs was used according to the Ag content of each composition determined by ICP-MS to keep the particle content constant between different compositions at a given QD dose.

MTT assay is a colorimetric assay based on the reduction of yellow MTT to purple formazan by metabolically active cells. Amount of formazan correlates with cell viability. ATP assay is a bioluminescence assay using recombinant firefly luciferase to measure the level of cellular ATP in viable cells [246]. The amount of luminescence is a measure of viable, metabolically active cells. MTT is frequently used, routine technique and ATP is a more sensitive method. [247]. Combination of the two should provide reliable HeLa and A549 cells were incubated with Ag₂S QD compositions for 48 h at a concentration range of 0.25 to 6 µg Ag/mL (Table 5. 2). In case of DOX loaded QDs, free DOX in the amount equivalent to the DOX content of FA-PEG-Ag₂S-DOX was used as a control. In general the cell viability significantly decreased with increasing concentrations of QDs, especially after DOX loading.

Based on the MTT and ATP assay results, , folic acid conjugation increased QD toxicity in HeLa cells, whereas no significant difference between Ag₂S and FA-PEG-Ag₂S was recorded in A549 cells (Figure 5. 5a to Figure 5. 5d). IC₅₀ of Ag₂S QDs, FA-PEG-Ag₂S and FA-PEG-Ag₂S-DOX for HeLa cells based on MTT assay were around 5.5, 3, 2.5 µg Ag/mL, and 4, 1.7, 1.4 µg Ag/mL based on ATP assay. However, IC₅₀ values of Ag₂S QDs, FA-PEG-Ag₂S for A549 cells was determined ca 5.5 µg Ag/mL by MTT and ca 3 µg Ag/mL by ATP assays. These indicate no significant change in the toxicity after FA conjugation and slightly more robust nature for A549 compared to HeLa (Figure 5. 5b and Figure 5. 5d). DOX loaded QDs reduced IC₅₀ for A549 to 3 and 1 µg Ag/mL based on MTT and ATP assays, respectively. Comparison of IC₅₀ values for HeLa and A549 cells, clearly shows enhanced toxicity due to receptor mediated enhanced uptake of FA-PEG-Ag₂S by HeLa cells with folate receptor overexpression. The toxicity seen in A549 cells can be explained with passive uptake of the particles, which was not affected by the FA conjugation [137]. The difference in calculated toxicity between ATP

and MTT assays is due to different mechanism in correlating collected data to cell viability, difference in strengths and weaknesses of protocols but as evident from the lower IC₅₀ values suggested by ATP assay, better sensitivity of the former especially at low doses [247].

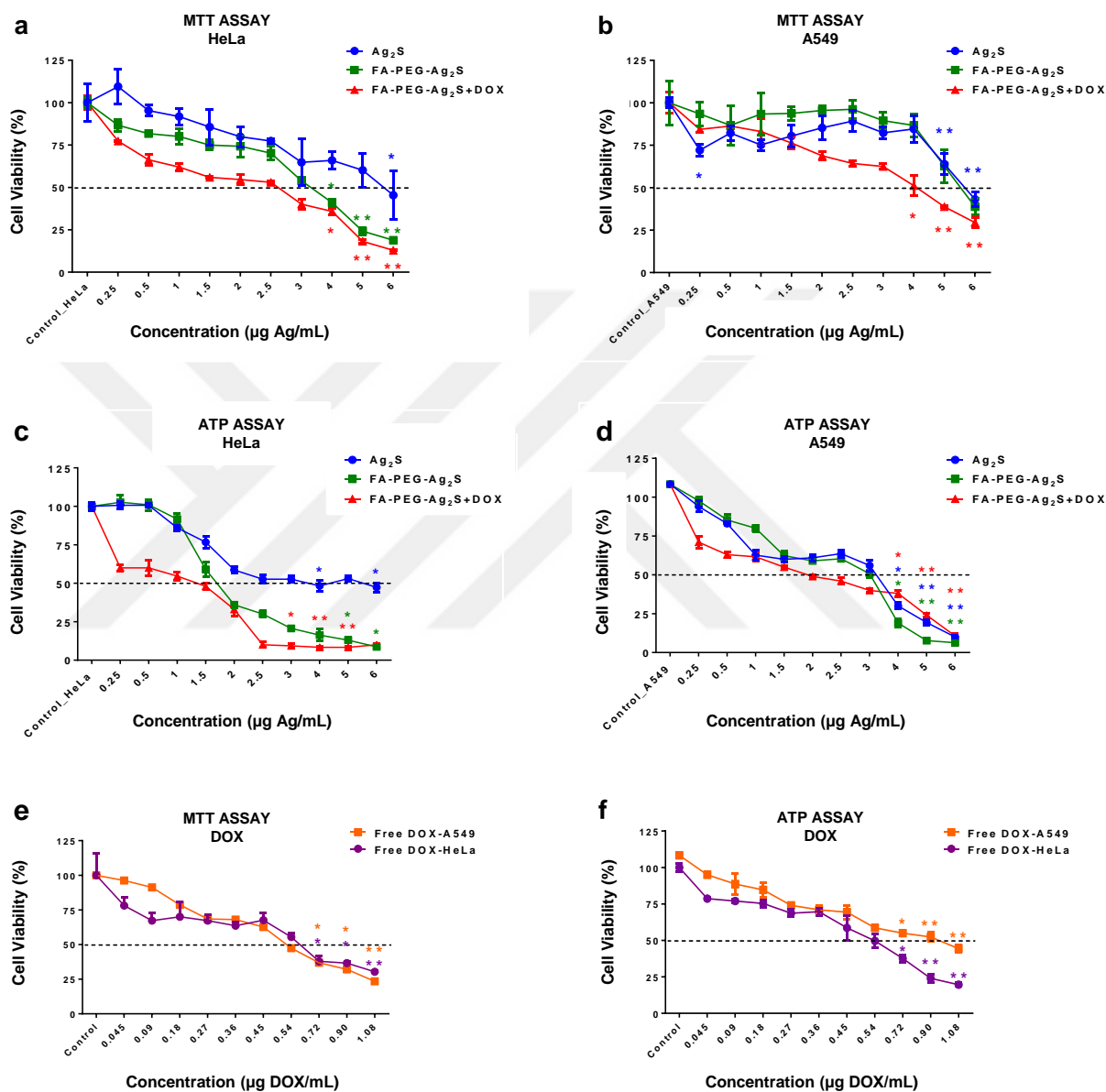


Figure 5. 5 Viability of HeLa and A549 cells treated with Ag₂S, FA-PEG-Ag₂S, FA-PEG-Ag₂S-DOX and free DOX after 48 hours incubation assessed by MTT and ATP assays. Viability of HeLa (a) and A549 (b) cells determined by MTT assay; viability of HeLa (c) and A549 (d) cells determined by ATP assay; viability of cells treated with free DOX based on MTT (e) and ATP (f) assays. Data are expressed as mean \pm S.D. ($n = 3$), ($p < 0.05$ (*), $p < 0.01$ (**)).

Toxicity of free DOX was also determined. MTT assay did not show a significant difference between the cell lines, but ATP assay showed significantly higher toxicity of free DOX to HeLa with about 0.54 versus 0.9 $\mu\text{g DOX/mL}$ for 50 % cell viability of HeLa and A549 cells, respectively (Figure 5. 5e and Figure 5. 5f). Based on these, both assays clearly show that loading DOX to FA conjugated QDs enhances its cytotoxic effect to HeLa, reducing IC₅₀ from 0.54 to 0.27 $\mu\text{g DOX/mL}$ for IC₅₀ (ATP assay). Results for A549 shows difference between the two assays. According to MTT loading DOX to QDs decreased its effectivity but according to ATP, increased its cytotoxic effect.

5.3.3 Cellular Uptake

In order to understand the viability data better, quantitative analysis of the intracellular uptake was done by determination of Ag in the cells after QD uptake. QD samples in fixed Ag amount (2 $\mu\text{g/mL Ag}$) were incubated with cells for 1 h and then, cells were digested with concentrated acid solutions and diluted to a certain volume with dH₂O. Ag amount in the cells were measured by ICP-MS using a freshly prepared Ag standard curve. As shown in Figure 5. 6, FA conjugation to QDs improved the uptake by FR positive HeLa cells about 3 fold. A slight increase in uptake by A549 cells was also determined, possibly as a side effect of FA free medium used in the cell culture, which usually slightly enhances the passive uptake. This is in agreement with the microscopy images (Figure 5. 7). After DOX loading, the uptake of nanoparticles demonstrated a decline in both cell lines, showing still about 2 fold more uptake by HeLa compared to A549 cells. This reduced uptake may be due to the decrease in zeta potential as shown in Table 5. 1. When viability results are re-examined with this data, it shows that although about 50 % less QDs enter to the cells, overall toxicity increased with DOX loaded particles, indicating a dramatic enhancement in drug efficacy. This may also explain decreasing viability in A549 cells after DOX loading to QDs as suggested by MTT assay.

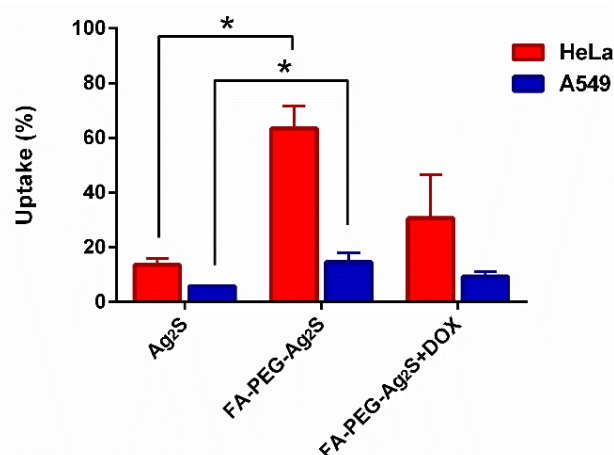


Figure 5. 6 Intracellular quantification of QDs in HeLa and A549 cells. Samples at 2 $\mu\text{g}/\text{mL}$ Ag concentration were incubated with cells for 1 h. Measurements were done by ICP-MS instrument. The data are expressed as mean \pm S.D. ($n = 3$), ($p < 0.05(*)$).

Internalization of QDs by cells were also confirmed by the fluorescence microscopy. The microscopy images of the cells incubated with FA-PEG-Ag₂S and FA-PEG-Ag₂S-DOX QDs for 1 h are shown in Figure 5. 7. Short incubation time was used to be able to differentiate receptor mediated endocytosis versus passive uptake between the two types of cells. NIR emission signal originating from QDs, demonstrated with red colour, is dramatically higher in HeLa cells (Figure 5. 7c and Figure 5. 7d) than A549 cells. This supported efficient targeting of HeLa cells via FA-receptor recognition and low amount of passive uptake by A549 cells [248]. Furthermore, the QDs were mainly distributed in cytoplasm, indicating cellular internalization instead of adhesion to the cell surface. DOX loading to nanoparticles made this difference more obvious. The strong red emission of DOX is stronger in FA positive HeLa cell lines (Figure 5. 7e and Figure 5. 7f) compared to FA deficient A549 cells (Figure 5. 7k and Figure 5. 7l). No DOX or QD signal was recorded in the control cells as seen in Figure 5. 7a-b and Figure 5. 7g-h. These experiments suggest that the FA conjugated and DOX loaded Ag₂S QDs were selectively targeted and internalized to the folate receptor positive cancer cells.

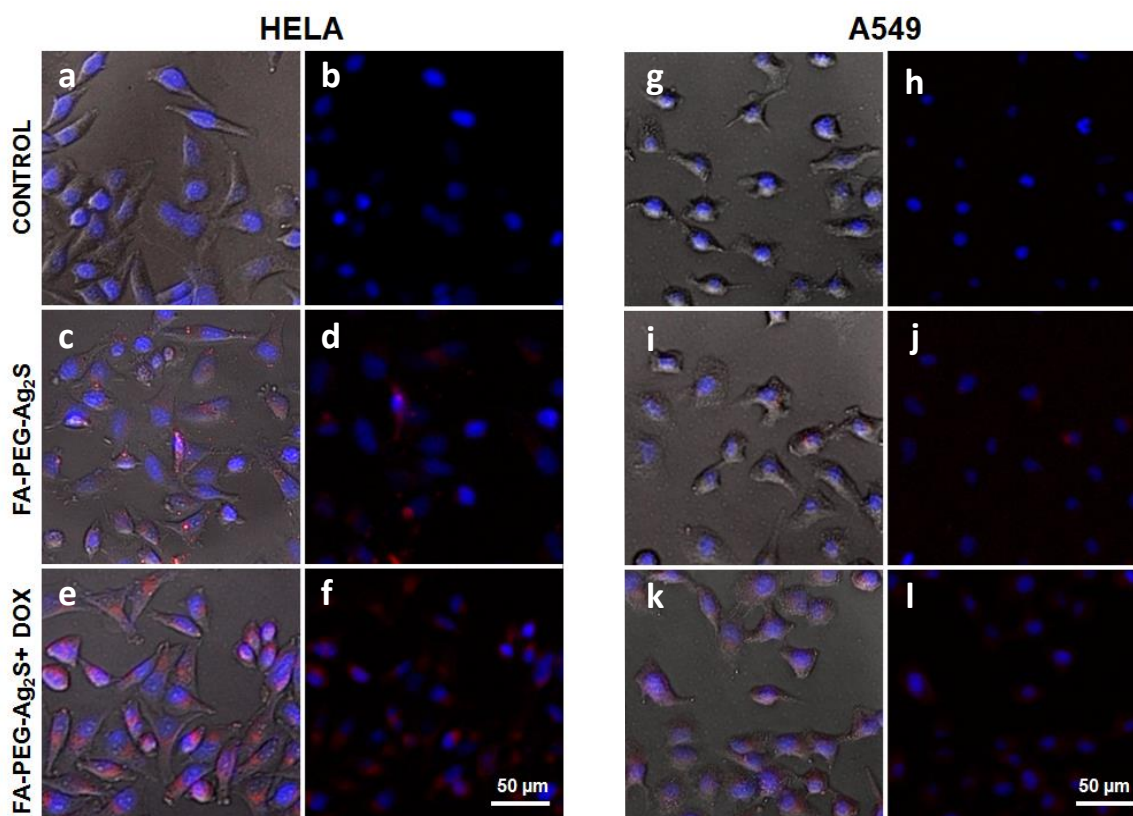


Figure 5. 7 Fluorescence microscopy images of control HeLa cells (a, b) and control A549 cells (g, h); HeLa cells after 1 h of incubation with FA-PEG-Ag₂S (c, d) and FA-PEG-Ag₂S-DOX QDs (e, f) at 2 μg/mL Ag concentration; A549 cells after 1 h of incubation with FA-PEG-Ag₂S (i, j) DOX FA-PEG-Ag₂S-DOX QDs (k, l) in 2 μg/mL Ag concentration. Images a and g are merged images from the bright field, DAPI, CY3 and NIR filters; b and h are merged images from DAPI, CY3 and NIR filters; images c and i are merged images from the bright field, DAPI and NIR filters; d and j are merged images from DAPI and NIR filters; e and k are merged images from the bright field, DAPI and CY3 filters; f and k are merged images from DAPI and CY3 filters. Blue emission indicates DAPI staining for cell nuclei. Red emission originates from QDs in images c, d, I and j; and from DOX in images e, f, k and l.

5.3.4 Determination of Apoptosis and Necrosis

To gain further information on the toxicity of the prepared QDs, apoptosis/necrosis amounts were determined using standard protocols. Firstly, Annexin V-FITC/PI apoptosis assay was used to determine early apoptotic, necrotic and viable cells. This technique is based on the detection of annexin V, which is one of the earlier markers of

apoptosis. The membrane phosphatidylserine (PS) is translocated from the inner side of the plasma membrane to the surface at the onset of apoptosis. Annexin V, which is a Ca²⁺-dependent phospholipid-binding protein, shows high affinity for PS and its labeling with a fluorescent tag, such as FITC, allows detection of apoptotic cells [249]. Annexin V-FITC can be also conjugated with propidium iodide, which enters and stains dead cells but is excluded from live cells [250]. So, combination of these dyes provides detection of early apoptotic (Annexin V-FITC positive, PI negative), necrotic (Annexin V-FITC positive, PI positive) and viable cells (Annexin V-FITC negative, PI negative). Representative images in Figure 5. 8A and Figure 5. 8B demonstrate the apoptotic and necrotic effects of the QDs on HeLa and A549 cells. No significant signal of Annexin V-FITC or PI was detected in the Ag₂S treated HeLa or A549 cells. But, FA conjugation enhanced both Annexin V-FITC and PI signals in HeLa cells, confirming effective receptor mediated targeting. Increase in the intensity of both signals dramatically increased after DOX loading as expected for HeLa. Reasonable amount of signal from both dyes were obtained only with FA-PEG-Ag₂S-DOX in A549. Compared to free DOX, FA-PEG-Ag₂S-DOX induce dramatically more apoptosis/necrosis only in HeLa, confirming FR mediated delivery of drug loaded FA tagged QDs and hence, significantly improved drug toxicity.

In addition, M30 assay was used to quantify the apoptosis induced by Ag₂S, FA-PEG-Ag₂S, FA-PEG-Ag₂S-DOX QDs and free DOX. The level of caspase-cleaved keratin 18 (ccK18, M30), which is a well-known marker of apoptosis was determined by this technique as a measure of apoptosis, and showed a clear difference between the two cell lines and QD compositions [253]. As summarized in Figure 5. 8C, results indicate significant enhancement of apoptosis in A549 compared to control only with FA-PEG-Ag₂S-DOX and there is no statistically significant difference between DOX loaded particle and free DOX. On the other hand, there is about 3 fold increase in M30 level induced by FA-PEG-Ag₂S-DOX compared to FA-PEG-Ag₂S. So, QDs do not cause a significant apoptosis unless loaded with a therapeutic drug and directed to the target cell.

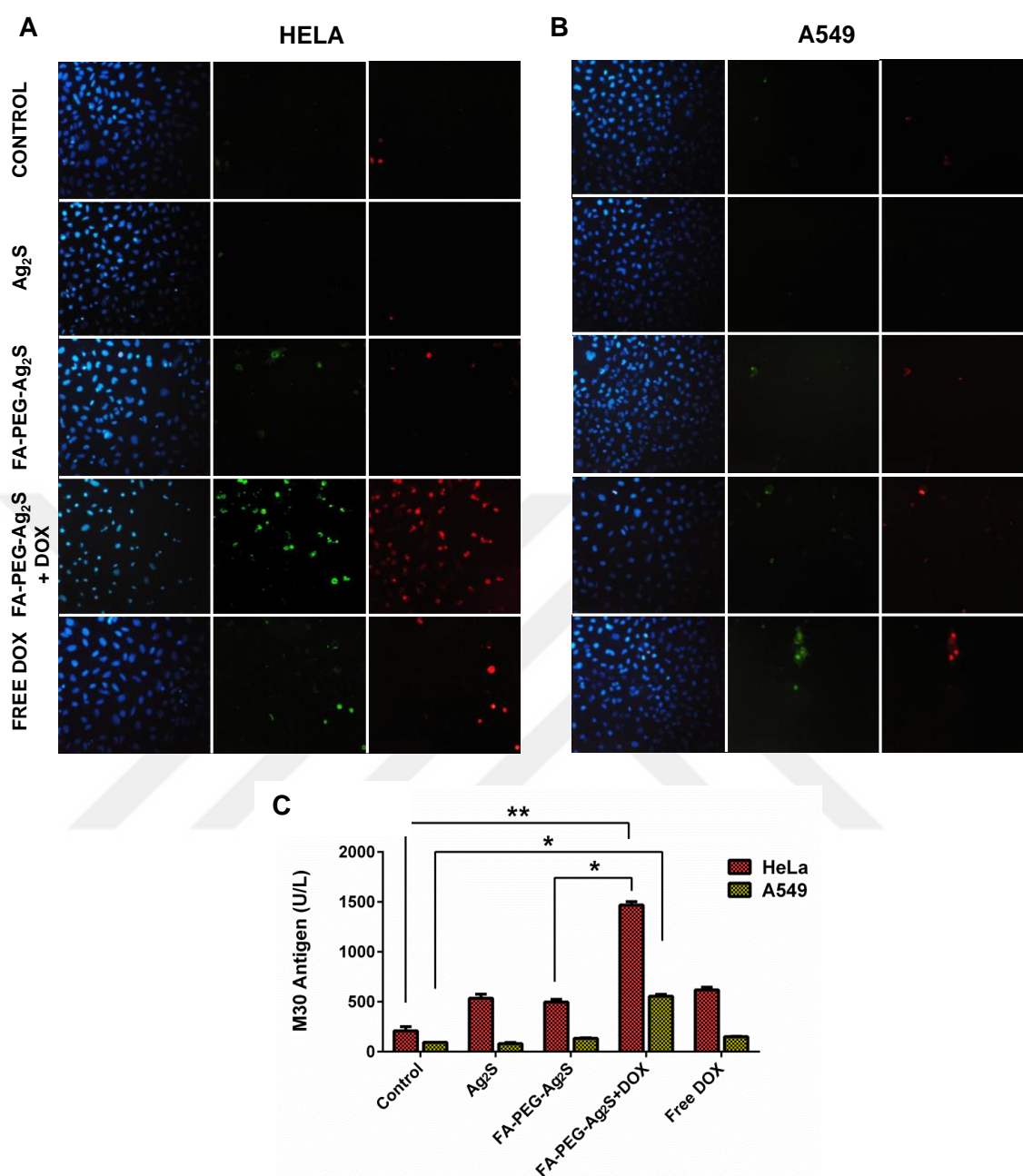


Figure 5. 8 (A) Fluorescence staining of HeLa and (B) A549 cells with Hoechst 33342 (blue), Annexin V-FITC (green) and Propidium Iodide (red) after being treated with Ag₂S, FA-PEG-Ag₂S, and FA-PEG-Ag₂S-DOX QDs at 1.5 μ g/ml Ag concentration and free DOX at 0.27 μ g/mL for 24 h ($n = 3$). Untreated cells were used as control. (C) M30 antigen level of HeLa and A549 cells incubated with nanoparticles at 1.5 μ g/ml Ag concentration for 48 h. The data are expressed as mean \pm S.D. ($n = 2$), ($p < 0.05$ (*), $p < 0.01$ (**)).

These results were also confirmed with the images obtained by mitochondrial membrane potential assay (Figure 5. 9). This assay detects changes in the mitochondrial $\Delta\psi_m$ as an early indication of apoptosis. JC-1, a lipophilic cationic fluorescence dye, can enter mitochondria and shows a fluorescence changing from red to green with decreasing membrane potential. This dye aggregates in health cells with high mitochondrial $\Delta\psi_m$, and emit red. In apoptotic cells, the mitochondrial $\Delta\psi_m$ is lost and JC-1 accumulates in the cytosol in a green fluorescent monomeric form [251, 252]. As seen in Figure 5. 9, this assay also indicated a dramatic difference between the two cell types when demonstrates FA-PEG-Ag₂S-DOX QDs were used, with significant amount of green luminescence observed only in HeLa. Free DOX failed to show same effect. This also confirms that DOX loaded on FA-tagged particles has higher efficacy due to selective delivery of DOX to HeLa cells, increasing the cellular uptake compared to free DOX. In folate receptor negative cells, A549, no apoptotic effect was detected with any of the compositions or free DOX, except a very low level of apoptosis with PEG-FA-Ag₂S-DOX. This is in agreement with previous observations and possibly due to enhanced uptake in FA free medium.

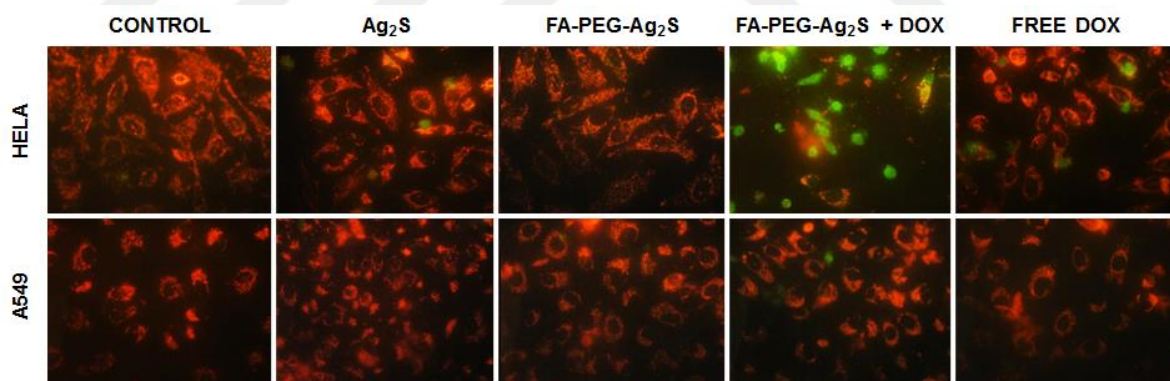


Figure 5. 9 Mitochondrial membrane potential assay in HeLa and A549 cells visualized by fluorescence microscopy. The cells were exposed to Ag₂S, FA-PEG-Ag₂S, FA-PEG-Ag₂S-DOX QDs at 1.5 $\mu\text{g}/\text{mL}$ Ag concentration and free DOX at equivalent concentrations of DOX-PEG-FA-Ag₂S QDs for 24 h. Untreated cells were used as control. Red fluorescence indicates high membrane potential and green fluorescence indicates loss of mitochondrial membrane potential.

5.4 Conclusion

In this study, we report the design, synthesis and theranostic application of folate targeted, DOX loaded multifunctional Ag₂S NIR emitting QDs. FA-PEG-Ag₂S-DOX

QDs have ultrasmall size which is critical for receptor mediated targeting. Larger particles are usually cleared by RES, losing selectivity. Particles are also cationic which can be utilized for gene/drug loading and enhance cell-QD interaction favorably. DOX was loaded in PBS to FA-PEG-Ag₂S QDs for targeted delivery to FR positive HeLa cells. Overall, FA-PEG-Ag₂S QDs have 0.0354 mg (8.02 μmol) FA and 0.0367 mg DOX/ mg of nanoparticle. This is a quite high DOX loading amount compared to literature and we suggest DOX loading to both PEI and PEG chains of the corona as the source of such high loading, since zeta potential decreases significantly upon DOX loading. Ag₂S QDs have strong emission around 750 nm which demonstrated strong optical signal suppressing the background significantly as shown in the fluorescent microscopy images.

FR mediated uptake of FA conjugated Ag₂S QDs selectively by HeLa in a comparative study with A549 cells was confirmed by Ag content of cells determined by ICP, and strong endosomal optical signal of QDs in fluorescence microscopy studies. This is in correlation with the toxicity studies performed by MTT, ATP, M30 assays as well as Annexin V-FITC and IP staining of QD treated cells. The results have clearly demonstrated the preferential targeting of HeLa cells and high apoptotic effect of DOX by means of higher uptake compared to A549 FR negative cells. DOX delivered to HeLa by FA-tagged Ag₂S QDs increased the drug efficacy, lowering IC₅₀ value. This effect points out a great importance in respect of reducing side effects of the existing chemotherapeutic drugs and their minimal introduction to biological systems. It is important to point out that, after DOX loading, internalization of FA-PEG-Ag₂S QDs is reduced by about 50 %. This indicates that after the initial interaction of FA with the FR, overall positive charge aids internalization via cell surface interaction.

Both targeted delivery of GFP and GFP-p53, and targeted delivery of combination therapy (poly I:C and DOX) were tried with FA-PEG-Ag₂S (Appendix B). But, the high transfection efficiency achieved with PEI/2MPA-Ag₂S have not been seen. In deed, there is no practical amount of transfection in HeLa, A549, MEF wt or MEF (p53 +) cells. This may be due to PEG chains which prevents effective release, or may be related to poly(I:C) release rate.

Strong near IR emission coming from QDs also proved promising imaging ability to determine the biodistribution of the drug and to follow the the progress of the therapy.

Chapter 6

6. CONCLUSIONS AND FUTURE DIRECTION

In this thesis work, cationic Ag₂S NIRQDs were developed in a very simple, one step synthetic route with polyethyleneimine (PEI)/small molecule mixture for coating at low temperatures. Ag₂S NIRQDs were synthesized directly in water from AgNO₃ and Na₂S / TAA under inert atmosphere. To obtain high emission efficiency, colloidal stability and low cytotoxicity, branched PEI in different MW (25kDa to 1.8 kDa) and small molecules: 2-mercaptopropionic acid (2MPA), l-cysteine (Cys), l-arginine, l-histidine and l-glutamic acid were combined as coating in a broad range of mole/mole ratio and the effect of the reaction variables such as Ag/S, Ag/coating ratio, synthesis duration, synthesis temperature, synthesis pH and pH after synthesis were studied. Low molecular weight PEI and small molecules other than 2MPA and Cys have failed. Two common feature of these two species are the thiol functionality which strongly binds to Ag sites on the crystal surface and the carboxylic acid in the alpha position which can provide a secondary stabilization on the crystal surface.

Highest quantum yield and colloidal stability were obtained with branched PEI/2MPA(80/20) and branched PEI/Cys (60/40) coated Ag₂S NIRQDs. The pH of the reaction solution was found to be critical and optimized at pH 9-10.5 to deprotonate PEI to allow its binding to the crystal surface electrostatically. Ag/S and coating/Ag ratio were optimized at 4 and 5, respectively. The highest QY was obtained with QDs synthesized at room temperature. Use of only PEI as a coating provided colloidal stability, but poor luminescence due to non-dense packing resulting in uncoordinated surface sites, acting as defects on crystal surface, decreasing quantum yield. Incorporation of 2MPA or Cys as a co-stabilizer diminished such defects, providing a better surface passivation, increasing the QY. Resulting QDs were in highest quantum yield reported until now (150 % - 157 % at pH 7.4) with an emission maximum wavelength between 700-850 nm and FWHM

between 100-170 nm. Synthesized Ag₂S QDs are spherical monoclinic crystals with about 2-4 nm diameter. They have high positive surface charge and small hydrodynamic size (below 100 nm), which is favourable for molecular targeting and long blood circulation in the *in vivo* applications of these nanoparticles. These Ag₂S QDs are the first cationic NIRQDs in the literature which is important for gene and anionic drug delivery applications.

In vitro cell viability results showed that binding of PEI to Ag₂S surface improves cytocompatibility dramatically with respect to free PEI. Ag₂S NIRQDs are cytocompatible below 5 µg Ag⁺/mL without any PEGylation. It equals to 23 µg/mL of PEI/2MPA(80/20); 17.6 µg /mL of PEI/Cys (60/40) Ag₂S NIRQDs in terms of total nanoparticle.

Ag₂S QDs demonstrated an efficient cell internalization and endosomal localization with strong luminescence. The exceptionally strong luminescence in the NIR I region, allows practical optical imaging of these QDs with good S/N ratio. This was further confirmed with *in vivo* studies on worms (*C. elegans*) and BALB/c mice which were subjected to an intraperitoneal injection of Ag₂S QDs. These NIR emitting QDs indicated high effective optical imaging with strong contrast in NIR I region, strongly suppressing the autofluorescence.

To increase the biocompatibility, Ag₂S QDs (PEI/2MPA coated) were conjugated with PEG. PEGylated Ag₂S QDs were loaded with DOX, anticancer drug, and tested as drug delivery vehicle which can be tracked by optical imaging. Enhanced apoptotic effect was obtained compared to free DOX. This approached utilized passive uptake of DOX loaded QDs using the EPR effect of cancer cells. In order to target the cancer cells and enhance the specific uptake, the Ag₂S PEI/Cys QDs were conjugated with folic acid via a PEG linker, and they were also loaded with DOX. Toxicity of the formulation to FR positive HeLa cells compared to FR negative A549 was dramatically different due to receptor mediated uptake of the particles by the former cells, resulting in much higher concentration of the QD and hence DOX in the targeted cells. This reduced IC₅₀ from 0.54 µg/mL free DOX to 0.27 µg/mL DOX when loaded to targeted QDs. This is very crucial in reduction of side effects of the chemotherapy while enhancing its efficacy in the target tissues. Although not as important in the cell culture but definitely a key

parameter is the small hydrodynamic size of the particles, which would provide opportunity for long blood circulation and targeted delivery *in vivo*.

In addition to drug delivery application, QDs were also used as a gene delivery agent because of high cationic nature coming from PEI, a golden standard for gene delivery. Here, two types of gene which were in plasmid structure, were employed. One of them was GFP, used usually to show the transfection ability of the materials and another one was p53-GFP, an apoptotic gene which is used for gene therapy in cancer. PEI/2MPA coated Ag₂S QDs showed high transfection efficiency which was about 40 % in MCF-7 and HeLa under unoptimized conditions. This level was lower with PEI/Cys Ag₂S QDs compared to PEI/2MPA Ag₂S according to microscopy images. Another point to be emphasized is that PEGylation dramatically dropped the transfection ability of the nanoparticles, while improving the biocompatibility.

As a conclusion, in this thesis, first cationic Ag₂S NIR QDs were synthesized in a simple, green route, with an exceptionally high fluorescent QY in the NIR I, which provided strong optical images with high contrast in the *in vitro* and *in vivo* studies. These QDs provide an excellent theranostic platform with ability to deliver genes and drugs via EPR effect or receptor-mediated endocytosis. Unlike PEI itself, these cationic Ag₂S NIR QDs offer better cytocompatibility which can be further tuned by PEGylation.

For future applications, transfection ability of PEGylated QDs especially explained in Chapter 3 will be investigated in detail decreasing the PEGylation amount without reducing biocompatibility and drug loading efficiency as well as targeting to cancer cells.

6.1 Publications, Conferences & Patents

Publications:

Fatma Demir Duman, Rouhullah Khodadust, Emek Goksu Durmusoglu, Mustafa Baris Yagci, Havva Yagci Acar, Impact of reaction variables and PEI/L-cysteine ratio on optical properties and cytocompatibility of cationic Ag₂S Quantum Dots as NIR Bio-Imaging probes, **RSC Advances**, 2016,**6**, 77644-77654 (DOI: 10.1039/C6RA13804G).

D. Asik, M. B. Yagci, F. Demir Duman, H. Yagci Acar, One step emission tunable synthesis of PEG coated Ag₂S NIR quantum dots and the development of receptor

targeted drug delivery vehicles thereof, **J. Mat. Chem. B**, 2016, 4, 1941-1950 (DOI: 10.1039/c5tb02599k).

Fatma Demir Duman, Ibrahim Hocaoglu, Deniz Gulfem Ozturk, Devrim Gozuacik, Alper Kiraz and Havva Yagci Acar, Highly luminescent and cytocompatible cationic Ag₂S NIR-emitting quantum dots for optical imaging and gene transfection, **Nanoscale**, 2015, 7, 11352-11362 (DOI: 10.1039/c5nr00189g).

Ibrahim Hocaoglu, Fatma Demir, Ozgur Birer, Alper Kiraz, Chantal Sevrin, Christian Grandfils and Havva Yagci Acar, Emission tunable, cyto/hemocompatible, near-IR-emitting Ag₂S quantum dots by aqueous decomposition of DMSA, **Nanoscale**, 2014, 6, 11921-1193 (DOI: 10.1039/c4nr02935f).

Conferences:

Fatma Demir Duman, Rouhollah Khodadust, Havva Yagci Acar, Synthesis and Characterization of PEGylated Near-IR-Emitting Ag₂S Quantum Dots for Tumor Imaging and Therapy, 10th World Biomaterials Congress (WBC 2016), May 17-22, 2016, Montreal, Canada (*Oral presentation*).

F.Demir Duman, R. Khodadust, D. Asik, H. Yagci Acar, Synthesis and Characterization of Cationic Ag₂S QDs for Tumor Targeted Gene Delivery, Characterisation of Nanomaterials and Nanomedicine- International Workshop Joint Research Center, Nov 23-25, 2015, Ispra, Italy (*Oral presentation*).

F.Demir, R. Khodadust, D. Asik, H. Yagci Acar, Synthesis and Characterization of Folate Targeted Poly(ethylene glycol) Coated Cationic Ag₂S QDs for Tumor Targeted Gene Delivery, Nanotech France 2015 International Conference & Exhibition (Nanotech France 2015), Jun 15-17, 2015, Paris, France (*Oral presentation*).

Didar Asik, Fatma Demir and Havva Yagci Acar, Synthesis of 1-PEI and 2MPA Coated Biocompatible Silver Sulfide QDs as Transfection Vectors, Nanotech France 2015 International Conference & Exhibition (Nanotech France 2015), Jun 15-17, 2015, Paris, France (*Oral presentation*).

Havva Funda Yagc, Acar, Ibrahim Hocaoglu, Fatma Demir, Alper Kiraz, Natali Çizmeciyen, Alphan Sennaroglu, Deniz Gulfem Ozturk, Devrim Gozuacik, Chantal Sevrin, Christian Grandfils, Rengin Erdem, Can Özen, Highly Luminescent Aqueous Ag₂S Quantum Dots as New Generation Quantum Dots, Fourth International Conference on Multifunctional, Hybrid and Nanomaterials (Hybrid Materials 2015), March 9 – 13, 2015, Sitges, Spain (*Oral presentation*).

Christian Grandfils, Ibrahim Hocaoglu, FatmaDemir, Ozgur Birer, Alper Kiraz, Chantal Sevrin, Havva Yagci Acar, *In vitro* hemocompatibility assessment of Near-IR-Emitting Ag₂S Quantum Dots (QD), Nanobiotechnology - International Workshop on Nanobioscience, Nov 24-26, 2014, Ispra, Italy (*Oral presentation*).

Fatma Demir, Ibrahim Hocaoglu, Deniz Gulfem Ozturk, Alper Kiraz, Devrim Gozuacik, Havva Yagci Acar, Ag₂S-Based NIR-emitting Quantum Dots as New Theranostic Materials, 2nd International Conference on Bioinspired and Biobased Chemistry & Materials, October 15-17, 2014, Nice, France (*Oral presentation*).

Havva Funda Yagci Acar, Ibrahim Hocaoglu, Didar Aşık, Recep Kaş, Fatma Demir, Development of luminescent_magnetic hybrid nanoparticles, 2nd International Conference on Bioinspired and Biobased Chemistry & Materials, October 15-17, 2014, Nice, France (*Oral presentation*).

Demir F., Bozdogan Pala B., Cirak T., Turk M., Denkbaz E.B., Cationic Peptide Nanoparticles for Cancer Gene Therapy, NanoTR VIII, June 25-29, 2012, Hacettepe University, Ankara, Turkey (*Poster presentation*).

Akbudak S., Demir F., Vural T., Bozdogan Pala B., Denkbaz E.B., Preparation and characterization of Peptide Nanotube -Single Wall Carbon Nanotube Structures, NanoTR VIII, June 25-29, 2012, Hacettepe University, Ankara, Turkey (*Poster presentation*).

Demir F., Bozdogan Pala B., Cirak T., Demirbilek M., Denkbaz E.B., Diphenylalanine Peptide Nanospheres for Targeted Therapy, NanoTR VII, June 27-July 1, 2011, Sabanci University, Istanbul, Turkey (*Oral presentation*).

Patents:

H. Yagci Acar, F. Demir Duman, PCT/TR2014/000317, Near-IR Emitting Cationic Silver Chalcogenide Quantum Dots.



A Appendix A

A. CALCULATION OF PARTICLE SIZE FOR Ag₂S QDs BY BRUS EQUATION

A.1 Band gap determination from absorption spectra

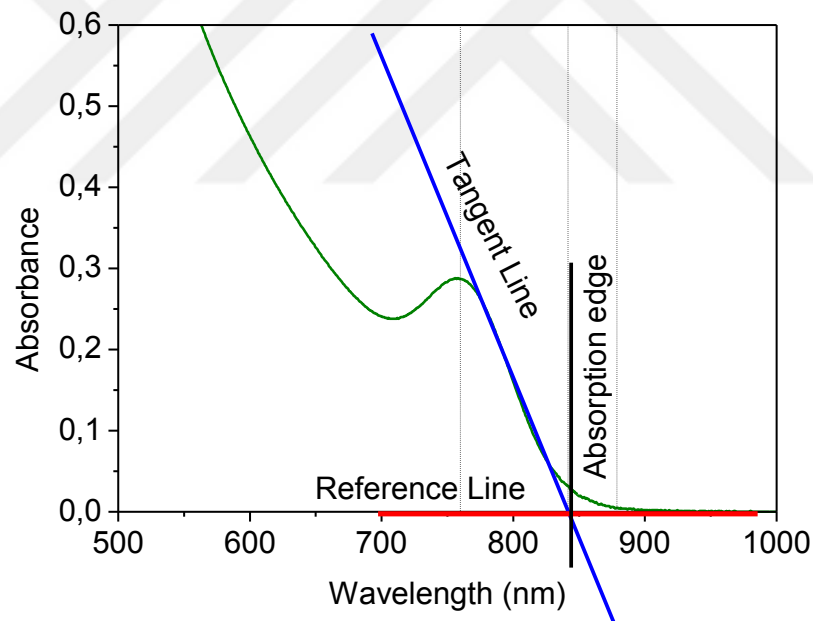


Figure A. 1 Absorbance spectrum of Ag₂S NIRQDs for determination of crystal band gap.

Band gap of QDs can be determined from the absorbance spectra of the nanocrystals. Absorption edge determined from the absorbance spectrum provides the band gap of the material as shown in the Figure A1. A reference line is drawn to base level where the absorption is zero and a tangent line is drawn to the excitonic peak. The intersection of these two lines presents the absorption edge. This edge corresponds to the band gap of

QD. Radius of the QD can be calculated from the Brus equation applying this band gap value (Eqn 1.2).

$$E_g(QD) = E_g(Bulk) + \frac{h^2}{8R^2} \left[\frac{1}{m_e} + \frac{1}{m_h} \right] - 1.8 \frac{e^2}{4\pi\epsilon\epsilon_0 R}$$

m_e (0.286 m_0) and m_h (1.096) are the respective effective electron and hole masses for Ag₂S. ϵ_{Ag_2S} (5.95) is the dielectric constant. Band gap energy of bulk ($E_g(Bulk)$) Ag₂S is 0.9 eV. Calculated particle sizes are listed on Table A.1 for different absorption wavelengths and corresponding band gap energies.

Table A. 1 Particle size of Ag₂S NIRQDs with respect to absorbance edges calculated from Brus equation.

Wavelength (nm)	Diameter (nm)	Band Gap (eV)	Wavelength (nm)	Diameter (nm)	Band Gap (eV)
601	2.04	2.07	622	2.10	2.00
602	2.04	2.06	623	2.10	1.99
603	2.05	2.06	624	2.10	1.99
604	2.05	2.06	625	2.10	1.99
605	2.05	2.05	626	2.11	1.98
606	2.05	2.05	627	2.11	1.98
607	2.06	2.05	628	2.11	1.98
608	2.06	2.04	629	2.11	1.97
609	2.06	2.04	630	2.12	1.97
610	2.06	2.04	631	2.12	1.97
611	2.07	2.03	632	2.12	1.96
612	2.07	2.03	633	2.12	1.96
613	2.07	2.03	634	2.13	1.96
614	2.08	2.02	635	2.13	1.96
615	2.08	2.02	636	2.13	1.95
616	2.08	2.02	637	2.13	1.95
617	2.08	2.01	638	2.14	1.95
618	2.09	2.01	639	2.14	1.94
619	2.09	2.01	640	2.14	1.94
620	2.09	2.00	641	2.15	1.94
621	2.09	2.00	642	2.15	1.93

Wavelength (nm)	Diameter (nm)	Band Gap (eV)	Wavelength (nm)	Diameter (nm)	Band Gap (eV)
643	2.15	1.93	680	2.25	1.83
644	2.15	1.93	681	2.25	1.82
645	2.16	1.92	682	2.25	1.82
646	2.16	1.92	683	2.26	1.82
647	2.16	1.92	684	2.26	1.82
648	2.16	1.92	685	2.26	1.81
649	2.17	1.91	686	2.26	1.81
650	2.17	1.91	687	2.27	1.81
651	2.17	1.91	688	2.27	1.80
652	2.17	1.90	689	2.27	1.80
653	2.18	1.90	690	2.28	1.80
654	2.18	1.90	691	2.28	1.80
655	2.18	1.90	692	2.28	1.79
656	2.18	1.89	693	2.28	1.79
657	2.19	1.89	694	2.29	1.79
658	2.19	1.89	695	2.29	1.79
659	2.19	1.88	696	2.29	1.78
660	2.20	1.88	697	2.29	1.78
661	2.20	1.88	698	2.30	1.78
662	2.20	1.88	699	2.30	1.78
663	2.20	1.87	700	2.30	1.77
664	2.21	1.87	701	2.31	1.77
665	2.21	1.87	702	2.31	1.77
666	2.21	1.86	703	2.31	1.77
667	2.21	1.86	704	2.31	1.76
668	2.22	1.86	705	2.32	1.76
669	2.22	1.86	706	2.32	1.76
670	2.22	1.85	707	2.32	1.76
671	2.22	1.85	708	2.33	1.75
672	2.23	1.85	709	2.33	1.75
673	2.23	1.84	710	2.33	1.75
674	2.23	1.84	711	2.33	1.75
675	2.24	1.84	712	2.34	1.74
676	2.24	1.84	713	2.34	1.74
677	2.24	1.83	714	2.34	1.74
678	2.24	1.83	715	2.34	1.74
679	2.25	1.83	716	2.35	1.73

Wavelength (nm)	Diameter (nm)	Band Gap (nm)	Wavelength (nm)	Diameter (nm)	Band Gap (nm)
717	2.35	1.73	754	2.46	1.65
718	2.35	1.73	755	2.46	1.64
719	2.36	1.73	756	2.46	1.64
720	2.36	1.72	757	2.46	1.64
721	2.36	1.72	758	2.47	1.64
722	2.36	1.72	759	2.47	1.64
723	2.37	1.72	760	2.47	1.63
724	2.37	1.71	761	2.48	1.63
725	2.37	1.71	762	2.48	1.63
726	2.38	1.71	763	2.48	1.63
727	2.38	1.71	764	2.48	1.63
728	2.38	1.71	765	2.49	1.62
729	2.38	1.70	766	2.49	1.62
730	2.39	1.70	767	2.49	1.62
731	2.39	1.70	768	2.50	1.62
732	2.39	1.70	769	2.50	1.61
733	2.40	1.69	770	2.50	1.61
734	2.40	1.69	771	2.51	1.61
735	2.40	1.69	772	2.51	1.61
736	2.40	1.69	773	2.51	1.61
737	2.41	1.68	774	2.51	1.60
738	2.41	1.68	775	2.52	1.60
739	2.41	1.68	776	2.52	1.60
740	2.42	1.68	777	2.52	1.60
741	2.42	1.68	778	2.53	1.60
742	2.42	1.67	779	2.53	1.59
743	2.42	1.67	780	2.53	1.59
744	2.43	1.67	781	2.53	1.59
745	2.43	1.67	782	2.54	1.59
746	2.43	1.66	783	2.54	1.59
747	2.44	1.66	784	2.54	1.58
748	2.44	1.66	785	2.55	1.58
749	2.44	1.66	786	2.55	1.58
750	2.44	1.66	787	2.55	1.58
751	2.45	1.65	788	2.56	1.58
752	2.45	1.65	789	2.56	1.57
753	2.45	1.65	790	2.56	1.57

Wavelength (nm)	Diameter (nm)	Band Gap (eV)	Wavelength (nm)	Diameter (nm)	Band Gap (eV)
791	2.57	1.57	827	2.68	1.50
792	2.57	1.57	828	2.68	1.50
793	2.57	1.57	829	2.68	1.50
794	2.57	1.56	830	2.69	1.50
795	2.58	1.56	831	2.69	1.49
796	2.58	1.56	832	2.69	1.49
797	2.58	1.56	833	2.70	1.49
798	2.59	1.56	834	2.70	1.49
799	2.59	1.55	835	2.70	1.49
800	2.59	1.55	836	2.71	1.49
801	2.60	1.55	837	2.71	1.48
802	2.60	1.55	838	2.71	1.48
803	2.60	1.55	839	2.72	1.48
804	2.60	1.54	840	2.72	1.48
805	2.61	1.54	841	2.72	1.48
806	2.61	1.54	842	2.72	1.47
807	2.61	1.54	843	2.73	1.47
808	2.62	1.54	844	2.73	1.47
809	2.62	1.53	845	2.73	1.47
810	2.62	1.53	846	2.74	1.47
811	2.63	1.53	847	2.74	1.47
812	2.63	1.53	848	2.74	1.46
813	2.63	1.53	849	2.75	1.46
814	2.64	1.53	850	2.75	1.46
815	2.64	1.52	851	2.75	1.46
816	2.64	1.52	852	2.76	1.46
817	2.65	1.52	853	2.76	1.46
818	2.65	1.52	854	2.76	1.45
819	2.65	1.52	855	2.77	1.45
820	2.65	1.51	856	2.77	1.45
821	2.66	1.51	857	2.77	1.45
822	2.66	1.51	858	2.78	1.45
823	2.66	1.51	859	2.78	1.45
824	2.67	1.51	860	2.78	1.44
825	2.67	1.50	861	2.79	1.44
826	2.67	1.50	862	2.79	1.44

Wavelength (nm)	Diameter (nm)	Band Gap (eV)	Wavelength (nm)	Diameter (nm)	Band Gap (eV)
863	2.79	1.44	898	2.92	1.38
864	2.80	1.44	899	2.92	1.38
865	2.80	1.44	900	2.92	1.38
866	2.80	1.43	901	2.93	1.38
867	2.81	1.43	902	2.93	1.38
868	2.81	1.43	903	2.93	1.37
869	2.81	1.43	904	2.94	1.37
870	2.82	1.43	905	2.94	1.37
871	2.82	1.43	906	2.94	1.37
872	2.82	1.42	907	2.95	1.37
873	2.83	1.42	908	2.95	1.37
874	2.83	1.42	909	2.95	1.37
875	2.83	1.42	910	2.96	1.36
876	2.84	1.42	911	2.96	1.36
877	2.84	1.42	912	2.97	1.36
878	2.85	1.41	913	2.97	1.36
879	2.85	1.41	914	2.97	1.36
880	2.85	1.41	915	2.98	1.36
881	2.86	1.41	916	2.98	1.36
882	2.86	1.41	917	2.98	1.35
883	2.86	1.41	918	2.99	1.35
884	2.87	1.40	919	2.99	1.35
885	2.87	1.40	920	2.99	1.35
886	2.87	1.40	921	3.00	1.35
887	2.88	1.40	922	3.00	1.35
888	2.88	1.40	923	3.01	1.35
889	2.88	1.40	924	3.01	1.34
890	2.89	1.40	925	3.01	1.34
891	2.89	1.39	926	3.02	1.34
892	2.89	1.39	927	3.02	1.34
893	2.90	1.39	928	3.02	1.34
894	2.90	1.39	929	3.03	1.34
895	2.90	1.39	930	3.03	1.34
896	2.91	1.39	931	3.04	1.33
897	2.91	1.38	932	3.04	1.33

Wavelength (nm)	Diameter (nm)	Band Gap (eV)	Wavelength (nm)	Diameter (nm)	Band Gap (eV)
933	3.04	1.33	962	3.16	1.29
934	3.05	1.33	963	3.16	1.29
935	3.05	1.33	964	3.16	1.29
936	3.05	1.33	965	3.17	1.29
937	3.06	1.33	966	3.17	1.29
938	3.06	1.32	967	3.18	1.28
939	3.07	1.32	968	3.18	1.28
940	3.07	1.32	969	3.18	1.28
941	3.07	1.32	970	3.19	1.28
942	3.08	1.32	971	3.19	1.28
943	3.08	1.32	972	3.20	1.28
944	3.09	1.32	973	3.20	1.28
945	3.09	1.31	974	3.20	1.27
946	3.09	1.31	975	3.21	1.27
947	3.10	1.31	976	3.21	1.27
948	3.10	1.31	977	3.22	1.27
949	3.10	1.31	978	3.22	1.27
950	3.11	1.31	979	3.23	1.27
951	3.11	1.31	980	3.23	1.27
952	3.12	1.30	981	3.23	1.27
953	3.12	1.30	982	3.24	1.26
954	3.12	1.30	983	3.24	1.26
955	3.13	1.30	984	3.25	1.26
956	3.13	1.30	985	3.25	1.26
957	3.14	1.30	986	3.25	1.26
958	3.14	1.30	987	3.26	1.26
959	3.14	1.29	988	3.26	1.26
960	3.15	1.29	989	3.27	1.26
961	3.15	1.29	990	3.27	1.25

B. Appendix B

B.GENE DELIVERY APPLICATIONS OF FA-PEG-PEI/Cys Ag₂S QDs

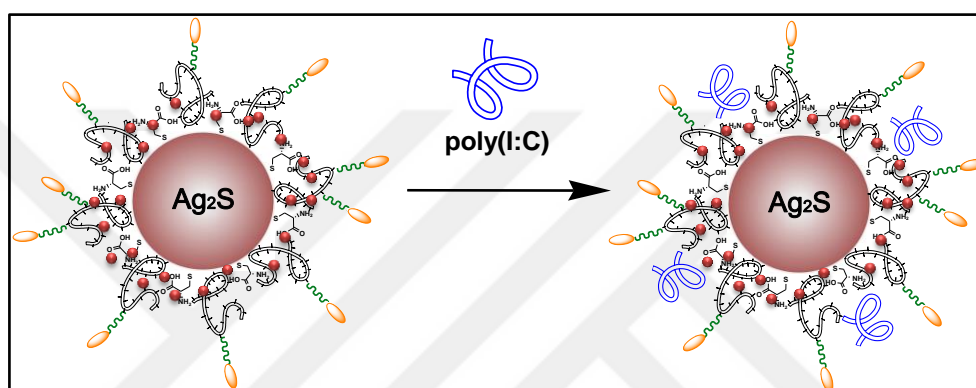
FA conjugated Ag₂S QDs are cationic and so, are candidates for targeted gene delivery, as well. In order to evaluate the transfection ability of the FA conjugated Ag₂S QDs, polyinosinic:polycytidylic acid (poly(I:C)), green fluorescent protein (GFP) and p53-GFP genes were loaded to these structures. In deed, combination therapy was also attempted with Poly(I:C) and DOX.

B.1 poly(I:C) transfection using DOX loaded FA-PEG-Ag₂S QDs

Since FA-PEG-Ag₂S QDs were successfully delivering DOX to folate receptor + cells selectively, poly(I:C) was loaded to DOX loaded FA-PEG-Ag₂S QDs, to achieve combination therapy. Among nucleic acid based therapeutics, poly (I:C) is an important immune supressor and synthetic analogue of double stranded RNA. It influences the activation of TLR3, RIG-1 and MDA-5 signaling pathways [253-255]. Poly (I:C) does not only alters the tumor microenvironment by enhancing innate and adaptive immune responses, but also directly triggers apoptosis in many types of human malignant cells including breast cancer, cervical cancer, melanoma and hepatoma cells [254, 256]. However, oligonucleotides are degraded rapidly by nucleases in the circulation [257, 258]. For successful delivery and release of poly(I:C) into cells, this dsRNA needs to be immobilized onto a specific carrier systems. Therefore, these cationic QDs are good delivery candidates for poly(I:C).

For transfection study, poly (I:C) dsRNA was dissolved in nuclease free water in 10 mg/mL of stock concentration for the activation, and was heated at 55 °C for 15 min. Then, the stock solution was cooled to room temperature to form ds-poly (I:C) according

to manufacturer's procedure (Sigma-Aldrich, USA). Poly (I:C) and DOX loaded FA-PEG-Ag₂S QDs were separately diluted in hepes-buffered glucose solution (HBG, 20 mM Hepes, 5 % (w/v) glucose) and they were mixed at a ratio of 40/1 (QD/poly(I:C, w/w). After stirred at 300 rpm and incubated at room temperature (25 °C) for 20 min, the complexes were introduced to HeLa and A549 cells lines. A schematic representation of electrostatic interaction between DOX loaded FA-PEG-Ag₂S QDs and poly(I:C) was presented in Scheme B. 1.



Scheme B. 1 Schematic representation of electrostatic interaction between poly(I:C) and DOX loaded FA-PEG-(PEI/Cys)-Ag₂S NIRQDs.

Hydrodynamic size of the nanoparticles increased after the poly(I:C) loading as well as the PDI and zeta potential as shown in Table B. 1.

As explained before, DOX loading decreased the nanoparticle size and lowered the zeta potential due to charge neutralization and increase the formation of protein corona. Increase in the size along with an increase in the zeta potential does indicate that some DOX was displaced by Poly(I:C). A significant increase in the PDI may be due to complexation of multiple particles with a single poly(I:C).

Table B. 1 Number-based size distribution and zeta potential values of QDs.

Sample Name	Size (nm)	PDI	Zeta (mV)
FA-PEG-Ag ₂ S + DOX	27.0 ± 2.9	0.291	30.2 ± 2.0
FA-PEG-Ag ₂ S + DOX + poly(I:C)	54.0 ± 30.4	0.426	39.6 ± 1.6

According to ATP assay results, poly(I:C) loading did not create any significant cytotoxicity on both HeLa and A549 cell lines (Figure B. 1). In addition, the apoptosis and necrosis studies demonstrated that DOX loaded particles are more effective than DOX-poly(I:C) loaded particles (Figure B. 2, Figure B. 3, Figure B. 4 and Figure B. 5). This may be due to unequal concentrations of DOX in each formulation. In HeLa, toxicity induced by DOX-poly(I:C) is similar to just DOX. But, in A549, it reduced IC50 concentration of particles from 2 to 0.4 $\mu\text{g}/\text{mL}$ Ag dose. This may be supported by the results of apoptosis/necrosis assay. This may indicate that A549 is more vulnerable to poly(I:C) which was delivered to these cells via passive uptake. But mitochondrial cell potential and M30 results do not suggest a dramatic effect with poly(I:C) delivery.

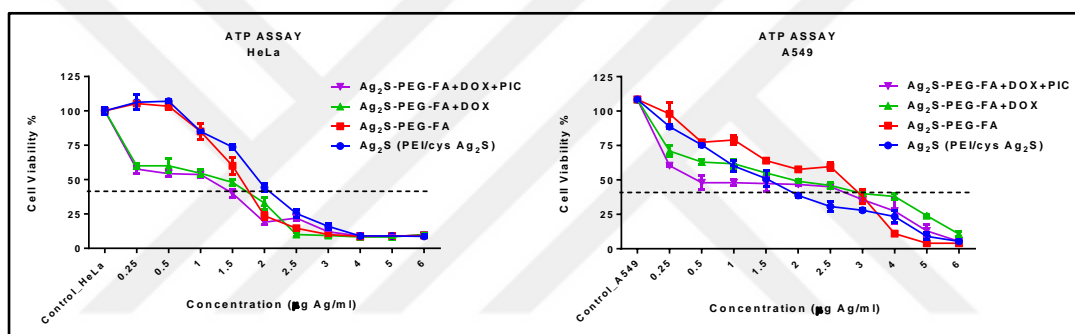


Figure B. 1 ATP cell viability assay on HeLa and A549 cells treated with Ag₂S, FA-PEG-Ag₂S, DOX+FA-PEG-Ag₂S and poly(I:C) loaded DOX+FA-PEG-Ag₂S NIRQDs for 48 hours. The data are expressed as mean \pm S.D. ($n = 3$).

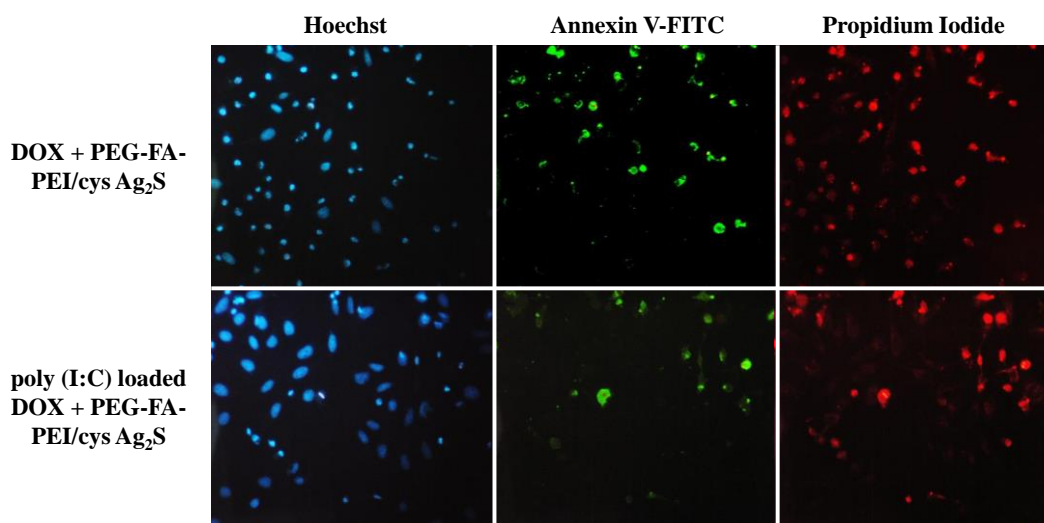


Figure B. 2 Indication of apoptosis and necrosis of HeLa cells induced by DOX+FA-PEG-Ag₂S or poly(I:C)-DOX+FA-PEG-Ag₂S NIRQDs. Fluorescence staining of HeLa

cells with Hoechst 33342 (blue), Annexin V-FITC (green) and Propidium Iodide (red) after being treated with QDs at 1.5 $\mu\text{g/ml}$ Ag concentration for 24 hours.

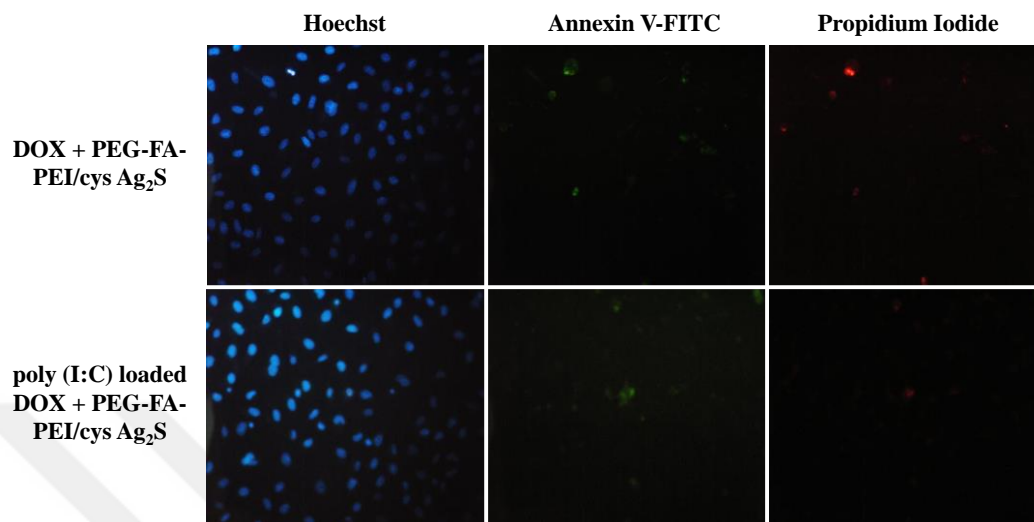


Figure B. 3 Indication of apoptosis and necrosis of A549 cells induced by DOX+FA-PEG-Ag₂S or poly(I:C)-DOX+FA-PEG-Ag₂S NIRQDs. Fluorescence staining of A549 cells with Hoechst 33342 (blue), Annexin V-FITC (green) and Propidium Iodide (red) after being treated with QDs at 1.5 $\mu\text{g/ml}$ Ag concentration for 24 hours.

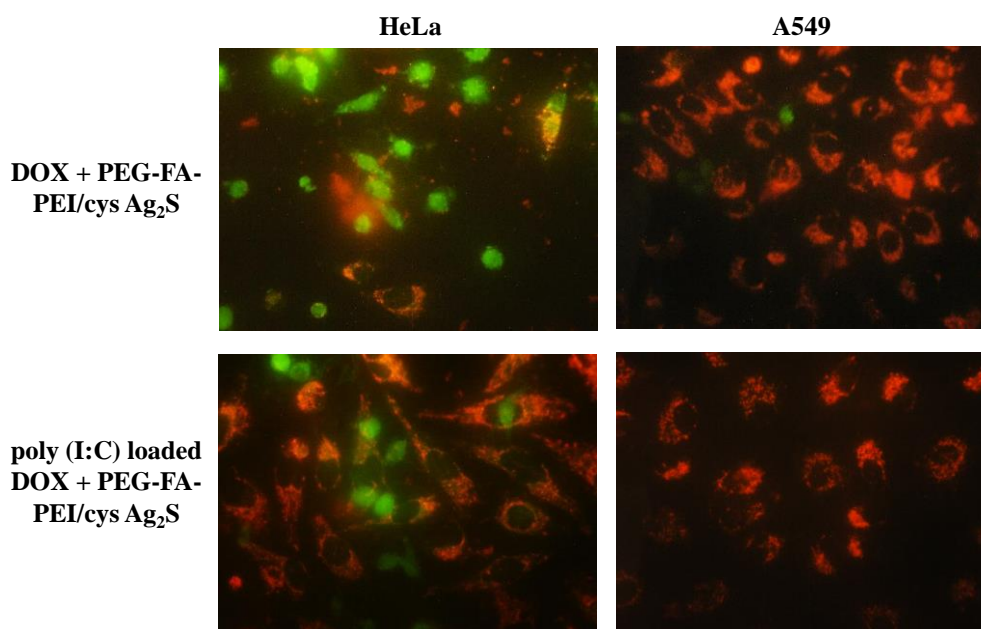


Figure B. 4 Mitochondrial membrane potential assay in HeLa and A549 cells visualized by fluorescence microscopy. The cells were exposed to DOX+FA-PEG-Ag₂S and poly(I:C)-DOX+FA-PEG-Ag₂S NIRQDs at 1.5 $\mu\text{g/mL}$ Ag for 24 hours. Red

fluorescence indicates high membrane potential and green fluorescence indicates loss of mitochondrial membrane potential depending on apoptotic event in the cells.

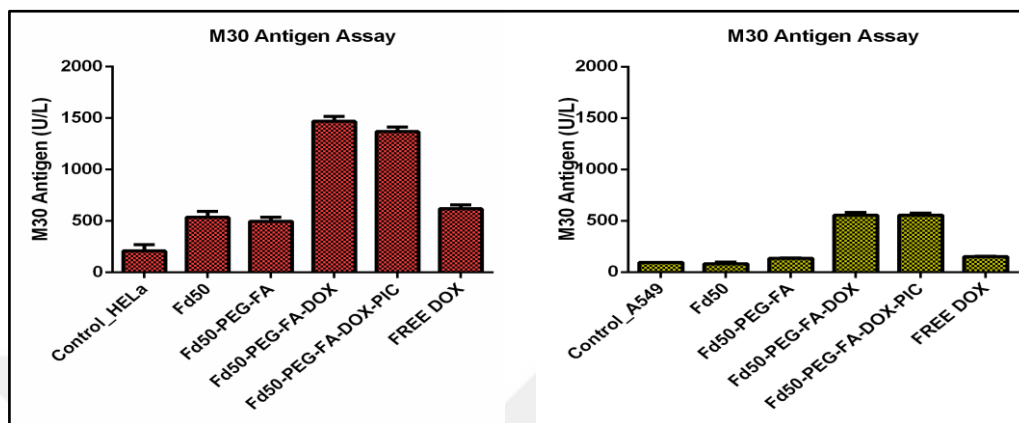
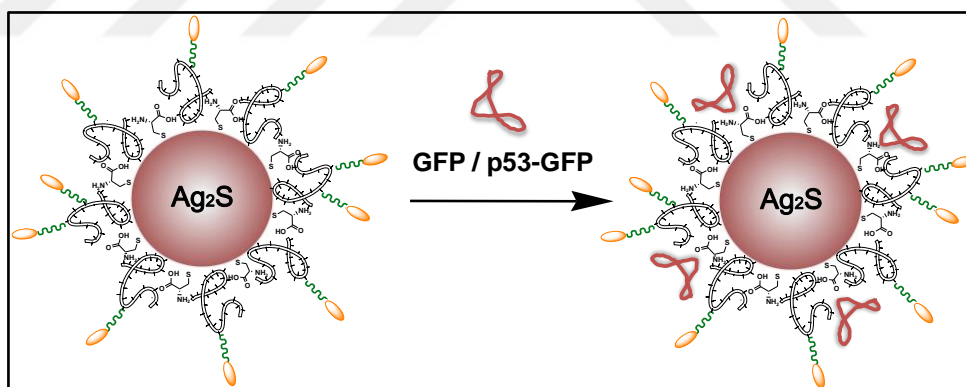


Figure B. 5 M30 antigen assay on HeLa and A549 cells incubated with nanoparticles at 1.5 $\mu\text{g/ml}$ Ag concentration for 48 hours ($n = 2$).

B.2 GFP and p53-GFP transfection using FA-PEG-Ag₂S QDs



Scheme B. 2 Schematic representation of electrostatic interaction between GFP or p53-GFP and DOX loaded FA-PEG-(PEI/Cys)-Ag₂S NIRQDs.

FA-PEG-Ag₂S QDs were also loaded with p53-GFP plasmid in order to induce apoptosis and enhance the theranostic value of these particles (Scheme B. 2). In addition, pGFP was used as standard gene to evaluate the transfection efficiency of the folate targeting nanoparticles. The transfection protocol and used concentrations were same with the transfection studies performed in Chapter 4. HeLa cells were seeded at a density of 25000 cells per well in a 24-well plate in RPMI 1640 complete medium and incubated for one day. The second day, QD/pGFP or QD/p53-GFP conjugates, prepared with 15/1

of N/P ratio were introduced into the cells according to the concentrations shown in Table B. 2. After 48 hour-incubation with nanoparticles, cells were fixed with 4 % paraformaldehyde solutions and visualized under a fluorescent microscope. The images presented in Figure B. 6 imply that FA-PEG-Ag₂S QDs are not very efficient as transfection agents.

Table B. 2 QD and plasmid DNA concentrations used in the transfection studies.

Concentrations	FA-PEG-Ag ₂ S (µg/mL)	pDNA(µg/mL)
Conc 1	2.36	0.5
Conc 2	4.71	1
Conc 3	7.07	1.5
Conc 4	9.42	2

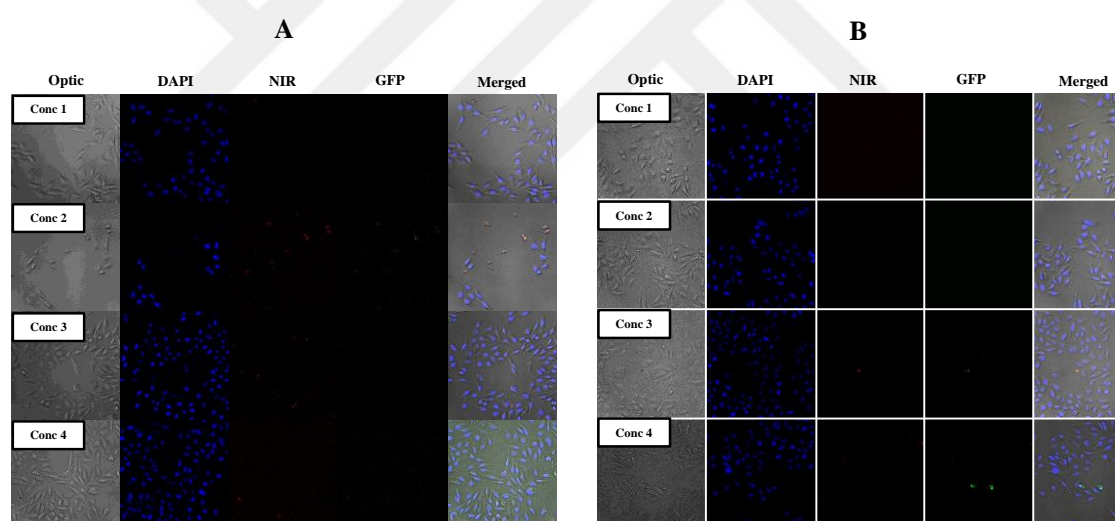


Figure B. 6 Transfection of HeLa cells with GFP (A) and p53-GFP (B) plasmids using FA-PEG-Ag₂S NIRQDs. QD/pDNA conjugates prepared at 15/1 N/P ratio were introduced into the cells in different concentrations. Images were taken with an inverted fluorescence microscope. DAPI staining was used to show nuclei of all cells in the field (blue color). Red signals indicate QD internalization into the cells. Green signals show GFP transfection.

To further confirm the transfection ability of FA-PEG-Ag₂S QDs, MEF p53^{-/-} and MEF wt cells were transfected with p53-GFP plasmid using the nanoparticles. The same concentrations were used (Table B. 2). However, as shown in Figure B. 7, the transfection

studies with FA-PEG-Ag₂S QDs gave unsuccessful results, even though there is a very little transfection in MEF p53 ^{-/-} in Conc 4.

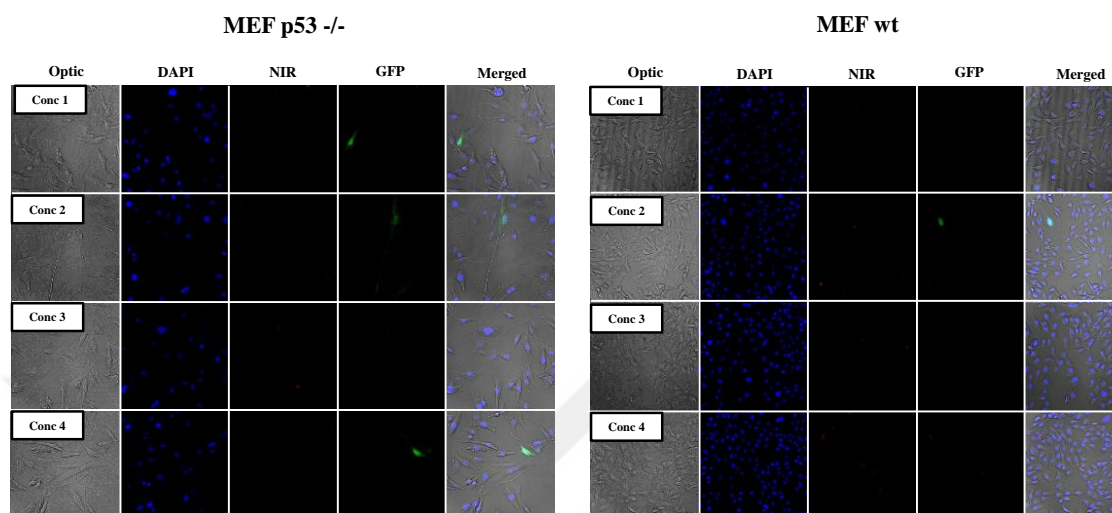


Figure B. 7 Transfection of MEF p53 ^{-/-} and MEF wt cells with p53-GFP plasmid using FA-PEG-Ag₂S NIRQDs. QD/pDNA conjugates prepared at 15/1 N/P ratio were used in different concentrations. Images were taken with an inverted fluorescence microscope. DAPI staining was used to show nuclei of all cells in the field (blue color). Red signals indicate QD internalization into the cells. Green signals show GFP transfection.

In this work, we have showed that PEGylation of nanoparticles decreases their transfection efficacy. These findings are actually parallel with the literature [259, 260].

BIBLIOGRAPHY

1. Kumar, N. and S. Kumbhat, *Essentials in Nanoscience and Nanotechnology*. 2016: John Wiley & Sons.
2. Ekimov, A.I., A.L. Efros, and A.A. Onushchenko, *Quantum size effect in semiconductor microcrystals*. Solid State Communications, 1985. **56**(11): p. 921-924.
3. Rossetti, R. and L. Brus, *Electron-hole recombination emission as a probe of surface chemistry in aqueous cadmium sulfide colloids*. The Journal of Physical Chemistry, 1982. **86**(23): p. 4470-4472.
4. Bera, D., et al., *Quantum dots and their multimodal applications: a review*. Materials, 2010. **3**(4): p. 2260-2345.
5. Peng, X., et al., *Shape control of CdSe nanocrystals*. Nature, 2000. **404**(6773): p. 59-61.
6. Murray, C.B., D.J. Norris, and M.G. Bawendi, *Synthesis and characterization of nearly monodisperse CdE (E = sulfur, selenium, tellurium) semiconductor nanocrystallites*. Journal of the American Chemical Society, 1993. **115**(19): p. 8706-8715.
7. Dabbousi, B.O., et al., *(CdSe)ZnS Core-Shell Quantum Dots: Synthesis and Characterization of a Size Series of Highly Luminescent Nanocrystallites*. The Journal of Physical Chemistry B, 1997. **101**(46): p. 9463-9475.
8. Peng, Z.A. and X. Peng, *Nearly Monodisperse and Shape-Controlled CdSe Nanocrystals via Alternative Routes: Nucleation and Growth*. Journal of the American Chemical Society, 2002. **124**(13): p. 3343-3353.
9. Li, H., W.Y. Shih, and W.-H. Shih, *Highly Photoluminescent and Stable Aqueous ZnS Quantum Dots*. Industrial & Engineering Chemistry Research, 2009. **49**(2): p. 578-582.
10. Xie, R., D. Battaglia, and X. Peng, *Colloidal InP nanocrystals as efficient emitters covering blue to near-infrared*. Journal of the American Chemical Society, 2007. **129**(50): p. 15432-15433.
11. Battaglia, D. and X. Peng, *Formation of High Quality InP and InAs Nanocrystals in a Noncoordinating Solvent*. Nano Letters, 2002. **2**(9): p. 1027-1030.
12. Ellingson, R.J., et al., *Highly Efficient Multiple Exciton Generation in Colloidal PbSe and PbS Quantum Dots*. Nano Letters, 2005. **5**(5): p. 865-871.
13. Bakueva, L., et al., *PbS Quantum Dots with Stable Efficient Luminescence in the Near-IR Spectral Range*. Advanced Materials, 2004. **16**(11): p. 926-929.
14. Pietryga, J.M., et al., *Pushing the Band Gap Envelope: Mid-Infrared Emitting Colloidal PbSe Quantum Dots*. Journal of the American Chemical Society, 2004. **126**(38): p. 11752-11753.

15. Pan, Y., et al., *Size controlled synthesis of monodisperse PbTe quantum dots: using oleylamine as the capping ligand*. Journal of Materials Chemistry, 2012. **22**(44): p. 23593-23601.
16. Rogers, B., J. Adams, and S. Pennathur, *Nanotechnology: understanding small systems*. 2008: CRC Press.
17. *Band Gap Measurement*. [cited 2016 16 Nov]; Available from: <http://archive.cnx.org/contents/d1c4c0c9-7bcb-4245-b320-6d6fdb3ade9e@1/band-gap-measurement>.
18. Kittel, C., *Introduction to Solid State Physics*. 8th Edition ed., United States of America: John Wiley & Sons.
19. *Dimensions in semiconductors: can something be zero dimensional and still be?* [cited 2016 19 Nov]; Available from: <http://whitenoise.kinja.com/dimensions-in-semiconductors-can-something-be-zero-dim-1543310309>.
20. Rizvi, S.B., et al., *Semiconductor quantum dots as fluorescent probes for in vitro and in vivo bio-molecular and cellular imaging*. Nano Reviews & Experiments, 2010. **1**.
21. Surana, K., et al., *Synthesis, characterization and application of CdSe quantum dots*. Journal of Industrial and Engineering Chemistry, 2014. **20**(6): p. 4188-4193.
22. Rabouw, F.T. and C. de Mello Donega, *Excited-State Dynamics in Colloidal Semiconductor Nanocrystals*. Topics in Current Chemistry, 2016. **374**(5): p. 58.
23. *9.4.C - Semiconductors*. [cited 2016 21 Nov]; Available from: <http://www.quarkology.com/12-physics/94-ideas-implementation/94C-Semiconductors.html>.
24. Brus, L., *Electronic wave functions in semiconductor clusters: experiment and theory*. The Journal of Physical Chemistry, 1986. **90**(12): p. 2555-2560.
25. Jasim, K.E., *Quantum Dots Solar Cells*. 2015.
26. Shukla, N. and M.M. Nigra, *Synthesis of CdSe quantum dots with luminescence in the violet region of the solar spectrum*. Luminescence, 2010. **25**(1): p. 14-18.
27. Chou, K.F. and A.M. Dennis, *Förster resonance energy transfer between quantum dot donors and quantum dot acceptors*. Sensors, 2015. **15**(6): p. 13288-13325.
28. Kimbrough, D.R., *The photochemistry of sunscreens*. J. Chem. Educ, 1997. **74**(1): p. 51.
29. Käs, J.A. *Introduction Fluorescence Microscopy* [cited 2016 16 Nov]; Available from: <http://home.uni-leipzig.de/pwm/web/?section=introduction&page=fluorescence>.
30. Guo, H., et al., *PbS quantum dot fiber amplifier based on a tapered SMF fiber*. Optics Communications, 2012. **285**(13): p. 3222-3227.
31. Lacroix, L.-M., et al., *New generation of magnetic and luminescent nanoparticles for in vivo real-time imaging*. Interface focus, 2013. **3**(3): p. 20120103.
32. Jin, S., et al., *Application of quantum dots in biological imaging*. Journal of Nanomaterials, 2011. **2011**: p. 13.
33. Farkhani, S.M. and A. Valizadeh, *Review: three synthesis methods of CdX (X= Se, S or Te) quantum dots*. IET nanobiotechnology, 2014. **8**(2): p. 59-76.
34. Chang, J. and E.R. Waclawik, *Colloidal semiconductor nanocrystals: controlled synthesis and surface chemistry in organic media*. RSC Advances, 2014. **4**(45): p. 23505-23527.

35. Murray, C.B., C. Kagan, and M. Bawendi, *Synthesis and characterization of monodisperse nanocrystals and close-packed nanocrystal assemblies*. Annual Review of Materials Science, 2000. **30**(1): p. 545-610.
36. Murray, C., D.J. Norris, and M.G. Bawendi, *Synthesis and characterization of nearly monodisperse CdE (E= sulfur, selenium, tellurium) semiconductor nanocrystallites*. Journal of the American Chemical Society, 1993. **115**(19): p. 8706-8715.
37. Talapin, D.V., et al., *CdSe/CdS/ZnS and CdSe/ZnSe/ZnS core-shell-shell nanocrystals*. The Journal of Physical Chemistry B, 2004. **108**(49): p. 18826-18831.
38. Bullen, C.R. and P. Mulvaney, *Nucleation and growth kinetics of CdSe nanocrystals in octadecene*. Nano Letters, 2004. **4**(12): p. 2303-2307.
39. Qu, L., W.W. Yu, and X. Peng, *In situ observation of the nucleation and growth of CdSe nanocrystals*. Nano Letters, 2004. **4**(3): p. 465-469.
40. Qu, L., Z.A. Peng, and X. Peng, *Alternative routes toward high quality CdSe nanocrystals*. Nano Letters, 2001. **1**(6): p. 333-337.
41. William, W.Y., et al., *Water-soluble quantum dots for biomedical applications*. Biochemical and biophysical research communications, 2006. **348**(3): p. 781-786.
42. Chen, N., et al., *The cytotoxicity of cadmium-based quantum dots*. Biomaterials, 2012. **33**(5): p. 1238-1244.
43. Tiwari, D.K., et al., *Synthesis and characterization of anti-HER2 antibody conjugated CdSe/CdZnS quantum dots for fluorescence imaging of breast cancer cells*. Sensors, 2009. **9**(11): p. 9332-9354.
44. Frecker, T., et al., *Review—Quantum Dots and Their Application in Lighting, Displays, and Biology*. ECS Journal of Solid State Science and Technology, 2016. **5**(1): p. R3019-R3031.
45. Gun'ko, Y.K. and S. Byrne, *Quantum Dot Synthesis Methods*. Quantum Dot Sensors: Technology and Commercial Applications, 2013: p. 1.
46. Callan, J. and F.M. Raymo, *Quantum Dot Sensors: Technology and Commercial Applications*. 2013: Pan Stanford Publishing.
47. Aldana, J., Y.A. Wang, and X. Peng, *Photochemical instability of CdSe nanocrystals coated by hydrophilic thiols*. Journal of the American Chemical Society, 2001. **123**(36): p. 8844-8850.
48. Wang, J.-H., et al., *Modification of CdTe quantum dots as temperature-insensitive bioprobes*. Talanta, 2008. **74**(4): p. 724-729.
49. Hocaoglu, I., et al., *Emission tunable, cyto/hemocompatible, near-IR-emitting Ag₂S quantum dots by aqueous decomposition of DMSA*. Nanoscale, 2014. **6**(20): p. 11921-11931.
50. Acar, H.Y., et al., *Emergence of 2MPA as an effective coating for highly stable and luminescent quantum dots*. The Journal of Physical Chemistry C, 2009. **113**(23): p. 10005-10012.
51. Choi, H.S., et al., *Renal clearance of quantum dots*. Nature biotechnology, 2007. **25**(10): p. 1165-1170.
52. Korgel, B.A. and H.G. Monbouquette, *Quantum Confinement Effects Enable Photocatalyzed Nitrate Reduction at Neutral pH Using CdS Nanocrystals*. The Journal of Physical Chemistry B, 1997. **101**(25): p. 5010-5017.
53. Sun, Y.H., et al., *Photostability and pH sensitivity of CdSe/ZnSe/ZnS quantum dots in living cells*. Nanotechnology, 2006. **17**(17): p. 4469.

54. Zhu, Y., et al., *One-pot preparation of highly fluorescent cadmium telluride/cadmium sulfide quantum dots under neutral-pH condition for biological applications*. Journal of colloid and interface science, 2013. **390**(1): p. 3-10.
55. Klostranec, J.M. and W.C. Chan, *Quantum dots in biological and biomedical research: recent progress and present challenges*. Advanced Materials, 2006. **18**(15): p. 1953-1964.
56. O'Farrell, N., A. Houlton, and B.R. Horrocks, *Silicon nanoparticles: applications in cell biology and medicine*. International journal of Nanomedicine, 2006. **1**(4): p. 451.
57. Karakoti, A.S., et al., *Surface functionalization of quantum dots for biological applications*. Advances in colloid and interface science, 2015. **215**: p. 28-45.
58. Gao, X., et al., *In vivo cancer targeting and imaging with semiconductor quantum dots*. Nature biotechnology, 2004. **22**(8): p. 969-976.
59. Gao, X., et al., *In vivo molecular and cellular imaging with quantum dots*. Current opinion in biotechnology, 2005. **16**(1): p. 63-72.
60. Ballou, B., et al., *Noninvasive imaging of quantum dots in mice*. Bioconjugate chemistry, 2004. **15**(1): p. 79-86.
61. Dahan, M., et al., *Diffusion dynamics of glycine receptors revealed by single-quantum dot tracking*. Science, 2003. **302**(5644): p. 442-445.
62. Lidke, D.S., et al., *Quantum dot ligands provide new insights into erbB/HER receptor-mediated signal transduction*. Nature biotechnology, 2004. **22**(2): p. 198-203.
63. Voura, E.B., et al., *Tracking metastatic tumor cell extravasation with quantum dot nanocrystals and fluorescence emission-scanning microscopy*. Nature medicine, 2004. **10**(9): p. 993-998.
64. Kim, S., et al., *Near-infrared fluorescent type II quantum dots for sentinel lymph node mapping*. Nature biotechnology, 2004. **22**(1): p. 93-97.
65. Lim, Y.T., et al., *Selection of quantum dot wavelengths for biomedical assays and imaging*. Molecular imaging, 2003. **2**(1): p. 50-64.
66. Altinoğlu, E.İ. and J.H. Adair, *Near infrared imaging with nanoparticles*. Wiley Interdisciplinary Reviews: Nanomedicine and Nanobiotechnology, 2010. **2**(5): p. 461-477.
67. Kobayashi, H., et al., *New strategies for fluorescent probe design in medical diagnostic imaging*. Chemical reviews, 2009. **110**(5): p. 2620-2640.
68. Ma, Q. and X. Su, *Near-infrared quantum dots: synthesis, functionalization and analytical applications*. Analyst, 2010. **135**(8): p. 1867-1877.
69. Frangioni, J.V., *In vivo near-infrared fluorescence imaging*. Current opinion in chemical biology, 2003. **7**(5): p. 626-634.
70. Michalet, X., et al., *Quantum dots for live cells, in vivo imaging, and diagnostics*. science, 2005. **307**(5709): p. 538-544.
71. Lin, C.-A.J., et al., *Bioanalytics and biolabeling with semiconductor nanoparticles (quantum dots)*. Journal of Materials Chemistry, 2007. **17**(14): p. 1343-1346.
72. Aswathy, R.G., et al., *Near-infrared quantum dots for deep tissue imaging*. Analytical and bioanalytical chemistry, 2010. **397**(4): p. 1417-1435.

73. Biju, V., et al., *Bioconjugated quantum dots for cancer research: present status, prospects and remaining issues*. Biotechnology advances, 2010. **28**(2): p. 199-213.
74. Yu, W.W., Y.A. Wang, and X. Peng, *Formation and stability of size-, shape-, and structure-controlled CdTe nanocrystals: ligand effects on monomers and nanocrystals*. Chemistry of Materials, 2003. **15**(22): p. 4300-4308.
75. Hines, M.A. and G.D. Scholes, *Colloidal PbS nanocrystals with size-tunable near-infrared emission: observation of post-synthesis self-narrowing of the particle size distribution*. Advanced Materials, 2003. **15**(21): p. 1844-1849.
76. Blackman, B., et al., *Control of the morphology of complex semiconductor nanocrystals with a type II heterojunction, dots vs peanuts, by thermal cycling*. Chemistry of materials, 2007. **19**(15): p. 3815-3821.
77. Kim, S., et al., *Type-II quantum dots: CdTe/CdSe (core/shell) and CdSe/ZnTe (core/shell) heterostructures*. Journal of the American Chemical Society, 2003. **125**(38): p. 11466-11467.
78. Ding, H., et al., *Non-invasive tumor detection in small animals using novel functional Pluronic nanomicelles conjugated with anti-mesothelin antibody*. Nanoscale, 2011. **3**(4): p. 1813-1822.
79. Morgan, N.Y., et al., *Real time in vivo non-invasive optical imaging using near-infrared fluorescent quantum dots I*. Academic Radiology, 2005. **12**(3): p. 313-323.
80. Su, Y., et al., *The cytotoxicity of CdTe quantum dots and the relative contributions from released cadmium ions and nanoparticle properties*. Biomaterials, 2010. **31**(18): p. 4829-4834.
81. Yan, M., et al., *An in vitro study of vascular endothelial toxicity of CdTe quantum dots*. Toxicology, 2011. **282**(3): p. 94-103.
82. Cao, Y. and U. Banin, *Growth and properties of semiconductor core/shell nanocrystals with InAs cores*. Journal of the American Chemical Society, 2000. **122**(40): p. 9692-9702.
83. Xie, R., M. Rutherford, and X. Peng, *Formation of high-quality I- III- VI semiconductor nanocrystals by tuning relative reactivity of cationic precursors*. Journal of the American Chemical Society, 2009. **131**(15): p. 5691-5697.
84. Allen, P.M. and M.G. Bawendi, *Ternary I- III- VI quantum dots luminescent in the red to near-infrared*. Journal of the American Chemical Society, 2008. **130**(29): p. 9240-9241.
85. Selvan, S.T., T.T. Tan, and J.Y. Ying, *Robust, Non-Cytotoxic, Silica-Coated CdSe Quantum Dots with Efficient Photoluminescence*. Advanced Materials, 2005. **17**(13): p. 1620-1625.
86. Wu, H., et al., *Water-Soluble Nanocrystals Through Dual-Interaction Ligands*. Angewandte Chemie International Edition, 2008. **47**(20): p. 3730-3734.
87. Yarema, M., et al., *Infrared emitting and photoconducting colloidal silver chalcogenide nanocrystal quantum dots from a silylamide-promoted synthesis*. ACS nano, 2011. **5**(5): p. 3758-3765.
88. Jiang, P., et al., *Emission-tunable near-infrared Ag₂S quantum dots*. Chemistry of Materials, 2011. **24**(1): p. 3-5.
89. Gui, R., et al., *Recent advances in synthetic methods and applications of colloidal silver chalcogenide quantum dots*. Coordination Chemistry Reviews, 2015. **296**: p. 91-124.

90. Madelung, O., *Semiconductors: data handbook*. 2012: Springer Science & Business Media.
91. Brelle, M.C., et al., *Synthesis and ultrafast study of cysteine-and glutathione-capped Ag₂S semiconductor colloidal nanoparticles*. The Journal of Physical Chemistry A, 1999. **103**(49): p. 10194-10201.
92. Gao, F., Q. Lu, and D. Zhao, *Controllable assembly of ordered semiconductor Ag₂S nanostructures*. Nano Letters, 2003. **3**(1): p. 85-88.
93. Liu, Z., et al., *A facile chemical route to semiconductor metal sulfide nanocrystal superlattices*. Chemical communications, 2004(23): p. 2724-2725.
94. Liu, J., et al., *Synthesis of Ag₂S quantum dots in water-in-CO₂ microemulsions*. Chemical communications, 2004(22): p. 2582-2583.
95. Du, Y., et al., *Near-Infrared Photoluminescent Ag₂S Quantum Dots from a Single Source Precursor*. Journal of the American Chemical Society, 2010. **132**(5): p. 1470-1471.
96. Li, C., et al., *In vivo real-time visualization of tissue blood flow and angiogenesis using Ag₂S quantum dots in the NIR-II window*. Biomaterials, 2014. **35**(1): p. 393-400.
97. Chen, G., et al., *Tracking of Transplanted Human Mesenchymal Stem Cells in Living Mice using Near-Infrared Ag₂S Quantum Dots*. Advanced Functional Materials, 2014. **24**(17): p. 2481-2488.
98. Zhang, Y., et al., *Biodistribution, pharmacokinetics and toxicology of Ag₂S near-infrared quantum dots in mice*. Biomaterials, 2013. **34**(14): p. 3639-46.
99. Zhang, Y., et al., *Biodistribution, pharmacokinetics and toxicology of Ag₂S near-infrared quantum dots in mice*. Biomaterials, 2013. **34**(14): p. 3639-3646.
100. Jiang, P., et al., *Water-soluble Ag₂S quantum dots for near-infrared fluorescence imaging in vivo*. Biomaterials, 2012. **33**(20): p. 5130-5.
101. Xu, Y.Y., et al., *Inhibitory effect of dsRNA TLR3 agonist in a rat hepatocellular carcinoma model*. Mol Med Rep, 2013. **8**(4): p. 1037-42.
102. Wang, Y. and X.-P. Yan, *Fabrication of vascular endothelial growth factor antibody bioconjugated ultrasmall near-infrared fluorescent Ag₂S quantum dots for targeted cancer imaging in vivo*. Chemical Communications, 2013. **49**(32): p. 3324.
103. Yang, H.-Y., et al., *One-pot synthesis of water-dispersible Ag₂S quantum dots with bright fluorescent emission in the second near-infrared window*. Nanotechnology, 2013. **24**(5): p. 055706.
104. Chen, J., et al., *Synthesis of ribonuclease-A conjugated Ag₂S quantum dots clusters via biomimetic route*. Materials Letters, 2013. **96**: p. 224-227.
105. Hocaoglu, I., et al., *Development of highly luminescent and cytocompatible near-IR-emitting aqueous Ag₂S quantum dots*. Journal of Materials Chemistry, 2012. **22**(29): p. 14674-14681.
106. Zhao, Y. and Z. Song, *Phase transfer-based synthesis of highly stable, biocompatible and the second near-infrared-emitting silver sulfide quantum dots*. Materials Letters, 2014. **126**: p. 78-80.
107. Li, C., et al., *In vivo real-time visualization of tissue blood flow and angiogenesis using Ag₂S quantum dots in the NIR-II window*. Biomaterials, 2014. **35**(1): p. 393-400.

108. Hong, G., et al., *In Vivo Fluorescence Imaging with Ag₂S Quantum Dots in the Second Near-Infrared Region*. *Angewandte Chemie*, 2012. **124**(39): p. 9956-9959.
109. Wang, C., et al., *Facile Aqueous-Phase Synthesis of Biocompatible and Fluorescent Ag₂S Nanoclusters for Bioimaging: Tunable Photoluminescence from Red to Near Infrared*. *Small*, 2012. **8**(20): p. 3137-3142.
110. Zhang, Y., et al., *Controlled synthesis of Ag₂S quantum dots and experimental determination of the exciton Bohr radius*. *The Journal of Physical Chemistry C*, 2014. **118**(9): p. 4918-4923.
111. Gao, J., et al., *Direct Synthesis of Water-Soluble Aptamer-Ag₂S Quantum Dots at Ambient Temperature for Specific Imaging and Photothermal Therapy of Cancer*. *Advanced Healthcare Materials*, 2016. **5**(18): p. 2437-2449.
112. Chen, H., et al., *Characterization of tumor-targeting Ag₂S quantum dots for cancer imaging and therapy in vivo*. *Nanoscale*, 2014. **6**(21): p. 12580-12590.
113. Wang, Y. and X.-P. Yan, *Fabrication of vascular endothelial growth factor antibody bioconjugated ultrasmall near-infrared fluorescent Ag₂S quantum dots for targeted cancer imaging in vivo*. *Chemical Communications*, 2013. **49**(32): p. 3324-3326.
114. Tan, L., A. Wan, and H. Li, *Synthesis of near-infrared quantum dots in cultured cancer cells*. *ACS applied materials & interfaces*, 2013. **6**(1): p. 18-23.
115. Hu, F., et al., *Real-time in vivo visualization of tumor therapy by a near-infrared-II Ag₂S quantum dot-based theranostic nanoplatfrom*. *Nano Research*, 2015. **8**(5): p. 1637-1647.
116. Tang, R., et al., *Tunable ultrasmall visible-to-extended near-infrared emitting silver sulfide quantum dots for integrin-targeted cancer imaging*. *ACS nano*, 2015. **9**(1): p. 220-230.
117. Zhang, Y., et al., *Ag₂S Quantum Dot: A Bright and Biocompatible Fluorescent Nanoprobe in the Second Near-Infrared Window*. *ACS Nano*, 2012. **6**(5): p. 3695-3702.
118. Asik, D., et al., *One step emission tunable synthesis of PEG coated Ag₂S NIR quantum dots and the development of receptor targeted drug delivery vehicles thereof*. *Journal of Materials Chemistry B*, 2016. **4**(11): p. 1941-1950.
119. Hocaoglu, I., et al., *Cyto/hemocompatible magnetic hybrid nanoparticles (Ag₂S-Fe₃O₄) with luminescence in the near-infrared region as promising theranostic materials*. *Colloids and Surfaces B: Biointerfaces*, 2015. **133**: p. 198-207.
120. Ojea-Jiménez, I., et al., *Engineered nonviral nanocarriers for intracellular gene delivery applications*. *Biomedical Materials*, 2012. **7**(5): p. 054106.
121. Roth, J.A., S.G. Swisher, and R.E. Meyn, *p53 tumor suppressor gene therapy for cancer*. *ONCOLOGY-WILLISTON PARK THEN HUNTINGTON-*, 1999. **13**: p. 148-154.
122. Lane, D.P., C.F. Cheok, and S. Lain, *p53-based cancer therapy*. *Cold Spring Harbor perspectives in biology*, 2010. **2**(9): p. a001222.
123. Pearson, S., H. Jia, and K. Kandachi, *China approves first gene therapy*. *Nature biotechnology*, 2004. **22**(1): p. 3-4.
124. Hill, A.B., et al., *Overcoming gene-delivery hurdles: Physiological considerations for nonviral vectors*. *Trends in biotechnology*, 2016. **34**(2): p. 91-105.

125. Nayerossadat, N., T. Maedeh, and P.A. Ali, *Viral and nonviral delivery systems for gene delivery*. Adv Biomed Res, 2012. **1**: p. 27.
126. Park, T.G., J.H. Jeong, and S.W. Kim, *Current status of polymeric gene delivery systems*. Advanced Drug Delivery Reviews, 2006. **58**(4): p. 467-486.
127. Pouton, C.W. and L.W. Seymour, *Key issues in non-viral gene delivery*. Advanced Drug Delivery Reviews, 2001. **46**(1-3): p. 187-203.
128. Dang, J.M. and K.W. Leong, *Natural polymers for gene delivery and tissue engineering*. Advanced Drug Delivery Reviews, 2006. **58**(4): p. 487-499.
129. Husseini, G.A. and W.G. Pitt, *Micelles and nanoparticles for ultrasonic drug and gene delivery*. Advanced Drug Delivery Reviews, 2008. **60**(10): p. 1137-1152.
130. Mastrobattista, E., et al., *Artificial viruses: a nanotechnological approach to gene delivery*. Nature reviews Drug discovery, 2006. **5**(2): p. 115-121.
131. Akinc, A., et al., *Exploring polyethylenimine-mediated DNA transfection and the proton sponge hypothesis*. The journal of gene medicine, 2005. **7**(5): p. 657-663.
132. Kichler, A., et al., *Polyethylenimine-mediated gene delivery: a mechanistic study*. The journal of gene medicine, 2001. **3**(2): p. 135-144.
133. Ding, Y., et al., *Gold nanoparticles for nucleic acid delivery*. Molecular Therapy, 2014. **22**(6): p. 1075.
134. Kumari, A., S.K. Yadav, and S.C. Yadav, *Biodegradable polymeric nanoparticles based drug delivery systems*. Colloids and Surfaces B: Biointerfaces, 2010. **75**(1): p. 1-18.
135. Foldvari, M. and M. Bagonluri, *Carbon nanotubes as functional excipients for nanomedicines: II. Drug delivery and biocompatibility issues*. Nanomedicine: Nanotechnology, Biology and Medicine, 2008. **4**(3): p. 183-200.
136. *Cancer nanotechnology, challenges and achievements*. 2013 [cited 2016 09 Dec]; Available from: <http://medglobe.blogspot.com.tr/2013/05/cancer-nanotechnology-challenges-and.html>.
137. Danhier, F., O. Feron, and V. Préat, *To exploit the tumor microenvironment: passive and active tumor targeting of nanocarriers for anti-cancer drug delivery*. Journal of Controlled Release, 2010. **148**(2): p. 135-146.
138. Toporkiewicz, M., et al., *Toward a magic or imaginary bullet? Ligands for drug targeting to cancer cells: principles, hopes, and challenges*. Int J Nanomedicine, 2015. **10**: p. 1399-1414.
139. Gupta, B., T.S. Levchenko, and V.P. Torchilin, *Intracellular delivery of large molecules and small particles by cell-penetrating proteins and peptides*. Advanced drug delivery reviews, 2005. **57**(4): p. 637-651.
140. Steichen, S.D., M. Caldorera-Moore, and N.A. Peppas, *A review of current nanoparticle and targeting moieties for the delivery of cancer therapeutics*. European journal of pharmaceutical sciences, 2013. **48**(3): p. 416-427.
141. Masotti, A., et al., *A Novel Near-Infrared Indocyanine Dye-Polyethylenimine Conjugate Allows DNA Delivery Imaging in Vivo*. Bioconjugate Chemistry, 2008. **19**(5): p. 983-987.
142. Aswathy, R., et al., *Near-infrared quantum dots for deep tissue imaging*. Analytical and Bioanalytical Chemistry, 2010. **397**(4): p. 1417-1435.
143. Rizvi, S.B., et al., *Semiconductor quantum dots as fluorescent probes for in vitro and in vivo bio-molecular and cellular imaging*. Nano Rev, 2010. **1**.
144. Lu, Y., et al., *In vivo behavior of near infrared-emitting quantum dots*. Biomaterials, 2013. **34**(17): p. 4302-4308.

145. Chien, Y.-H., et al., *Near-Infrared Light Photocontrolled Targeting, Bioimaging, and Chemotherapy with Caged Upconversion Nanoparticles in Vitro and in Vivo*. ACS Nano, 2013. **7**(10): p. 8516-8528.
146. Escobedo, J.O., et al., *NIR dyes for bioimaging applications*. Current Opinion in Chemical Biology, 2010. **14**(1): p. 64-70.
147. Wehrenberg, B.L., C. Wang, and P. Guyot-Sionnest, *Interband and Intraband Optical Studies of PbSe Colloidal Quantum Dots*. The Journal of Physical Chemistry B, 2002. **106**(41): p. 10634-10640.
148. Harrison, M.T., et al., *Wet chemical synthesis and spectroscopic study of CdHgTe nanocrystals with strong near-infrared luminescence*. Materials Science and Engineering: B, 2000. **69-70**(0): p. 355-360.
149. Schumann, K., *[The toxicological estimation of the heavy metal content (Cd, Hg, Pb) in food for infants and small children]*. Z Ernährungswiss, 1990. **29**(1): p. 54-73.
150. Priyam, A., et al., *Synthesis and spectral studies of cysteine-capped CdS nanoparticles*. Research on chemical intermediates, 2005. **31**(7): p. 691-702.
151. Carrillo-Carrión, C., et al., *Selective quantification of carnitine enantiomers using chiral cysteine-capped CdSe (ZnS) quantum dots*. Analytical chemistry, 2009. **81**(12): p. 4730-4733.
152. Zhang, Y.-h., et al., *L-Cysteine-coated CdSe/CdS core-shell quantum dots as selective fluorescence probe for copper (II) determination*. Microchemical Journal, 2008. **89**(2): p. 142-147.
153. Ding, L., et al., *Spectroscopic studies on the thermodynamics of L-cysteine capped CdSe/CdS quantum dots—BSA interactions*. Journal of fluorescence, 2011. **21**(1): p. 17-24.
154. Li, M., et al., *Preparation and purification of L-cysteine capped CdTe quantum dots and its self-recovery of degenerate fluorescence*. Journal of luminescence, 2010. **130**(10): p. 1935-1940.
155. Turunen, M., et al., *Efficient adventitial gene delivery to rabbit carotid artery with cationic polymer-plasmid complexes*. Gene therapy, 1999. **6**(1): p. 6-11.
156. Honoré, I., et al., *Transcription of plasmid DNA: Influence of plasmid DNA/polyethylenimine complex formation*. Journal of Controlled Release, 2005. **107**(3): p. 537-546.
157. Jeong, G.-J., et al., *Biodistribution and tissue expression kinetics of plasmid DNA complexed with polyethylenimines of different molecular weight and structure*. Journal of Controlled Release, 2007. **118**(1): p. 118-125.
158. Patil, S., D. Rhodes, and D. Burgess, *DNA-based therapeutics and DNA delivery systems: A comprehensive review*. The AAPS Journal, 2005. **7**(1): p. E61-E77.
159. Lee, Y., *Enhancement of the Transfection Efficiency of Poly(ethylenimine) by Guanidylation*. Bull. Korean Chem. Soc., 2008. **29**(3): p. 666-668.
160. Li, Y., et al., *Quantum dot-antisense oligonucleotide conjugates for multifunctional gene transfection, mRNA regulation, and tracking of biological processes*. Biomaterials, 2011. **32**(7): p. 1923-31.
161. Duan, H. and S. Nie, *Cell-Penetrating Quantum Dots Based on Multivalent and Endosome-Disrupting Surface Coatings*. Journal of the American Chemical Society, 2007. **129**(11): p. 3333-3338.

162. Song, E.Q., et al. *Tumor cell targeting using folate-conjugated fluorescent quantum dots and receptor-mediated endocytosis*. Clin Chem, 2009. **55**, 955-63 DOI: 10.1373/clinchem.2008.113423.
163. Hong, G., et al., *In Vivo Fluorescence Imaging with Ag₂S Quantum Dots in the Second Near-Infrared Region*. Angewandte Chemie International Edition, 2012. **51**(39): p. 9818-9821.
164. Yang, H.Y., et al., *One-pot synthesis of water-dispersible Ag₂S quantum dots with bright fluorescent emission in the second near-infrared window*. Nanotechnology, 2013. **24**(5): p. 055706.
165. Hocaoglu, I., et al., *Development of highly luminescent and cytocompatible near-IR-emitting aqueous Ag₂S quantum dots*. Journal of Materials Chemistry, 2012. **22**(29): p. 14674.
166. Acar, H.Y., et al., *Emergence of 2MPA as an Effective Coating for Highly Stable and Luminescent Quantum Dots*. Journal of Physical Chemistry C, 2009. **113**(23): p. 10005-10012.
167. Celebi, S., et al., *Synthesis and Characterization of Poly(acrylic acid) Stabilized Cadmium Sulfide Quantum Dots*. The Journal of Physical Chemistry B, 2007. **111**(44): p. 12668-12675.
168. *A Guide to Recording Fluorescence Quantum Yields 2012*; Available from: <http://www.horiba.com/fileadmin/uploads/Scientific/Documents/Fluorescence/quantumyieldstrad.pdf>.
169. Li, H., W.Y. Shih, and W.-H. Shih, *Synthesis and Characterization of Aqueous Carboxyl-Capped CdS Quantum Dots for Bioapplications*. Industrial & Engineering Chemistry Research, 2007. **46**(7): p. 2013-2019.
170. Choosakoonkriang, S., et al., *Biophysical characterization of PEI/DNA complexes*. Journal of Pharmaceutical Sciences, 2003. **92**(8): p. 1710-1722.
171. Ziebarth, J.D. and Y. Wang, *Understanding the protonation behavior of linear polyethylenimine in solutions through Monte Carlo simulations*. Biomacromolecules, 2010. **11**(1): p. 29-38.
172. von Harpe, A., et al., *Characterization of commercially available and synthesized polyethylenimines for gene delivery*. Journal of Controlled Release, 2000. **69**(2): p. 309-322.
173. Acar, H.Y., et al., *Development of Highly Stable and Luminescent Aqueous CdS Quantum Dots with the Poly(acrylic acid)/Mercaptoacetic Acid Binary Coating System*. J Nanosci Nanotechnol, 2009. **9**(5): p. 2820-2829.
174. Madelung, O., *Semiconductors: Data Handbook*. 2004: Verlag Berlin Heidelberg Newyork: Springer.
175. Chen, R., et al., *Silver sulfide nanoparticle assembly obtained by reacting an assembled silver nanoparticle template with hydrogen sulfide gas*. Nanotechnology, 2008. **19**(45): p. 455604.
176. Li, J., et al., *Enhanced-electrocatalytic activity of Ni_{1-x}Fe_x alloy supported on polyethyleneimine functionalized MoS₂ nanosheets for hydrazine oxidation*. RSC Advances, 2014. **4**(4): p. 1988.
177. Kaletta, T. and M.O. Hengartner, *Finding function in novel targets: C. elegans as a model organism*. Nature Reviews Drug Discovery, 2006. **5**(5): p. 387-399.
178. Perkins, L.A., et al., *Mutant sensory cilia in the nematode Caenorhabditis elegans*. Developmental biology, 1986. **117**(2): p. 456-487.

179. Smith, H. and W.C. Campbell, *Effect of ivermectin on Caenorhabditis elegans larvae previously exposed to alcoholic immobilization*. The Journal of parasitology, 1996. **82**(1): p. 187-188.
180. Choy, R.K., J.M. Kemner, and J.H. Thomas, *Fluoxetine-resistance genes in Caenorhabditis elegans function in the intestine and may act in drug transport*. Genetics, 2006. **172**(2): p. 885-892.
181. Duman, F.D., et al., *Highly luminescent and cytocompatible cationic Ag 2 S NIR-emitting quantum dots for optical imaging and gene transfection*. Nanoscale, 2015. **7**(26): p. 11352-11362.
182. Arvizo, R.R., et al., *Effect of nanoparticle surface charge at the plasma membrane and beyond*. Nano letters, 2010. **10**(7): p. 2543-2548.
183. Cho, E.C., et al., *Understanding the role of surface charges in cellular adsorption versus internalization by selectively removing gold nanoparticles on the cell surface with a I2/KI etchant*. Nano letters, 2009. **9**(3): p. 1080-1084.
184. Schipper, M.L., et al., *Particle Size, Surface Coating, and PEGylation Influence the Biodistribution of Quantum Dots in Living Mice*. Small, 2009. **5**(1): p. 126-134.
185. Xie, J., et al., *Controlled PEGylation of Monodisperse Fe₃O₄ Nanoparticles for Reduced Non-Specific Uptake by Macrophage Cells*. Advanced Materials, 2007. **19**(20): p. 3163-3166.
186. Huang, F.-W., et al., *PEGylated PEI-based biodegradable polymers as non-viral gene vectors*. Acta biomaterialia, 2010. **6**(11): p. 4285-4295.
187. Bouma, J., et al., *Anthracycline antitumour agents*. Pharmaceutisch Weekblad, 1986. **8**(2): p. 109-133.
188. Alakhov, V., et al., *Block copolymer-based formulation of doxorubicin. From cell screen to clinical trials*. Colloids and surfaces B: Biointerfaces, 1999. **16**(1): p. 113-134.
189. Andreopoulou, E., et al., *Pegylated liposomal doxorubicin HCL (PLD; Caelyx/Doxil®): Experience with long-term maintenance in responding patients with recurrent epithelial ovarian cancer*. Annals of Oncology, 2007. **18**(4): p. 716-721.
190. Sharma, P.K. and S.R. Bhatia, *Effect of anti-inflammatories on Pluronic® F127: micellar assembly, gelation and partitioning*. International journal of pharmaceutics, 2004. **278**(2): p. 361-377.
191. Chandra, S., et al., *Dendrimer–Doxorubicin conjugate for enhanced therapeutic effects for cancer*. Journal of Materials Chemistry, 2011. **21**(15): p. 5729-5737.
192. He, Q., et al., *In vivo biodistribution and urinary excretion of mesoporous silica nanoparticles: effects of particle size and PEGylation*. small, 2011. **7**(2): p. 271-280.
193. Meng, H., et al., *Use of size and a copolymer design feature to improve the biodistribution and the enhanced permeability and retention effect of doxorubicin-loaded mesoporous silica nanoparticles in a murine xenograft tumor model*. ACS nano, 2011. **5**(5): p. 4131-4144.
194. Skinner, S.A., P.J. Tutton, and P.E. O'Brien, *Microvascular architecture of experimental colon tumors in the rat*. Cancer research, 1990. **50**(8): p. 2411-2417.
195. Matsumura, Y. and H. Maeda, *A new concept for macromolecular therapeutics in cancer chemotherapy: mechanism of tumorotropic accumulation of proteins*

- and the antitumor agent smancs. *Cancer research*, 1986. **46**(12 Part 1): p. 6387-6392.
196. Greish, K., et al., *Enhanced permeability and retention (EPR) effect and tumor selective delivery of anticancer drugs*. *Delivery of protein and peptide drugs in cancer*, 2006: p. 37-52.
197. Sigal, A. and V. Rotter, *Oncogenic mutations of the p53 tumor suppressor: the demons of the guardian of the genome*. *Cancer research*, 2000. **60**(24): p. 6788-6793.
198. Efeyan, A. and M. Serrano, *p53: guardian of the genome and policeman of the oncogenes*. *Cell cycle*, 2007. **6**(9): p. 1006-1010.
199. Campbell, C., et al., *p53 mutations are common and early events that precede tumor invasion in squamous cell neoplasia of the skin*. *Journal of investigative dermatology*, 1993. **100**(6): p. 746-748.
200. Biegging, K.T. and L.D. Attardi, *Deconstructing p53 transcriptional networks in tumor suppression*. *Trends in cell biology*, 2012. **22**(2): p. 97-106.
201. Chen, G., et al., *MRI-visible polymeric vector bearing CD3 single chain antibody for gene delivery to T cells for immunosuppression*. *Biomaterials*, 2009. **30**(10): p. 1962-1970.
202. Michael D. Abramoff, P.J.M., Sunanda J. Ram, *Image Processing with ImageJ*. *Biophotonics International*, 2004. **11**: p. 36-42.
203. Riccardi, C. and I. Nicoletti, *Analysis of apoptosis by propidium iodide staining and flow cytometry*. *Nature protocols*, 2006. **1**(3): p. 1458-1461.
204. Larsen, A.K., A. Skladanowski, and K. Bojanowski, *The roles of DNA topoisomerase II during the cell cycle*, in *Progress in cell cycle research*. 1996, Springer. p. 229-239.
205. Adina, A.B., et al., *Combination of ethanolic extract of Citrus aurantifolia peels with doxorubicin modulate cell cycle and increase apoptosis induction on MCF-7 cells*. *Iranian Journal of Pharmaceutical Research*, 2014. **13**(3): p. 919-926.
206. Hope, F. *Studies Link Topoisomerase Interrupting Drugs to Autism*. [cited 2016 15 Dec]; Available from: <https://floxiehope.com/2015/04/27/studies-link-topoisomerase-interrupting-drugs-to-autism/>.
207. Chang, L., et al., *PI3K/Akt/mTOR pathway inhibitors enhance radiosensitivity in radioresistant prostate cancer cells through inducing apoptosis, reducing autophagy, suppressing NHEJ and HR repair pathways*. *Cell death & disease*, 2014. **5**(10): p. e1437.
208. M. Laird Forrest, J.T.K., and Daniel W. Pack, *A Degradable Polyethylenimine Derivative with Low Toxicity for Highly Efficient Gene Delivery*. *Bioconjugate Chemistry*, 2003. **14**: p. 934-940.
209. Lv, H., et al., *Toxicity of cationic lipids and cationic polymers in gene delivery*. *Journal of Controlled Release*, 2006. **114**(1): p. 100-109.
210. *Amino Acid Structures*. [cited 2016 5 Dec]; Available from: <http://www.cem.msu.edu/~cem252/sp97/ch24/ch24aa.html>.
211. *Zetasizer Nano Series User Manual*. 2004.
212. Gibson, N., et al., *Colloidal stability of modified nanodiamond particles*. *Diamond and Related Materials*, 2009. **18**(4): p. 620-626.
213. Boyer, C., et al., *The design and utility of polymer-stabilized iron-oxide nanoparticles for nanomedicine applications*. *NPG Asia Mater*, 2010. **2**: p. 23-30.

214. Tabata, Y. and Y. Ikada, *Phagocytosis of polymer microspheres by macrophages*, in *New Polymer Materials*. 1990, Springer Berlin Heidelberg. p. 107-141.
215. Soo Choi, H., et al., *Renal clearance of quantum dots*. *Nat Biotech*, 2007. **25**(10): p. 1165-1170.
216. Wang, Y., et al., *One-Pot Synthesis of CdSe Quantum Dots Using Selenium Dioxide as a Selenium Source in Aqueous Solution*. *Bulletin of the Korean Chemical Society*, 2011. **32**(7): p. 2316-2318.
217. Sivasankar, K. and N. Padmavathy, *Green synthesis of CdSe nanoparticles at room temperature and its characterisation*. *Micro & Nano Letters*, 2011. **6**(3): p. 144-146.
218. Sun, Q., et al., *Aqueous synthesis and characterization of TGA-capped CdSe quantum dots at freezing temperature*. *Molecules*, 2012. **17**(7): p. 8430-8.
219. <1-s2.0-S0022175910000323-main.pdf>.
220. Laverdant, J., et al., *Experimental Determination of the Fluorescence Quantum Yield of Semiconductor Nanocrystals*. *Materials*, 2011. **4**(7): p. 1182.
221. Jiang, P., et al., *Emission-Tunable Near-Infrared Ag₂S Quantum Dots*. *Chemistry of Materials*, 2012. **24**(1): p. 3-5.
222. Mir, W.J., et al., *Origin of Unusual Excitonic Absorption and Emission from Colloidal Ag₂S Nanocrystals: Ultrafast Photophysics and Solar Cell*. *The Journal of Physical Chemistry Letters*, 2015. **6**(19): p. 3915-3922.
223. Madelung, O., *Semiconductors: Data Handbook*. 3rd edition ed. 2004.
224. Marlene C. Morris, H.F.M., Eloise H. Evans, Boris Paretzkin, Harry S. Parker, Nicolas C. Panagiotopoulos, *Standard X-ray Diffraction Powder Patterns*. 1960: Washington D.C.. UNT Digital Library.
225. Duman, F.D., et al., *Highly luminescent and cytocompatible cationic Ag₂S NIR-emitting quantum dots for optical imaging and gene transfection*. *Nanoscale*, 2015. **7**(26): p. 11352-62.
226. Cassette, E., et al., *Design of new quantum dot materials for deep tissue infrared imaging*. *Adv Drug Deliv Rev*, 2013. **65**(5): p. 719-31.
227. Gao, X., et al., *In vivo molecular and cellular imaging with quantum dots*. *Curr Opin Biotechnol*, 2005. **16**(1): p. 63-72.
228. Smith, A.M., et al., *Bioconjugated quantum dots for in vivo molecular and cellular imaging*. *Adv Drug Deliv Rev*, 2008. **60**(11): p. 1226-40.
229. Chen, G., et al., *Tracking of transplanted human mesenchymal stem cells in living mice using near-infrared Ag₂S quantum dots*. *Advanced Functional Materials*, 2014. **24**(17): p. 2481-2488.
230. Schroeder, J., et al., *Folate-mediated tumor cell uptake of quantum dots entrapped in lipid nanoparticles*. *Journal of Controlled Release*, 2007. **124**(1): p. 28-34.
231. Zhang, Y., J.M. Liu, and X.P. Yan, *Self-assembly of folate onto polyethyleneimine-coated CdS/ZnS quantum dots for targeted turn-on fluorescence imaging of folate receptor overexpressed cancer cells*. *Anal Chem*, 2013. **85**(1): p. 228-34.
232. Pan, J. and S.S. Feng, *Targeting and imaging cancer cells by folate-decorated, quantum dots (QDs)- loaded nanoparticles of biodegradable polymers*. *Biomaterials*, 2009. **30**(6): p. 1176-83.
233. Geszke, M., et al., *Folic acid-conjugated core/shell ZnS:Mn/ZnS quantum dots as targeted probes for two photon fluorescence imaging of cancer cells*. *Acta Biomater*, 2011. **7**(3): p. 1327-38.

234. Song, Y., et al., *Fluorescent carbon nanodots conjugated with folic acid for distinguishing folate-receptor-positive cancer cells from normal cells*. Journal of Materials Chemistry, 2012. **22**(25): p. 12568.
235. Lee, S., et al., *Mechanism of doxorubicin-induced cell death and expression profile analysis*. Biotechnology Letters, 2002. **24**(14): p. 1147-1151.
236. Carvalho, C., et al., *Doxorubicin: the good, the bad and the ugly effect*. Current medicinal chemistry, 2009. **16**(25): p. 3267-3285.
237. Savla, R., et al., *Tumor targeted quantum dot-mucin 1 aptamer-doxorubicin conjugate for imaging and treatment of cancer*. Journal of controlled release, 2011. **153**(1): p. 16-22.
238. Qi, L. and X. Gao, *Emerging application of quantum dots for drug delivery and therapy*. Expert opinion on drug delivery, 2008. **5**(3): p. 263-267.
239. Duman, F.D., et al., *Impact of reaction variables and PEI/l-cysteine ratio on the optical properties and cytocompatibility of cationic Ag 2 S quantum dots as NIR bio-imaging probes*. RSC Advances, 2016. **6**(81): p. 77644-77654.
240. Chan, W.C., et al., *Luminescent quantum dots for multiplexed biological detection and imaging*. Current opinion in biotechnology, 2002. **13**(1): p. 40-46.
241. Xue, B., et al., *Synthesis of NAC capped near infrared-emitting CdTeS alloyed quantum dots and application for in vivo early tumor imaging*. Dalton transactions, 2012. **41**(16): p. 4935-4947.
242. Deng, D., et al., *High-quality CuInS₂/ZnS quantum dots for in vitro and in vivo bioimaging*. Chemistry of Materials, 2012. **24**(15): p. 3029-3037.
243. Wang, Y., et al., *Hepatocyte-targeting gene transfer mediated by galactosylated poly(ethylene glycol)-graft-polyethylenimine derivative*. Drug Des Devel Ther, 2013. **7**: p. 211-21.
244. Patil, S., et al., *Protein adsorption and cellular uptake of cerium oxide nanoparticles as a function of zeta potential*. Biomaterials, 2007. **28**(31): p. 4600-4607.
245. Reddy, J.A. and P.S. Low, *Folate-mediated targeting of therapeutic and imaging agents to cancers*. Critical Reviews™ in Therapeutic Drug Carrier Systems, 1998. **15**(6).
246. Andreotti, P.E., et al., *Chemosensitivity testing of human tumors using a microplate adenosine triphosphate luminescence assay: clinical correlation for cisplatin resistance of ovarian carcinoma*. Cancer research, 1995. **55**(22): p. 5276-5282.
247. Ulukaya, E., et al., *The MTT assay yields a relatively lower result of growth inhibition than the ATP assay depending on the chemotherapeutic drugs tested*. Toxicology in vitro, 2008. **22**(1): p. 232-239.
248. Minko, T., et al., *Molecular targeting of drug delivery systems to cancer*. Current Drug Targets, 2004. **5**(4): p. 389-406.
249. Schutte, B., et al., *Annexin V binding assay as a tool to measure apoptosis in differentiated neuronal cells*. Journal of neuroscience methods, 1998. **86**(1): p. 63-69.
250. Aubry, J.-P., et al., *Annexin V used for measuring apoptosis in the early events of cellular cytotoxicity*. Cytometry, 1999. **37**(3): p. 197-204.
251. Perry, S.W., et al., *Mitochondrial membrane potential probes and the proton gradient: a practical usage guide*. BioTechniques, 2011. **50**(2): p. 98-115.

252. Pendergrass, W., N. Wolf, and M. Poot, *Efficacy of MitoTracker Green™ and CMXrosamine to measure changes in mitochondrial membrane potentials in living cells and tissues*. Cytometry Part A, 2004. **61**(2): p. 162-169.
253. Kovalcsik, E., et al., *Poly(I:C)-induced tumour cell death leads to DC maturation and Th1 activation*. Cancer Immunology, Immunotherapy, 2011. **60**(11): p. 1609-1624.
254. Jiang, Q., H. Wei, and Z. Tian, *Poly I:C enhances cycloheximide-induced apoptosis of tumor cells through TLR3 pathway*. BMC Cancer, 2008. **8**: p. 12.
255. Vercammen, E., J. Staal, and R. Beyaert, *Sensing of viral infection and activation of innate immunity by toll-like receptor 3*. Clin Microbiol Rev, 2008. **21**(1): p. 13-25.
256. Chin, A.I., et al., *Toll-like receptor 3-mediated suppression of TRAMP prostate cancer shows the critical role of type I interferons in tumor immune surveillance*. Cancer Res, 2010. **70**(7): p. 2595-603.
257. Liu, F., et al., *Mechanism of naked DNA clearance after intravenous injection*. The journal of gene medicine, 2007. **9**(7): p. 613-619.
258. Chiou, H.C., et al., *Enhanced resistance to nuclease degradation of nucleic acids complexed to asialoglycoprotein-polylysine carriers*. Nucleic acids research, 1994. **22**(24): p. 5439-5446.
259. Fitzsimmons, R. and H. Uludağ, *Specific effects of PEGylation on gene delivery efficacy of polyethylenimine: interplay between PEG substitution and N/P ratio*. Acta biomaterialia, 2012. **8**(11): p. 3941-3955.
260. Rangelov, S. and A. Pispas, *Polymer and polymer-hybrid nanoparticles: from synthesis to biomedical applications*. 2013: CRC Press.

VITA

Fatma Demir Duman was born in Adana, Turkey in 1986. She completed Bahcelievler Anatolian High School (Istanbul) in 2004. She received her B.S. degree from the Department of Molecular Biology and Genetics and second B.S. degree from Chemistry (double major program) at Istanbul Technical University in 2010. During her B.S, she has visited Technical University of Munich, Germany, for 11 months as an Erasmus exchange student (2007-2008). In 2012, she completed her M.S. degree in Bioengineering department of Hacettepe University. In 2012, she started Ph.D. programme in the department of Material Science and Engineering, Koc University (Istanbul).